Structure and preparation of polar and semipolar InN surfaces

vorgelegt von
Diplom-Physikerin
Daria Skuridina
aus Moskau

Von der Fakultät II - Mathematik und Naturwissenschaften
der Technischen Universität Berlin
zur Erlangung des akademischen Grades
Doktor der Naturwissenschaften
Dr. rer. nat.

genehmigte Dissertation

Promotionsausschuss:

Vorsitzender: Prof. Dr. rer. nat. M. Lehmann
Gutachter: Prof. Dr. rer. nat. N. Esser
Gutachter: Prof. Dr. rer. nat. M. Kneissl
Gutachter: Dr. P. Ruterana

Tag der wissenschaftlichen Aussprache: 20. Mai 2014

Berlin 2014
D 83

Parts of this work have already been published in:

- D. V. Dinh, M. Pristovsek, S. Solopow, **D. Skuridina**, and M. Kneissl, Physica Status Solidi C **9**, 977-981, (2012), *Comparison study of N- and In-polar {0001} InN layers grown by MOVPE.*

- S. Pandey, D. Cavalcoli, A. Minj, B. Fraboni, A. Cavallini, **D. Skuridina**, P. Vogt, M. Kneissl, Acta Materialia **60**, 3176-3180, (2012), *Mobility-limiting mechanisms in polar semiconductor heterostructures.*

- D. V. Dinh, **D. Skuridina**, S. Solopow, F. Ivaldi, S. Kret, M. Pristovsek, P. Vogt, M. Kneissl, Journal of Applied Physics **112**, 013530, (2012), *Growth and characterization of semipolar ($11\bar{2}2$) InN.*

- D. V. Dinh, **D. Skuridina**, S. Solopow, M. Pristovsek, P. Vogt and M. Kneissl, Journal of Crystal Growth **376**, 17-22, (2013), *Role of nitridation on polarity and growth of InN by metal-organic vapor phase epitaxy.*

- **D. Skuridina**, D. V. Dinh, B. Lacroix, P. Ruterana, M.Hoffmann, Z. Sitar, M. Pristovsek, M. Kneissl and P. Vogt, Journal of Applied Physics **114**, 173503, (2013), *Polarity determination of polar and semipolar ($11\bar{2}2$) InN and GaN layers by valence band photoemission spectroscopy.*

- **D. Skuridina**, D. V. Dinh, M. Pristovsek, B. Lacroix, M.-P. Chauvat, P. Ruterana, M. Kneissl and P. Vogt, Applied Surface Science **307**, 461-467, (2014), *Surface and crystal structure of nitridated sapphire substrates and their effect on polar InN layers.*

Abbreviations and Acronyms

CBED	Convergent Beam Electron Diffraction
DFT	Density Functional Theory
DOS	Density of States
FWHM	Full Width at Half Maximum
HRTEM	High-Resolution Transmission Electron Microscopy
FWHM	Full Width at Half Maximum
LEED	Low Energy Electron Diffraction
MBE	Molecular Beam Epitaxy
MEAglow	Migration Enhanced Afterglow
ML	Monolayer
MOVPE	Metal-Organic Vapor Phase Epitaxy
PES	Photoemission (Photoelectron) Spectroscopy
STM	Scanning Tunneling Microscopy
STS	Scanning Tunneling Spectroscopy
TEM	Transmission Electron Microscopy
UHV	Ultra-High Vacuum
VB	Valence Band
VBM	Valence Band Maximum
XPS	X-ray Photoelectron Spectroscopy
RMS	Root-Mean Square

Contents

1 Introduction

Over the past 20 years group-III nitrides have evolved from being the subject of academic research and general interest into practical applications in optoelectronic devices. Especially, a remarkable increase of attention is observed by the fabrication of light emitting diodes (LED) that cover a wide spectral range: from deep ultraviolet through the visible up to the near infrared. The direct band gap of binary and ternary group-III alloys, e.g. GaN, InN, InGaN, AlInN, makes these materials perhaps one of the most efficient system for light generation.

Nowadays, LEDs are slowly replacing light blubs (filament lamps) for street, buildings and home illumination, as well as for industrial purposes. One of the main purposes to replace filament lamps and other kind of illumination by LEDs is the extremely high energy saving capacity of the later. Moreover, LEDs can be found in cell-phones, displays, traffic lights, while laser diodes based on nitrides are used in memory storage systems like CD and DVD-players.

Among all nitrides, particulary InN has attracted much attention in the last decade due to its unexpected low band gap of $\sim 0.7\,\mathrm{eV}$ [1], electron accumulation layer [2, 3] and theoretically predicted high electron mobility [4]. This rising of interest is also caused by the possible applications of InN not only in LEDs [5] but also in sensors [6], high-speed field-effect transistors operating at near THz region [7] and solar cells [8]. However, the poor crystalline quality, build-in electrostatic fields and challenges related with the *p*-doping of InN have slowered the progress of achieving and fabricating cheap and high efficient InN-based optoelectronic devices.

Nevertheless, the build-in electrostatic fields in the crystal and rough surfaces are not always an undesired material property. For instance, rough surfaces of layers were found to be preferable for solar cell applications, where the surface roughness is used to keep the light trapped in the material instead of letting it reflect back from the system [9]. For nitride-based high-electron mobility transistors (HEMT), the surface is found to be a main source of electrons for the two-dimensional electron gas [10], hence, spontaneous and piezoelectric polarization fields are beneficial for HEMTs but crucial for solar cells, sensors, terahertz radiation and radiative efficiency of LEDs [11].

Most of the aforementioned devices consist of multi-layer homo- and/or heterostructures, which imply the formation of several interfaces in a grown material system. Poor quality of the homo- or heterointerfaces can strongly influence and degrade the performance of any electronic device. Improvement of the surface and interface quality of the crystals is of a great interest and implies a good understanding of the properties of a sin-

gle layer. However, surface properties of nitrides, e.g InN, are still not fully understood and contradictory results can be found in the literature.

Growth of optoelectronic devices for industrial purposes and a world-wide market are mainly performed by metal-organic vapor phase epitaxy (MOVPE). Thus, high crystalline quality layers have to be grown by MOVPE which is still a challenging issue in the case of InN, where the smoother and thicker layers are usually grown by molecular beam epitaxy (MBE) [12, 13].

Nowadays, III-nitrides based devices are mainly grown along the polar *c*-plane direction. Crystal polarity was found to affect surface morphology and roughness of InN and GaN layers [14–17], which also influences the interfacial properties, e.g. of a multi-layer optoelectronic device and its performance. While for the *c*-plane InN and GaN layers the polarity is well-investigated, not much is known about the possible influence of the polarity along the *c*-direction for semipolar orientations. An example for this influence was given recently: electroluminescence from the semipolar $(20\bar{2}\bar{1})$ LED was found to be more strongly polarized than the light from $(20\bar{2}1)$ LEDs [18]. Thus, knowing the polarity is important to control the electronic and structural properties of a subsequently grown device.

However, in last couple of years more and more attention has been paid to the devices on semipolar or nonpolar planes [18], due to the suppression or elimination of the build-in electrostatic fields. A challenge in the fabrication of the semi- or nonpolar-based devices is the lack of high quality layers and expensive cost caused by small surface area of the free-standing substrates. Growth kinetics, crystal and surface quality of the semi- and nonpolar layers are poorly understood and requires more investigation.

As a consequence of the described above problems and challenges, this thesis is mainly dedicated to the understanding and investigation of the surface properties of single InN layers. In the frame of this work, the surface properties of the quality InN layers grown by MOVPE has been studied, and compared to the InN layers grown by alternative commercial techniques, e.g. molecular beam epitaxy and migration enhanced afterglow epitaxy [19,20]. Atomic surface structure of polar (0001), $(000\bar{1})$ and semipolar $(11\bar{2}2)$ InN layers have been analyzed by a number of microscopy and spectroscopy techniques under ultra high vacuum conditions. Moreover, one chapter is dedicated to thin semipolar $(20\bar{2}1)$ $In_xGa_{1-x}N$ $(6\% < x < 10\%)$ layers.

Chapters 2-3 of this work introduce fundamental properties and state-of-the-art of InN layers, as well as describe analytical methods and UHV equipment used in this work. Chapter 4 is dedicated to a new method for polarity determination of polar and semipolar thin InN and GaN layers. The method is based on photoelectron emission from the layers and has a number of advantages, compared to the commonly used methods, e.g. wet etching and convergent beam electron diffraction. Chapter 5 deals with an important issue of sapphire substrate nitridation process and its effect on the overgrown polar InN layers. The atomic structure of clean sapphire substrates prior and after the nitridation process will be analyzed in details and discussed in terms of improvement of the InN surface and crystal quality. The surface analysis of the different reconstructed

N- and In-polar InN layers will be described in Chapter 6. The crystal and electrical properties of the polar InN layers grown by different deposition methods will be investigated and compared. Thermal oxidation of the In-polar InN layer and formation of a thin In_2O_3 layer on top of InN upon this treatment will be discussed in Chapter 7. The last Chapter 8 deals with semipolar $(11\bar{2}2)$ InN and semipolar $(20\bar{2}1)$ $In_xGa_{1-x}N$ layers with low amount of indium ($6\% < x < 10\%$). Surface topography, atomic reconstruction and electrical properties of these layers will be described and compared with the polar layers. A summary and an outlook of this thesis will be given in Chapter 9.

2 Fundamental Properties of Indium Nitride

2.1 Structural Properties

Indium nitride belongs to the group-III-V semiconductors and crystalizes in hexagonal wurtzite or cubic zinc blende structure. From the thermodynamic point of view, the wurtzite structure (also called α-InN phase) of InN is stable, while the zinc blende phase is metastable. The structural models of InN are shown in Fig. 2.1 (a). Wurtzite InN is formed by two sublattices, where each lattice is occupied by either group-III or nitrogen atoms and has a hexagonal close-packed (hcp) lattice. The hcp lattice arrangement implies a sequence of alternating layers along the [0001] direction, such as ABAB, where A and B correspond to each atomic stack, as shown in Fig. 2.1 (a). The zinc blende structure consist of two (i.e. group-III and nitrogen) face-centered cubic (fcc) lattices, which form ABCABC stacking sequence along the [111] direction. Wurtzite and zinc blende crystal structures have a tetrahedral coordination, meaning that each atom has four neighboring atoms of different type. The tetrahedral bonding is caused by the sp^3 hybridization of the group-III (e.g. indium) and group-V (e.g. nitrogen) atoms, where an *s* orbital is combined with three *p* orbitals resulting in bond angles of $109° 28´$ between atoms in crystal. In this work, investigations were performed only on wurtzite group-III nitride layers due to their stable structure and growth on hexagonal substrates or templates.

The wurtzite structure is defined by the length of the basal hexagon (*a* lattice constants), the height of the hexagon (*c* lattice constant) and the parameter *u*, which is the anion-cation bond length along the *c*-axis. The parameter *u* is defined as $u = (c/a)^2$, where for the the ideal wurtzite structure $u = 3/8 = 0.375$. However, effects in crystal lattice, i.e. electric fields originating from crystal anisotropy, can deform the ideal crystal structure, hence the parameter *u* for InN has been reported to be 0.379 [21]. In the case of InN, the *a* and *c* lattice constants are determined to be 3.532 nm and 5.669 nm for the wurtzite crystal [22]. The zinc blende structure is characterized by the $a = 4.980$ nm lattice constant [23].

The Miller-Bravais indexing system is used for a hexagonal structure to identify the different crystal directions, planes or axis. In this indexing system a fourth axis is introduced in the plane of *x* and *y* axes in order to avoid a dissimilar indices for crystallographically equivalent planes. Hence, the indices (*hkil*), where $i = -(h+k)$, are used

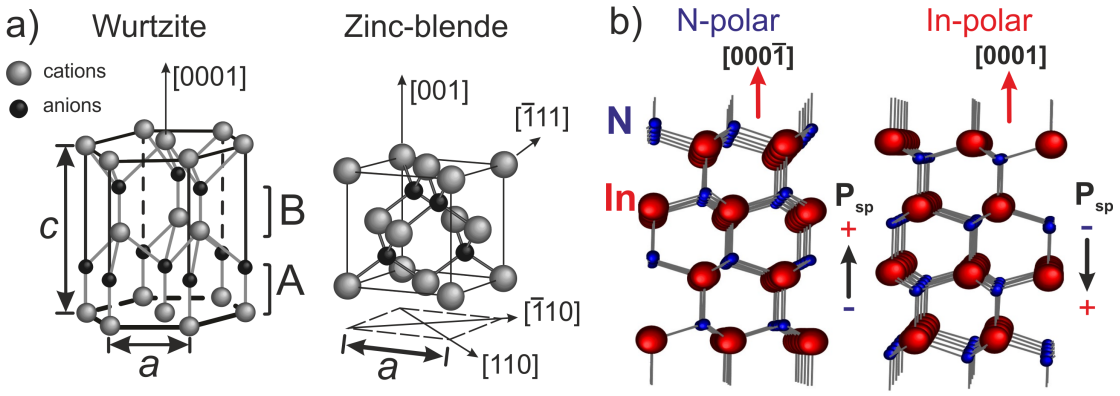

Figure 2.1: a) Wurtzite and zinc blende crystal structure of III-nitrides, b) crystal structure of N- and In-polar InN.

in this case. The [0001] direction in the wurtzite structure is equivalent to the [111] direction in the zinc blende (see Fig. 2.1 (a)). The {0001} plane is also called polar, while the plane perpendicular to it is called non-polar, e.g. m-plane ($1\bar{1}00$) and a-plane ($11\bar{2}0$). Other planes are called semipolar and form an angle of $0° < \alpha < 90°$ with the hexagon base, e.g. for semipolar ($11\bar{2}0$) $\alpha \approx 58°$, for semipolar ($20\bar{2}1$) $\alpha \approx 75°$ (see Fig. 2.2).

The wurtzite group-III-nitride crystal is non-centrosymmetric with a $P6_3mc$ space group symmetry. This results in the anisotropic properties of the wurtzite crystal, i.e. thermal and optical properties vary depending on the crystallographic direction. The *c*-direction is not isotropic along the [0001] and the [000$\bar{1}$] directions and group-III- and N-polar orientations can be distinguished, as shown in Fig. 2.1 (b) for InN. Polarity is known to affect the surface topography during epitaxial growth of the nitride materials, e.g. surfaces of N-polar layers tend to be smoother compared to In-polar InN layers [14, 15]. However, the situation is reversed for polar AlN and GaN layers [16, 17]. It is important to separate terms "surface or crystal polarity" that refers to crystallographic direction, and "surface termination" that correspond to the topmost atoms terminated the grown layer.

The hexagonal lattice symmetry without inversion center and the large electronegativity difference between nitrogen (electronegativity 3.04 [24]) and the group-III atoms (for instance, electronegativity of indium atom is 1.78 [24]) lead to strong charge transfer between the bonded atoms. This results in strong piezoelectric and spontaneous polarization fields along the *c*-direction [25, 26]. Hence, the total polarization field in a wurtzite crystal is the sum of piezoelectric and spontaneous polarization fields.

In N-polar group-III-nitride wurtzite layers, the polarization-induced charges are positive at the surface and negative at the substrate, thus an internal electric field points towards the [0001] direction, whereas the spontaneous polarization P_{sp} points toward the surface as sketched in Fig. 2.1 (b). For the group-III-polar nitrides, induced charges and field directions are inverted. Direction of the piezoelectric field in nitrides depends on

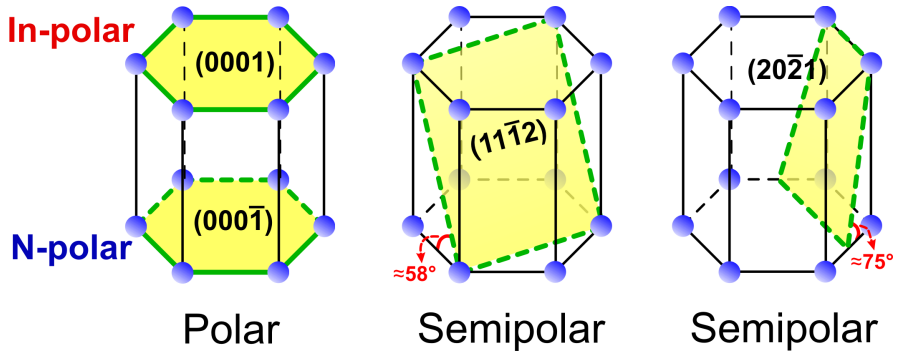

Figure 2.2: Crystal orientations of the wurtzite group-III-nitrides (e.g. InN): polar (0001) and (000$\bar{1}$) , semipolar (11$\bar{2}$2) and (20$\bar{2}$1)planes are highlighted.

Table 2.1: Spontaneous polarization constants for AlN, GaN and InN layers reported in Ref. [26].

	P_{sp} (C/m^2)
AlN	-0.081
GaN	-0.029
InN	-0.032

the induced strain: for group-III-polar layers with compressive or tensile strain, piezoelectric field points towards the [000$\bar{1}$] or [0001] directions, respectively [26, 27]. Values of spontaneous polarization and piezoelectric constants for III-nitrides are shown in Tab.2.1.

The built-in electric field significantly influences the material properties, e.g. the carrier distribution, consequently affecting the performance of optoelectronic devices due to the quantum-confined Stark effect [28]. However, the built-in electric fields can be reduced on semipolar planes [29] or eliminated on non-polar planes [11].

2.1.1 Methods for Polarity Determination

The crystal polarity affects not only the surface topography of InN layers, as was already mentioned, but also their optoelectronic properties. It has been shown that In-polar InN layers exhibit a shift for the low-temperature photoluminescence (PL) peak to higher energies compared to N-polar layers [14]. The shift is associated with residual biaxial compressive stress of In-polar InN layers, while N-polar layers are relaxed. In Ref. [30] it was reported that In-polar InN layers have a stronger surface downward band bending (hence, stronger surface electron accumulation) than N-polar orientated layers, due to the different energetic positions of occupied surface states for each layer. Moreover, the electron affinity of polar InN surfaces was found to be different depending on polarity:

4.7 eV for In-polar and 4.6 eV for N-polar layers [31]. This difference was attributed to the spontaneous polarization in the crystal. Thus, knowing the polarity of the InN layer is important to control its surface, structural and optoelectronic properties.

Different experimental methods have been demonstrated for polarity determination of polar III-nitrides, e.g. co-axial impact collision ion scattering spectroscopy [32, 33], atomic hydrogen irradiation [34], convergent beam electron diffraction (CBED) [35,36] or method based on the circular photogalvanic effect [37]. The most commonly used methods for polar (0001) and $(000\bar{1})$ InN and GaN remain wet chemical etching by potassium hydroxide (KOH) and CBED [14, 35, 36, 38, 39]. Muto et al. have shown that after the etching by KOH for over 60 min, the N-polar InN layers etched roughly and exhibited hexagonal pyramids, while the In-polar InN layers were etched smoothly showing hexagonal and dot type pits on the surface [38]. The GaN layers etched by KOH showed similar results: N-polar layers formed hexagonal pyramids, while Ga-polar layers remain smooth and unaffected [39]. The CBED method is based on the polarity determination by comparing the experimental diffraction patterns with the CBED patterns simulated through Bloch wave procedures for certain polarity.

All these methods have a number of limitations. For example, obtaining CBED patterns might be impossible due to high defect densities in the crystal structure or insufficient layer thickness. Wet etching can be affected by incorporated impurities or decoration of defects.

Recently, it was shown that the polarity of polar InN layers can be determined by X-ray photoelectron spectroscopy (XPS) using Al K_α X-ray radiation as an excitation source [40]. The method is based on the observation of different valence band (VB) states and their relative intensities. As shown in Fig. 2.3 (a), the domination of the VB peak at ~ 3.5 eV was attributed to the In-polarity, while the domination of the VB peak at ~ 6.7 eV was assigned to the N-polar InN layers. The layers with a mixed polarity (consisting of In- and N-polar coalesced domains) show equal intensity of the VB peaks.

The polar direction of the semipolar orientated III-nitride layers does not point towards the surface normal, thus, its determination is more complicated. The polarity of semipolar $(11\bar{2}2)$ layers along the *c*-direction has been exclusively measured by CBED on 1.5 μm thick GaN layers [41, 42]. An effect of polarity along the *c*-direction on surface and crystal properties of semipolar III-nitride layers has not been studied much yet. However, it was shown recently that electroluminescence from a semipolar $(20\bar{2}\bar{1})$ LED is more polarized than the light from $(20\bar{2}1)$ LEDs [18].

2.2 Band Gap, Electronic Properties and Band Structure

In the literature up to year 2002 the band gap (E_G) of InN was argued to be between 1.8-2.2 eV by measuring absorption spectra of polycrystalline InN layers [43, 44]. Experiments performed by optical absorption and photoluminescence in 2002 by

V. Yu. Davydov et al. revealed the band gap of InN to be around 0.7 eV [1]. Additionally, they explained the reason of the previously reported larger band gap values due to the formation of indium oxide on the surface of the InN layers after sputtering. This assumption is in agreement with Ref. [45], where oxygen incorporation and formation of In_2O_3 crystal grains on InN layers were suggested to be the responsible for the overestimation of the InN band gap. Later, the band gap of InN was reported to be 0.65 eV from optical absorption measurements and 0.63 eV from photoluminescence performed at room temperature [46].

Among all group-III-nitride compounds, InN has the smallest band gap. Therefore, alloys of InN, AlN and GaN cover a wide spectral range: from the near-infrared for InN up to the ultraviolet (UV) for GaN ($E_G = 3.4$ eV) and deep-UV for AlN ($E_G = 6.2$ eV).

InN has also the smallest electron effective mass ($m^* = 0.11 m_o$) compared to GaN and AlN [47], leading to high mobility and saturation velocity. At room temperature, the theoretically calculated mobility for InN was around 4400 $cm^2/(V \cdot s)$, while at 77 K the maximum mobility was estimated to be higher than 30 000 $cm^2/(V \cdot s)$ [4]. Experimentally, one of the highest reported values for electron mobility of InN is $\sim 4000\,cm^2/(V \cdot s)$ [48]. All these make InN a promising candidate for applications in high-speed field-effect transistors operating at near THz region [7], light-emitting diodes [5], sensors [6] and solar cells [8]. However, one of the main reasons that prevents the broad application of InN in optoelectronic devices is the lack of high quality single crystalline layers.

The band structure of wurtzite InN across the Brillouin zone from first principle calculations based on density functional theory (DFT) and quasiparticle (QP) theory is shown in Fig. 2.3 (b). The calculation of the InN band structure was a challenging issue for a long time due to the underestimation of the band gap, where DFT calculations in the local density approximation (LDA) resulted in a negative band gap, i.e. overlap of conduction and valence band states [50]. In order to overcome this problem the In $4d$ electrons were frozen into the core, while considering the In $4d$ electrons as valence electrons resulted in a negative band gap originated from the repulsion between the In $4d$ and N $1s$ electrons [51].

An important characteristic of the InN band structure is a very low position of the conduction band minimum (CBM) at the Γ-point compared to the entire **k** space (Fig. 2.3 (b)). This feature was predicted to be a consequence of the large electron affinity of InN [52]. Fig. 2.3 (b) shows a horizonal lines along the whole band structure labeled as E_B that correspond to the branch point energy that is defined as the average midgap across the entire Brillouin zone [53]. It also defines, which type of defects will be formed: donor-type native defects are favorable if the bulk Fermi level lies below E_B, while acceptor-type defects form if the bulk Fermi level is above the E_B. A strong CB dispersion results in the position of the E_B at 0.87 eV above CBM for wurtzite InN [54], in contrast to other III-V semiconductors, where the E_B lies well below the CBM. As a consequence, the bulk Fermi level lies below the branch point and uninten-

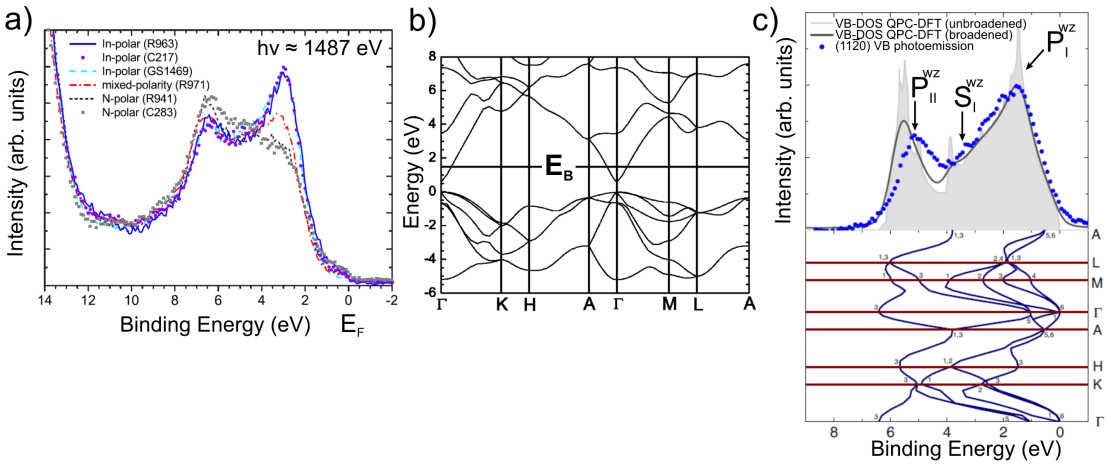

Figure 2.3: a) VB XPS spectra recorded from polar InN layers at normal emission by using an Al K_α X-ray source [40]. b) Quasipartical corrected density functional theory (QPC-DFT) band structure across the Brillouin zone for wurtzite InN, where E_B is a branch point energy [2], c) VB XPS photoemission spectrum of InN after the background subtraction (dots) and calculated QPC-DFT valence band density of states (top image); QPC-DFT VB structure (bottom image) for wurtzite InN layer [49]. The photoemission spectrum is shifted to align the VBM position at 0 eV.

tionally formed native defects are donors. This explains the high unintentional n-type bulk conductivity of InN [55].

Experiments have shown that the surface Fermi level (E_F) is located above the conduction band minimum. In the literature, the reported positions of the surface Fermi level vary between 1.6 eV and 1.0 eV above the valence band maximum (VBM), corresponding to the downward band bending at the surface region [2, 30, 56, 57]. It has been shown that In-polar InN layers possess stronger downward band bending (E_F is $\sim$ 1.4 eV above the VBM), compared to non-polar a-, m-plane and N-polar layers (E_F is $\sim$ 1.0 eV above the VBM) [30]. The consequence of the downward band bending is an electron accumulation layer formed in the near surface region of the InN layer. There is still some discussion concerning the origin of the accumulation layer. First reports assumed that it is an intrinsic property of the InN due to its band structure: for the E_F below the branch point, some donor surface states will remain unoccupied (positively charged), at the same time, this charge will be balanced by a negative space charge that leads to increase of electron concentration near the surface [2,56]. However, recently it has been reported that E_F is pinned well below the CBM on cleaved $(11\bar{2}0)$ InN by using cross-sectional scanning photoelectron microscopy/spectroscopy or cross-sectional scanning tunneling microscopy/spectroscopy (STM/STS) [58,59]. In the work of Ebert et al., it was shown that the intrinsic surface states are absent in the band gap of the cleaved InN layer [59]. Hence, an electron accumulation was attributed rather to an ex-

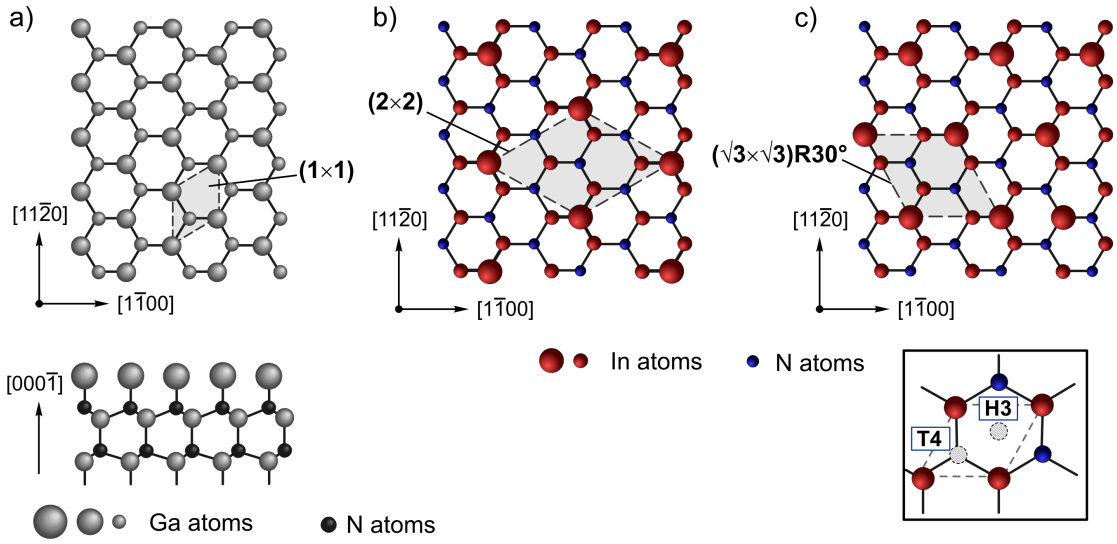

Figure 2.4: a) Top and side view of the (000$\bar{1}$) GaN layer with (1×1) reconstruction [61]. Atom arrangement of the (0001) InN with b) (2×2) and c) ($\sqrt{3}\times\sqrt{3}$)R±30° surface reconstruction for adatoms located at T4-sites (adopted from [62]). Insert in the image (c) shows the positions of atoms located at H3 and T4-sites (labeled by empty circles).

trinsic property of InN, and occurs due to surface contamination (e.g. carbon, oxygen) or material decomposition. Moreover, the performed STS measurements confirmed the band gap of InN to be 0.7 eV.

The valence band photoemission spectrum with a calculated valence band density of states (VB-DOS) are shown in Fig. 2.3 (c) [49]. The experimental spectrum is in good agreement with theoretical calculations. The VB-DOS of the wurtzite InN consists of three main regions: two peaks at lower and higher energies, labeled as $P_I{}^{WZ}$ and $P_{II}{}^{WZ}$, respectively, and a shoulder between them, labeled as $S_I{}^{WZ}$ [60]. Based on the band diagram, the $P_I{}^{WZ}$ peak is mainly attributed to p-like states with a small contribution of *d*-states near ∼ 1.8 eV, while the $P_{II}{}^{WZ}$ peak consist of *s* and *p* orbital states [49]. Intensity of the photoemission spectrum above the VBM is attributed to the metallic adlayer formed on the InN surface. It is important to note that at binding energies higher than VB, In 4*d* orbitals are located very close to the N 2*s* orbitals resulting in a s-d hybridization of In 4*d* and N 2*s* core-levels [49, 55]. This fact, for instance, prevents an accurate fitting procedure of the In 4*d* core-level by chemical components, since the line shape of the s-d hybridized peak is unknown.

2.3 Surface Reconstructions of III-nitrides

Surfaces play an important and critical role in the crystal structure of a layer due to the break of crystal symmetry in the surface region. Compared to the bulk, the top-

most layer of atoms does not have neighboring atoms above them and, therefore, they change their arrangement (reconstruct) to have an energetic favorable position. Thus, the properties of surfaces can be significantly different from those of the bulk. Surface reconstructions can act as sources for additional electrons that lead to higher surface carrier concentration of material.

Surface reconstruction of GaN and AlN are quite well studied, while knowledge of InN and InGaN surface reconstructions is still missing in the literature. This fact can be explained by challenges in growing atomically smooth InN (InGaN) surfaces that strongly affects some spectroscopy or microscopy techniques, e.g. STM and STS.

Depending on the polarity of III-nitride layers, their growth conditions (e.g. N-rich or group-III-rich) and surface preparation methods (e.g. sputtering, annealing) different reconstructions can be obtained for the III-nitride surfaces. It was reported that Ga-polar GaN layers can have (1×1), (2×2), (5×5), (6×4), ($\sqrt{3}\times\sqrt{3}$)R±30° and so-called pseudo "1×1" reconstructions, depending on the amount of Ga on the surface [63, 64]. The (2×2) reconstruction was proposed to have a N-adatom layer; models for (5×5) and (6×4) reconstructions consisted of Ga, N adatoms and Ga vacancies. The pseudo "1×1" reconstruction is believed to have a fluid-like Ga-adlayer. The N-polar GaN layers are reconstruct into (1×1) surface, consisting of a Ga-adlayer or into (3×3) surface, which contains Ga-adatoms bonded to a Ga-adlayer [65]. A model of the (1×1) reconstructed N-polar GaN is shown in Fig. 2.4 (a). The study of polar (0001) InGaN layers revealed that these layers can have (1×1), (2×2), ($\sqrt{3}\times\sqrt{3}$)R±30°, and "1×1" surface symmetries depending on the surface preparation conditions and the Ga/N ratio on the surface [66].

Compared to a large variety of surface reconstructions for GaN and InGaN layers, only few surface reconstructions have been experimentally observed on polar InN layers: (1×1), (2×2) and ($\sqrt{3}\times\sqrt{3}$)R±30° reconstructions have been found on the In-polar InN surfaces, while only the (1×1) reconstruction has been reported for the N-polar InN layer. In the literature, the evidences of the (1×1) reconstructed polar InN surfaces have been provided only by low energy electron diffraction (LEED) measurements [31, 32, 67, 68].

Himmerlich et al. reported a (2×2) and ($\sqrt{3}\times\sqrt{3}$)R±30° reconstructed In-polar InN layers consisting of a single In adlayer, as shown in Fig. 2.4 (b) and (c) [62]. However, the surface reconstruction was determined only by one experimental technique – reflection high-energy electron diffraction (RHEED). At the same time, studies performed by Veal et al. suggested that the ($\sqrt{3}\times\sqrt{3}$)R±30° InN layer consisted of ∼ 3.4 atomic layers (monolayers) of In: the (0001) InN layer is terminated by an In-adlayer with a laterally contracted and rotated to 30° topmost In layer [40, 69]. However, this model was not confirmed by other experimental groups nor theoretical calculations [70]. This discrepancy indicates that the InN surfaces and their reconstructions are still poorly understood and require further investigation.

Theoretical calculations based on density-functional theory (DFT) for (0001) InN layers predicted that at N-rich and moderate In/N ratio, the (2×2) In_{T4} structure is stable,

where the In-adatoms are formed at T4-sites, while under In-rich conditions the contracted In-bilayer is favorable [70]. The atomic positions located at T4 and H3-sites are sketched in the insert to Fig. 2.4 (c). Another theoretical study showed that under N-rich conditions, the (0001) InN layer is relaxed and unreconstructed with In-termination, while under In-rich conditions a trimer of In adatoms is formed on T4 or H3-sites corresponding to the 3/4 of In monolayer (ML) [71]. The $(000\bar{1})$ InN layer was found to have a stable (1×1) structure with an In-adlayer over the entire range of In chemical potentials [70,71]. Interestingly, in these studies even under N-rich conditions no N terminated surfaces or N-adatoms have been found to form on both In- and N-polar InN layers.

LEED and reflection high-energy electron diffraction (RHEED) are usually used to determine surface reconstructions of the studied layers, while STM is a technique that allows to observe surface atomic structures and confirm predicted surface symmetry of the layers. However, there are only few publications reporting on STM performed on InN layers [59, 72, 73]. In the work of Ebert et al., the cross-sectional STM was performed on a freshly cleaved $(11\bar{2}0)$ InN surface [59] and accompanied by STS studies. Nevertheless, the presented cross-section STM image of the InN is poorly resolved and can hardly give any information about the layer structure.

Good-resolved STM images of InN layers are only available in the case of indium deposition on GaN or Si in a cracked ammonia environment in amount of several monolayers [72,73] but not for InN layers with thickness of few hundreds nm. As mentioned, the main reason for this is the lack of atomically smooth InN layers. Surface roughness and defects strongly affect the tunneling condition during STM on InN layers, making it a very challenging issue. Moreover, one can assume that presence of the surface electron accumulation layer on InN may also effect tunneling conditions during STM/STS. According to the literature, the atomically resolved STM images can be found for AlN and GaN surfaces [64,74], which do not exhibit surface accumulation, while no atomic-resolved STM images could be obtained on the InN layer so far. In the work of Nörenberg et al., the authors show STM images of (2×2) and (4×4) reconstructed areas after depositing 8 ML of InN on Si (111) (7×7) [72]. However, the authors presume that the observed reconstructions may be assigned to indium adsorbate structures on the Si surface rather than to InN material. Based on this discussion, it becomes clear that InN surface structure is not yet understood in terms of STM study.

2.3.1 Surface States

The end of the crystal periodicity on a surface and rearrangement of the atoms on the topmost layer lead to the appearance of surface electronic states that differ from the bulk electronic band structure. Based on DFT calculations, C. G. Van de Walle and D. Segev have studied stable surface states formed on (0001) and $(000\bar{1})$ InN surfaces at moderate In/N ratio and In-rich conditions, discussed in the previous section [75–77].

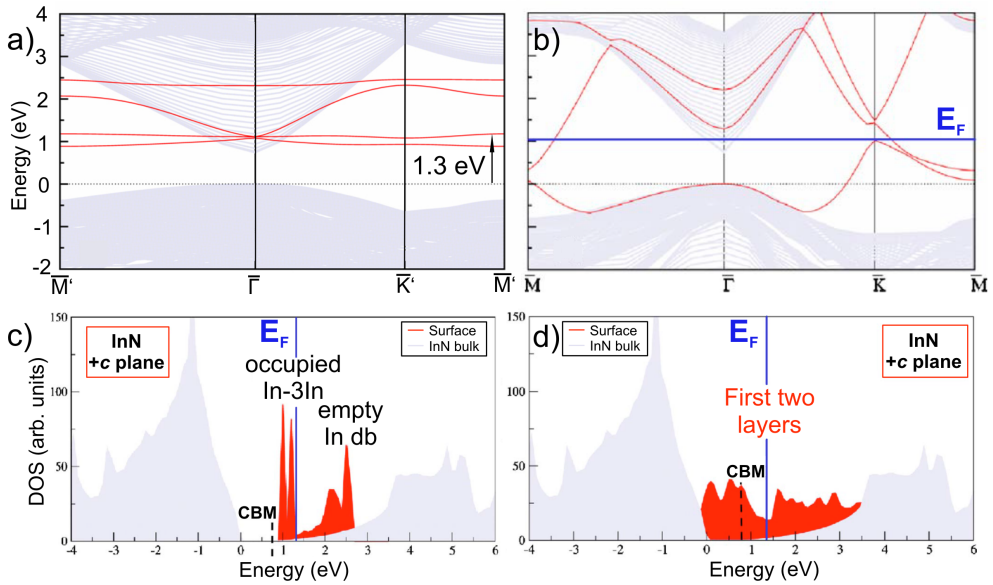

Figure 2.5: Electronic band structure of a) (0001) InN surfaces with (2×2) In_{T4} structure and b) (000$\bar{1}$) InN with (1×1) structure (with In-adlayer). Gray and red lines indicate bulk and surface band structures, respectively. DOS on the polar (0001) InN surfaces with c) (2×2) In_{T4} structure (for moderated In/N ratio) and d) laterally contracted In-bilayer (for In-rich conditions). Images are adopted from Ref. [75].

Two sets of surface states on (0001) InN layers with (2×2) structure (In-adatoms at T4-sites) were found to exist in the electronic band structure above the CBM (see Fig. 2.5 (a), red lines) [75]. Surface states on (000$\bar{1}$) InN with (1×1) structure (formed In-adlayer) result in a dispersive electronic band structure (see Fig. 2.5 (b), red lines) [75]. Hence, surfaces are predicted to be semiconducting for the above mentioned (2×2) (0001) InN and metallic for (1×1) (000$\bar{1}$) InN layers.

The microscopic origin of these states could be identified by analyzing the surface states electronic charge densities. As shown in Fig. 2.5 (c) for the (2×2) (0001) InN structure, the surface states formed at higher and lower energies correspond mainly to the empty In dangling bonds on the In adatoms and occupied states on bonds between the In adatom and three In surface atoms (In-3In), respectively. Thus, occupied surface states (negatively charged) above the CBM serve as a source of electrons and explain the surface electron accumulation layer on polar InN layers. The Fermi level position, for this case, is approximately determined by the upper position of the occupied surface states and located $\sim$0.6 eV above the CBM [75]. For the (1×1) (000$\bar{1}$) InN structure, dispersive surface states are caused by the interaction of neighboring In adatoms.

As was already mentioned, for In-rich conditions, the (0001) InN layer is covered by a laterally contracted double layer of In (bilayer), where occupied In-3In bonds and empty In dangling bonds now strongly interact, leading to an energy dispersion within

the band gap, as shown in Fig. 2.5 (d). The surface states from this layer are mainly localized on In-In bonds within the underlaying In adlayer, additional with dangling bonds from the upper adlayer. The Fermi level lies at approximately 0.7 eV above the CBM. For the $(000\bar{1})$ InN layer under In-rich condition the formed (1×1) structure consists of an In-adlayer bonded to the uppermost N layer, where the Fermi level is ~ 0.3 eV above the CBM, similar to the case of a moderate In/N ratio [75, 77].

It is worth to mention that compared to polar surfaces, nonpolar InN surfaces are predicted to have absence of electron accumulation layer for reconstructions with a dimer structure [75]. Unfortunately, no information concerning surface states on semipolar InN surfaces is available in the literature so far.

2.4 Growth of InN, GaN and InGaN layers

As already mentioned above, the surface structure and the related electronic properties of group-III-nitrides will be significantly influenced by the growth and preparation methods. In order to prepare layers with different surface atomic structures, morphology and polarity, different methods were used for the growth of the InN layers investigated in this work. The polar and semipolar InN, InGaN and GaN layers investigated within this work were grown by metal-organic vapor phase epitaxy (MOVPE), molecular beam epitaxy (MBE) and migration enhanced afterglow (MEAglow) epitaxy [19].

All layers are grown on a substrate which should be chosen considering its cost, abundance on the market, lattice mismatch with the overgrown layer, thermal expansion coefficient, etc. Substrates can strongly affect the growth and therefore the quality of the overgrown group-III-nitride layers. Sapphire (Al_2O_3), silicon carbide (SiC), cubic Si (111) can be used as substrates for the growth of nitrides with wurtzite structure. However, the fabrication of high quality single crystalline SiC substrates is difficult and expensive. On the other hand, the growth of wurtzite nitride layers on cubic Si (111) substrates is a very challenging issue. Nowadays, *c*-plane sapphire remains the most conventional substrate for the growth of polar wurtzite nitrides. The main advantages of sapphire substrates are its low cost, variety of available wafer sizes, high crystal and surface quality and high temperature stability. However, the growth parameters and procedure should be chosen carefully to overcome the lattice mismatch between the *c*-plane sapphire and group-III material, e.g., a lattice mismatch of $\sim$27% with InN, 16% with GaN and 13% with AlN layers [23, 78].

2.4.1 Sapphire Nitridation and its Effect on Group-III-Nitrides

Among all nitrides, InN and sapphire have the largest lattice mismatch. In order to reduce the lattice mismatch and improve the interfacial properties, a nitridation process of sapphire is often performed prior to the InN growth or III-nitride growth. Sapphire nitridation implies a growth of a thin AlN layer which reduces the lattice mismatch

between InN and sapphire layer to ∼13%. It has been found that in particular InN is very sensitive to the nitridation process. The InN crystal quality, surface topography, carrier concentration, Hall mobility and optical properties are directly affected by the nitridation process [13, 14, 79–83].

The growth parameters of InN layers are also affected by the nitridation. It was shown that the nitridation is performed faster on $(11\bar{2}0)$ nonpolar (*a*-plane) sapphire substrates than on *c*-plane sapphire due to the different bond arrangements of the sapphire surfaces [84]. This results, for instance, in the growth of N-polar InN layers on the *a*-plane sapphire at 50°C lower nitridation temperature compared to the layers grown on the *c*-plane sapphire. The above mentioned facts make the study and understanding of nitridation mechanism an important issue for the improvement of InN quality.

For the polar InN layers grown by MOVPE and investigated in this work, the following nitridation process was performed. First, the purchased *c*-plane sapphire substrates were cleaned by sequential immersion into acetone, iso-propanol and de-ionized water. Afterwards, the sapphire substrates were thermally cleaned at 1050°C in a H_2 gas flow of 3 l/min for 10 min. Then, the gas was switched to N_2 with a flow rate of 3 l/min for the nitridation process. The sapphire nitridation was performed by exposing the sapphire substrates to ammonia flux for 2 min at temperatures berween 600 °C and 1050 °C.

2.4.2 MOVPE Growth

Polar (0001), $(000\bar{1})$ and semipolar $(11\bar{2}2)$ InN and GaN layers were grown by metal-organic vapor phase epitaxy (MOVPE).

The polar InN layers were grown by D. V. Dinh at Technische Universität Berlin (TU Berlin) on *c*-plane sapphire using three steps: sapphire nitridation, growth of InN nucleation layer and InN epitaxial growth [84]. Nitrogen was used as a carrier gas; trimethyl-indium (TMIn) and ammonia (NH_3) were used as In- and N-precursors, respectively. The sapphire substrate treatment and nitridation was performed as described above. The InN nucleation layers were grown at 500 °C for 20 min, while the InN epilayers were grown at 560 °C for 2 hours. Additionally, the In-polar InN layers were grown on (0001) GaN/Al_2O_3 templates and directly on sapphire substrates without nitridation. The estimated thickness of the grown polar InN layers varies in the range from 70 nm to 200 nm.

Polar GaN layers with thickness of 1.2 μm were grown on AlN nucleation layers (Ga-polar layers) or bare sapphire (N-polar layers) by M. Hoffmann at NCSU, USA (research group of Prof. Z. Sitar).

The semipolar $(11\bar{2}2)$ InN layers $\approx$ 90 nm thick were grown on 1-2 μm thick $(11\bar{2}2)$ GaN templates grown by MOVPE on *m*-plane sapphire substrates [85]. Prior to the used three-step growth for the semipolar InN layer, a 200 nm thick GaN buffer layer was grown for 15 min at 980 °C. The studied $(11\bar{2}2)$ InN layers in this work were grown at 530°C, 550°C and 560°C. The semipolar InN layers were grown by D. V. Dinh at TU Berlin. The semipolar $(11\bar{2}2)$ GaN layer was grown on a Ga-polar $(11\bar{2}2)$ GaN

substrate at a temperature around 1000 °C by S. Ploch at TU Berlin, using trimethylgalium (TMGa) and ammonia (NH_3) as Ga- and N-precursors, respectively [86].

The semipolar $(20\bar{2}1)$ $In_xGa_{1-x}N$ layers with $x = 6.5\%$ and x = 10.2% were grown by MOVPE on HVPE-grown GaN bulk substrates with semipolar $(20\bar{2}1)$ orientation and a threading dislocation density of the order of $10^6\,cm^{-2}$. Prior to the growth of the InGaN layers, the 700 nm of un-intentionally doped GaN was grown using TMGa and NH_3 as precursors, and H_2 as a carrier gas, at a temperature of 980°C and pressure of 50 mbar. Subsequently, the temperature was reduced and the pressure increased to 400 mbar, and 22 nm of InGaN was grown using N_2 as a carrier gas, and TEG, TMI and NH_3 as precursors. Growth temperatures for InGaN were nominally 725°C and 750°C, resulting in an indium compositions of 10.2% and 6.5%, respectively. The growth was performed by I. Koslow and T. Wernicke at Ferdinand-Braun-Institut, Berlin, Germany. The indium concentration in the layers was determined by XRD.

2.4.3 MBE Growth

The investigated InN layer was grown by MBE on a GaN/Al_2O_3 template which was grown by MOVPE. The growth was performed by R. Aidam in Fraunhofer Institute IAF, Freiburg, Germany. The thickness of the grown InN layer was estimated to be approximately 1 μ m. In order to achieve a smooth surface, the InN layer was grown under excess of indium supply which resulted in the formation of 10-15μm diameter indium droplets on the surface, as was observed by scanning electron microscope (SEM). The indium droplets were chemically etched from the surface after the growth by using HCl. The surface under the indium droplets was partially damaged by etching, while other areas of the layer remained unaffected. The InN layer has In-polar orientation as was determined by XPS VB.

2.4.4 MEAglow Growth

The MEAglow deposition technique was developed by K. S. A. Butcher, where he used a especially built prototype growth system. In his reports (Ref. [19, 20]) it was shown that InN layers grown by MEAglow exhibit very smooth surfaces with good crystalline structure. Moreover, this technique enables homogenous and fast growth of InN layers on 2 inch sapphire wafers for fabrication purposes (MEAglow Ltd.) and can be an alternative method for the growth of thick, high quality InN layers.

The MEAglow deposition implies a particulary designed nitrogen plasma source and chemical vapour deposition (CVD) environment for the growth of InN as well as GaN layers [19, 20]. The growth method is based on the number of cycles, where at first, the metal (indium) is deposited on the substrate for a short time, afterwards the layer is subsequently nitridated with the nitrogen plasma source. TMIn is used for an indium supply with no carrier gas. By applying this procedure, the metal atoms have enough time to migrate to energetically favorable positions caused by adatom surface

diffusion, before they combine with the nitrogen atoms. This technique enables much faster growth rates compared to conventional migration enhanced epitaxy, where the growth rate is limited by a small amount of metallic indium, which can be deposited on the surface within one cycle, in order to avoid formation of metallic droplets. Compared to MOVPE, MEAglow deposition is performed at a very low growth temperature (330-400°C) and low operating pressure during the growth (up to several Torr, 1 Torr = 1.33 mbar). These parameters are expected to improve the quality of InN layers. More information about the growth procedure and equipment can be found in Ref. [19, 20]. It is important to note, that the InN layers grown by this technique are presumed to have a nitrogen excess in the crystal structure due to the formation of the native nitrogen-rich defects during the growth as was determined by elastic recoil detection analysis [87].

The InN layers analyzed in this work were grown by K. S. A. Butcher (MEAglow Ltd., Ontario, Canada). Prior to the growth, the sapphire substrates were nitridated for 1 min at the growth temperature of the layer by the nitrogen plasma system. One sample was grown on a 2 inch sapphire wafer at 330°C, while the second sample was grown on sapphire at 400°C by using an InN buffer layer grown at 330°C. The layer grown at lower temperature (330°C) is expected to be 15-30% nitrogen-rich, while the layer grown at higher temperature (400°C) is assumed to be only 2-3% nitrogen rich. The thickness of the layers was estimated by measuring the interference fringes from optical transmission measurements and equals ≈ 500 nm and ≈ 370 nm for the layers grown at low and high growth temperatures, respectively. Both InN layers were found to be N-polar as determined by XPS.

3 Experimental Techniques for Surface Analysis

This chapter describes the main experimental techniques for the surface analysis of III-nitride semiconductor materials under ultra high vacuum (UHV) conditions used in this work. Moreover, the preparation methods such as surface decontamination of investigated group-III-nitride layers, will be described briefly.

Depending on the object of interest, different characterization techniques should be used. Surface topography, surface atomic and surface electronic properties can be determined by scanning tunneling microscopy (STM) and spectroscopy (STS). The STM images correspond to the surface local density of states, while STS curves can show, for instance, whether the surface has metallic or semiconducting behavior. Chemical analysis of surfaces can be performed by photoelectron spectroscopy (PES) and Auger electron spectroscopy (AES). Both methods show qualitative and quantitative information about elements presented in the near surface region. Information about the chemical bonding configurations and surface band bending can be obtained after detailed analysis of the core-levels and valence band photoemission spectra recorded by PES. Finally, the surface periodicity, e.g. atoms reconstruction, size of the unit cell, can be obtained by low energy electron diffraction (LEED). Combination of the mentioned methods gives a detailed understanding of the surface nature of III-nitrides.

3.1 Scanning Tunneling Microscopy

Scanning tunneling microscopy (STM) was developed in 1982 by G. Binning, H. Rohrer, Ch. Gerber, and E. Weibel by observing the tunneling effect from a metallic wolfram tip into Au(110) and Si(111) layers [88–90]. In 1986 G. Binning and H. Rohrer shared the Nobel prize in physics for their invention.

The principle of STM is based on the electron tunneling between a metallic tip and a conducting sample placed in several angstrom away from the tip. The vacuum in this case plays a role of a potential barrier that has to be overcome. In the simplest way, the vacuum is assumed as a rectangular barrier Φ_b in one dimension (z). The voltage bias is applied between the tip and the sample, therefore, when the tip approaches the sample close enough, their wave functions overlap and the probability for electrons to cross the potential barrier increases (Fig. 3.1). The transmission probability for an electron of energy E to tunnel through a barrier can be found by solving the Schrödinger equation.

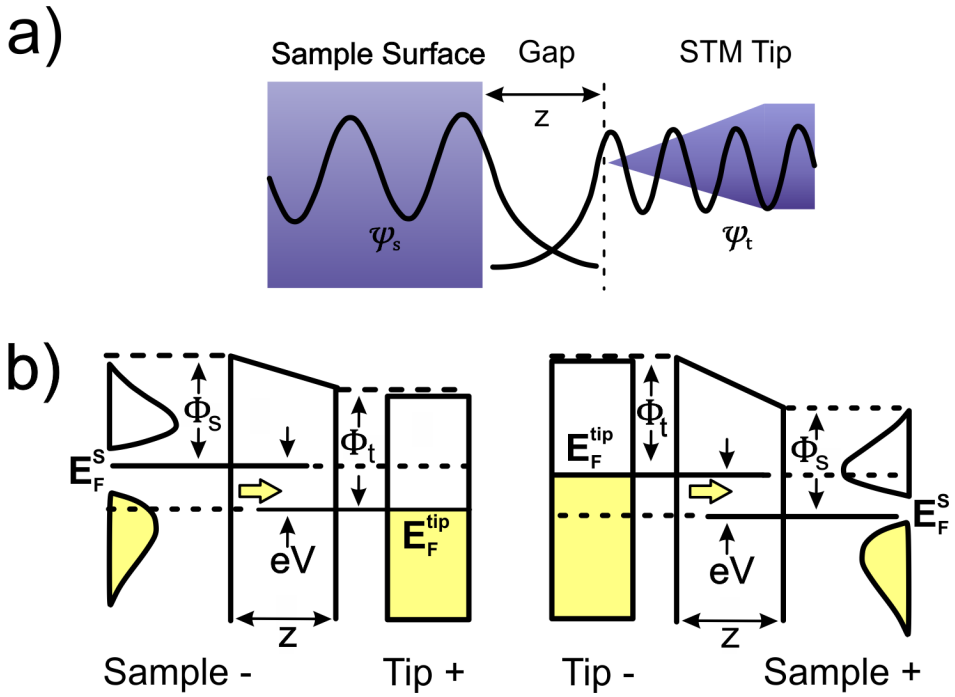

Figure 3.1: Principle of STM. a) Overlap of the sample (ψ_s) and tip (ψ_t) wavefunctions, when the tip is placed close enough to the surface. b) Principle of quantum mechanical tunneling: by a negative applied sample bias, electrons tunnel from the filled states of the sample into the unoccupied states of the tip, by a positive applied sample bias, electrons tunnel from the filled states of the tip into the unoccupied state of the sample. Φ_t and Φ_s are the local tip and sample barrier heights; $E_F{}^t$ and $E_F{}^s$ are the tip and sample Fermi levels.

The tunneling current is proportional to the probability density $|\Psi(z)|^2$ of finding an electron at a distance z from the barrier, and is given by:

$$I \approx |\Psi(z)|^2 = |\Psi(0)|^2 e^{\frac{\sqrt{8m_e(\Phi_b - E)}}{\hbar} \cdot z}, \tag{3.1}$$

where m_e is the electron mass, $\hbar$ is the Planck's constant and Φ_b is approximated by the average potential barrier of the sample Φ_s and the tip Φ_t (Fig. 3.1 (b)). In the simplest approach Φ_b corresponds to the vacuum level, if so, Φ_b - E is the work function for the states at the Fermi level that mainly contribute to the tunneling current. However, the simplest approach can be attributed to the nanometer scale but not to the atomic scale. The first-order perturbation theory describes a more precise interpretation of the STM images. Thus, by considering only elastic tunneling and low temperatures, the tunneling current can be given by:

$$I = \frac{4\pi q_e}{\hbar} \int_0^{q_e V} d\varepsilon \rho_{tip}(E_F^{tip} - q_e + \varepsilon) \rho_{sample}(E_F^{sample} + \varepsilon) \, |M|^2 , \tag{3.2}$$

where ρ_{tip} is the tip density of state, ρ_{sample} is the sample density of state, $|M|$ is a tunneling matrix element [91], E_F^{tip} and E_F^{sample} are the Fermi energies of tip and sample, respectively. However, knowing the wavefunction of the tip is generally not possible, since the tip atomic structure is unknown. The solution to this problem would be an approximation regardless of the tip properties and was given by J. Tersoff and D. R. Hamann [92, 93]. They have shown that if the tip is described as a mathematical point source of current (single atom) with an *s*-wavefunction and a constant density of state, the tunneling current can be simplified as following:

$$I(\mathbf{r}_t) \approx \int_{E_F}^{E_F+q_eV} \rho_S^{local}(\mathbf{r}_t, E)dE. \tag{3.3}$$

This equation simplifies the matrix M shown by J. Bardeen [91]. Therefore, the tunneling current depends only on the sample local density of states (LDOS) for the tip located at the position $\mathbf{r}$ above the surface regardless of the tip size. Based on this, the STM images should be interpreted as the electron density of states integrated over a chosen energy range. An STM image shows the occupied sample states by applying the negative sample bias, and the unoccupied energy states of the sample by applying the positive sample bias, as shown in Fig. 3.1 (b).

Since the tunneling current depends exponentially on the tip-sample separation, its increase by one angstrom would lead to a decrease of the current by one order of magnitude. This fact enables the control of the distance between the tip and the sample with a very high vertical resolution that is essential for obtaining any atomically resolved images. The lateral resolution is limited by the shape of the tip – very sharp tips are required.

The atomic-resolved imaging is achieved by a raster scan of the sample with a sharp tip in x- and y-directions, where the current is measured between the tip and the sample at each position. STM can be operated in two modes: constant current and constant height. In the *constant current mode*, the tunneling current is kept constant that requires a constant tip-sample separation. During scanning, the vertical position of the tip is altered to achieve the constant separation and gives the topographic imaging. In the *constant height mode*, the applied bias and the height between the tip and the sample are kept constant during the scanning. In this case a variation in current gives a topographic structure.

Note that the simplification of Eg. 3.3 ignores several important aspects that can take place during the measurements, e.g. tip-induced band bending, tip-sample interaction, negative differential resistance. Despite these facts, theoretical calculations used for STM simulations based on the Eg. 3.3 are in good agreement with the experimental results. Further description of the STM basics and theoretical interpretation of LDOS can be found in textbooks, such as [94–98].

In this work a commercial OMICRON STM setup was used under UHV conditions at room temperature for the topography characterization of the layers and determination

of the surface reconstructions. The tungsten STM tips were etching in NaOH solution and used for the measurements.

3.1.1 Scanning Tunneling Spectroscopy

Scanning Tunneling Spectroscopy (STS) is performed by varying the voltage between the tip and the sample and recording the tunneling current at the fixed position of the tip above the sample. STS provides information about the surface electronic band structure. The current at a specific voltage corresponds to the DOS of the sample at that energy. As a result, the obtained *I(V)* curve can give information about the local electronic surface structure, e.g. surface band gap of semiconductor, surface electronic states [99]. By assuming that ρ_S^{local} is constant, the differential conductivity from Eg.(3.3) would be described by:

$$\frac{dI(eU)}{dV} \approx \rho_S^{local}(\mathbf{r}_t, E_F + q_e V)dE. \tag{3.4}$$

Therefore, $\frac{dI(eU)}{dV}$ directly relates to the surface LDOS of the sample. J. A. Stroscio and R. M. Feenstra [100] proposed a more reliable interpretation of STS spectra by normalizing the $\frac{dI(eU)}{dV}$ to an absolute value of conductance *I/V*. This approach cancels out the exponential dependence of the transmission coefficient on bias voltage.

In this work both, *I(V)* and *(dI/dV)/(I/V)* curves are used in order to determine the surface band gap and surface behavior, e.g. metallic or semiconducting.

3.2 Photoelectron Spectroscopy

Photoelectron Spectroscopy (PES) is based on the photoelectron effect – emission of the electrons from solids, liquids or gases after light irradiation. It is a surface characterization technique that can give qualitative and quantitative information about elements on the surface, chemical binding configurations of the atoms, surface band bending, etc. The photoemission effect was observed for the first time by H. Hertz in 1887 and further refined in the works by J. J. Thompson (1899) and P. Lenard (1900) [101–103]. However, the first correct explanation to this effect based on the quantum nature of light was given by A. Einstein in 1905 [104]. Later in 1921 he was awarded the Nobel Prise for this discovery.

In this work PES was performed on crystal (solid) materials, where the kinetic energies E_{kin} of electrons emitted from the surface is recorded and converted to the binding energies of electrons in the solid. By knowing the energy of the irradiated light ($\hbar\nu$) and

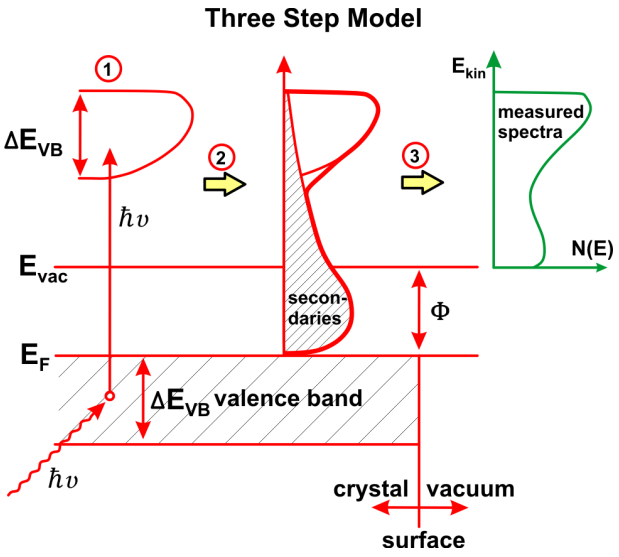

Figure 3.2: The three step model of the photoelectron process: 1) photoexcitation of the electron, 2) transport to the surface, and 3) transmission through the surface.

the work function (Φ) of the analyzer, the binding energy E_B of the electrons emitted from a sample can be determined as follows:

$$E_B = \hbar\nu - \Phi - E_{kin} \tag{3.5}$$

The work function of the sample (Φ_{samp}) does not contribute to the kinetic (or binding) energy of the photoelectrons. It cancels out in the energy balance by placing a sample in contact with the spectrometer that results in the same reference Fermi energy level.

Depending on the applied excitation energy different regimes of PES can be achieved: ultraviolet photoelectron spectroscopy ($\hbar\nu = 10$ - 45 eV) and X-ray photoelectron spectroscopy (XPS) ($\hbar\nu > 100$ eV). Throughout this work all experiments were performed by XPS using a PHOIBOS100 energy analyzer (SPECS) and a monochromated Al K_α X-ray source with an incoming photon energy of ≈ 1487 eV.

The photoemission process is usually described by the so-called *three-step model* consisting of three independent processes, as shown in Fig. 3.2: **(1)** photoexcitation of the electron, **(2)** electron transport to the surface, and **(3)** transmission of the electron through the surface [105]. In the **first step**, the electron absorbs the photon energy and is excited from its ground state to the final state. The photocurrent produced inside the sample is described by the excitation of electrons from the initial state i (with wavefunction ψ_i) to the final state f (with wavefunction ψ_f) by the photon field with the vector

potential $\overrightarrow{A}$. The probability of this transition per unit time is given by the Fermi's golden rule:

$$\omega_{fi} = \frac{2\pi}{\hbar} |\langle f| \mathbf{A} \cdot \mathbf{p} |i\rangle|^2 \delta(E_f - E_i - h\nu) \tag{3.6}$$

It is assumed that after the excitation of the electron, the final state of the remaining orbitals (passive orbitals) is the same as their initial state (so-called frozen-orbital approximation). Based on this approximation, no relaxation of the remained N-1 electrons occurs after the electron photoemission and all the final state effects can be neglected. Therefore, the electron binding energies determined from Eq.(3.5) correspond to the binding energies of the electrons in the initial states, and the photoemission intensity is associated with the density of electrons at the initial states.

In the **second step**, the exited electron transfers to the surface of the solid. During the transfer, electron can fully or partially lose its energy by undergoing an inelastic collision with plasmon, photon or another electron. This influences the number of electrons that reach the surface. The secondary electron background that is observed in every photoemission spectrum (Fig. 3.2) is formed by inelastic scattered electrons. The average distance that an electron can travel in the sample without undergoing any collision is given by the electron mean free path (escape depth) λ that depends on the kinetic energy of the photoemitted electron, as shown in Fig. 3.3.

In the **third step**, the electron escapes through the surface into the vacuum. The electron can undergo the transmission through the surface only if its kinetic energy is higher than the work function and its velocity component is normal to the surface. In this process, the wave vector component parallel to the surface $\mathbf{k}_{\parallel}$ is conserved, while the component normal to the surface $\mathbf{k}_{\perp}$ is not conserved, due to the break in the translation symmetry.

PES is a surface sensitive technique. The information depth achieved by PES can be determined by looking at the "universal" electron inelastic mean free path λ. Fig. 3.3 shows λ with its minimum at 20 - 50 eV as a function of electron kinetic energy measured for the different elements [106]. It has been shown that almost independent from the investigated material, the obtained data suits the "universal" curve. Therefore, for the excitation energy $\hbar\nu \approx 1487$ eV used in this work, the information depth is less than 10 nm. Electrons emitted from a material without undergoing any scattering, thus, carry information about the electronic structure of the material from a thin surface region. Moreover, by using different excitation energies the core-level and valence band emission can be achieved for various regions of the layer: from a very surface sensitive up to a bulk area.

The detailed theoretical background of PES, experimental equipments and its possible applications can be found in the following textbooks [105, 108–110].

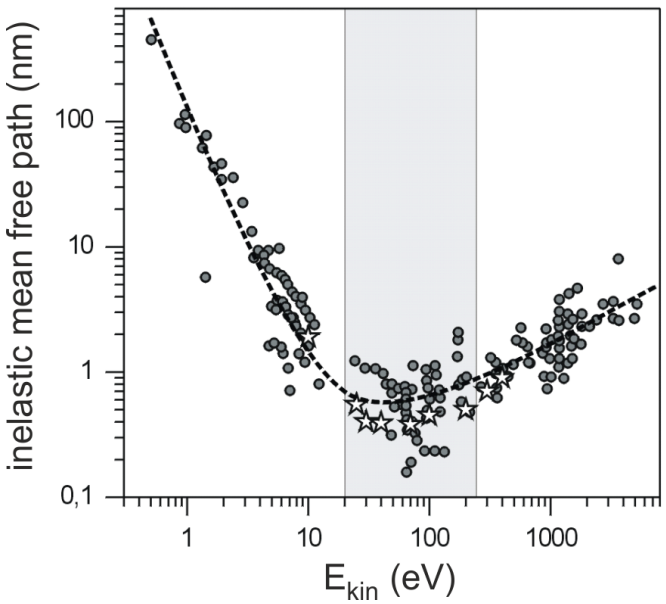

Figure 3.3: The electron inelastic mean free path (escape depth) of photoelectrons dependent on their kinetic energy measured for various materials [106] (e.g. stars represent data for GaAs [107]). The minimum at $E_{kin} \approx 20$ - 50 eV corresponds to the maximum surface sensitivity.

Core-level Spectroscopy

Electrons with binding energies above 10 eV correspond to electrons from the core-levels shells that do not contribute to the direct bonding between atoms in a solid. Although the binding energies of core-level electrons depend on the electronic and chemical environment of the atom they belong to. Therefore, analysis of the core-level emission spectra, i.e. the line shape of emission lines, gives information about the chemical bonding configuration between atoms.

At a surface or interface the chemical environment of an atom changes compared to the bulk structure, hence the atom undergoes an electron charge distribution according to the electronegativity of the atoms for given elements and type of the chemical bonds (e.g. π, σ, single, double, ionic bonds). If the atom experiences a relative charge accumulation (depletion), the positive nucleus charge is screened more (less) effectively and the emitted core-level electron has a lower (higher) binding energy. This phenomenon is called a core level shift and can be observed in the bulk or at the surface due to the different bonding configurations of the atoms, e.g., caused by a surface reconstruction, absorption of contaminations or interface.

In this work, the study of the chemical shifts and line shapes of core-levels were performed by fitting experimentally obtained spectra with theoretical model curves using a commercial UNIFIT software [111]. The background signal from inelastically scattered electrons, was fitted by a polynomial of third order. The theoretically fitted model curves consisted of the convoluted Lorentzian and Gaussian line shapes – Voigt profile. The Lorentzian line shape refers to the natural broadening (γ) attributed to the life time of the core hole, while the Gaussian broadening (σ) is associated with the instrumental resolution, broadening caused by surface-potential variation or sample in-

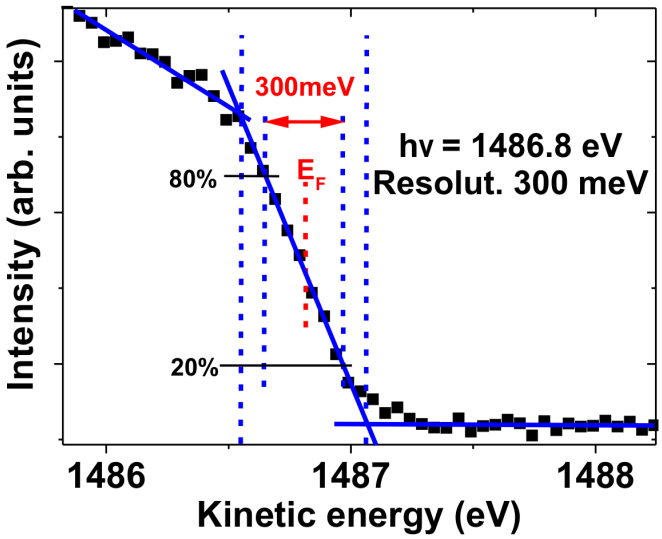

Figure 3.4: Determination of the Fermi edge (E_F) and instrumental energy resolution performed on the molybdenum sample holder by XPS using pass energy of 10 eV.

homogeneity. The difference between the fit and the measured data is represented as a residual spectrum beneath each experimental curve that shows the accuracy of the performed core-level fit.

The absolute values of the binding energies for core-level peaks were determine by calibrating the energy scale on the Fermi edge (E_F). Since the layers investigated in this work were not metallic, the energy scale was calibrated on the Fermi edge of the molybdenum sample holder placed in electrical contact with the investigated sample. Fig. 3.4 shows the energy distribution around E_F measured on molybdenum. The FWHM of the Fermi edge corresponds to the total instrumental resolution for the used XPS system and was ≈ 300 meV by using a pass energy of 10 eV. The energy at the middle of the FWHM corresponds to the Fermi edge and gives an accurate value of the excitation energy, i.e. $h\nu = 1486.8$ eV as shown in Fig. 3.4. The Fermi level was determined each time after adjustment of the analyzer or monochromator in order to obtain accurate and comparable values of electron binding energies for different experiments.

Valence Band Spectroscopy and Determination of the Valence Band Maximum

The study of the valence band (VB) photoelectrons can give information about surface states and the VB diagram of solids. The ultraviolet photoelectron spectroscopy (UPS) and/or angle-resolved X-ray photoelectron spectroscopy (ARPES) are usually performed for these purposes (not used in this work). Compared to the core-level emission, in the VB photoemission ($E_B < 10$ eV) the wave vector $\mathbf{k}$ strongly depends on the electronic state, due to the delocalization of the valence electrons.

ARPES measures the momentum $\mathbf{k}$-resolved electronic structure of solids. A surface states dispersion and a band dispersion can be achieved by performing a $\mathbf{k}_{||}$-scan, where

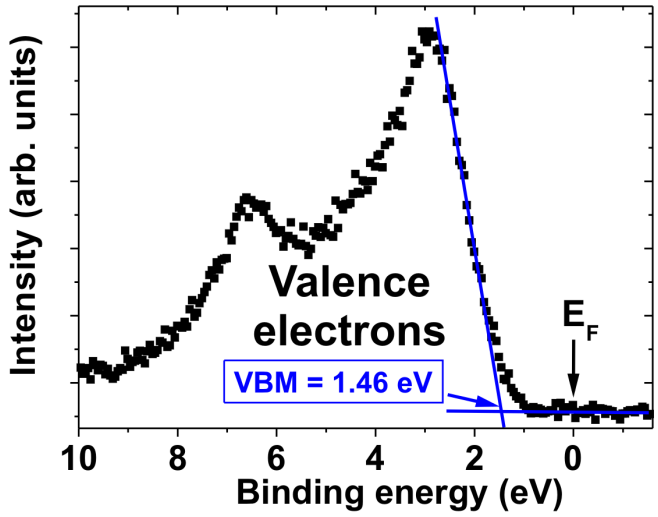

Figure 3.5: VB of an InN layer measured by XPS illustrating the determination of the VBM position by linear extrapolation. The VBM position corresponds to the crossing of the extrapolated lines.

the angle θ between the detected electrons and surface normal is varied. For polar III-nitride crystals the normal emission corresponds to the emission along the [0001] or [000$\bar{1}$] direction, where $\mathbf{k}_{||} = 0$ (Γ point in the band diagram), while for any semipolar layer the normal emission would correspond to the $\mathbf{k}_{||} \neq 0$ and altering of the θ angle is required in order to obtain emission along the *c*-direction. This fact will be used in some experiments discussed in the following chapters.

Another important information that can be gained from the VB spectra is a surface Fermi level pinning. The distance between the valence band maximum (VBM) and the Fermi level can be obtained by a linear extrapolation of the VB leading edge to the background [112], as shown in Fig. 3.5. Such extrapolation eliminates the instrumental resolution-induced tail and gives a most convincing result. Photoemission occurred at binding energies lower than VBM but higher than E_F corresponds to the emission from surface states. However, for XPS measurements the intensity of surface states is very low and an accurate study of surface states can not be performed. UPS measurements are usually used for the investigation of surface states. However, metallic surface states or surface metallicity can be distinguished also by XPS. For instance, the VB in Fig. 2.3 (a) from Ref. [40] measured from *c*-plane InN layer shows an obvious presence of the Fermi edge at 0 eV that probably corresponds to the metallic surface states originated from indium droplets or indium enrichment of the InN surface.

By knowing the band gap (E_g) of an investigated material and the VBM to the Fermi level separation (χ), the distance between the Fermi level and conduction band minimum, known as a barrier height or a barrier potential Φ_B, can be determined, as $\Phi_B = E_g - \chi$. The barrier height is analogous to the Schottky barrier height of a metal/semiconductor contact. A positive Φ_B refers to an upward band bending, while for a negative Φ_B the bands bend downwards as shown in Fig. 3.6.

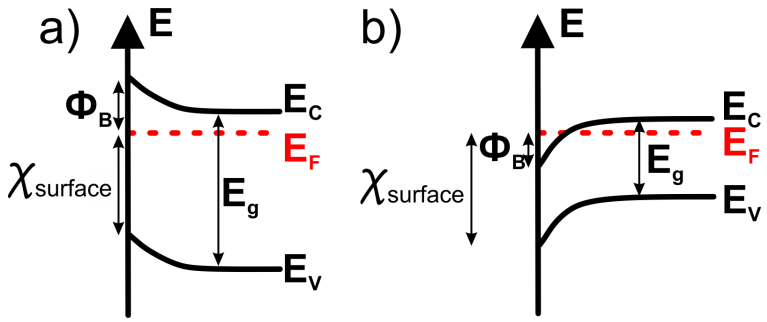

Figure 3.6: Sketch of a) upward and b) downward band bending. Φ_B is the barrier hight, E_g is the band gap of the solid, χ is the separation between the Fermi level (E_F) and the determined VBM.

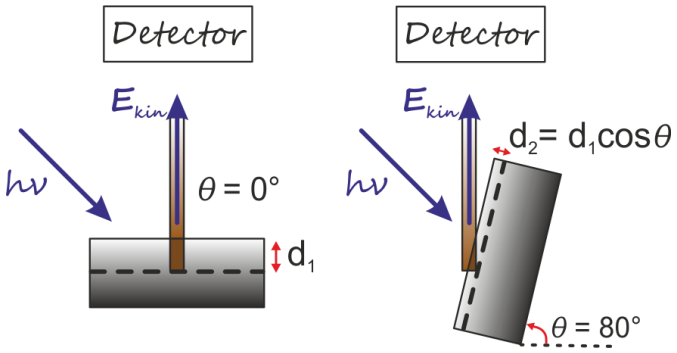

Figure 3.7: Changing of the information depth by varying the angle θ between the direction of detected electrons and the surface normal. Normal emission $\theta = 0°$ corresponds to the bulk (or bulk-like) measurements, while emission at $\theta = 80°$ refers to the surface sensitive measurements. A sketched vertical bar represents the escape depth and direction of the detected electrons.

Surface Sensitive Measurements

The information depth of the XPS measurements and therefore, the surface sensitivity, can be changed by altering the excitation energy. Change of the excitation energy results in different kinetic energies of the emitted photoelectrons and, therefore, different electron mean free path (Fig. 3.3), which is responsible for the information depth obtained by XPS. Surface and bulk contributions to the photoemission peaks can be distinguished by varying the angle θ, as shown in Fig. 3.7. For normal emission ($\theta = 0°$) the distance that the electron travels in solid coincides with the obtained information depth (d), however by increasing the angle θ (e.g. $\theta = 80°$) the information depth is decreases and should be multiplied by $\cos\theta$, as shown in Fig. 3.7.

An excitation energy of $\hbar\nu \approx 1487$ eV as the one used in this work Al K_α X-ray radiation corresponds to an information depth of less than 10 nm for the normal emission (e.g. around 35 monolayers (ML) of InN layers). In order to obtain surface sensitive

measurements, the samples can be tilted by 80 ° with respect to the surface normal that corresponds to an information depth < 1.7 nm or 6 ML of InN layers.

3.2.1 Quantitative Analysis of XPS Data

As was already mentioned, the energetic position of the recorded core-level peak (i.e. its kinetic or binding energy) gives information about an element specification and its chemical binding configuration, while the quantitative information about element concentration can be obtained from the peak intensities. Two main aspects must be considered for the XPS quantitative evaluation: the photoionization cross section and transmission function.

The photoionization cross section of an electron is the probability to emit an electron from its initial electronic state per unit time as a function of the photon energy. The cross section depends on the atomic number of the element, its subshell and the applied excitation energy. Detailed information about cross sections of the elements can be found in Ref. [113] and [114].

The transmission correction is used to calibrate the instrumental influences on the recorded spectra (e.g. lens mode, energy resolution, aperture settings). Comparison of the results measured from the same sample without a correction on the corresponding transmission function, for instance, by using different lens operating modes, would give a significant variation in atomic concentration.

The atomic composition of the elements was determined by using the CasaXPS software, where the cross sections and transmission functions for the used system were taken into account. The calculation of atomic concentration X_i was based on the following equation:

$$X_i = 100\,\% \frac{A_i}{\sum_{j=1}^{m} A_j}, \quad \text{where} \quad A_i = \frac{I_i}{T(E_i) R_i E_i^{0.7}} \tag{3.7}$$

A_i is so-called adjusted intensity, I_i is a measured intensity of the corresponding core-level peak, T is the transmission function for electrons with recorded energy E_i, R_i is the relative sensitivity factor that depends on the cross sections of the electrons. Since the escape depth of electrons depends on their kinetic energy, the electrons from different core-levels would correspond to the different information depths. The used CasaXPS software implies transmission and escape depth correction terms that are fixed for all samples and corrects the recorded intensities for instrumental influences. The escape depth compensation is expressed by $E_i^{0.7}$, where the power of 0.7 is commonly used by surface science instruments (SSI) and found to give the most accurate results [115].

3.3 Auger Electron Spectroscopy

The Auger process was discovered by Pierre Auger in 1925 by irradiating inert gases in the Wilson chamber with an X-ray beam, where he observed the tracks corresponding to the paired electrons originated from the ionized atoms [116].

Auger electron spectroscopy (AES) is a characterization technique used for the chemical analysis of a layer in the surface region: the information depth is less than 2 nm. The Auger electron has a characteristic kinetic energy that corresponds to certain element present on the surface. Therefore, the Auger positions give information about present elements, while the Auger intensity is proportional to the element concentration.

The Auger process includes the three following steps: 1) the primary electron (or X-ray) beam excites an electron from the inner shell forming a vacancy, 2) the electron from the higher shell fills the vacancy simultaneously giving additional energy to a third electron (called Auger electron), 3) this third electron is excited from the solid with its characteristic kinetic energy. Compared to the photoelectron effect, the Auger process is independent from the excitation energy and leaves the atom in the double-ionized state. Due to the high background level caused by inelastic scattered electrons, it is more common to use the derivation ($dN(E)/dE$) of the obtained AES spectrum, where the peak-to-peak height (I_x) is proportional to the atomic concentration of first order. Detailed information about the Auger transition can be found, for instance, in the following textbooks [117, 118].

In this work, the investigated layers were irradiated by a high energetic electron beam of 3 keV. The relative amount of the elements was calculated by taking into account the relative Auger sensitivity factors (S_x) for each element taken from Ref. [119] for a primary electron beam of 3 keV. The S_x factors have been determined by comparing the signal from the sample with that from a pure silver target. Therefore, the relative sensitivity between any element X and silver is given by $S_{x,Ag} = I_x/I_{Ag}$. By knowing the peak height ratio I_x for each element, the concentration of an element X can be found by:

$$C_x = \frac{I_x/S_x}{\sum_y I_y/S_y}\,100\,\%, \tag{3.8}$$

where the sum is taken over all elements present in the surface region. This quantitative method does not take into account the electron escape depths λ for different kinetic energies (i.e. for different elements), thus, the absolute values of the elements concentrations can be determined within an error of $\sim 20\,\%$. However, the relative concentration values obtained under identical experimental conditions from different samples can be compared to each other and give higher accuracy.

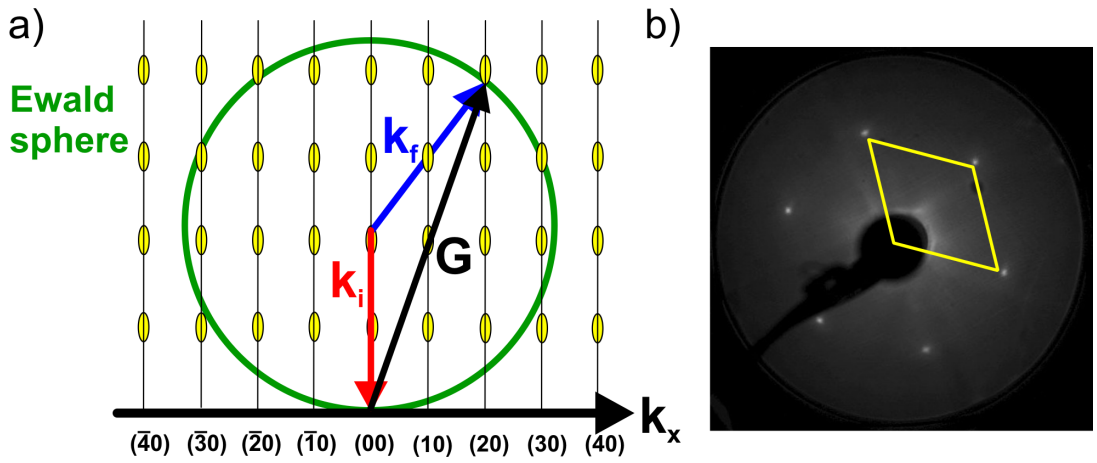

Figure 3.8: a) Principal of LEED: intersection of reciprocal lattice rods with the Ewald sphere leads to intensity maxima on the LEED screen; k_i is the incident wave vector, k_f is the scattered wave vector, and G is the reciprocal lattice vector. b) LEED pattern of a well-ordered (1×1) GaN layer taken at E = 120 eV.

3.4 Low Energy Electron Diffraction

Low energy electron diffraction (LEED) is a technique based on the electron diffraction from a surface and used for surface structure determination, e.g. surface periodicity, size of a unit cell. The energy of the emitted electrons used in LEED lies in the range of 10 -200 eV. According to the electron mean free path shown in Fig. 3.3, the escape depths for the electrons in this range correspond to ≈ 1 nm, making LEED very sensitive to the surface reconstruction and roughness. Since electrons with an energy of 100 eV have a wavelength of 0.12 nm, a relative large surface area contributes to the LEED diffraction pattern compared to reflection high-energy electron diffraction (RHEED), where much smaller crystallites can be analyzed.

LEED is described as a process, where an incident electron beam normal to the sample surface causes the scattering from a two-dimensional array of scattering sites. The diffraction spots (or reflexes) observed in the LEED patterns are the intensity maxima that fulfil the two-dimensional Laue condition and occur at the positions where the reciprocal lattice rods intersect the Ewald sphere – the wave vector of the incident electron beam (Fig. 3.8 (a)). The obtained LEED patterns, thus, represent reciprocal space maps of crystals. Symmetry of the LEED patterns reflects symmetry of the atomic arrangement in the real-space of the surface. A detailed theoretical description and applications of LEED can be found in the following books [120, 121].

The size, shape and brightness of the spots on the diffraction patterns can deliver qualitative information of the investigated surfaces. For instance, big and blurred reflexes may correspond to a rough surface with poor atomic periodicity (originated, for example, from a polycrystalline structure). In the case of a polycrystalline material, the

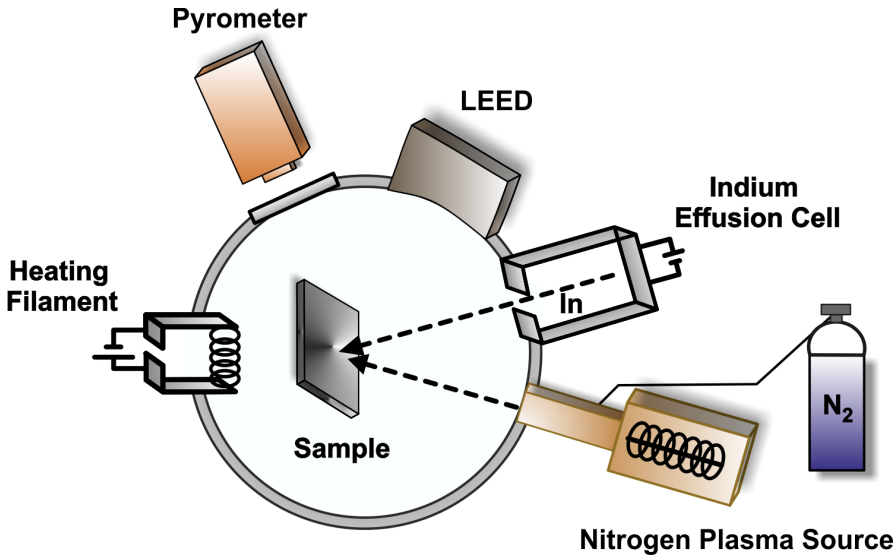

Figure 3.9: Sketch of the preparation UHV chamber equipped with a pyrometer, LEED, nitrogen plasma source and indium effusion cell.

Bragg's law may be fulfilled on the crystalline planes that are slightly tilted to each other resulting in enlargement of the diffraction spots. Defects on the surface or in the near surface region may affect the diffraction condition and also lead to blurred reflexes in the LEED pattern. In the case of oxidized layers, the incident electron beam scatters on the unstructured oxide layer before reaching the surface and no diffraction pattern are obtained. Only on clean, well-ordered and smooth surfaces the LEED patterns show bright and small reflexes, as shown in the example for a GaN layer in Fig. 3.8 (b).

In this work all LEED measurements were performed by using OMICRON LEED 4 grid optics, which provides information about the surface symmetry (reconstruction) and quality of the surface, e.g. roughness, crystalline structure.

3.5 Surface Treatment and Deoxidation

The as-grown layers investigated here were transferred from the growth chamber into a UHV chamber for further surface analysis. The layers were transferred through ambient air, where they undergo surface contamination. Further in this work it will be addressed to the surface contamination upon exposure to ambient air as to (native) oxidation process. Hence, a layer decontamination process must be performed in order to obtain a clean, contamination free surface. The preparation conditions strongly depend on the type of III-nitride semiconductor (e.g. its surface orientation, compound of elements), and appropriate parameters for surface treatment must be found for each type of material. It is also very important that an applied surface treatment does not affect the crystalline and surface properties of the investigated layer.

Conventional methods used for surface treatment of III-nitrides are thermal annealing [122], atomic hydrogen cleaning (AHC) [40, 67, 123] and ion sputtering, e.g., by using argon ion beam [122, 124] or xenon [125]. However, InN layers were found to be especially sensitive to the surface treatment. Foley et al. observed adsorbed C, H_2O and OH impurities on the oxidized untreated InN surfaces that led to a formation of an In-NO complex at the first stage of oxidation [125]. After surface cleaning by sputtering, the In-NO complex was found to oxidize and form an In-NO_2 complex. In another work, it was assumed that InN oxidation leads to the formation of an In-O component originating from In_2O_3, InOH or In_2O indium oxides [123]. An AHC cleaning resulted in a shift of the In-O component, indicating a change in the In-O bonding configuration of the native oxide. Moreover, a surface indium enrichment and formation of indium droplets might occur on InN layers by applying the AHC process [126] (especially for the N-polar InN layers [34]) and ion sputtering with subsequent annealing [127]. Therefore, in this work, in order to avoid any surface modification, the investigated layers were thermally annealed under UHV conditions or by using a nitrogen plasma source.

For the annealing process under UHV conditions, the layers were fixed on a molybdenum sample holder and thermally annealed from the backside by a heating filament. During the thermal treatment, the UHV chamber pressure was kept in the range of $1\times10^{-10} - 1\times10^{-9}$ mbar. The annealing temperature should be high enough to desorb the oxide built on the surface, but at the same time prevent the crystal from damage or melting. The effect of the annealing temperature on the surface structure for each material (InN, GaN, InGaN) will be discussed in the corresponding chapters.

For the annealing process in nitrogen plasma, a microwave electron cyclotron resonance plasma source (SPECS mini Plasma Source MPS-ECR) was used. The plasma source was maintained at 2.45 GHz and a current of 15-25 mA, producing nitrogen ions into the vacuum chamber, where the chamber pressure increases up to 1.5×10^{-4} mbar.

The annealing temperature was measured by an infrared pyrometer (operating wavelength 1.1-1.7 μm) directly from the surface of the layer (emission coefficient was set depending on the studied material) and by a thermocouple, located near the sample holder. However, an accurate determination of the absolute surface annealing temperature is challenging for both methods. The thermocouple is placed near the layer itself and the temperature gradient occurred during annealing results in an underestimated recorded temperature values. In this case, the relative values can be used during the surface treatment. On the other hand, temperatures determined by the infrared pyrometer may correspond not to the top-most surface region but to the layer underneath, e.g. substrate, since many materials are transparent to infrared radiation (e.g. GaN, Al_2O_3). Additionally, the appropriate emission coefficient must be carefully chosen to improve accuracy of the measured temperature. Nevertheless, reproducible reading can be achieved by using the same emission coefficient for the same materials.

4 Polarity Determination of Polar and Semipolar InN and GaN Layers by Photoemission Spectroscopy

As it was already shown in Chap. 2, the polarity of III-nitrides affects their topography, crystal and electrical properties. Therefore, the polarity of the investigated layers should be determined prior to the further characterization of the layers. Not many of the already existing methods for polarity determination can be applied to the thin III-nitride layers. This chapter will introduce a method for polarity determination of polar and semipolar $(11\bar{2}2)$ InN and GaN layers that is based on valence band X-ray photoemission spectroscopy. Unlike the conventional methods for polarity determination, e.g. chemical etching and CBED, XPS does not affect the surface structure and can be applied to thin layers. Moreover, it will be shown that polarity of the layers with high roughness and layers oxidized on ambient air can be also determined by XPS.

At the beginning, a short introduction to different methods for polarity determination will be described. Further, in the first part of this chapter the attention will be concentrated on the polar and semipolar $(11\bar{2}2)$ InN layers, while the second part will be dedicated to the polar and semipolar $(11\bar{2}2)$ GaN layers.

4.1 Introduction

The effect of polarity on the surface topography and optoelectronic properties of the group-III-nitride layers described in Chap. 2 emphasizes a great importance to know the polarity of a layer prior to its characterization and utilization.

Despite a large number of the methods for polarity determination, e.g., co-axial impact collision ion scattering spectroscopy, atomic hydrogen irradiation, CBED or method based on the circular photogalvanic effect, they all have a number of limitations. For example, obtaining CBED patterns might be impossible due to high defect densities in the crystal structure or insufficient layer thickness. Wet etching can be affected by incorporated impurities or decoration of defects, leading to an imprecise interpretation of results. Thus, the mentioned methods cannot be applied for the thin polar layers with thickness below $\sim$100 nm and/or polycrystalline layers with high density of defects. Moreover, polarity determination of semipolar layers along the *c*-direction has been achieved until now only by CBED for the 1.5 μm thick GaN layers with a good

crystalline quality [41, 42]. However, growth of similar layers is not always possible for other materials (e.g. InN) or desirable, while polarity determination remains an important characteristic property. In order to solve this problem, an alternative method for polarity determination of thin polar and semipolar group-III nitride layers would be a great advantage.

Recent observation made by Veal et al., where they attributed relative valence band (VB) peak intensities to different polarities of the thin InN layers, has attracted attention for further research. In this chapter, the method for polarity determination by X-ray photoelectron spectroscopy (XPS) will be analyzed in details and discussed. It will be shown that XPS can be also used to determine polarity on the thin polar and semipolar InN and GaN layers.

4.2 Samples

In this chapter polar (0001), (000$\bar{1}$) and semipolar (11$\bar{2}$2) InN and GaN layers grown by MOVPE were investigated.

The polar (0001), (000$\bar{1}$) InN layers were grown on sapphire substrates after sapphire nitridation process at temperatures from 600 °C to 1050 °C. Additionally, the In-polar InN layers were grown on (0001) GaN/Al_2O_3 template and directly on sapphire substrate without nitridation. The semipolar (11$\bar{2}$2) InN and GaN layers were grown on (11$\bar{2}$2) GaN template. The growth procedure for each sample is described in details in Sec. 2.4.2.

The polarities of all investigated polar InN layers were determined by wet chemical etching. N-polar InN layers were grown after nitridation of sapphire substrates at temperatures above 800 °C, while In-polar layers were grown after nitridation at temperatures below 700 °C. After sapphire nitridation at 750 °C the InN layers consisted of the In- and N-polar domains coalesced during the growth and partially rotated to each other. These layers are called mixed-polar layers.

For either type of layer material (i.e. InN and GaN) and layer polarity (N- and group-III-polar) 3-5 samples have been investigated.

4.3 Polar InN Layers

The VB spectra of various polar InN layers recorded at the normal photoelectron emission by XPS using the X-ray Al K_α line for excitation are shown in Fig. 4.1 (a) and (b). Each spectrum exhibits two main peaks: P_I at a lower binding energy (~ 3.5 eV) and P_{II} at a higher binding energy (~ 6.7 eV). The P_I peak is mainly associated with *p*-like VB orbital states (N 2*p*), while P_{II} peak is contributed by *s*-like states (In 5*s*) [49, 56, 128]. The shoulder at the high-binding-energy side of P_I corresponds to a peak with a smaller

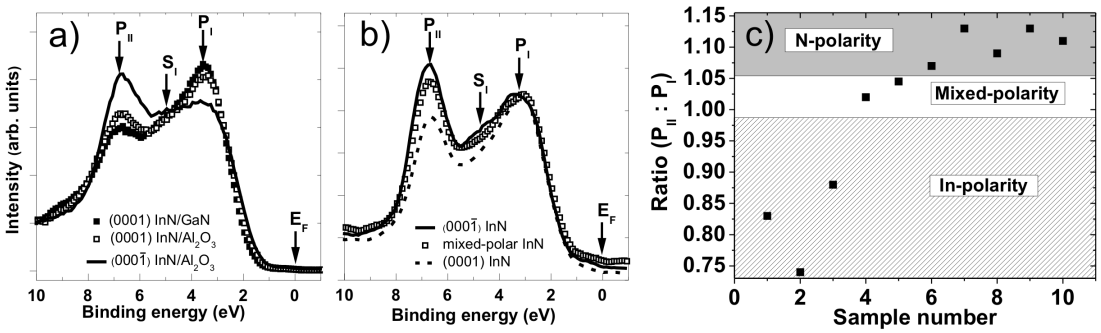

Figure 4.1: The XPS valence band (VB) spectra of a) oxidized In-polar InN layers grown on GaN template (filled squares) and on sapphire without nitridation process (empty squares), and N-polar InN layer grown on sapphire nitridated at 1050 °C (solid line). b) The VB spectra recorded from the thermally annealed polar InN layers grown on sapphire substrate nitridated at temperatures of 800 °C (solid line), 750 °C (empty squares) and 600 °C (dashed line), corresponding to the growth of N-, mixed-, and In-polar layers, respectively. The spectra in (b) were normalized to the P_I peak. The Fermi edge (E_F) refers to the 0 eV on the energy scale. c) The values of the $P_{II} : P_I$ peak ratios after the background subtraction for the series of thermally annealed InN samples with defined regions for the N-, mixed- or In-polar layers.

intensity denoted as S_I (~ 4.9 eV), which is assigned to the *p*-orbital states and to the surface adsorbates [60, 129].

Fig. 4.1 (a) shows the VB spectra recorded from the oxidized polar InN layers. The peak P_I is dominant for the (0001) InN /GaN and (0001) InN /Al_2O_3 layers, which were In-polar, while P_{II} has a higher intensity for the N-polar (000$\bar{1}$) InN /Al_2O_3 layer. The peak heights correlation with the polarity is in agreement with the results observed previously [40].

It is important to mention that the different VB intensities strongly depend on the excitation energy and the statements in this work are valid only for the excitation with the Al K_α line. An advantage of this technique is that the Al K_α radiation is used as a standard X-ray source for XPS equipment in laboratories. Thus, the proposed method can be widely used and does not require an excitation energy that can be achieved only from a synchrotron radiation.

By using another excitation source, e.g. Mg K_α ($h\nu \approx 1254$ eV) for XPS or He I ($h\nu \approx 21.2$ eV) for UPS measurements, the correlation between the VB peak intensities and crystal polarity may be different and require an additional investigation. For instance, the VB spectra recorded from InN layers by using the He I and He II radiation sources have a different shape compared to the one shown in Fig. 4.1, and consist of several well-pronounced peaks [129, 130]. This difference can be explained by a higher surface sensitivity of UPS technique and its higher total energy resolution (~ 0.1 eV) compared to XPS [62].

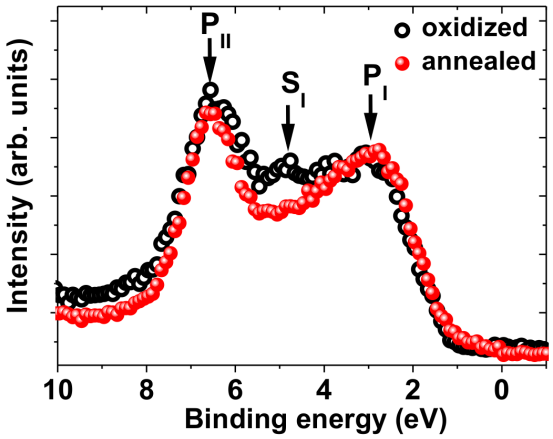

Figure 4.2: VB of oxidized (empty circles) and subsequently annealed (filled circles) at 450°C in UHV N-polar InN layer grown on sapphire substrate nitridated at 800°C. The VB spectrum of the oxidized layer is normalized to the spectrum of annealed layer.

The VB spectra recorded from thermally annealed in UHV N-, mixed- and In-polar InN layers are represented in Fig. 4.1 (b). The layers were annealed at 450 °C for 10 min and exhibited a maximum reduction of the native oxide, while the surface topography and the surface symmetry remained unchanged upon annealing, as observed by AFM and LEED, respectively. The chosen preparation conditions for InN layers will be discussed in details in the next chapters. The stability of InN layers at 450 °C is in agreement with Ref. [131]. By normalizing the spectra to the P_I peak intensity (Fig. 4.1 (b)), changes in the P_{II} peak intensity can be clearly defined: higher intensity of P_I is observed for the In-polar InN layer, while higher intensity of P_{II} is observed for the N-polar InN layer. The peaks in the VB spectrum are about equal in intensity for the mixed-polar layers. The polarities of all investigated InN layers determined by XPS were in good agreement with the results obtained from wet chemical etching. However, due to the insufficient thickness of the layers, performance of CBED on the layers did not succeed.

After annealing, the S_I peak on each spectrum in Fig. 4.1 (b) decreases, exhibiting a deep valley between P_I and P_{II} peaks, compared to the oxidized layers in Fig. 4.1 (a). Indeed, since the S_I peak is assigned to surface contaminants (and *p*-orbital states of InN), desorption of contaminations from the surface upon annealing leads to lower intensity of the S_I peak. This is in agreement with the UPS VB study of the N- and In-polar InN layers covered by oxygen and water, where the states in the VB appear at the same binding energy as the S_I peak, i.e. $\sim$4.8 eV for N-polar and $\sim$5.1 eV for In-polar InN layers [129, 130]. These VB states are associated with the oxygen and/or hydrogen containing adsorbates.

An important observation is that deoxidation does not affect the peak dominations for certain polarity. An example of the VB spectrum of the oxidized and subsequently annealed InN layer is shown in Fig. 4.2. The intensity of P_I and P_{II} peaks remains almost unchanged after annealing, while the S_I peak decreases. Thus, polarity determination by XPS can be performed on the oxidized InN layers with the same accuracy as on the clean annealed layers. This simplifies the polarity determination procedure.

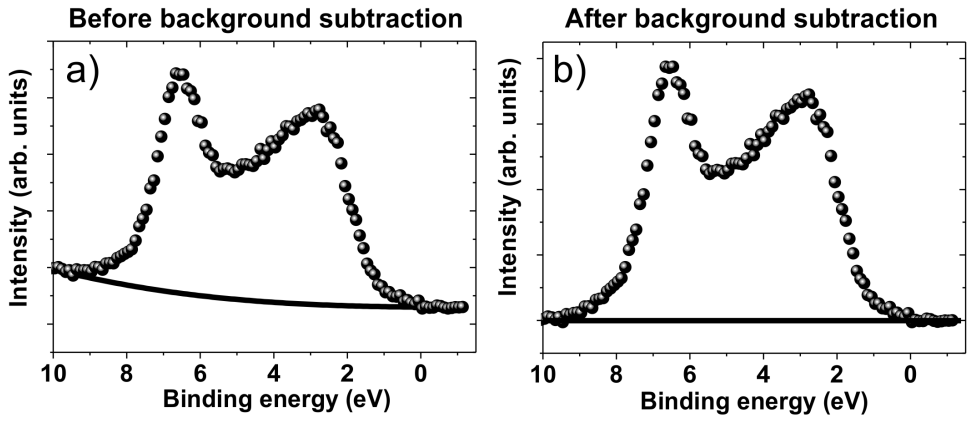

Figure 4.3: a) The VB of the N-polar InN layer with an approximated background. b) The VB spectra after subtraction of the background.

Differences in the VB peak intensities enable to define the value of the ratio between P_{II} and P_I, which can be correlated to the observed InN polarity, as shown in Fig. 4.1 (c). The $P_{II} : P_I$ ratios were determined by taking into account the absolute maximum intensity of the VB peaks after the background subtraction. The background was approximated by a polynomial of third order, which was numerically fitted to the experimental photoemission spectra, as shown in Fig. 4.3. The $P_{II} : P_I$ values are strongly dependent on the chosen experimental conditions, e.g. X-ray excitation energy, energy resolution, acceptance angle of photoelectrons. Therefore, the calculated values give only a qualitative character. Mean value of the $P_{II} : P_I$ ratio for the N-polar orientation was found to be 1.12 ± 0.05, while for the In-polar orientation it amounts to 0.72 ± 0.15, based on the results obtained from 5 samples of each polarity. The InN layers with a mixed-polarity have a mean $P_{II} : P_I$ ratio of 1.00 ± 0.05. Without background subtraction essentially the same $P_{II} : P_I$ ratios are obtained, i.e. 1.16 ± 0.05 for N-polar and 0.78 ± 0.14 for In-polar InN, meaning that a background correction is not necessarily needed for the determination of the $P_{II} : P_I$ ratio. As shown in Fig. 4.3 (b), the domination of the VB peak at higher binding energies after background subtraction is comparable with the spectrum in Fig. 4.3 (a), where no background correction was performed. This is another advantage for the practical use of this method.

Additionally, the independent two-sample pooled *t*-test (Student's *t*-test) was performed to determine a statistical significance between the two $P_{II} : P_I$ mean values for the N-polar and In-polar InN layers. Statistical significance determines if the observed experimental results happen by chance or the observation is a result of particular factors (e.g. crystal or surface properties of layers). The *t* value for the equal sample size of 5 (number of samples in each statistical group) was found to be 5.758 and the *p*-value (two-tailed test) calculated from the *t* distribution was found to be 0.0004 that is smaller than 0.01. Therefore, the difference between the mean values of $P_{II} : P_I$ for the N- and In-polar InN layers is statistically significant at the 0.01 level. In other words, a

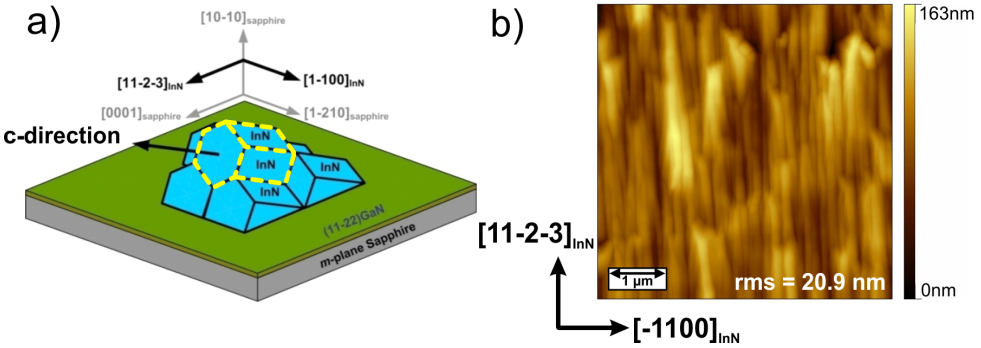

Figure 4.4: a) The $(11\bar{2}2)$ InN unit cell model with the sketched crystallographic directions for InN and sapphire substrate. The unit cell is marked by a dashed line. b) AFM image of semipolar $(11\bar{2}2)$ InN layer.

probability that changes of the $P_{II} : P_I$ ratios with polarity occurs by chance is only 1%. Detailed calculation of the statistical significance for two mean values is described in Appendix A.

Another important aspect for polarity determination by XPS is its an ability to determine polarity of a very thin layer without damaging the surface. X-ray radiation is non-destructive, hence a surface morphology and topography of the examined layer are not affected by XPS, unlike wet etching and CBED, where the sample is partially or fully destroyed after polarity determination. As was described in Sec. 3.2, the information depth for the XPS measurements using Al K_α X-ray excitation is less than 10 nm. Therefore, the polarity of InN layers with thicknesses below 100 nm can be investigated by XPS, while application of CBED on the such thin layers remains challenging. An example of the VB spectrum for the InN layer with thickness $\sim$ 70 nm is shown in Fig. 4.1 (a) for the (0001) InN grown on GaN layer (filled squares). This spectrum is comparable with the one recorded from the $\sim$ 150-200 nm thick (0001) InN layer grown on sapphire without nitridation process (empty squares). This is a good evidence of XPS application for the polarity determination of very thin InN layers.

4.4 Semipolar $(11\bar{2}2)$ InN

Compared to the well-investigated polarity of the *c*-plane InN layers and its effect on surface and electrical properties of a layer, not much is known about the possible influence of the polarity along the *c*-direction for semipolar orientations. For instance, surface topography of a semipolar layer may strongly depend on the polarity along the *c*-direction for this layer. Thus, knowing the polarity would be advantageous for improving and controlling the quality of semipolar layers. Until now, polarity determination of a semipolar orientated layer was achieved only by CBED on 1.5 μm thick GaN layers [41, 42]. Hence, polarity determination of thin semipolar layers with high defect

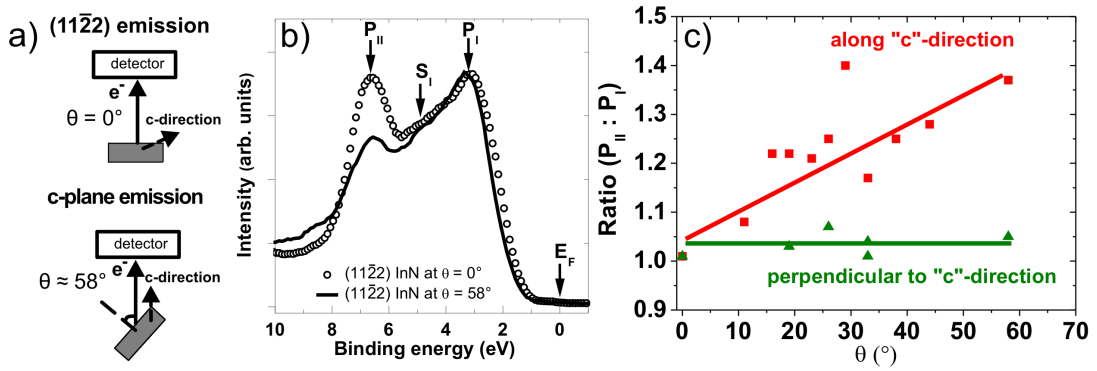

Figure 4.5: a) Sample orientations with respect to detector for two cases: (11$\bar{2}$2) emission and *c*-plane emission. b) The VB XPS spectra of the (11$\bar{2}$2) semipolar InN layer recorded at the normal emission $\theta = 0°$ (circles) and the *c*-plane emission $\theta \approx 58°$ (solid line) with respect to the surface normal. c) The $P_{II} : P_I$ peak ratio depending on the tilt angle θ along the $[11\bar{2}\bar{3}]_{InN}$ (labeled as *"c"*-direction) and $[\bar{1}100]_{InN}$ directions (labeled as perpendicular to *"c"*-direction). The lines are a guide to the eye.

density can be challenging or impossible for CBED. The XPS technique was used to determine polarity along the *c*-direction of the semipolar (11$\bar{2}$2) InN layer based on the principle described for polar InN layers.

The model of the (11$\bar{2}$2) InN unit cell grown on semipolar GaN/*m*-plane sapphire template is shown in Fig. 4.4 (a). A single unit cell is marked by a dashed line. The angle between the *c*-direction and the surface normal equals $\approx 58°$. The AFM image in Fig. 4.4 (b) shows the surface topography of the layer with undulation along the $[\bar{1}100]_{InN}$ direction and the rms roughness of 20.9 nm (measured on $(5\times5)\,\mu m^2$). It has been shown that the surface undulation is formed due to the anisotropic diffusion of indium atoms on the (11$\bar{2}$2) surface: a faster lateral growth rate is assumed to occur along the $[11\bar{2}\bar{3}]_{InN}$ direction compared to the growth rate along the $[\bar{1}100]_{InN}$ [85].

In order to use XPS for polarity determination of a thin semipolar (11$\bar{2}$2) InN layer, the emitted photoelectrons should be measured along the *c*-direction [85]. This can be achieved by tilting the sample by 58° with respect to the surface normal (Fig. 4.5 (a)). The P_I and P_{II} peaks have nearly equal intensities for emission along the [11$\bar{2}$2] direction, while tilting the sample results in a relative increase of the P_I peak indicating the In-polarity along the *c*-direction (Fig. 4.5 (b)). Note that polarity of the used (11$\bar{2}$2) GaN template has been measured by CBED and revealed Ga-polar orientation along the *c*-direction [41]. The polarity of the InN layer is expected to follow the polarity of the GaN template and in good agreement with obtained results. Unfortunately, an alternative polarity determination of the thin (11$\bar{2}$2) InN layers is yet not possible.

Additionally, the VB peaks ratio were measured along the $[11\bar{2}\bar{3}]_{InN}$ direction that corresponds to the *c*-direction at 58 ° and perpendicular to it – along the $[\bar{1}100]_{InN}$ direction. The $P_{II} : P_I$ ratios were estimated for different tilt angles θ, as shown in

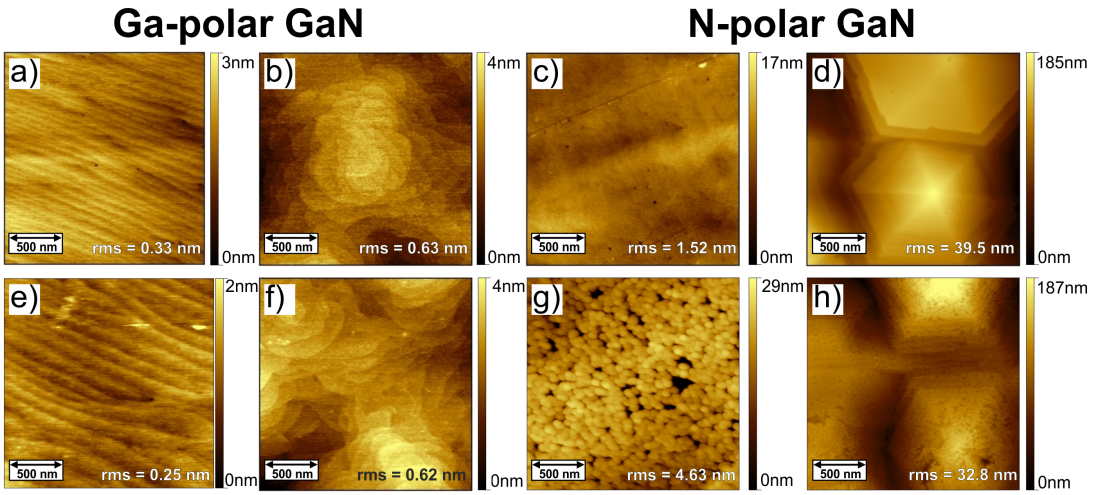

Figure 4.6: AFM images of a), b) the Ga-polar GaN layers with different topography before wet etching, and e),f) after etching. AFM images of c) the smooth and d) rough N-polar GaN layers before wet etching and g),h) after wet etching. Rms roughness is measured on $(2\times2)\,\mu m^2$.

Fig. 4.5 (c). The $P_{II}:P_I$ ratio increases with increasing θ along the $[11\bar{2}\bar{3}]_{InN}$ direction ("c"-direction), while the ratio remains constant by measuring along the $[\bar{1}100]_{InN}$ (perpendicular to the *"c"*-direction). Since the VB peaks consist of a complex structure, an exact interpretation of the $P_{II}:P_I$ ratio alteration with an angle is quite complicated. However, this experiment demonstrates that VB peaks ratio strongly depends on the crystal orientation and the $[\bar{1}\bar{1}23]_{InN}$ and $[1\bar{1}00]_{InN}$ directions can be distinguished by XPS.

This experiment demonstrates that the polarity of the thin semipolar $(11\bar{2}2)$ InN layers can be determined by XPS by measuring the VB along the *c*-direction. This is a clear advantage of XPS over other methods, which are not suitable for polarity determination of thin semipolar layers.

4.5 Polar GaN Layers

The polarity determination by XPS was performed on polar and semipolar GaN layers. However, in order to confirm polarity of the investigated layers, first, it is necessary to determine polarity of the GaN layers by conventional techniques, i.e. wet etching and/or CBED.

The polarity of the GaN layers was determined by both methods, chemical wet etching and CBED, to avoid a mistake in polarity determination. The layers were etched in 40 % KOH solution for 20 min at room temperature. The surface topography of the layers was investigated by AFM prior and after the wet etching process, as shown in Fig. 4.6. The smooth GaN layers with a terrace-like surface structure (Fig. 4.6 (a)) and

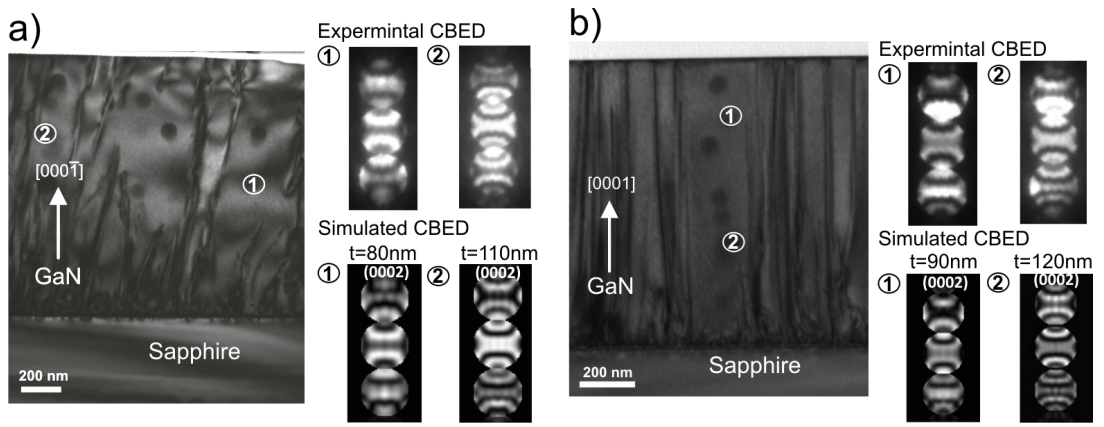

Figure 4.7: Cross-sectional TEM images and CBED patterns of a) N-polar and b) Ga-polar GaN layers with sketched crystallographic directions and labeled positions, where the CBED patterns were recorded. The experimental and simulated CBED patterns are shown for different thicknesses (t) of the TEM foil. The measurements were performed by P. Ruterana´s group at CIMAP, Caen, France.

a spiral-like topography (Fig. 4.6 (b)) show no surface modification after the etching, as shown in Fig. 4.6 (e) and (f), respectively. The rms roughness of the layers shown in the AFM images, also remained unchanged after the etching. As reported in Ref. [39], GaN layers with the Ga-polar orientations are not affected by KOH solution, while topography of the N-polar oriented layers undergoes a significant modification. Hence, the layers shown in Fig. 4.6 (a) and (b) correspond to the Ga-polar GaN.

The AFM images of the GaN layers with a planar smooth (Fig. 4.6 (c)) and hexagon-like (Fig. 4.6 (d)) surface structure exhibit an obvious change after the wet etching. The smooth GaN layer in Fig. 4.6 (c) shows pits and threading dislocations on the surface before etching and a grainy topography after etching by KOH (Fig. 4.6 (g)). The etched regions are also clearly observed on the rough GaN layer with hexagon-like terraces shown in Fig. 4.6 (h). According to Ref. [39], this is an indication for the N-polar orientation of these layers.

For polar GaN layers, cross sectional transmission electron microscopy (TEM) and CBED were performed along the [10$\bar{1}$0] zone axis [132] in an analytical JEOL 2010 microscope operated at 200 keV. The measurements were performed by P. Ruterana´s group at CIMAP, Caen, France. The observations were systematically compared to CBED patterns simulated through Bloch wave procedures using the JEMS software [133]. Electron transparent $<1\bar{1}00>$ cross-sections were prepared by mechanical polishing using the tripod method and then ion-milled in a Gatan Precision Ion Polishing System (PIPS).

The bright field TEM images in Fig. 4.7 show smooth N-polar and Ga-polar GaN layers with threading dislocations along the growth direction [134]. In contrast to earlier reports, [135] no traces of inversion domains have been noticed at this micron scale

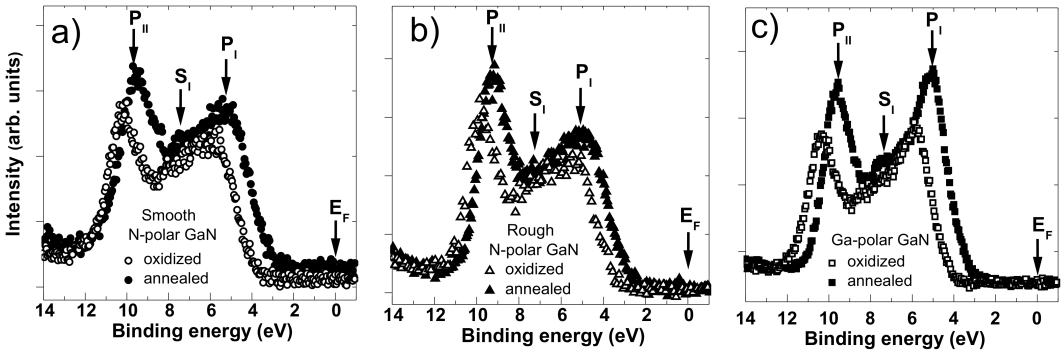

Figure 4.8: XPS VB spectra of the oxidized and annealed a) smooth N-polar GaN, b) rough N-polar GaN and c) Ga-polar GaN layer with the spiral-like morphology.

even inside N-polar layers. The CBED patterns were recorded in non-defective areas indicated on the TEM bright field images shown in Fig. 4.7 (a) and (b). The simulation patterns were performed for different thicknesses of the layers. As can be seen, the experimental patterns for Ga-polar and N-polar GaN layers agree with the simulations. Therefore, determined polarity is in good agreement with the results obtained by wet etching. Therefore, after precise determination of GaN polarity by conventional methods, XPS was used to check if polarity of GaN layers can be determined as was performed for InN layers in the previous Section 4.3.

The VB spectra of N- and Ga-orientated GaN layers were recorded by XPS at the normal photoelectron emission from the oxidized and annealed at 600 °C in UHV layers. The annealing temperature of 600 °C for GaN layers yielded maximum reduction of the surface contaminations without changing the surface topography nor the surface symmetry, as observed by AFM and LEED, respectively. According to Ref. [136], the thermal decomposition of GaN layers do not occur at the chosen annealing temperature.

The VB spectra of the GaN layers consist of two pronounced peaks that mainly correspond to the *s*- and *p*-like VB orbital states [137, 138]. The peak denoted as S_I corresponds to the VB orbital states as well as to the surface adsorbates [60, 139]. The VB spectra of both kind of N-polar GaN layers shown in Fig. 4.8 (a) and (b), are dominated by the peak P_{II} at higher binding energy (≈ 9.5 eV), as was also observed in N-polar InN mentioned before (Fig. 4.1).

For the Ga-polar GaN layers with the planar smooth and spiral-like morphology, P_I at ≈ 5.2 eV slightly dominates the spectrum, as shown in Fig. 4.8 (c) for the Ga-polar GaN layer with the spiral-like surface dislocations. Again the trend remains the same as for In-polar InN layers (Fig. 4.1), although intensity of P_I is not that high compared to P_{II} as in the case of InN. The $P_{II} : P_I$ mean values calculated after the background subtraction from the series of samples for the N- and Ga-polar orientations are found to be 1.25 ± 0.12 and 0.88 ± 0.05, respectively. The determined $P_{II} : P_I$ mean values without

Table 4.1: Relative amount of the carbon and oxygen surface contaminations calculated from the XPS measurements for oxidized and annealed N- and Ga-polar GaN layers with the spiral-like topography. The percentage atomic concentration of the elements was calculated by taking into account the area under the Ga 3s, C 1s and O 1s core-level peaks after the background subtraction.

Surface	Rough N-polar GaN		Smooth N-polar GaN		Ga-polar GaN	
condition	C:Ga	O:Ga	C:Ga	O:Ga	C:Ga	O:Ga
oxidized	0.65	0.30	0.56	0.65	0.27	0.10
annealed	0.24	0.09	0.33	0.05	0.11	0.03

background subtraction are 1.21±0.08 for N-polar and 0.92±0.05 for Ga-polar GaN layers. Therefore, the background correction does not influence the ratio of $P_{II} : P_I$.

The same statistical *t*-test as in the case of InN layers was performed for GaN layers to determine the difference between the mean values of $P_{II} : P_I$ for the N- and Ga-polar orientations. Description of the statistical *t*-test can be found in Appendix A. The statistic *t* value was calculated to be 5.276 for the sample sizes 3 and 2 for the Ga- and N-polar GaN layers, respectively. The calculated *p* values as 0.0133 is smaller than 0.05 but greater than 0.01. Thus, the two mean values ($P_{II} : P_I$) for the N- and Ga-polar GaN layers are different at the 0.05 significance level, implicating that there is only 5% possibility that performed observation occur by chance, e.g., due to a random error.

An important observation can be done by comparing surface topography and the VB spectra for GaN layers. The VB spectra of the rough and smooth N-polar GaN layers are shown in Fig. 4.8 (a), (b). They were measured under the same preparation conditions and exhibited similar stoichiometry (III/V ratio) as determined by XPS. Regardless of the surface topography and significant difference in rms values (1.5 nm and 39.5 nm for the smooth and rough layers, respectively), both GaN layers have a higher intensity of the P_{II} peak, compared to P_I. This is a clear indication that surface structure and roughness have no effect on the correlation of the two VB peak intensities.

The N-polar GaN surface exposed to ambient conditions has a tendency to form an enhanced native oxide layer compared to the Ga-polar GaN surface [140], which was predicted by theoretical calculations [141]. Based on the XPS results, C:Ga and O:Ga ratios were estimated before and after thermal annealing of the layers in UHV (Tab. 4.1). Indeed, investigated N-polar GaN layers exhibit higher amount of carbon and oxygen on the surfaces compared to Ga-orientated layers.

For the oxidized smooth and rough N-polar GaN layers the C:Ga and O:Ga ratios were three times higher than for the Ga-polar GaN layer. After annealing, despite of the high annealing temperature of 600 °C, the N-polar layers still exhibited a large amount of residual contaminations, approximately 2-3 times higher than the Ga-polar GaN layer (Tab. 4.1). Nevertheless, the VB spectra in Fig. 4.8 of these layers are either dominated by P_{II} for the N-polar GaN layers or by P_I for the Ga-polar GaN, regardless of the

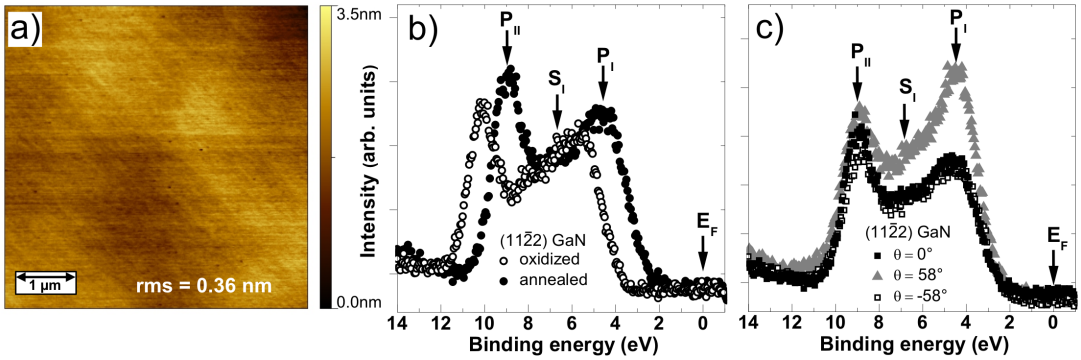

Figure 4.9: a) AFM image of the semipolar (11$\bar{2}$2) GaN layer. b) The VB spectra of the oxidized and annealed (11$\bar{2}$2) GaN layer recorded at normal emission. c) The VB spectra of the annealed (11$\bar{2}$2) GaN layer recorded at normal emission $\theta = 0\,^\circ$ and $\theta = 58\,^\circ$ with respect to the surface normal that corresponds to emission along the *c*-direction and emission at θ = -58 °, respectively.

residual surface contamination. The VB spectra of oxidized and subsequently annealed N-polar GaN layer in Fig. 4.8 (a) and (b) are dominated by P_{II}. Similar results were obtained for Ga-polar GaN, i.e. P_I dominated on oxidized and annealed layers as shown in Fig. 4.8 (c). Thus, contamination has no influence on polarity determination by XPS and the height of the VB peaks correlates only to the crystal polarity.

4.6 Semipolar (11$\bar{2}$2) GaN

Similar to the semipolar InN, also smooth semipolar (11$\bar{2}$2) GaN layer (Fig. 4.9 (a)) with rms roughness of 0.36 nm measured on $(5\times5)\mu m^2$ was analyzed by XPS in order to determine the polarity along the *c*-direction. The model of the (11$\bar{2}$2) GaN unit cell is identical to the one shown for the (11$\bar{2}$2) InN layer in Fig. 4.4 (a), except for the fact that studied semipolar GaN layer was grown on (11$\bar{2}$2) GaN substrate (without sapphire).

The VB spectra in Fig. 4.9 (b) show that at normal emission the intensity of P_{II} is slightly higher compared to P_I for oxidized and annealed semipolar layer. Thus, surface contaminations do not change the dominant peak in the VB spectra of semipolar GaN layer, and this is in good agreement with the observation performed for polar GaN layers. Tilting the sample to the *c*-plane emission increases drastically the intensity of P_I in the VB spectrum shown in Fig. 4.9 (c). The dominance of P_I in the spectrum obtained at $\theta = 58\,^\circ$ indicates Ga-polar orientation along the *c*-direction in the (11$\bar{2}$2) semipolar GaN layer. Polarity of the used (11$\bar{2}$2) GaN template was determined by CBED and showed Ga-polar orientation [86]. Thus, the Ga-polarity of the template is expected to be reproduced on the overgrown (11$\bar{2}$2) GaN layer that is in agreement with obtained results.

In addition, the VB spectrum corresponded to the emission at θ = -58 ° was recorded from the same layer (Fig. 4.9 (c)). The spectrum is almost identical to the one recorded

at normal emission. This fact demonstrates the importance of knowing the crystal direction that corresponds to the *c*-plane emission of the studied sample. The photoemitted VB electrons strongly depend on the crystal orientations and choosing the wrong emission plane can result in the misleading interpretation of results.

4.7 Discussion

The observed effect of different VB peak ratios $P_{II} : P_I$ for N- and group-III-polar InN and GaN layers should originate from the surface or crystal properties of the layers.

One of the possible interpretation can be related to the difference in the binding configurations on the N-polar and group-III-polar layers (see Fig. 2.1 (b)) resulting in different charge distribution within the crystal. A large difference in electronegativity between N and In atoms and spontaneous polarization field along the *c*-direction may affect charge distribution of the valence electrons that is observed in the VB spectrum as domination of P_I or P_{II} peak. Moreover, surface terminated layers may also strongly affect the VB structure. For instance, depending on the type of the terminated atoms, e.g. N or In (Ga), and surface reconstruction, e.g. formation of metallic adlayer, different atomic binding configurations and dangling bonds can be formed on the surface, leading to increase or decrease of the surface electron charge. Another possible influence may arise from a number of atomic monolayers that contribute to the XPS VB spectrum. Depending on the surface termination and bonds alignment between terminated monolayer and the underneath layer, different number of N and In (Ga) monolayers may contribute to the final spectrum. However, this effect is probably insignificant, since one should also consider such facts as presence of defects in crystal structure, steps and dislocations on surface, etc. Moreover, as was mentioned for GaN layers, surface roughness and topography do not affect the $P_{II} : P_I$ ratio. However, the proposed origins of the correlation between the VB peak ratios $P_{II} : P_I$ and metal- or N-polar InN and GaN layers are only assumptions and speculations. Obviously, further experimental investigations accompanied by theoretical interpretation and calculation are needed.

Interesting is the fact that the similar peak dependencies of the VB states with respect to the crystal polarity were observed for the wurtzite II-VI semiconductor materials, such as ZnO and CdS [142]. In these cases, the group-II-polar (Zn-polar and Cd-polar) layers showed higher intensities of the VB peak at lower binding energy (P_I), while the group-VI-polar ZnO and CdS layers showed the dominance of the VB peak at higher binding energy 8 P_{II}). Application of the XPS technique for polarity determination of AlN layers and ternary group-III nitride alloys has not been investigated yet. Outlook for possible experimental measurements on these materials will be discussed in summary of this.

4.8 Summary

It was shown that XPS is a reliable and non-destructive method for polarity determination of polar (0001), (000$\bar{1}$) and semipolar (11$\bar{2}$2) InN and GaN layers. The polarity can be determined by recording the VB spectrum for emission perpendicular to the c-plane, i.e., normal emission for polar layers and emission at 58 ° with respect to the surface normal for semipolar (11$\bar{2}$2) orientations. A higher peak intensity at lower binding energy (P_I) correlates with the III-polar layers, while a higher peak intensity at higher binding energy (P_{II}) correlates to the N-polar GaN and InN layers. The $P_{II} : P_I$ ratio strongly depends only on the crystal orientation and can be calculated from spectra without a background subtraction procedure. It was shown that surface morphology and surface contaminations do not effect the VB peak intensities and thus, the ratio between P_{II} and P_I. The polarities of the layers determined by XPS are in good agreement with chemical wet etching and CBED results. Moreover, it was shown that XPS can be used for polarity determination of the layers with thickness below 100 nm without causing any damage to the surface.

5 Effect of Sapphire Nitridation on Polar InN Layers

A sapphire nitridation process is usually performed prior to the growth of InN layers on sapphire substrates in order to reduce a lattice mismatch from 27% between InN and *c*-plane sapphire to 13.9% between InN and formed by nitridation AlN layer [78]. It was shown that sapphire nitridation affects surface topography, electrical and optical properties of InN layers [13, 79, 82]. However, a contradictory information concerning the most appropriate nitridation conditions for a growth of high quality InN layers can be found in the literature. Despite of the many publications about sapphire nitridation process, investigations with an emphasis on the surface properties of the nitridated layers have been only rarely performed. Thus, this chapter is dedicated to the surface study of the nitridated sapphire layers,including the chemical bonding configurations and the detailed atomic structure on the layers, and their effect on subsequently grown polar InN layers.

The chapter will be focused on the comprehensive surface analysis of the MOVPE grown thin nitridated sapphire layers, starting from the study of the oxidized and clean bare *c*-plane sapphire substrates prior to nitridation. It will be shown that the growth conditions influence the surface reconstructions, topography and chemical binding configurations of the nitridated layers of sapphire. Moreover, the effect of the nitridated sapphire layers on the surface and crystal properties of the overgrown *c*-plane InN layers will be discussed. The most suitable nitridation conditions for the growth of the good quality InN layers will be introduced. Polarity, topography and crystallinity of the InN layers is found to depend on the chemical binding configurations of the nitridated layers.

5.1 Samples

The bare *c*-plane sapphire substrates were firstly cleaned by sequential immersion into acetone, iso-propanol and de-ionized water. Afterwards, the substrates were thermally annealed at 700 °C in UHV chamber or at a temperature of 1050 °C in the MOVPE system in an H_2 gas flow (3 l/min). The nitridation of the clean *c*-plane sapphire substrates was performed after annealing in MOVPE by exposing the layers to ammonia flux of 1 l/min for 2 min at temperatures between 500 °C and 1050 °C.

The *c*-plane InN layers were grown on the nitridated sapphire layers by MOVPE at 560 °C for 2 h as described in Sec. 2.4.2. More details about the growth procedure can be found elsewhere [84]. The estimated thickness of the grown polar InN layers varied in the range of 70 nm to 200 nm. MOVPE growth of InN layers and nitridated sapphire layers was performed by D. V. Dinh at TU Berlin.

5.2 Surface Properties of Nitridated Sapphire

As was already mentioned, the sapphire nitridation process can improve quality of InN layers [13, 79, 82]. The InN growth is directly affected by the crystal property and quality of the nitridated layers, e.g. defects formed in the nitridated layers might propagate into the InN bulk structure. Therefore, InN/nitridated layer interface becomes a critical issue and must be studied and well understood. For this, it is important to know the surface atomic structure of the nitridated layers, their chemical binding configurations.

5.2.1 The Clean Sapphire Surfaces

First, a surface analysis of the bare *c*-plane sapphire substrates was performed in order to understand its effect on the nitridation process.

Surface topography of *c*-plane sapphire substrates thermally cleaned at 700 °C in the UHV chamber and at 1050 °C in MOVPE system was analyzed by AFM. In both cases, AFM images (top row) shown in Fig. 5.1 (a) and (b) represent a terrace step-like topography of the layers with monoatomic steps. No obvious differences in the surface structure can be distinguished. The *c*-plane sapphire layer thermally cleaned in the MOVPE system was later transferred into the UHV chamber, where the surface symmetry of both layers was analyzed by LEED. The LEED pattern showed a (1×1) symmetry for the sapphire layer annealed under UHV conditions (Fig. 5.1 (a), bottom row). However, a $(\sqrt{31}\times\sqrt{31})\mathrm{R}\pm9\,^\circ$ surface reconstruction was observed for the layer annealed in the MOVPE system (Fig. 5.1 (b), bottom row). In the latter case, the sapphire layer was additionally annealed in UHV at 350°C in order to desorb surface oxide formed on the layer after transfer through air. Thus, although the surface topography for both layers is the same, surface atomic reconstruction is different for each layer.

It was reported previously that the *c*-plane sapphire layers are known to change from the (1×1) into the $(\sqrt{31}\times\sqrt{31})\mathrm{R}\pm9\,^\circ$ surface reconstruction after annealing in vacuum at temperature above 1200 °C [143, 144] or after annealing under Al-rich condition at 800 °C [143]. Moreover, a weak $(\sqrt{3}\times\sqrt{3})\mathrm{R}\pm30\,^\circ$ reconstructed surface was observed on aluminum oxide layers if the annealing temperature was not high enough to achieve the rotated $(\sqrt{31}\times\sqrt{31})$ surface structure [143]. Fig. 5.1 (c) schematically shows the diffraction patterns achieved on sapphire layers. Due to a low intensity of the diffraction spots in Fig. 5.1 (b) (bottom row), not all reflexes can be distinguished in this LEED pattern, however, the similarity with the sketched $(\sqrt{31}\times\sqrt{31})\mathrm{R}\pm9\,^\circ$

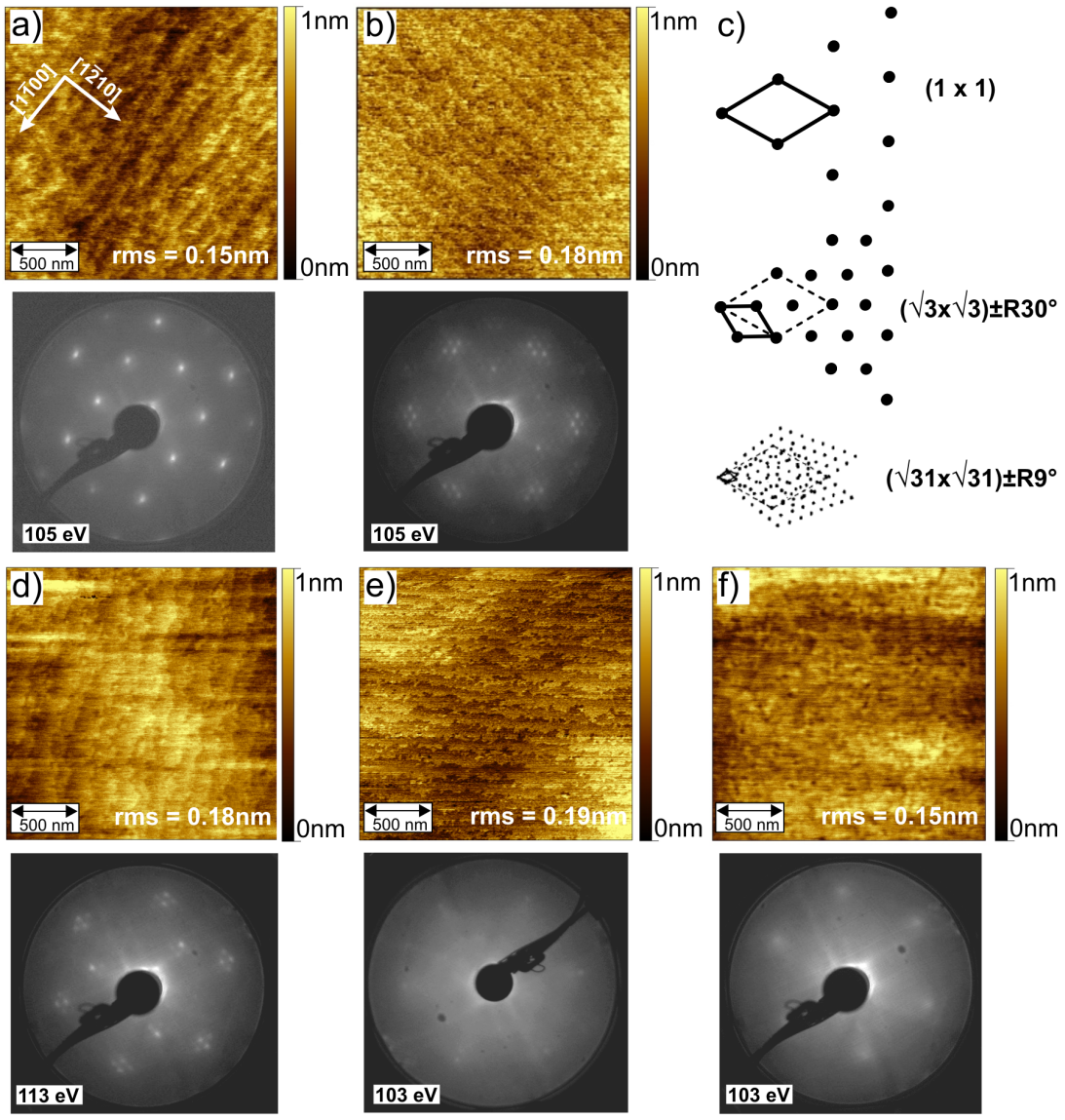

Figure 5.1: AFM images of $(2\times2)\,\mu m^2$ (top row) and LEED diffraction patterns (bottom row) of the sapphire substrates a) annealed at 700 °C in UHV, b) annealed at 1050 °C in MOVPE system in H_2 ambient, d) nitridated at $T_{nitr} = 700$ °C, e) at $T_{nitr} = 800$ °C, and f) at $T_{nitr} = 1050$ °C. Image (c) schematically represents diffraction patterns observed on the *c*-plane sapphire substrates upon annealing at different temperatures [143]. AFM images were measured by D. V. Dinh, TU Berlin.

reconstruction is obvious. For the (1×1) reconstructed layer shown in Fig. 5.1 (a), the annealing temperature of 700 °C was not enough to achieve the $(\sqrt{31}\times\sqrt{31})R\pm9\,^\circ$ surface symmetry that is in agreement with the previous observations [143, 144]. However, the $(\sqrt{3}\times\sqrt{3})R\pm30\,^\circ$ structure was not observed in the investigated layers.

It was proposed that the $(\sqrt{31}\times\sqrt{31})\mathrm{R}\pm 9^\circ$ surface reconstruction occurs due to the loss of oxygen after annealing at high temperature and stems from a cubic Al overlayer on top of the hexagonal sapphire substrate [143]. As a consequence, it is assumed that the topmost layer consists of the reduced aluminum oxide, e.g. Al_2O or AlO.

Additionally, the Al/O ratios were calculated from the XPS measurements performed at 80° (surface sensitive measurements). For the (1×1) sapphire substrate, the Al/O ratio equals 0.85, while for the $(\sqrt{31}\times\sqrt{31})\mathrm{R}\pm 9^\circ$ reconstructed surface this value increases to 0.88 that corresponds to the decrease of oxygen amount on the surface in the second case. This observation confirms the assumption that the reduced aluminum oxide layer is formed on the $(\sqrt{31}\times\sqrt{31})\mathrm{R}\pm 9^\circ$ reconstructed sapphire surface.

Since the $(\sqrt{31}\times\sqrt{31})\mathrm{R}\pm 9^\circ$ symmetry was observed even after transfer of the annealed sapphire through ambient air, it seems that oxidation does not affect the surface reconstruction. Thus, the formed Al_xO top-layer remains oxygen deficient and the strong stability of the $(\sqrt{31}\times\sqrt{31})\mathrm{R}\pm 9^\circ$ reconstruction might be explained if the layer is Al-terminated [145]. Note that the (1×1) sapphire surface is presumed to be oxygen terminated [84, 145].

5.2.2 The Nitridated Sapphire Layers

During the sapphire nitridation process nitrogen atoms diffuse into the sapphire substrate and substitute oxygen atoms bonded to aluminum atoms. However, nitridation does not take place on every sapphire surface. The investigated nitridated layers in this work were grown on the $(\sqrt{31}\times\sqrt{31})\mathrm{R}\pm 9^\circ$ reconstructed surface, while the nitridation process was not achieved on the O-terminated (1×1) sapphire surface. A similar observation was reported for nitridation by exposure sapphire substrates to low pressure ammonia [146]. The lower coordination of aluminum ions on the $(\sqrt{31}\times\sqrt{31})\mathrm{R}\pm 9^\circ$ surface seem to achieve a higher reactivity with ammonia, which is essential for the nitridation process [146]. This leads to the conclusion that Al-termination of sapphire surface is necessary for successful nitridation [84].

The topography and surface symmetry of the investigated nitridated layers were analyzed by AFM and LEED. The layers nitridated at 700 °C (Fig. 5.1 (d)) and 800 °C (Fig. 5.1 (e)) show topography similar to the annealed sapphire. However, for the nitridation at 1050 °C, the surface topography changes, as shown in Fig. 5.1 (f), where a smooth textured nitridated layer is observed. The rms roughness of the AFM image measured on $(2\times2)\,\mu\mathrm{m}^2$ is 0.15 nm that is comparable with the layers nitridated at lower temperatures.

At the same time, an increase of the nitridation temperature leads to the changes in the surface symmetry observed after transfer to UHV. The surface reconstruction changes from the $(\sqrt{31}\times\sqrt{31})\mathrm{R}\pm 9^\circ$ surface for the sapphire substrate nitridated at 700 °C (Fig. 5.1 (d), bottom row) into (1×1) for the sapphire nitridated at 1050 °C (Fig. 5.1 (f), bottom row). The transition of the surface reconstruction takes place for the layer nitridated at 800 °C (Fig. 5.1 (e)), where the diffraction spots of the main (1×1) reflexes

remain visible in the LEED pattern, while the diffraction spots corresponding to the $(\sqrt{31}\times\sqrt{31})\mathrm{R}\pm 9^{\circ}$ reconstruction are blurred. The observed changes of surface symmetry confirm the formation of the nitridated layers on the top of sapphire substrates. Indeed, by increasing the nitridation temperature, the ammonia decomposition rate in the MOVPE system also increases [147], leading to the larger amount of active nitrogen ions reacting with the sapphire surface. However, the intensity of the (1×1) spots in Fig. 5.1 (f) is lower compared to the clean (1×1) sapphire, hence it can correspond to both, either a formed (poly-)crystalline (AlN) [148] or an amorphous (AlN_xO_y) [149] layer.

It is important to note that due to the insulating behavior of the sapphire substrates and thin nitridated layers, the energy of the incident electron beam used by LEED has to be above 100 eV in order to overcome a surface charging effect. At these energies the surface charging effect was suppressed and has no influence on the geometry of the diffraction patterns [143, 150].

The chemical bonding analysis of the nitridated layers was performed by using XPS. The line shapes for normal emission of N 1*s*, Al 2*p* and O 1*s* core-level peaks of sapphire layers nitridated at different temperature were fitted with several components and analyzed in details. Additionally, surface sensitive measurements of the N 1*s* core-level emission line were performed on the sapphire layers nitridated at nitridation temperature (T_{nitr}) of 700°C and 1050°C.

The numerical analysis of the N 1*s* core-level gives the best fit by using four chemical components labeled as N-O, N-Al, N_d and N_x (Fig. 5.2 (a)-(c)). The number of the N 1*s* components found in the literature for the nitridated sapphire and bulk AlN layers usually varies from 2 [151, 152] to 4 [153, 154]. For the N 1*s* core-level peaks recorded at the pass energy of 20 eV, a lifetime broadening (γ) of 0.2 eV and an experimental broadening (σ) of 1.8 eV were used. The lifetime broadening value is in agreement with the fit performed on the Al 2*p* and O 1*s* core-levels for the same examined layers. Overall fit parameters for the N 1*s*, Al 2*p* and O 1*s* core-level states can be found in Appendix B. A surface charging effect was observed on all investigated layers due to the insulating behavior of sapphire and thin nitridated layers, resulting in the energy shift of the core-level emission lines. For correction of the energy scale all core-level spectra were re-calibrated to the N-Al bulk component of the N 1*s* core-level peak at 398.5 eV [154].

The integrated intensity of the N 1*s* core-level for the layer nitridated at 700 °C (Fig. 5.2 (a)) is about 5 times smaller compared to that of the layer nitridated at 1050 °C. The increased nitridation temperature results in more active ammonia that can react with a surface [147]. Hence, a larger number of N-Al bonds form on the surface by substituting oxygen atoms in sapphire by nitrogen atoms and forming the nitridated layer. This can be observed in Fig. 5.2 (a)-(c), where the N-Al component rapidly increases with nitridation temperature.

The component of the N 1*s* core-level shifted by 1.65 eV toward higher binding energies with respect to the N-Al component is assigned to nitrogen bonded to oxygen

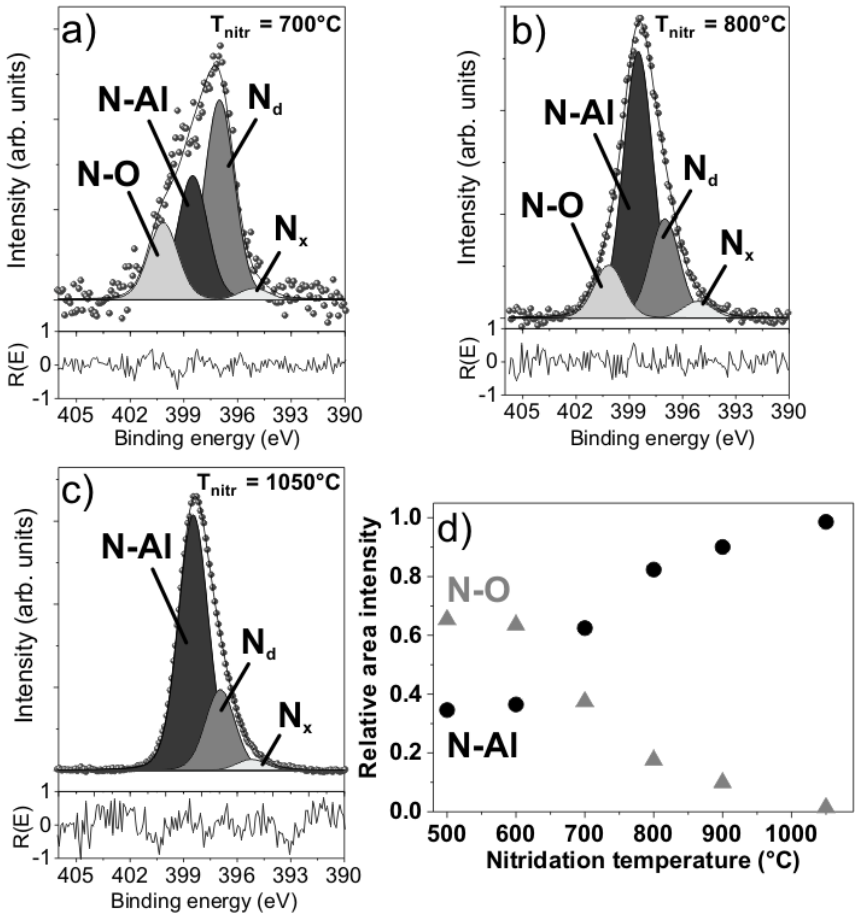

Figure 5.2: The N 1*s* core-level spectra recorded at the normal emission from the sapphire substrates nitridated at a) $T_{nitr} = 700°C$, b) $T_{nitr} = 800°C$, c) $T_{nitr} = 1050°C$. The deviation R(E) of the measured and fitted spectra are shown below each core-level peak. d) The relative area intensities of the N-O and N-Al components of the N 1*s* core-levels for different temperatures of sapphire nitridation.

(N-O component). The energetic shift is in agreement with electronegativity of the atoms: the electronegativity of oxygen (3.44) is larger than the ones for nitrogen (3.04) and aluminum (1.61) atoms (here and further electronegativity corresponds to Pauling scale). Thus, the N-O bond is associated with a relative charge depletion at the N atom, leading to a lower electron screening effect of that atom. As a consequence, the electrons related to this atom have higher binding energy. As shown in Fig. 5.2, the N-O component is clearly observed on the sapphire substrate nitridated at low temperatures, e.g. 700 °C and 800 °C, but almost vanishes at $T_{nitr} = 1050$ °C, where the bulk N-Al component dominates the spectrum.

The component shifted by 1.5 eV toward lower binding energies, denoted as N_d, must correspond to the nitrogen atom bonded to the atom with an electronegativity value

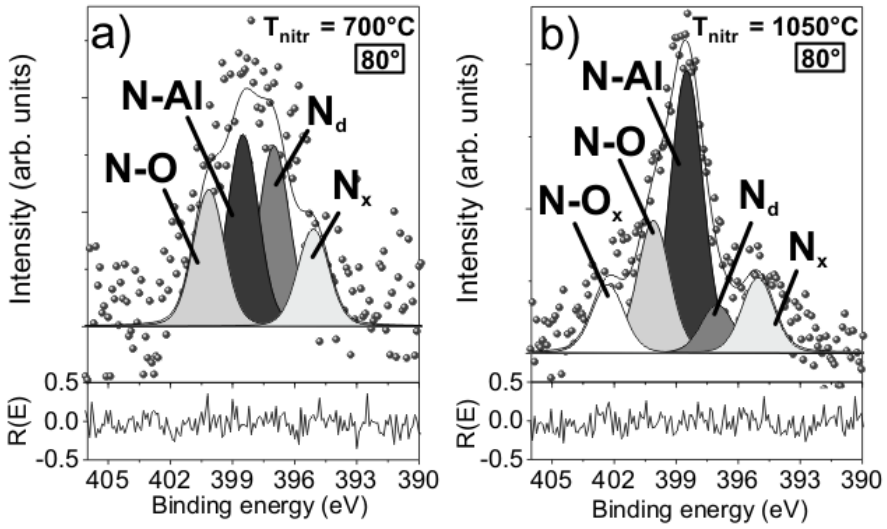

Figure 5.3: The N 1*s* core-level peaks recorded at photoelectron emission of 80° with respect to the surface from the sapphire substrates nitridated at a) $T_{nitr} = 700°C$ and b) $T_{nitr} = 1050°C$.

lower than that for aluminum (1.61). The integrated intensity of the N_d component remains almost constant with respect to the intensity of the N-Al component for the layers nitridated above 800 °C (Fig. 5.2 (b) (c)). A similar component was reported by Rosenberger et al. for 0.2 - 2.0 μm thick AlN layer and was assigned to the N-N bonded defects [153], in which the N atoms have less than 4 chemical bonds [155]. The AlN layers in that study were grown by plasma source MBE, where the N-N bonds can be formed from the $N_2{}^+$ ions. However, it has been shown that the N-N bonds can also be formed during the layer by layer growth [155]. In this work the nitridation process has been performed by using N_2 carrier gas [84] that may be responsible for the formation of the N-N bonds in the crystal or/and due to decomposition of ammonia into N species. In the earlier study of AlN layers by Laidani et al., the component in the N 1*s* core-level shifted by 1.4 eV towards lower binding energies was assigned to a substoichiometric nitride phase AlN_x [156]. In both Ref. [153, 156] the N_d component remains almost constant with respect to the Al-N bulk component. Similar behavior of the N_d component is observed for the layers nitridated above 800 °C (Fig. 5.2). Moreover, as will be shown later by HRTEM measurements, a crystalline AlN layer (not an amorphous layer) was formed on the sapphire substrate nitridated at $T_{nitr} = 1050$ °C that excludes an assumption that the component labeled as N_d originates from oxinitrides, as assigned by Prieto et al [157]. Based on these discussions, it is difficult to clearly define whether the N_d component originates from the N-N defects or AlN_x phase. However, both cases refer to the defects in the structure, therefore, N_d is assigned to the defects inside the nitridated layers.

The surface sensitive measurements of the N 1*s* emission line shows a decrease of the N_d component compared to the intensity of the N-Al component for $T_{nitr} = 700°C$ and

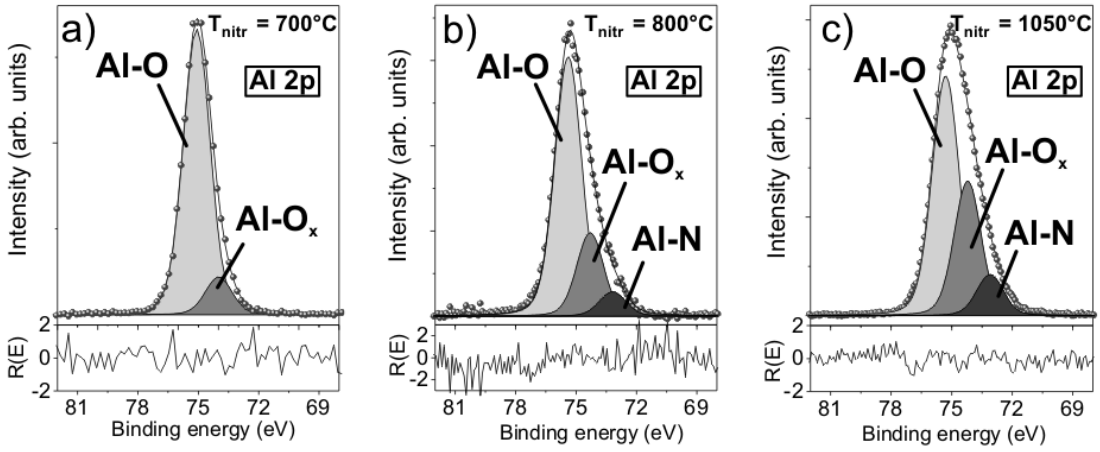

Figure 5.4: The Al 2*p* core-level peaks recorded at normal emission from the sapphire substrates nitridated at a) $T_{nitr} = 700°C$, b) $T_{nitr} = 800°C$, c) $T_{nitr} = 1050°C$. The deviation R(E) of the measured and fitted spectra are shown below each core-level peak.

$T_{nitr} = 1050°C$, as represented in Fig. 5.3 (a) and (b), respectively. This is an evidence that the chemical bonds associated with N_d originate from the inner region of the nitridated layers and not from its surface. This is in good agreement with the assumption that the N_d component corresponds to the defects within the layers structure.

The fourth component N_x shifted by 3.4 eV toward lower binding energies compared to the N-Al bond has only a very small contribution to the N 1*s* emission line for all cases. However, the fit is significantly worse if this fourth component is not considered due to the asymmetric shoulder of the N 1*s* peak at lower binding energies, as shown in Fig. 5.2. Also the use of a Shirley background instead of used in this work a third order polynomial background does not significantly modify the fitting results including the N_x component. The surface sensitive measurements at an emission angle of 80° with respect to the surface normal in Fig. 5.3 showed an increase of the N_x component compared to the normal emission spectra, indicating that the N_x component originates from the surface region. Hence, the N_x is a real component present even after surface preparation under UHV conditions.

Moreover, an additional component labeled as N-O_x appears on the N 1*s* spectrum for the surface sensitive measurement for the sapphire layer nitridated at 1050°C (Fig. 5.3 (b)). This component is shifted by 3.8 eV towards higher binding energies compared to the N-Al and originates from a very surface region. Hence, it is assigned to the N atoms that are bonded with residual surface contaminations (O_x) in agreement with Ref. [154, 158].

As shown in Fig. 5.2 (d), an increase of the nitridation temperature results in a significant increase of the relative amount of the N-Al component and decrease of the N-O component. Obviously, a crystalline AlN layer can be formed by nitridation, when the N-Al component dominates in the N 1*s* spectrum ($T_{nitr} > 800\,°C$) and at the same time,

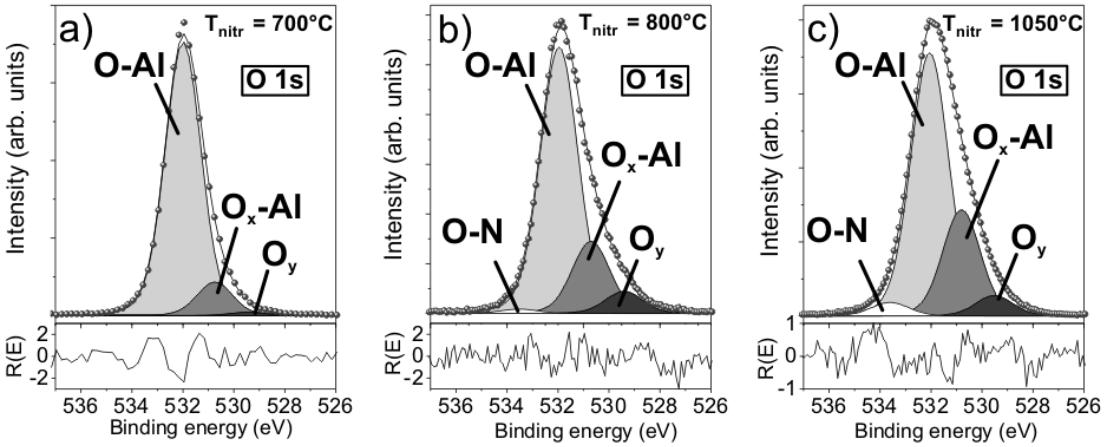

Figure 5.5: The O 1s core-level peaks recorded at normal emission from the sapphire substrates nitridated at a) $T_{nitr} = 700°C$, b) $T_{nitr} = 800°C$, c) $T_{nitr} = 1050°C$. The R(E) is a deviation of the measured and fitted spectra.

the N-O component is negligibly small or vanishes. A significant contribution of the N-O component in the N 1*s* core-level spectrum at $T_{nitr} < 800\,°C$ corresponds rather to a formation of an amorphous AlN_xO_y nitridated layer on sapphire substrate. Notice that nitrogen species, responsible for the formation of a nitridated layer, are detected even at a very low nitridation temperature, e.g. 500-700 °C, though in a small amount.

The fitting of the Al 2*p* and O 1*s* are depicted in Fig. 5.4 and Fig. 5.5, respectively. For the Al 2*p* peak, the Al-N component, assigned to the binding of aluminum with nitrogen atom in the nitridated layer, can be distinguished at $T_{nitr} > 800°C$. The intensity of Al-N component increases with increasing the nitridation temperature, in agreement with the N-Al component in the N 1*s* core-levels. Since amount of nitrogen on the surface is very low for $T_{nitr} = 700°C$, the Al-N component is not observed in Fig. 5.4 (a). Besides the Al-O component that corresponds to the chemical bonds between Al and O in sapphire substrate, the Al 2*p* peak includes another component labeled as Al-O_x. This component increases with increase of the nitridation temperature and a corresponding compound can be also found in the O 1*s* peak (O_x-Al component), as shown in Fig. 5.5. The Al-O_x component might originate from the interface between the nitridated layer and sapphire. Some of the oxygen atoms that escaped the crystal due to the high nitridation temperature, might not be substituted by the nitrogen atoms. As a result, the Al_xO_y phase could be formed on the nitridated layer/sapphire interface.

The O 1*s* peak in Fig. 5.5 mainly consists of the O-Al component associated with the sapphire structure and the O_x-Al component assigned to the Al_xO_y phase. Two other components labeled as O-N and O_y are very small for all investigated layers and probably originate from the surface contaminations on the surfaces.

Thus, the XPS measurements reveal the formation of AlN layer after nitridation at $T_{nitr} < 800\,°C$ that confirms the interpretation of the LEED patterns, showing a change

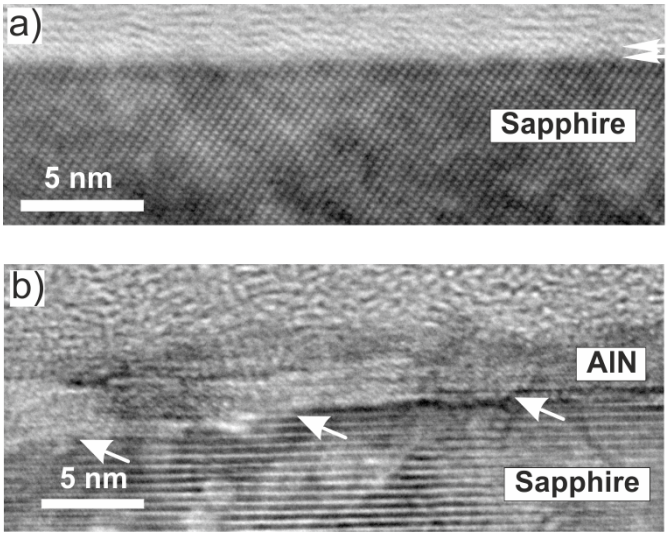

Figure 5.6: HRTEM images of the sapphire substrates nitridated at a) $T_{nitr} = 800\,^{\circ}C$ and b) $T_{nitr} = 1050\,^{\circ}C$. Arrows in the image (a) correspond to the amorphous layer, while arrows in the image (b) refer to the step-like structure. Measurements were performed by B. Lacroix, research group of P. Ruterana at CIMAP, Caen, France.

in surface symmetry for the layers grown at this temperature range. In order to confirm the interpretation of the XPS results, HRTEM was performed on the layers nitridated at 800 °C and 1050 °C. All TEM and HRTEM measurements shown in this chapter were performed by B. Lacroix, research group of Dr. P. Ruterana at CIMAP, Caen, France.

In the HRTEM image (Fig. 5.6 (a)) the sapphire substrate exhibits a flat surface. However, there is a lighter contrast of a disordered very thin layer extending to less than 0.5 nm, which is different from the above covering glue. The glue has been used to protect the surface during the TEM sample preparation. As the nitridation has been carried out on a clean surface with atomic steps, this observation is a strong indication that at 800°C, the nitridation has only taken place inside the superficial area where one should usually see steps [159]. Therefore, a thin layer (see arrows) has undergone extensive structural transformation during the nitridation stage. This is in agreement with the XPS results, where it was expected that a very thin amorphous layer was formed at the surface for $T_{nitr} = 800\,^{\circ}C$.

Fig. 5.6 (b) shows a thin crystalline AlN layer grown on the sapphire substrate at 1050 °C. The AlN layer is homogeneously formed on top of the sapphire surface and varies in thickness from 2 nm to 5 nm. Moreover, in this case the sapphire substrate shows a step-like surface structure (see arrows), which is a good indication that the grown nitridated layer may have followed the steps of the starting surface. This surface topography of the nitridated layers is in agreement with the results obtained by AFM, where the sapphire surface is still observed after 800 °C (Fig. 5.1 (e)) but a smooth nitridated layer is formed at 1050 °C (Fig. 5.1 (f)). Unfortunately, the presumed from XPS measurements Al_xO_y phase formed on nitridated layer/sapphire interface can not be clearly distinguished in the HRTEM images.

Thereby, formation of the crystalline AlN layer on the sapphire surface starts at temperatures above 800 °C, corresponding to the significant amount of the N-Al chemical

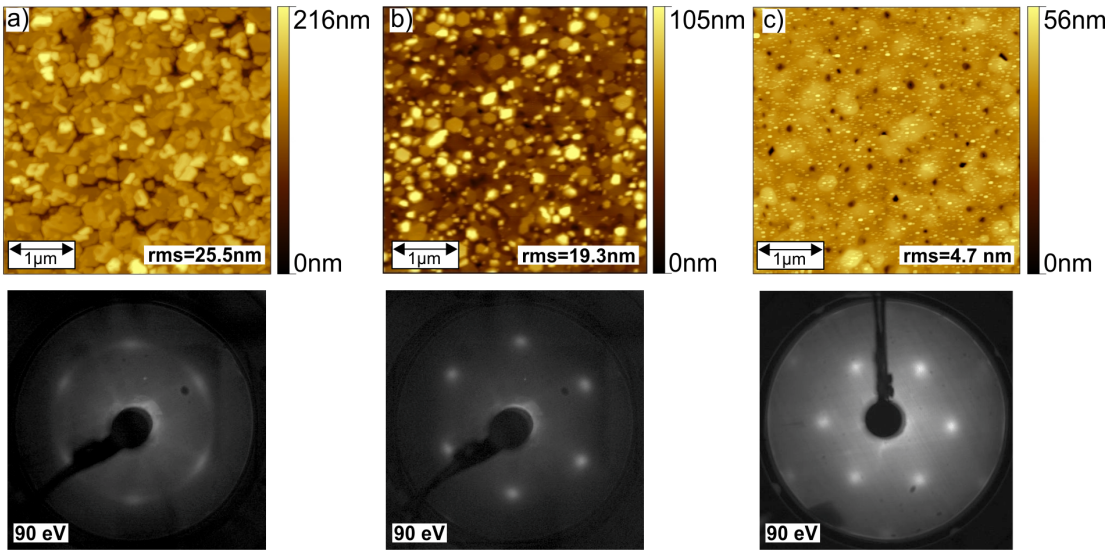

Figure 5.7: The AFM images ($(5\times5)\,\mu m^2$) and LEED patterns of a) the In-polar InN layer grown at $T_{nitr} = 600°C$, b) the mixed-polar InN layer grown at $T_{nitr} = 750\,°C$ and c) the N-polar InN layer grown at $T_{nitr} = 1050°C$. The AFM images were measured by D. V. Dinh at TU Berlin.

bonds on the surface compared to amount of the N-O bonds. For temperatures $\leq 800\,°C$ an amorphous AlN_xO_y layer is formed on the sapphire surface that correlates with the presence of the N-O component in the N 1*s* core-level spectra.

5.3 Properties of Subsequently Grown Polar InN Layers

It is reasonable to assume that different type of sapphire nitridated layers (i.e., crystalline and amorphous layers) will have a strong impact on the crystalline quality of the subsequently grown InN layers. In order to confirm this assumption, the surface and crystal properties of the polar InN layers were detailed investigated.

At first, the surface topography of the polar InN layers overgrown on the nitridated sapphires were measured by AFM. Fig. 5.7 shows topography of the InN layers grown on the sapphire substrates nitridated at 600 °C, 750 °C and 1050 °C. With increase the nitridation temperature the rms roughness of the InN layers decreases from 25.5 nm at $T_{nitr} = 600\,°C$ to 4.7 nm at $T_{nitr} = 1050\,°C$ that is one of the best values for the MOVPE grown InN layers in the literature [14]. The trend of the InN rms roughness with increase of the nitridation temperature is represented in Fig. 5.8. Besides the surface roughness, also the surface structure of the polar InN layers undergoes modification: the InN layer grown on the amorphous AlN_xO_y layer ($T_{nitr} = 600\,°C$) consists of partially coalesced islands as shown in Fig. 5.7 (a); the InN layer grown on the amorphous AlN_xO_y layer ($T_{nitr} = 750\,°C$) shows hexagonal structures on the surface (Fig. 5.7 (b));

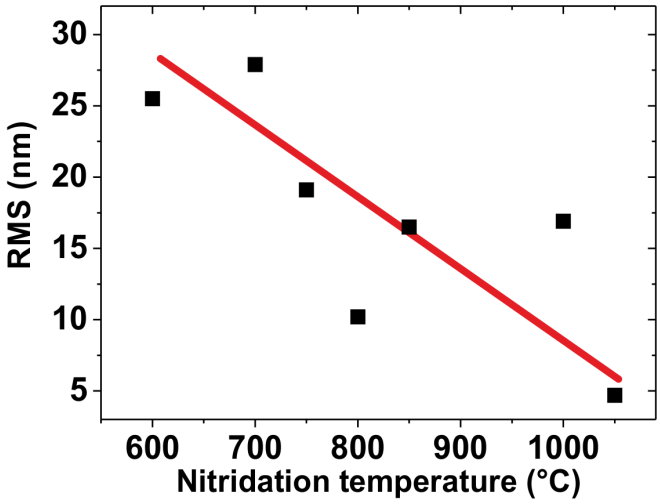

Figure 5.8: The rms roughness measured on $(5\times5)\,\mu m^2$ of the polar InN layers dependent on the nitridation temperatures. Line is a guide to the eye.

the InN layer grown on the thin AlN layer ($T_{nitr} = 1050\,^{\circ}C$) exhibits a smooth layer, although with some pits and hillocks on the surface.

Additionally, the surface periodicity of the InN layers were determined by LEED under UHV conditions. All layers exhibit a (1×1) surface symmetry as shown in Fig. 5.7. However, the shape of the diffraction spots that corresponds to the surface crystalline quality, differs for some of the InN layers. For the InN layers grown at $T_{nitr} \leq 700\,^{\circ}C$ the LEED reflexes have a diffused shape corresponding to a poor surface crystalline quality (Fig. 5.7 (a)). The surface quality of the InN layers improves using a nitridation temperature $\geq 750\,^{\circ}C$, where the LEED patterns show a well-ordered (1×1) periodicity as shown in Fig. 5.7 (b) and (c). Hence, the crystal and surface quality of the polar InN layers strongly depend on the temperature used for sapphire nitridation.

Moreover, the polarity of the *c*-plane InN layers was also found to depend on the morphology of sapphire nitridated layers, i.e. amount of N incorporated into sapphire surface. The polarity of the InN layers were determined by XPS, as described in Chap. 4. The VB spectra recorded from the thermally annealed polar InN layers show domination of the different VB peaks for the InN layers grown after different sapphire nitridation temperatures, Fig. 5.9 (a)-(f). The dominance of the VB peak at lower binding energy (P_I) is observed for the InN layers grown after the sapphire nitridation temperature below $650\,^{\circ}C$ that corresponds to the In-polarity of the InN layers. An example of the VB for In-polar InN layer, which was grown at $600\,^{\circ}C$, is shown in Fig. 5.9 (a), where the P_{II}/P_I ratio equals 0.9. The peak at higher binding energy (P_{II}) is dominant for the InN layers grown after $T_{nitr} \geq 800\,^{\circ}C$ that is associated with the N-polar orientation of the layers (Fig. 5.9 (d)-(f)). The determined P_{II}/P_I ratio for these layers is approximately 1.17. Moreover, the VB peaks have similar intensity (P_{II}:P_I close to 1) for the InN layers grown after $T_{nitr} = 700$ - $750^{\circ}C$, corresponding to the mixed-polar InN.

The polarity of heteroepitaxially grown layers tends to follow the polarity of the used substrate or template. As discussed in Sec. 5.2, the sapphire substrates have Al-

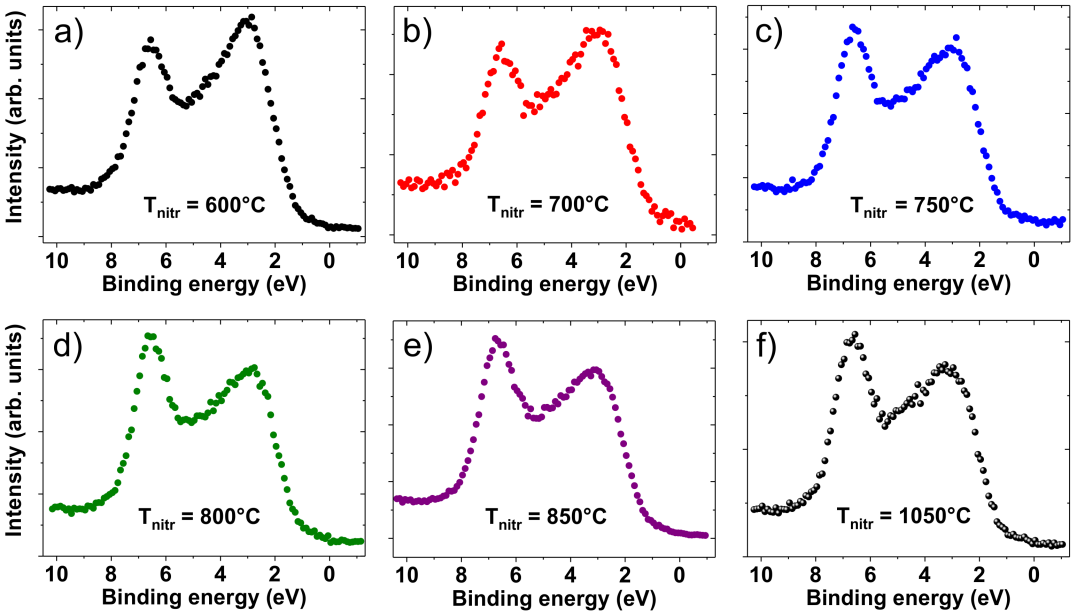

Figure 5.9: The VB spectra recorded from the thermally annealed polar InN layers grown on sapphire substrates nitridated at a) $T_{nitr} = 600°C$, b) $T_{nitr} = 700°C$, c) $T_{nitr} = 750°C$, d) $T_{nitr} = 800°C$, e) $T_{nitr} = 850°C$, and f) $T_{nitr} = 1050°C$. The Fermi edge refers to the 0 eV on the energy scale.

terminated surfaces after annealing at 1050°C. Therefore, the grown InN layers reproduce the group-III-polar growth from the sapphire substrate if the nitridation temperature is rather low (below 650 °C) and the Al-termination is still predominate. By increasing the nitridation temperature, the thin crystalline AlN layer is formed and affects the polarity of the InN layer. An assumption that the grown AlN layer is N-polar could explain the reproduced N-polar orientation on the subsequently overgrown InN layer. For the mixed-polar InN layers, the morphology of the nitridated layers probably results in the formation of both, In- and N-orientated InN domains.

The crystal properties of the InN layers and InN/sapphire interface were investigated by TEM and HRTEM. TEM observations made on the In-polar InN layer grown after sapphire nitridation at 600°C show a rough surface layer with numerous crystalline defects and voids at the interface with the sapphire substrate (Fig. 5.10 (a)), as well as inside the layer (labeled by white arrows). The voids have various orientations and sizes and the whole layer appears in the form of domains which are more or less tilted from one another as well as from the growth axis. The highly tilted ones are marked by stars. Therefore, the film is mainly polycrystalline, with crystallites of various sizes and tilts from which some may exhibit a different polarity (an example of such structure is marked by cross) [135]. The TEM image the N-polar InN layer grown after nitridation at 1050°C in Fig. 5.10 (c) exhibits a homogeneous layer with a smooth surface and high

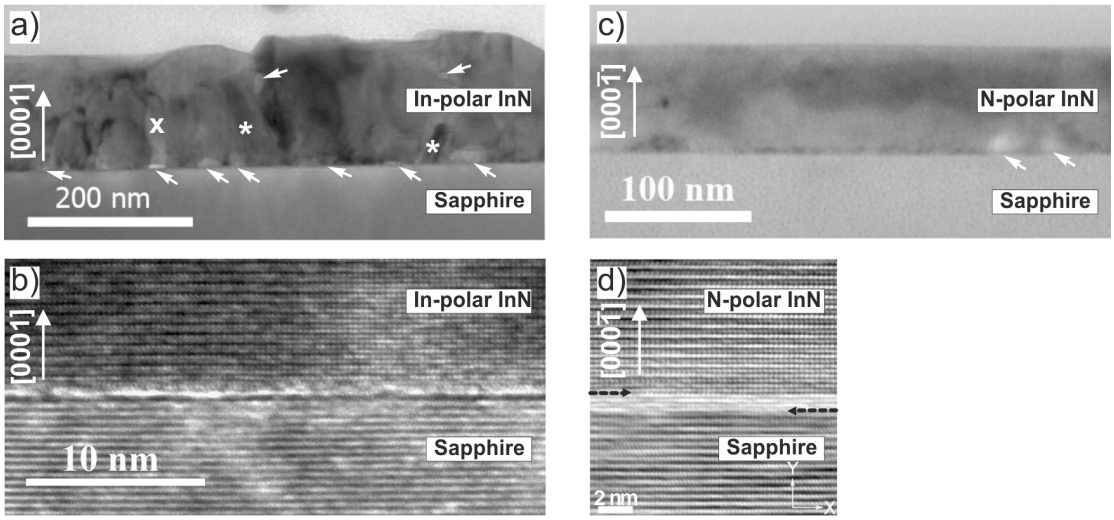

Figure 5.10: TEM images of (a) the In-polar InN layer grown after $T_{nitr} = 600\,^{\circ}C$ and (c) the N-polar InN layer grown after $T_{nitr} = 1050\,^{\circ}C$. Defects and voids are labeled by white arrows, stars correspond to the domains highly tilted to each other, cross marks a domain that might possess a different polarity. HRTEM images obtained on the interface between nitridated sapphire viewed along $<11\bar{2}0>$ zone axis and (b) In-polar InN, (d) N-polar InN. Black arrows delimit the image (d) show grown AlN layer. Measurements were performed by B. Lacroix, research group of P. Ruterana at CIMAP, Caen, France.

crystalline quality. Some voids can also be observed at the interface with the substrate (marked by white arrows).

An interface between the InN layers and sapphire substrate measured by HRTEM is shown in Fig. 5.10 (b) and (d) for the In-polar and N-polar orientations, respectively. A well-pronounced thin AlN layer formed after the nitridation process can be observed on the InN/sapphire interface for the N-polar InN layer as shown by the light contrast interlayer in Fig. 5.10 (d) (see arrows). The thickness of this layer is about 4 monolayers ($\sim$1 nm), which is in good agreement with the results obtained by *in situ* spectroscopic ellipsometry during the growth [84]. However, the thickness of the AlN layer is smaller than for the one observed on the nitridated sapphire substrate in Fig. 5.6 (b). This fact can be explained by additional procedures performed for the continuous growth of InN layers, e.g. altering of the reactor pressure and temperature, switching of the carrier gases and precursors.

In the case of the In-polar InN layer, the interface area is highly disturbed probably due to the coexistence of possible residual amorphous oxide and strain. Only a blurred thin interlayer can be distinguished in Fig. 5.10 (b). Therefore, based on the above discussion, this residual interlayer should correspond to the amorphous AlN_xO_y layer, which is formed during the nitridation at $T_{nitr} \leq 800\,^{\circ}C$. The amorphous layer with its complex atomic binding configurations as well as the local strains leads to the growth of low crystalline quality film with voids and independent crystalline InN domains, which

may exhibit various orientations as well as polarity with the dominance of the measured In-polarity.

Similar polar InN layers with a high density of threading dislocations were carefully analyzed by TEM and photoluminescence (PL) by Ruterana et al. in Ref. [36]. In this work, the investigated InN layers were grown by HVPE, MBE and MOVPE, and exhibit different density of screw and edge dislocations. However, it was shown that threading dislocations do not play a big role in the optical properties of the InN layers, while the residual carrier concentration and incorporation of native point defects [160] are critical parameters that degrade an optical performance of the layers. Thus, although the In-polar InN layers studied in this work have a polycrystalline structure with a number of defect, their optical properties might be comparable with N-polar InN layers.

Unfortunately, due to the high dislocation density of the In-polar InN layer and insufficient thickness of the N-polar InN layer, the CBED measurements for polarity determination of these layers could not be performed. It was reported, that the thickness of the MOVPE grown InN layers should be thicker than 150 nm to carry out CBED analysis [36]. There is only one published work in the literature reporting on the polarity determination of 50 nm thick InN layers by CBED measurements [35].

5.4 Summary

The atomic binding configurations on the thin nitridated sapphire layers and its effect on the surface and crystal quality of subsequently grown polar InN layers have been studied in details.

It has been found that no nitridation can take place if the sapphire surface exhibits a (1×1) symmetry. The (1×1) sapphire reconstructs into the oxygen deficient $(\sqrt{31}\times\sqrt{31})\mathrm{R}\pm9\,^{\circ}$ surface after annealing at 1050 °C. This is found to be an essential condition for the nitridation process and further epitaxial growth of InN layers.

Chemical composition analysis showed that domination of the N-Al chemical bonds in the nitridated layers occurred at temperatures above 800 °C corresponding to the formation of the crystalline AlN layers. The amorphous AlN_xO_y layers were formed when the amount of the N-O bonds was dominant or significantly large that is the case for the nitridation temperatures $\leq 800\,^{\circ}$C. Moreover, in both cases formation of the defects (e.g. N-N bonds) within the nitridated layers have been observed.

Morphology of the nitridated layers significantly affects surface and crystal quality of the overgrown polar InN layer. It was found that the nitridation temperature of 1050°C is the most suitable for the subsequent growth of the good quality InN layer. Upon this nitridation temperature, the 1 nm thick AlN layer is formed on the interface between the sapphire, leading to the drastic quality improvement of the subsequently grown InN layers.

Moreover, it was shown that polarity of the grown InN layers strongly depends on the morphology of the nitridation layer: the InN layers grown on top of an amorphous

nitridated layers have the mixed- or In-polarity, while the InN layers grown on the crystalline AlN layers possess N-polarity. Thus, the N-polar InN layers with a smooth surface and a single crystalline structure were grown in the case of the crystalline nitridated layer, while the In-polar InN layers with a rough surface and polycrystalline structure were grown if the nitridated layer had an amorphous structure.

Note that due to a poor quality of the In-polar InN layers investigated in this chapter, further surface characterizations on the In-polar InN layers have been performed on the smooth MBE grown (0001) InN layer. The surface properties and surface reconstruction of the MBE grown (0001) InN layer will be compared and discussed to the good quality $(000\bar{1})$ InN layer grown by MOVPE after nitridation temperature of 1050°C shown in this chapter.

6 Surface Properties of N-polar and In-polar InN Layers

As has been shown in the previous chapter, a high quality N-polar InN layers with a smooth surface and single crystalline structure can be grown by MOVPE on sapphire substrates by using a high temperature for the sapphire nitridation process. A surface analysis of these InN layers is essential in order to know and understand their properties and predict their applicability in optoelectronic devices.

An alternative method, called migration enhanced afterglow (MEAglow), was recently developed for fabrication of the InN/Al_2O_3 templates, where the InN layers were found to be N-polar. This deposition technique attracts much attention due to the possible growth of the thick, high quality InN layers, which are available on the market (MEAglow Ltd.) [19]. Hence, study and comparison of these layers with the MOVPE grown N-polar InN layers are of great interest.

The quality and surface properties of InN layers may be different for the In-polar orientated layers and should be investigated as well. However, the In-polar InN layers have not been grown so far by MEAglow and the In-polar InN layers grown by MOVPE possess poor crystalline quality and rough surface, as shown in the previous chapter. Another growth method that can be used for InN layers is MBE, which is known to result in the growth of the smooth and thick In-polar InN layers. Therefore, the In-polar InN layer grown by MBE was chosen for surface analysis in this work.

In this chapter the surface and crystalline properties of the N-polar InN layers grown by MOVPE and MEAglow, and the In-polar InN layer grown by MBE will be analyzed and compared to each other. Three main topics will be discussed for each polar orientation of the InN layer: analysis of the oxidized InN layers, their surface decontamination and surface characterization of the clean InN layers under UHV conditions. The chemical and electrical properties of the clean polar InN layers will be analyzed in details by using XPS and STS techniques, respectively. The LEED and STM will be used for study of the surface reconstructions and atomic arrangements. The models of the surface reconstructions, surface morphology and topography of the N- and In-polar InN layers will be discussed and compared to the literature.

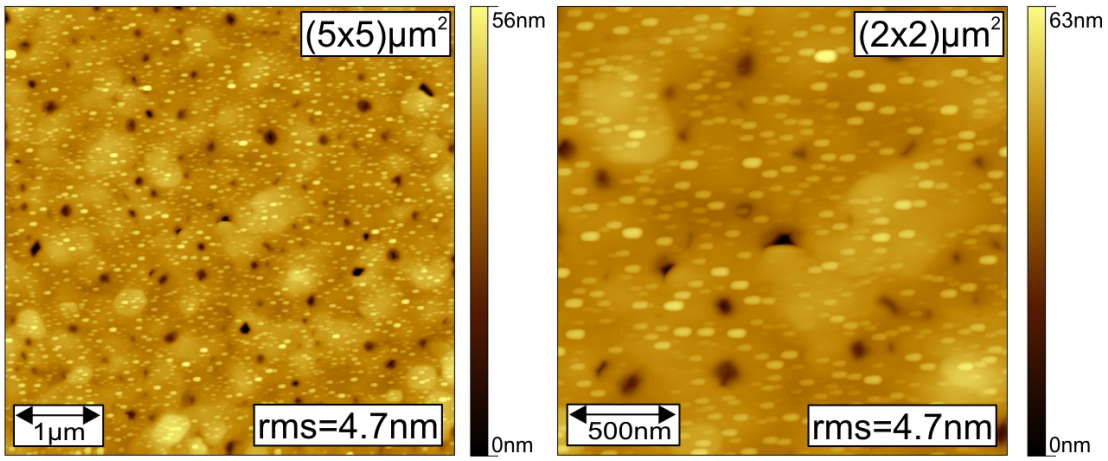

Figure 6.1: AFM topographic images of the N-polar InN layer grown by MOVPE on the scale of $(5\times5)\,\mu m^2$ and $(2\times2)\,\mu m^2$. Measured by D. V. Dinh, TU Berlin.

6.1 N-polar InN surfaces

6.1.1 Samples

For the analysis of the MOVPE grown N-polar InN layer, the layer grown at the nitridation temperature of 1050°C was selected. It exhibits a smooth topography and a very good crystalline quality compared to other MOVPE grown N-polar InN layers, as was shown and discussed in Sec. 5.3. Although the surface topography of the N-polar InN layer in Fig. 5.7 showed presence of pits and hillocks on the surface, the rms roughness of this layer is significantly better than any other MOVPE grown InN layer (see Fig. 5.8) [14]. Details to the MOVPE growth procedure of the N-polar InN layer can be found in Sec. 2.4.2.

Two InN layers grown on sapphire at 330°C and 400°C by MEAglow deposition technique were studied in this work. The growth procedure of these layers is described in Sec. 2.4.4. The MEAglow grown InN layers exhibit N-polarity and were predicted to have a good surface and crystalline quality. Therefore, these layers were chosen for surface analysis and were compared to N-polar InN layer grown by the conventional technique, i.e. MOVPE.

The N-polar InN layers grown by MBE have not been investigated in this work, since their surface and crystal quality is very similar to the MOVPE grown InN layer. Moreover, MBE growth technique of InN layers is not used for industrial purposes yet, unlike MEAglow growth of InN layers, whose surface properties are not yet well-known and investigated.

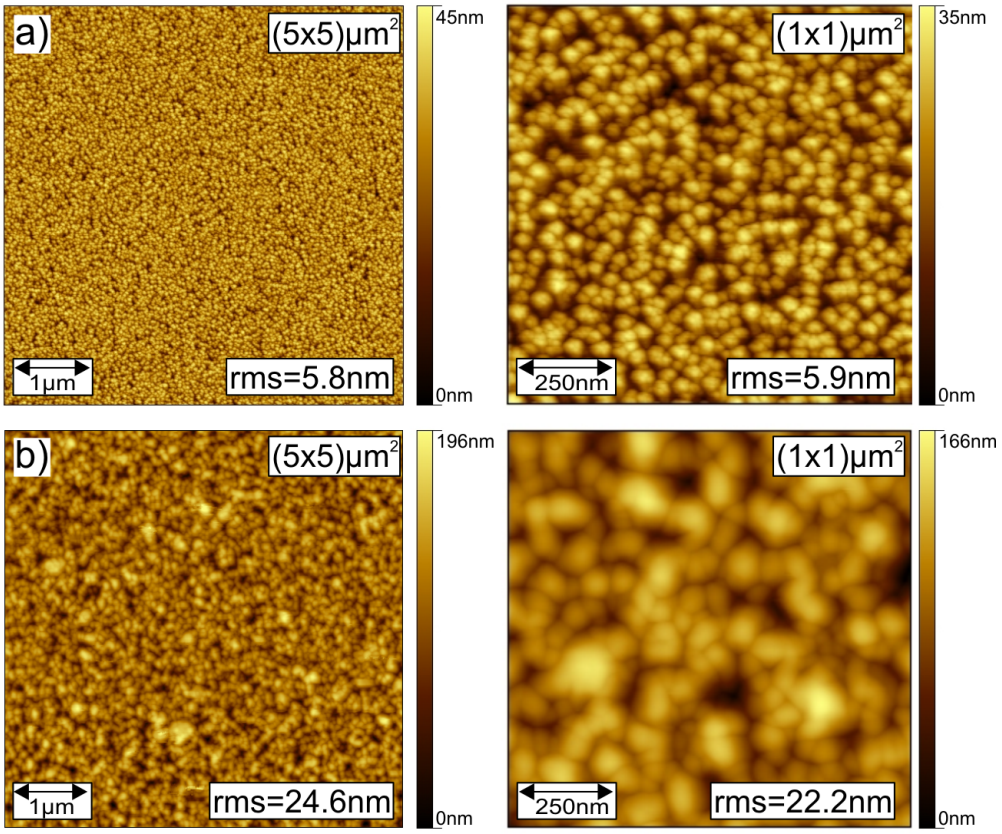

Figure 6.2: AFM topographic images of the N-polar InN layers grown by MEAglow a) at 330°C and b) at 400°C. The layers are shown at the scales of $(5\times5)\,\mu m^2$ and $(1\times1)\,\mu m^2$.

6.1.2 Oxidized N-polar InN surfaces

InN layers are usually exposed to ambient air after the growth, where the surface gets immediately oxidized and consequently, is covered by a thin oxidation layer ($\sim$ 1-2 nm thick [161]) consisting of water, carbon and oxygen species, i.e. H_2O, OH, C_xH_y, C_x. Surface oxidation can affect properties of InN layers, e.g. band bending, atomic reconstruction. For a better understanding of this effect, surface characterization of the oxidized N-polar InN layers was performed. Additionally, crystal properties of the MEAglow grown InN layers were analyzed by TEM and compared to the MOVPE grown InN layer.

The topography and crystallinity of the N-polar InN layer grown by MOVPE were already partially discussed in Sec. 5.3. In Fig. 6.1 the AFM images of the MOVPE grown InN layer is shown on the scales of $(5\times5)\,\mu m^2$ and $(2\times2)\,\mu m^2$. The hillocks (bright spots) represented on the surface have a height of 5-15 nm and exhibit a prolonged shape probably caused by a tip artifact. It is likely that they correspond to the indium droplet formed on the surface, in good agreement with the observed metallic

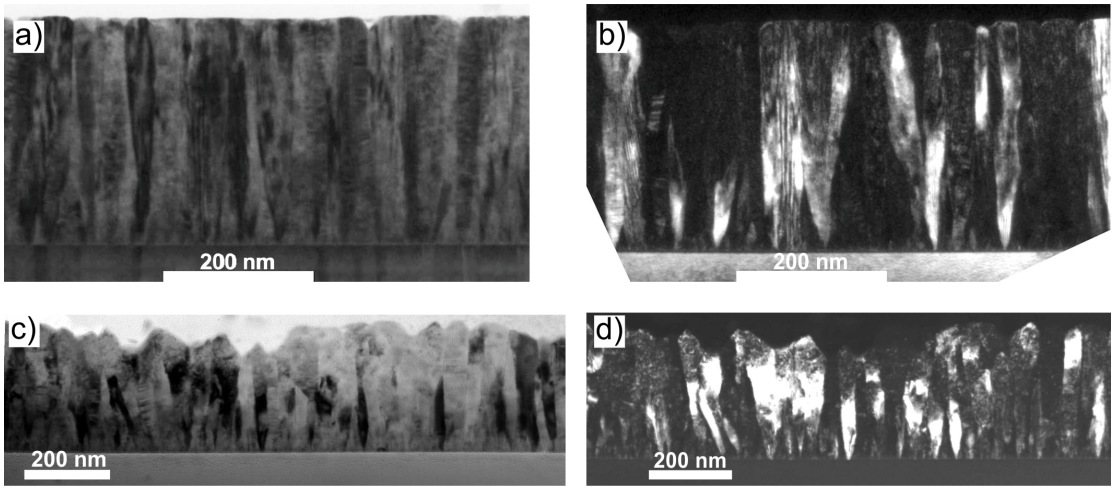

Figure 6.3: TEM images of the N-polar InN layer grown by MEAglow recorded in a) bright field and b) dark field mode for the layer with the smooth topography and c) bright- and d) dark-field mode for the layer with the rough topography. Measurements were performed by P. Ruterana´s group at CIMAP, Caen, France.

In (101) peak from the X-ray diffraction (XRD) measurements [162]. The pits formed on the surface have a hexagonal shape, also called V-shape, and consist of six $(10\bar{1}1)$ or $(11\bar{2}2)$ facets [162]. The V-pits correspond to the screw and mixed threading dislocations [163]. Although not all polar InN layers grown by MOVPE showed formation of In droplets, their surface roughness and topography were significantly poor than the one shown in Fig. 6.1 [162]. Therefore, surface and crystal analysis of another MOVPE grown InN layers have not been investigated within this work and attention was paid to the N-polar layer with the best surface quality.

The topography of the InN layers grown by MEAglow was analyzed by AFM, as shown in Fig. 6.2. The N-polar InN layers grown by MEAglow at 330°C (Fig. 6.2 (a)) and 400°C (Fig. 6.2 (b)) exhibit three dimensional surface structure with a rms roughness of ≈ 6 nm and ≈ 24 nm, for the low and high growth temperatures, respectively (further in this work it will be addressed to these layers as to smooth and rough MEAglow grown InN layers). The surface structure of the smooth MEAglow grown InN layer consist of little grains with diameter 5-40 nm, while much larger crystallites can be distinguished in the AFM image for the rough InN layer. In the latter case, the formed structures vary in size between 45 nm and 250 nm in diameter, moreover, some of the crystallites coalesced to one another. No direct evidence of the indium droplets on the studied surfaces was observed by AFM.

For the structural characterization of the MEAglow InN layers, TEM images were carried out in dark- and bright-field modes as shown in Fig. 6.3 (measurements performed at Dr. P. Ruterana group at CIMAP in Caen, France). For the sample grown at low temperature, the bright-field image in Fig. 6.3 (a) shows a 300 nm thick layer

that is continuously grown on the sapphire substrate and has no voids formed at the InN/sapphire interface in contrast to what has been observed for the MOVPE grown N-polar InN (Fig. 5.10). The measured thickness of 300 nm is smaller than the estimated 500 nm thickness from interference fringe measurements optical transmission technique. The surface of the sample is rather smooth in agreement with the AFM observations. The change in contrast, which is clearly visible in the dark field image (Fig. 6.3 (b)), takes place at scales between 100 nm and 200 nm corresponding to the grainy structure observed on the surface by AFM. At the surface, no indium droplets are distinguished in these cross-section TEM images, which is not a definite proof of the absence of indium droplets as it may be also due to the limited field of observations and corresponding statistical errors. However, as the XRD measurements (will be discussed later) showed no metallic indium peak, this means that the layer was mainly grown without indium segregation on the surface. As also attested by the dark field image, the layer has a pronounced polycrystalline structure, with the individual single crystallites highly textured around the $[000\bar{1}]$ direction, originating from the sapphire substrate and growing up until the layer surface. Therefore, the used growth technique with deposition of indium on the surface and its subsequent nitridation results in the formation of the crystallites separated by boundaries at the first step of the growth, which grows parallel at equal rate and form a nanocrystalline layer with a highly smooth surface.

In contrast, the InN layer grown at higher temperature layer exhibits a rough surface and a more disturbed polycrystalline structure with less texturing around the $[000\bar{1}]$ axis as can be seen in bright and dark field modes that are shown in Fig. 6.3 (c) and (d), respectively. The thickness of the layer varies from 230 nm up to 320 nm that is smaller compared to the predicted value of 370 nm estimated from optical measurements. The XRD measurements showed that the screw dislocation density of this layer equals 3.47×10^{11} cm^{-2} and similar to the previous layer, no metallic In(101) peak was observed in the spectra. In this case, some of the crystallites can be larger in size compared to the smooth MEAglow layer, and the texture around the $[000\bar{1}]$ is almost absent which leads to a relatively poor overall quality of the layer. Therefore, the higher growth temperature used for this layer results in a degradation of the InN quality.

The chemical bonding configurations of the oxidized N-polar InN layers were analyzed in details by XPS. Fig. 6.4 shows an overview XPS spectra recorded at normal emission from all three investigated oxidized N-polar InN layers. Each emission line (peak) in the spectrum corresponds to the core-level electron state, as labeled in the image. The following core-levels can be detected in the shown energetic range (from 0 eV to 570 eV): In $3d$, In $4d$ and N $1s$ corresponded to the InN layer, and O $1s$, C $1s$ states assigned to the surface contaminations caused by native oxidation. No other impurities or contaminations on the studied InN layers were detected by XPS.

The XPS spectra in Fig. 6.4 exhibit higher intensity of the O $1s$, C $1s$ core-level peaks for the rough MEAglow grown layer compared to the smooth layer or the one grown by MOVPE. Indeed, the quantitative XPS analysis of the contaminations showed that the

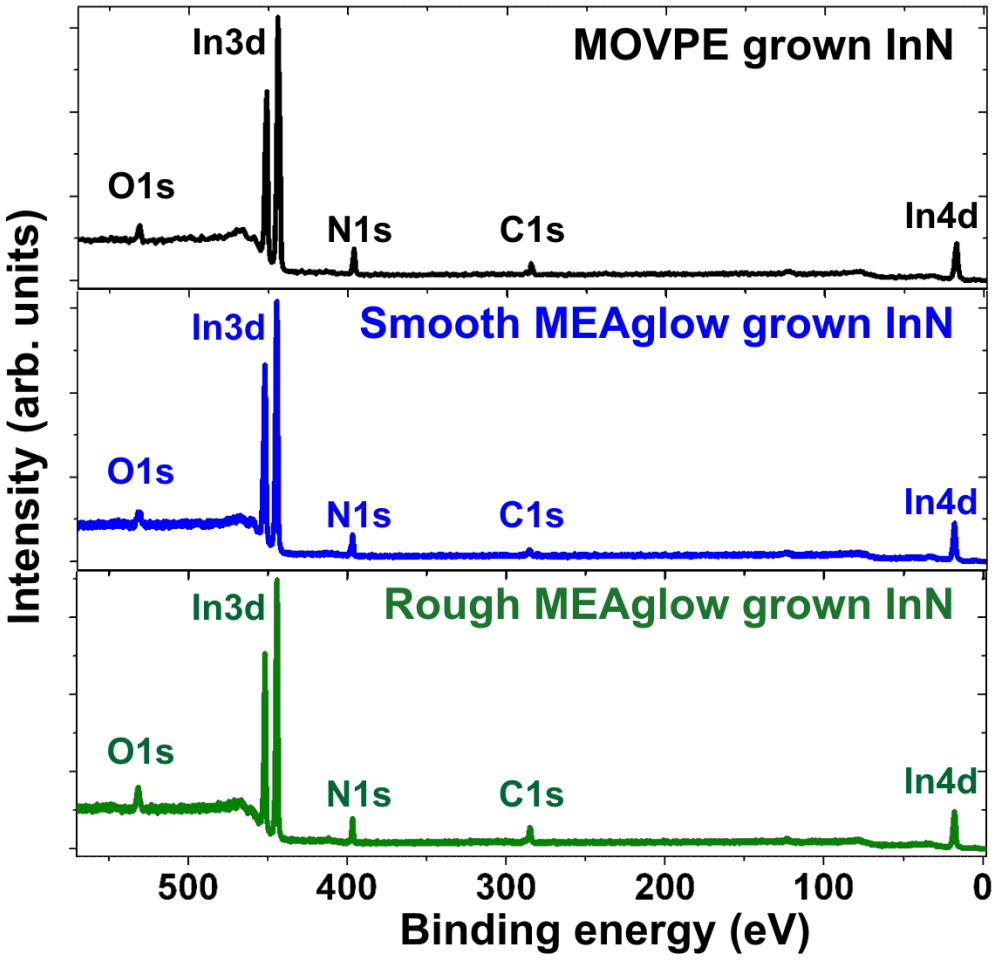

Figure 6.4: The wide range XPS spectra of three investigated InN layers recorded at normal emission from the oxidized layers. Each emission line corresponds to the core-level electron labeled in the image.

O/N ratio is 0.50 ± 0.05 for the MOVPE and smooth MEAglow InN layers, while the O/N is higher and equals 0.90 ± 0.05 for the rough MEAglow grown InN. Moreover, the C/N ratio has the smallest value of 0.70 ± 0.05 for the smooth MEAglow InN and the highest value of 1.50 ± 0.05 for the rough MEAglow InN layer. The C/N ratio for the MOVPE grown InN equals 0.90 ± 0.05. Therefore, the amount of the surface contaminations (oxygen and carbon species) on the oxidized layers was found to be the same for the smooth MEAglow and MOVPE grown InN layers but higher for the rough MEAglow InN. The rough InN layer has a larger number of crystal defects and grain boundaries compared to another samples. The carbon and oxygen contaminations are expected to act similar to hydrogen, which is known to reside on grain boundaries [162, 164]. This can explain a higher amount of incorporated impurities into the rough InN layers.

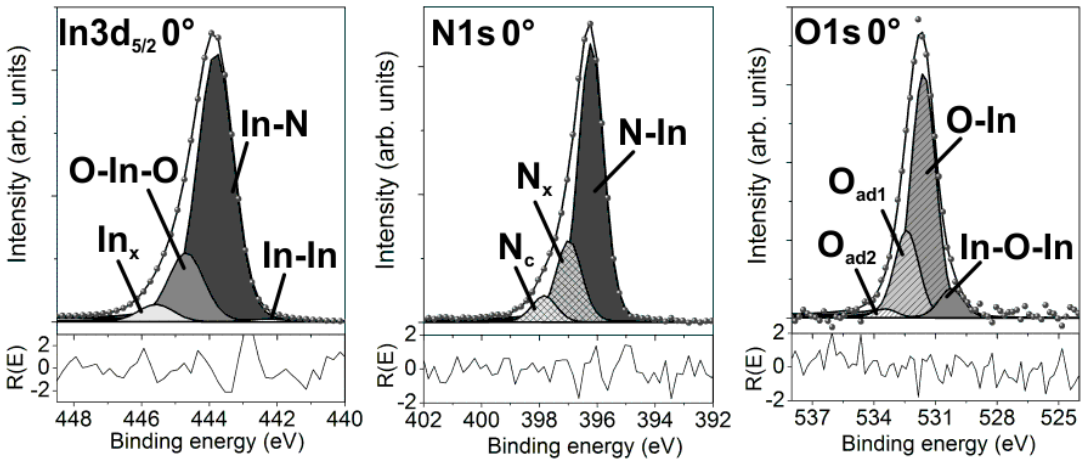

Figure 6.5: The In $3d$, N $1s$ and O $1s$ core-levels of the oxidized N-polar InN layers grown by MOVPE.

In order to analyze chemical bonding configurations of the oxidized N-polar InN layers, the numerical fit of the In $3d_{5/2}$, N $1s$ and O $1s$ core-level states were performed. The fitting parameters can be found in Appendix B. As will be shown further, the surface of the studied N-polar InN layer has a metallic behavior, therefore, the asymmetric parameters were used for the fitting of every core-level for both oxidized and clean N-polar InN layers. The fitting of the In $4d$ peak is more challenging and uncertain due to the s-d hybridization of the In $4d$ and N $2s$ states [49, 55]. Therefore, in this work only the In $3d_{5/2}$ core-level will be used for analyzing the bonding configurations of indium atoms. Since stoichiometry and core-level line shapes of the rough and smooth MEAglow grown InN layers were very similar, the core-level chemical analysis will be shown only for the MOVPE and rough MEAglow grown InN layers.

Fig. 6.5 represents the numerically fitted In $3d_{5/2}$, N $1s$ and O $1s$ states recorded at normal emission from the InN layer grown by MOVPE. The In $3d_{5/2}$ peak consists of 4 components labeled as In-In, In-N, O-In-O and In_x. The In-N component with the largest relative intensity is assigned to the InN bulk atomic bonds between indium and nitrogen and lies at 443.8 eV. The O-In-O component is shifted by 0.85 eV towards higher binding energy compared to the bulk component and attributed to the indium bonded to oxygen species. As reported previously, an indium oxide is known to form on InN surface upon exposure of InN layers to air, e.g. In_2O_3 [165, 166]. In this case, indium atom has more than one bond to oxygen and therefore assigned as O-In-O component. The In-In and In_x components are necessary in the fitting procedure in order to achieve a better residual curve (R(E)). The In-In component lies at the lowest binding energy corresponding to the lowest energy transition between the bonded atoms. This component refers to the metallic indium to indium binding configuration originated from the indium droplets formed on the surface, in agreement with the AFM and XRD results. The In_x component is shifted by 1.77 eV towards higher binding energy with

respect to In-N, hence, the corresponding indium atom is bonded to the atom with the largest electronegativity resulting in the highest binding energy of In_x compared to other In $3d_{5/2}$ components. The nature of In_x may correspond to the defects or complex chemical species associated with surface contaminations and will be detailed discussed in the section for the clean N-polar InN layers.

The fitting of the N 1*s* by 3 components gives a good agreement with the recorded spectrum. The component with a highest intensity is assigned to the bulk N-In bond (396.2 eV). The origins of another two components (N_x and N_c) are assigned to contaminations and will be described later by analyzing the clean InN surface and looking at emission lines recorded at 80° with respect to surface normal. The O 1*s* peak consists of 4 components, where the O-In (531.6 eV) and In-O-In (530.2 eV) components are attributed to the different bonding configurations between oxygen and indium atoms. Another components labeled as O_{ad1} and O_{ad2} correspond to the physisorbed surface adsorbates. The binding configurations of all these components will be detailed described in the section for the clean InN layers.

The core-level fittings for the rough InN layer grown by MEAglow for emission at 0° and 80° with respect to surface normal are shown in Fig. 6.6. Similar to the previous InN layer, the In $3d_{5/2}$ peak consists of the In-N (at 443.8 eV), O-In-O, In_x components and an additional component at the low binding energy side labeled as In-C. The In-C is assigned to the chemical bond between indium and carbon atom, since carbon has a smallest electronegativity (2.55) compared to oxygen and nitrogen. As will be shown further, intensity of this component decreases upon annealing and therefore, it originates from surface contaminations. Although the intensity of the In-C component is very small, this components is required to achieve a good correlation between the recorded and fitted spectrum. The intensities of the In-C, O-In-O and In_x components increase for the surface sensitive measurements (emission at 80°) representing than these components originate from the surface-like region.

The N 1*s* core-level contains four components labeled as N-In, N_x, N_y and N_z. For the measurements at 80°, the intensities of the N_x, N_y and N_z components increase compared to the N-In, hence, the corresponding atomic bonds are formed at the near-surface region. The bulk N-In component at 396.2 eV and the N_x component are similar to the one observed from the MOVPE grown InN layer. However, the N_y component shows different behavior upon the surface decontamination compared to the N_c shown in Fig. 6.5, as will be discussed in Sec. 6.1.5. Thus, the N_y component is not the same as N_c, and will be attributed to the nitrogen species produced by N-plasma source, as will be detailed described for the XPS measurements performed on the clean InN layers. The fourth component, N_z, is required for the N 1*s* peak fit and probably originate from the defects in the near-surface region (Sec. 6.1.5).

The O 1*s* core-level has similar chemical states (components) as for the MOVPE grown InN layer. The relative intensity for each component remains almost unchanged for the emissions at 0° and 80°, meaning that the entire O 1*s* peak mainly originates from the InN surface. Compared to the MOVPE grown InN layer, integrated intensities

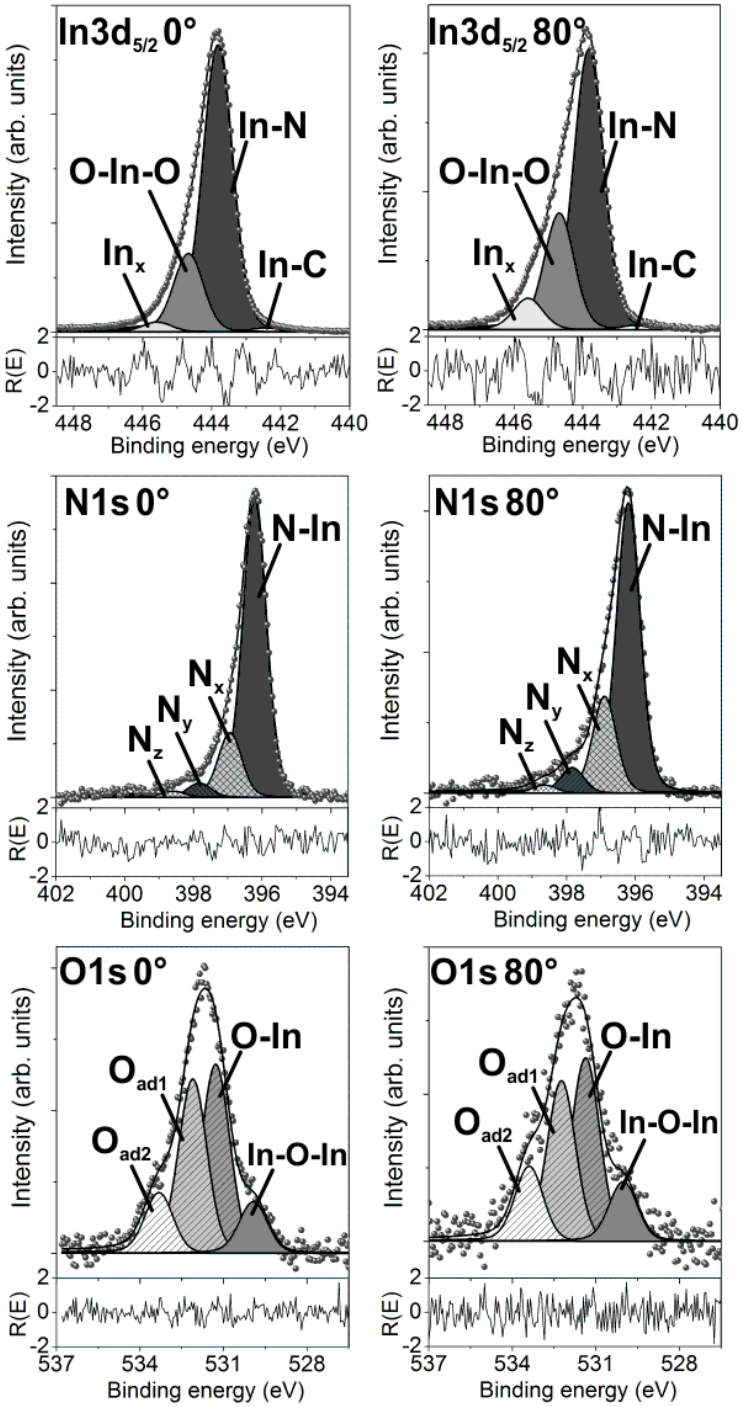

Figure 6.6: The In 3*d*, N 1*s* and O 1*s* core-levels of the oxidized rough N-polar InN layers grown by MEAglow recorded at normal emission (left column) and emission of 80° with respect to surface normal (right column).

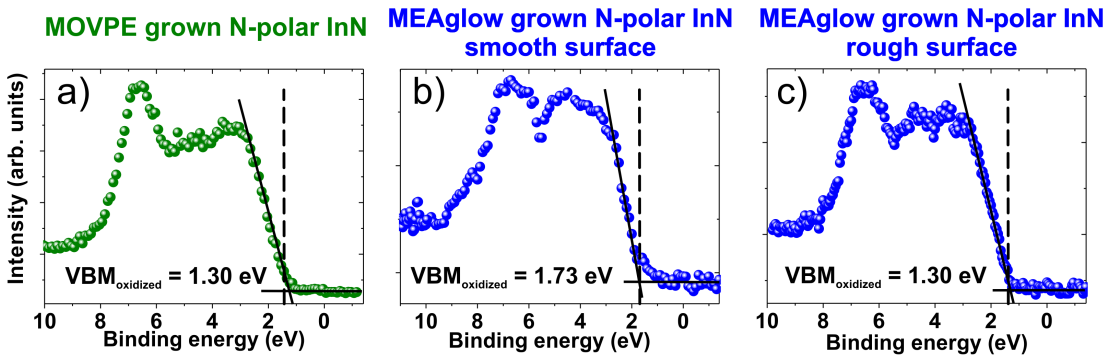

Figure 6.7: VB spectra of the oxidized a) MOVPE grown N-polar InN layer, b) smooth and c) rough MEAglown grown N-polar InN layers. The VBM positions above the Fermi level were determined for each layer.

of the O-In-O component in the In $3d_{5/2}$ and O $1s$ peaks for the rough InN layers are higher; moreover, the In-C component appears in the In $3d_{5/2}$ emission line. This observation is in good agreement with the highest O/N and O/C ratios calculated for the rough MEAglow grown InN layer compared to the MOVPE grown InN sample.

The XPS VB spectra recorded from all three layers are shown in Fig. 6.7. The position of the VBM for the smooth MEAglow grown N-polar InN layer of 1.73 ± 0.10 eV is higher compared to the rough MEAglow InN layer and MOVPE grown InN layer (VBM = 1.30 ± 0.10 eV). Thus, all three layers exhibit obvious downward band bending on the oxidized surface, however, the band bending is stronger for the smooth MEAglow grown N-polar InN layer.

Surface oxidation is known to affect the position of the VBM by shifting it to the higher binding energies in the case of the N-polar InN layers, leading to the increase of the downward band bending [130]. As discussed previously, among the studied N-polar InN layers, the rough MEAglow InN layer was found to have a higher amount of surface contaminations (oxygen and carbon), however, this layer does not possess the strongest band bending. Hence, the strongest band bending observed on the smooth MEAglow InN layer (Fig. 6.7 (b)) can not be explained by surface contaminations and is rather associated with intrinsic surface properties of the layer, e.g. surface morphology, topography and surface states.

6.1.3 Surface Decontamination

The study of InN surface properties requires a decontamination process to desorbing the native oxide from the surface. The N-polar InN layers were annealed under UHV conditions at different temperatures in order to find an appropriate annealing temperature that leads to the maximum reduction of surface contaminations but at the same time, does not result in a surface or crystal destruction.

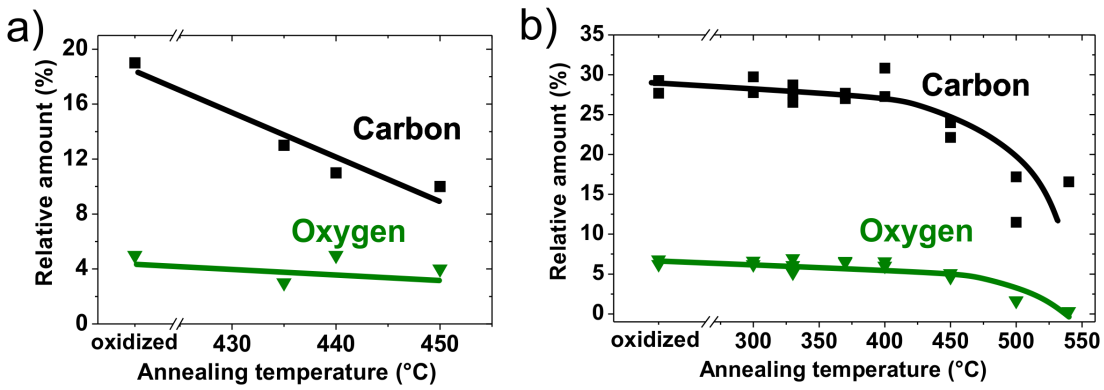

Figure 6.8: Relative amount of surface contaminations calculated from AES measurements for a) MOVPE and b) MEAglow (rough layer) grown N-polar InN layers. The layers were annealed at each temperature for 10 min. Lines are guide to the eye.

Previous studies performed on the BESSY II synchrotron in Berlin by C. Friedrich have shown that for the MOVPE grown polar InN layers annealing temperature of 450°C under UHV conditions results in a significant reduction of the surface contaminants, i.e. carbon and oxygen. The XRD measurements confirmed that the annealing temperatures below 480°C do not lead to the formation of indium droplets on the surface, surface damaging or crystal destruction. Fig. 6.8 (a) shows the relative amount of carbon and oxygen on the MOVPE grown N-polar InN layer determined by AES after annealing at different temperatures for 10 min. (The relative amount of C and O was calculated by considering all detected elements, i.e. In, N, O and C, as 100%.) For the annealing temperature of 450°C the amount of carbon and oxygen reduces by 48% and 43%, respectively. Further increase of the annealing temperature up to 480°C did not improve surface decontamination and therefore, was not required.

In the case of the MEAglow grown InN layers, an appropriate temperature for the surface deoxidation need to be found, especially by taking into account that these layers were predicted to have nitrogen-rich defects [87] (see Sec. 2.4.4) that can make the layers more sensitive to annealing temperature. In order to find an appropriate condition for the surface treatment, the MEAglow grown InN layers were annealed under UHV conditions at 300-540°C for 10 min at each annealing step. Higher temperatures were not applied, since the InN layers start to dissociate to indium and nitrogen at temperature above 500-600°C [167].The amount of carbon and oxygen on the surface after each annealing step was determined by AES as represented in Fig. 6.8 (b) for the rough InN layer. Significant reduction of carbon and oxygen species from the InN surface occurred at 450°C that was 50°C higher than the growth temperature of this layer. For the annealing temperature of 540°C the amount of carbon reduces by 55%, while amount of oxygen reduces by 92.5%. Similar trend of the surface decontamination was observed for the smooth InN layer grown by MEAglow.

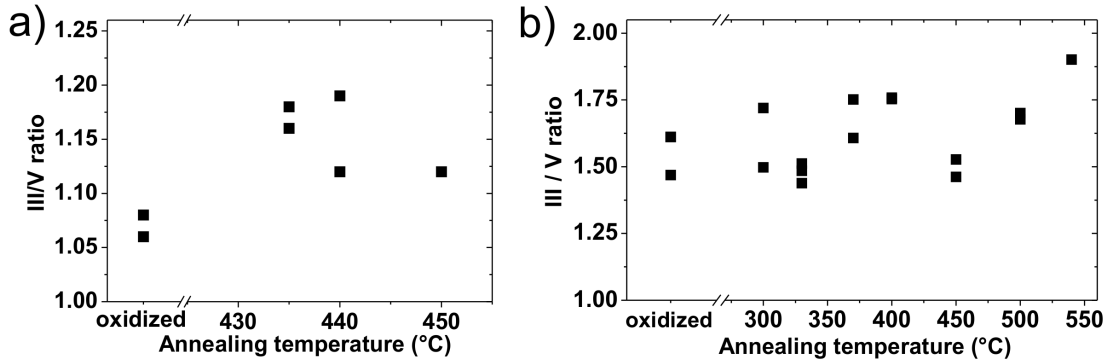

Figure 6.9: The III/V ratio calculated from AES measurements for a) MOVPE and b) MEAglow (rough layer) grown N-polar InN layers in accordance with Fig. 6.8.

The III/V (In/N) ratios were calculated in order to give information about surface stoichiometry after annealing and to reveal if undesirable nitrogen desorption from the surface (indium enrichment of the surface) occurred. The III/V ratio was determined by AES after each annealing step for the N-polar InN layers grown by MOVPE and MEAglow, as shown in Fig. 6.9 (a) and (b), respectively. The III/V ratio of the MOVPE grown InN layer after annealing equals 1.15 ± 0.10 and did not change with increase of the temperature, as represented in Fig. 6.9 (a). Thus, the annealing temperature of 450°C does not lead to a surface destruction and can be applied for the surface decontamination of the layer. Fig. 6.9 (b) shows that the III/V ratio for the annealed MEAglow grown InN layer with the rough surface equals 1.60 ± 0.15 and remains constant for the annealing temperature up to 500°C. The III/V ratio for the MEAglow grown InN layer with the smooth surface equals 1.80 ± 0.15 for the annealed layers that is similar to the rough layer within an error bar. Annealing step at the 540°C leads to an undesirable increase of the III/V ratio up to 1.90 that can be associated with the desorption of nitrogen from the surface and formation of indium droplets or indium segregation.

In order to analyze the effect of the annealing temperature on the surface topography, the topographic AFM images were recorded from the MOVPE grown InN layer annealed at 450°C and the MEAglow grown rough InN layer annealed at 540°C (Fig. 6.10). The AFM image of the InN layer grown by MOVPE represented in Fig. 6.10 (a) shows no obvious difference in topography compared to the untreated layer shown in Fig. 6.1. Although, for the annealed layer, a lower number of bright spots is observed than for the untreated surface. As was shown by AES, the III/V ratio does not change significantly after the surface treatment, therefore, a lower amount of detected hillocks can be explained by the fact that AFM measurements were performed on another position of the sample. Based on the represented results for the MOVPE grown InN layer, the annealing temperature of 450°C is most suitable for the surface decontamination of this layer.

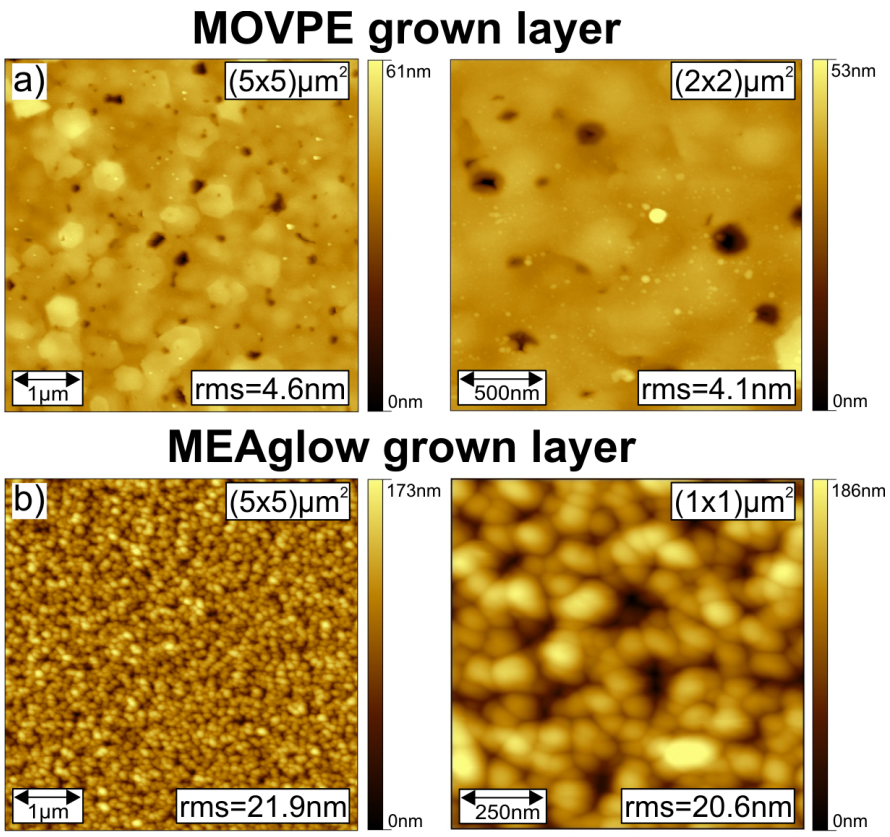

Figure 6.10: AFM images of the a) N-polar InN layer grown by MOVPE after annealing at 450°C and b) rough N-polar InN layer grown by MEAglow after annealing at 540°C. Images are taken at the scale of $(5\times5)\,\mu m^2$ (left) and $(2\times2)\,\mu m^2$ or $(1\times1)\,\mu m^2$ (right).

No difference in topography was also observed for the MEAglow grown InN layer, where the surface annealed at 540°C shown in Fig. 6.10 (b) is similar to the one shown in Fig. 6.2 (b). Thus, although AES showed an indium enrichment of the InN surface annealed at 540°C, no evidence of the surface modification could be confirmed by AFM.

Further, an effect of the annealing at 540°C on the crystal properties of the MEAglow grown InN layer (rough layer) was analyzed by XRD. All represented XRD measurement were performed by F. Mehnke at TU Berlin. The ω-2θ and ω scans for the untreated and annealed at 540°C InN layers are shown in Fig. 6.11 (a) and (b), respectively. The ω-2θ scan shows peaks corresponding to the InN (00.2) and Al_2O_3 (00.6) reflections, where the Al_2O_3 (00.6) peak originates from the sapphire substrate. The cubic In (101) peak that refers to the metallic indium, was observed neither in the spectrum for the untreated layer nor after annealing of the layer. Thus, no indium enrichment of the layer was confirmed by XRD. The increase of the III/V ratio for the annealed InN layer observed by AES could be an indicator for a very near-surface effect that is below the XRD sensitivity.

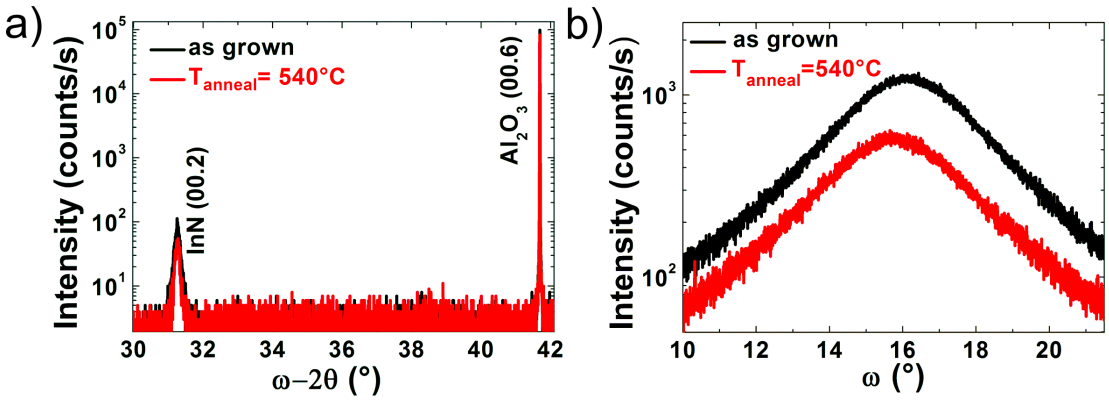

Figure 6.11: a) XRD ω-2θ scan of the rough InN layer grown by MEAglow on *c*-plane sapphire and b) ω scan of the of the symmetric (00.2)InN reflection prior and after annealing (T_{anneal}) at 540°C. Measurements were performed by F. Mehnke, TU Berlin.

Table 6.1: The *c*-lattice constant determined for the InN layer grown by MEAglow before and after annealing at 540°C. Calculations are based on the ω-2θ scan from XRD measurements.

Treatment	h	k	l	2θ	*c*-lattice constant
No	0	0	2	31.258°	0.571(8) nm
Annealing at 540°C	0	0	2	31.265°	0.571(7) nm

The full width at half maximum (FWHM) of the symmetric InN (00.2) reflection measured from the XRD ω-2θ scans was found to be 0.128° for the InN layer prior surface annealing and 0.134° after annealing at 540°C. The value of FWHM slightly increases after the surface treatment, which corresponds to the degradation of a crystallinity structure. The measured FWHM of 0.128° is in good agreement with the reported value for the MEAglow grown InN layer [19] that can be also improved up to 0.081° by varying the growth conditions [20]. Nevertheless, the XRD analysis performed on the MOVPE grown InN layer showed a significantly better crystal quality of this layer, where the FWHM of the (00.2) InN reflection equals 0.040° [162].

Based on the 2θ scan the *c*-lattice constant was determined for the InN layer grown by MEAglow, as shown in Tab. 6.1. The equations for the calculation of the lattice constant can be found in Appendix C. For the layer prior and after annealing at 540°C the *c*-lattice constant remains almost unchanged, ≈ 0.572 nm. This value is in good agreement with the reported *c*-lattice constant of 0.571 nm [168] and 0.567 nm [22] for a strain-free InN layer.

The screw threading dislocation densities (DD) of the MEAglow grown InN layer prior and after surface treatment were determined from the ω scan of the InN (00.2)

Table 6.2: Screw dislocation density (DD) determined for the InN layer grown by MEAglow before and after annealing at 540°C. Calculations are based on the ω scan measured by XRD.

Treatment	FWHM InN (00.2)	Screw DD
No	3.988 °	3.47×10^{11} cm^{-2}
Annealing at 540°C	4.108 °	3.68×10^{11} cm^{-2}

reflection, represented in Fig. 6.11 (b). The equations for the calculation of the screw DD were taken from the thesis of T. Böttcher [169] and is described in Appendix C. As shown in Tab. 6.2, the screw DD increases from 3.47×10^{11} cm^{-2} to 3.68×10^{11} cm^{-2} after annealing the InN layer at 540°C.

The MEaglow InN layers show high resistivity to high annealing temperature: no formation of indium droplets was detected on the surface, meaning no desorption of nitrogen atoms upon annealing at 540°C, however, a slight increase of the screw DD was observed. Therefore, applied annealing temperature of 540°C is not appropriate for the surface treatment.

Nevertheless, as was shown by AES (Fig. 6.8 (b) and Fig. 6.9 (b)), unlike annealing at 540°C, the annealing temperature of 500°C does not lead to the increase of the III/V ratio, however, results approximately in the same decontamination of carbon and oxygen from the surface as in the case of annealing at 540°C. Thus, the annealing temperature of 500°C is found to be most appropriate for the surface decontamination of the MEAglow grown N-polar InN layers. This temperature is 50°C higher compared to the one found for the MOVPE grown InN layers. This difference might be explained by the different surface topography of these two layers, where the MEAglow InN layer has the 3D structures on the surface leading to larger effective surface area compared to the MOVPE grown InN layer. Moreover, large number of the grain boundaries and defects of the MEAglow InN layers may lead to the diffusion of contaminations deeper into the layer, hence, a higher annealing temperature is required to transfer contamination species to the surface region and desorb from the surface.

Note that although thermal annealing does not lead to the complete surface deoxidation, a significant reduction of surface contaminations does occur. As will be shown in the further sections of this chapter, the achieved reduction of contaminations upon chosen preparation conditions is enough to observed the LEED diffraction patterns.

6.1.4 Surface Reconstructions of Clean N-polar InN Layers

After the above described preparation, surface reconstructions of the MOVPE and MEAglow grown InN samples were analyzed by LEED. Fig. 6.12 (a) and (b) show the LEED patterns recorded at low (76 eV) and high (165 eV) energies from the MOVPE grown

N-polar InN representing the first and second order of reflexes, respectively. Both patterns correspond to the (1×1) surface reconstruction with a sketched (1×1) unit cell. The LEED patterns show bright and sharp spots which refer to the clean surface with a well-ordered structure that also confirms a good chosen preparation condition for this layer.

Fig. 6.12 (c) and (d) show the LEED patterns of the rough MEAglow grown N-polar InN layer recorded at two different energies. The represented patterns correspond to the $(\sqrt{3}\times\sqrt{3})\text{R}\pm30^\circ$ surface reconstruction, where the larger sketched unit cell refers to the (1×1) reflexes, while the smaller unit cell that is rotated by 30° with respect to the (1×1) unit cell, represents the $(\sqrt{3}\times\sqrt{3})$ reconstruction. The LEED patterns for this layer exhibits a higher background than in the case for the MOVPE grown InN layer. The blurred reflexes and high background are a direct indicator of a higher surface roughness as well as formed 3D structures on the surface, which is in good agreement with the topography images of the MEAglow grown InN layers. The same reconstruction was observed for the smooth MEaglow grown InN layer.

Although the LEED patterns were recorded at the same energy, the sketched (1×1) hexagonal unit cell for both samples (e.g. Fig. 6.12 (a) and (c)) exhibit a slightly different size, i.e. size of the (1×1) unit cell for the MEAglow InN layer is larger than the MOVPE InN layer. This difference is caused by the different distances between the LEED fluorescence screen and the sample in each case. For instance, by moving the sample closer to the LEED screen, the diffraction spots will move towards the outer screen edge. Since experiments were performed in different UHV chambers, the distance between the fluorescence screen and the sample was slightly different for each case, explaining a larger size of the unit cell for MEAglow grown InN layer.

The N-polar InN layers are known to possess the (1×1) surface symmetry, while the $(\sqrt{3}\times\sqrt{3})\text{R}\pm30^\circ$ surface reconstruction on the N-polar InN layer has not been observed previously. Therefore, it is important to perform a detailed analysis of this reconstruction and compare it to the usually observed (1×1) N-polar InN surfaces. Further in this chapter, the surface characterization results of the (1×1) and $(\sqrt{3}\times\sqrt{3})\text{R}\pm30^\circ$ N-polar InN layers performed by STM and XPS will be presented.

6.1.5 Electronic and Chemical Properties of the N-polar InN Layers

Since the N-polar InN layers grown by MOVPE and MEAglow exhibit different surface reconstructions, i.e. the (1×1) and $(\sqrt{3}\times\sqrt{3})\text{R}\pm30^\circ$, respectively, it is important to know their chemical bonding configurations and electrical properties, e.g. band alignment. The XPS analysis of the VB and core-level electrons was performed on the clean MOVPE grown InN layer and MEAglow grown InN layer with a rough surface. As was mentioned for the oxidized layers, the MEAglow grown InN layer with a smooth surface showed very similar fitting results as the layer with a rough surface. Therefore, in this work the numerical fit is shown for the MEAglow grown InN layer with the rough surface only, whose properties were also analyzed in details by STM and STS.

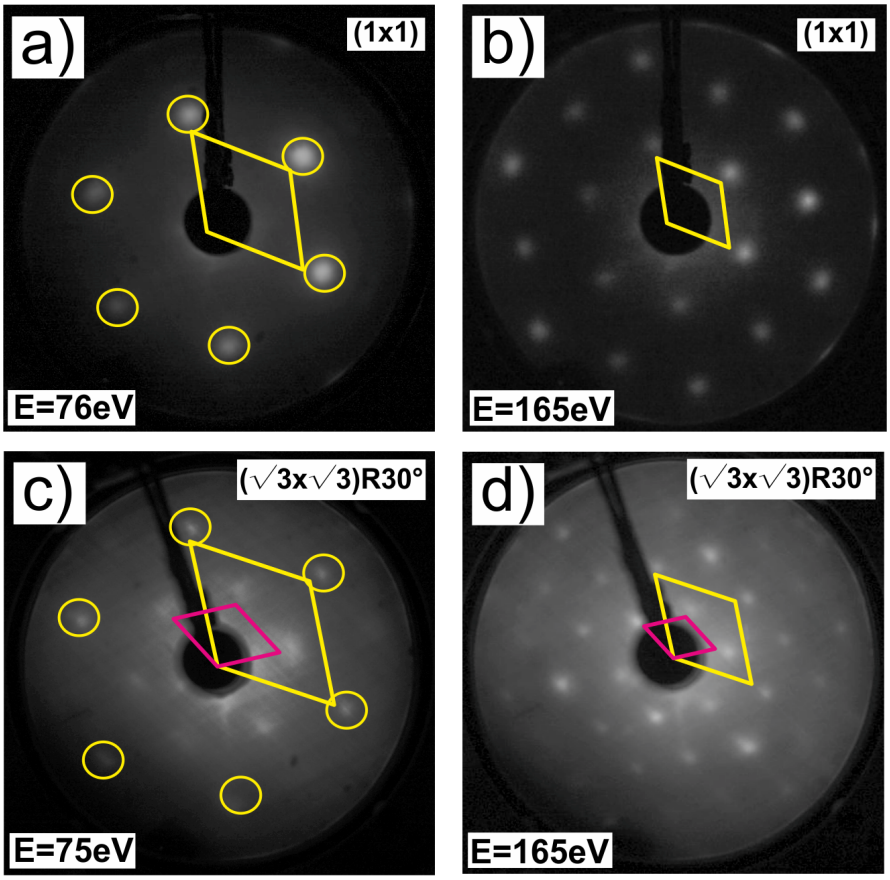

Figure 6.12: LEED diffraction patterns recorded at a) 76 eV and b) 165 eV from the N-polar InN layer grown by MOVPE corresponding to the (1×1) surface reconstruction. LEED patterns recorded at c) 75 eV and d) 165 eV from the N-polar InN layer grown by MEAglow corresponding to the $(\sqrt{3}\times\sqrt{3})$R$\pm30^\circ$ surface reconstruction. The sketch shows the (1×1) and $(\sqrt{3}\times\sqrt{3})$R$\pm30^\circ$ unit cells in yellow and red colors, respectively. The (1×1) reflexes are marked by circles in images (a) and (c).

First, a quantitative analysis of the chemical elements located at the near surface region was derived from the XPS measurements. The III/V ratios calculated from the XPS spectra at normal emission show approximately the same values for all the three N-polar InN layers: 1.54 ± 0.05 and 1.42 ± 0.05 for the smooth and rough $(\sqrt{3}\times\sqrt{3})\mathrm{R}\pm30^\circ$ InN layers, respectively, and 1.50 ± 0.05 for the (1×1) InN layer. As was mentioned in Sec. 2.4.4, the smooth and rough InN layers grown by MEAglow are expected to be nitrogen rich due to the crystal defects. However, no difference in the III/V ratio was found between the N-rich MEAglow grown layers and the stoichiometric MOVPE grown InN layer. Therefore, the claim that the MEAglow grown layers have a nitrogen excess in the crystal structure could not be confirmed [87]. This fact also was not confirmed by AES, where the determined In/N ratios for the MEAglow InN layers were

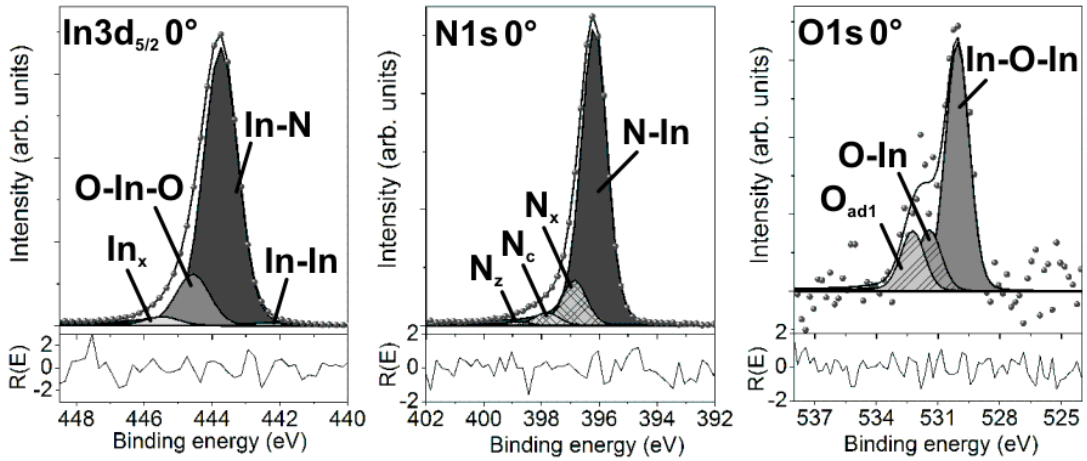

Figure 6.13: The In 3d, N 1s and O 1s core-levels of the clean N-polar (1×1) InN layer at the normal emission (0 °).

much higher than 1 and higher than for the MOVPE grown InN. Note that the information depth of XPS at normal emission by using Al K_α X-ray radiation is less than 10 nm and this may be a reason why the nitrogen excess is not observed in the layer. Nevertheless, the surface region of the MEAglow layers is shown to be indium rich.

The In $3d_{5/2}$, N $1s$ and O $1s$ core-level peaks of the N-polar (1×1) InN layer recorded at the normal emission are shown in Fig. 6.13. The relative energetic positions of the fitted components with respect to the bulk component (i.e. In-N and N-In) in the represented core-levels remained the same as for oxidized InN layer (Fig. 6.5), meaning that no chemical shift occurred after surface decontamination. The position of the bulk In-N component at 443.7 eV is in good agreement with the same component observed in Refs. [165, 170] for clean InN layers. The intensity of the O-In-O component in the In $3d$ state is decreased with respect to the oxidized surface. Hence, this component should be assigned to the surface contamination. The component attributed to indium oxide, e.g. In_2O_3, is usually reported to be shifted by ~ 1 eV towards higher binding energies compared to In-N [165, 171]. This confirms the assumption that the component O-In-O shifted by ~ 0.9 eV compared to the bulk In-N component in Fig. 6.13 corresponds to the formed indium oxide. The In_x component lies at the highest binding energy compared to all other indium components, hence, the corresponding indium atom must undergo the largest relative charge depletion resulting in the highest binding energy. Moreover, intensity of this component decreases upon annealing. One can assume, that In_x originates from indium dangling bonds, some of them may reconstruct upon annealing resulting in decrease of the In_x component. Another assumption is that In_x originates from defects and/or complex chemical species attributed to surface contaminations. The integrated intensity of the In-In component remains unchanged, indicating that this component does not originate from contaminations but rather from

metallic indium. The same In-In component has been observed in Ref. [171] for surface sensitive measurements on the c-plane InN layer.

A position of the N-In component in the N 1*s* core-level on the clean InN surface is 396.3 eV. This is in agreement with the reported values for the bulk N-In component that vary from 395.9 eV [171] up to 397.5 eV [125]. Besides N atoms bonded to In atoms, there are three another chemical environment for the nitrogen atoms on the layer, labeled as N_x, N_c, which were observed on the oxidized surface (Fig. 6.13) and the new component N_z which is required for good fitting results. The intensity of the N_x and N_c components in the N 1*s* peak decreases upon surface annealing. Hence, one can assume that one of these components correspond to the N-O bonds. However, the reported values for the N-O component in the N 1*s* peak measured on InN are shifted by 1.1 eV [130], 1.3 eV or 3.4 eV [172] towards higher binding energies with respect to N-In. These values do not correlate with the shifts observed in this work, i.e. 0.7 eV for N_x, 1.6 eV for N_c and 2.6 eV for N_z towards higher binding energies compared to the bulk N-In component. Moreover, no related O-N components can be observed in the O 1*s* peak. Therefore, the observed nitrogen compounds refer rather to other chemical configurations. For instance, Nagata et al. observed the component attributed to the overlap between N-H and N-C chemical states shifted by 1.8 eV towards higher energies compared to N-In [171]. This shift is very close to the shift for N_c, hence, the N_c component probably originates from the bonds with residual H and/or C atoms. Further investigation of the clean MEAglow grown InN layer will help to understand the origin of the N_x and N_z components.

The four different oxidation states in O 1*s* were observed on the oxidized InN layer (Fig. 6.5). The spectrum recorded from the clean layer in Fig. 6.13 shows a significant intensity reduction of the O 1*s* core-level peak, where the O_{ad2} component is completely vanished, while the O-In and O_{ad1} are reduced by ca. 95% and 87% of their initial intensity values, respectively. The O 1*s* peak is dominated by the In-O-In component, whose intensity was reduced only slightly. Two different chemical components between indium and oxygen atoms (O-In and In-O-In) can be explained by their different binding configurations. The In-O-In component is attributed to the indium oxide, e. g. In_2O_3, formed on the surface. This component also can be found in the In $3d_{5/2}$ core-level (O-In-O). An energetic position of the In-O-In component is in good agreement with Ref. [165]. Since In and O atoms have more than one chemical bond between each other (In-O-In), and intensity of the corresponding component decreases only slightly upon annealing, one can assume that this bond is relatively strong compared to another oxygen bonds and cannot be broken easily by annealing. The O-In component is attributed to the bond, where oxygen and indium atoms are bonded weaker, e.g., with only one chemical bond for example in the N-In-O complex. Thermal annealing is sufficient to break O-In bonds resulting in significant reduction of the O-In component. However, the corresponding component (O-In) is not observed in the In $3d_{5/2}$ peak, most probably because it overlaps with the intensive In-N bulk component. A numerical fitting of the In-O component in the In $3d_{5/2}$ peak can be done only artificially with

a high uncertainty and therefore, was not performed in this work. The O-In and O_{ad1} (as well as O_{ad2} component for the oxidized layer) components cannot be attributed to any other components in the In $3d$ or N $1s$ core-levels, since no other components have shown such a strong reduction upon annealing. The O_{ad1} (and O_{ad2}) correspond to physisorbed oxygen atoms [166], e.g. CO_x, H_2O, and can be easily, almost completely removed from the surface upon thermal annealing.

Fig. 6.14 represents the In $3d_{5/2}$, N $1s$ and O $1s$ core-level peaks of the MEAglow grown $(\sqrt{3}\times\sqrt{3})$R$\pm$30° N-polar InN layer with the rough surface recorded at the normal emission (0°) and emission at 80° corresponding to the surface sensitive measurements. Again, the relative energetic positions of the components in the core-level peaks with respect to the bulk components remain the same as for the oxidized layers.

Intensities of the O-In-O and In_x components in the In $3d$ peak reduced after annealing and increased for the emission at 80°. It confirms the assumption that the corresponding chemical bonds originate from the near-surface region. The origin of the O-In-O and In_x components is the same as for the MOVPE grown N-polar InN layer. The intensity of the component at the lowest binding energy, labeled as In-C, is decreased after annealing, corresponding to the surface contamination origin, unlike the metallic In-In component for the MOVPE grown InN. The In-C is shifted by 1.3 eV towards lower binding energies compared to the In-N, while the In-In component is shifted by 1.4 eV. Hence, these components indeed originate from the different binding configurations. The position of the In-C component at the lowest binding energy refers to the chemical bond between indium and atom less electronegative than nitrogen atom. Hence, this can be the bond between indium and carbon atom from surface contamination.

For the MEAglow InN layer, intensities of the N_y and N_z components in N $1s$ increase after annealing, while intensity of the N_x component reduces. Moreover, the surface sensitive measurements show that these three components dominate on the surface sensitive region with the same relative intensities.

The O $1s$ core-level peak consists only of the O-In and In-O-In components, while the chemical species corresponding to the O_{ad1} and O_{ad2} components are completely adsorbed from the surface. An absolute intensities of the O-In and In-O-In components are reduced by 95% and 47%, respectively.

The behavior of the N_x components is very similar to the In_x component from the In $3d_{5/2}$ state: the intensity of N_x reduces after annealing and predominates at the near-surface region. One can assume that the N_x component corresponds to the contaminations adsorbed, for instance, on surface defects. The N_x component cannot be assigned to the chemical bond with oxygen, since its intensity did not decrease as significantly as any of the O_{ad1} and O_{ad2} components.

Since intensities of the N_y and N_z components increase after annealing, they cannot be assigned to the surface contaminations. They may originate from the defects within the crystal structure and therefore, their intensity increase once the oxidation layer is

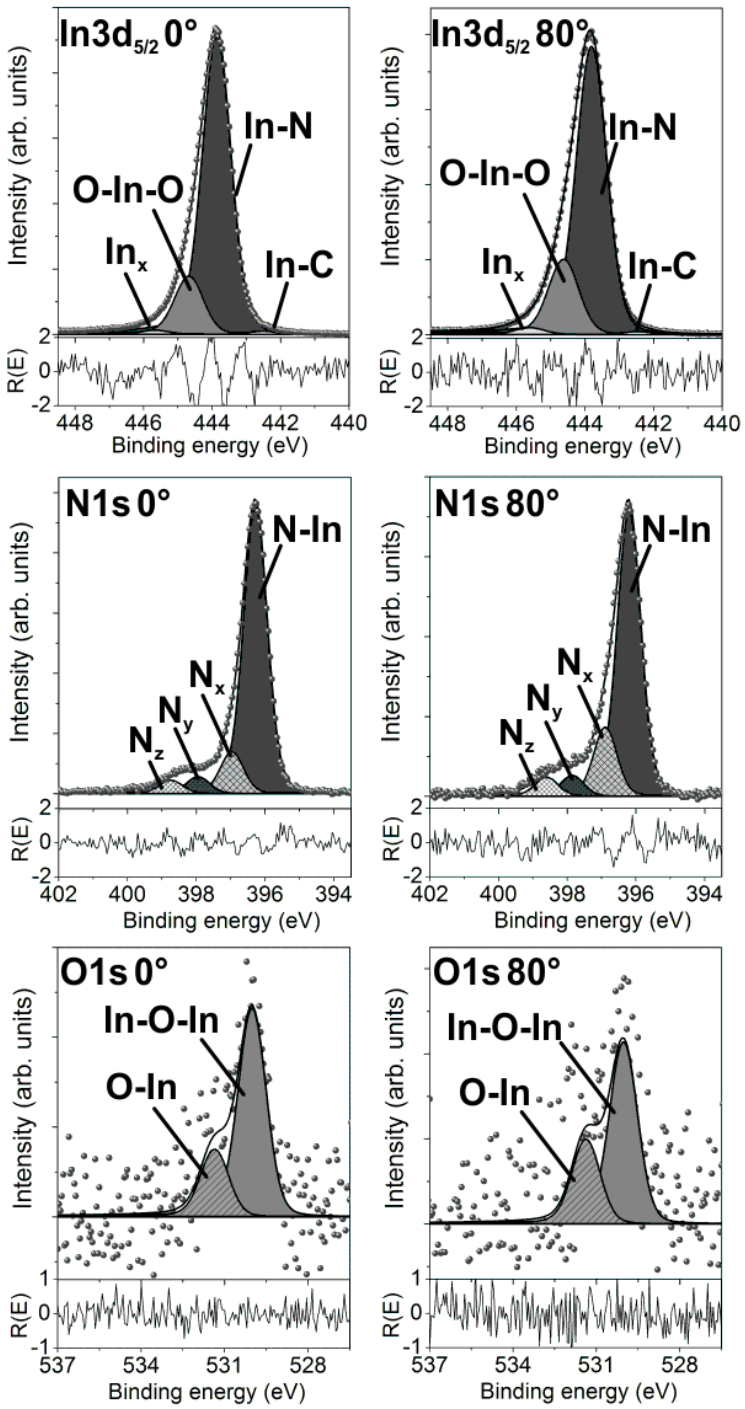

Figure 6.14: The In 3d, N 1s and O 1s core-levels of the clean rough N-polar $(\sqrt{3}\times\sqrt{3})$R$\pm$30° InN layer at normal emission (0 °) and emission at 80 °.

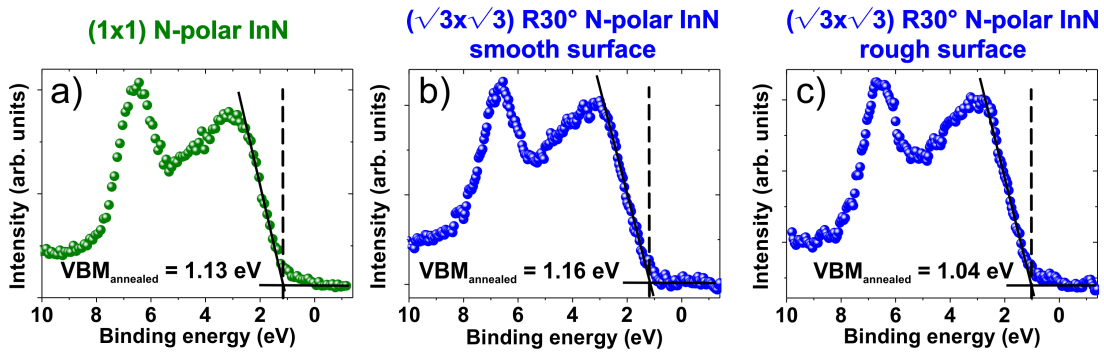

Figure 6.15: The VB spectra of the clean a) MOVPE grown N-polar InN layer, b) smooth and c) rough MEAglown grown N-polar InN layers. Positions of the VBM is determined for each layer.

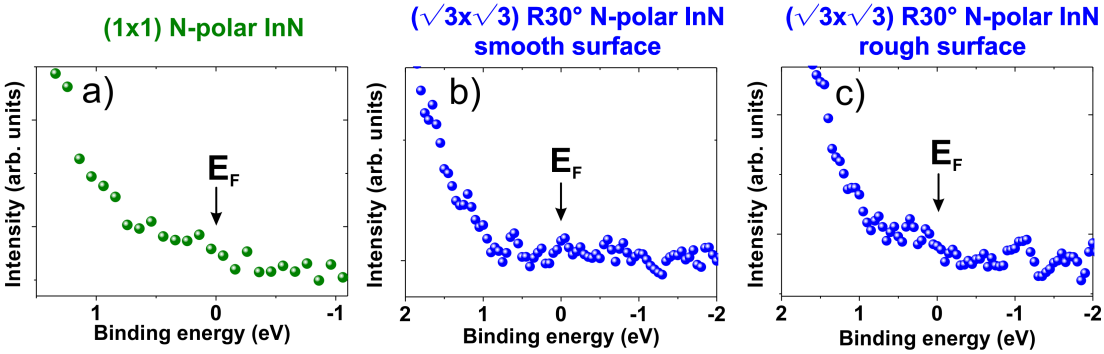

Figure 6.16: The Fermi edge (E_F) of the clean a) MOVPE grown N-polar InN layer, b) smooth and c) rough MEAglown grown N-polar InN layers.

removed from the InN layer. Since the analyzed InN layer was grown by MEAglow by using the nitrogen plasma source, different nitrogen species, e.g. molecular nitrogen (N_2), nitrogen ions, are produced and could incorporate into a crystal structure. The molecular nitrogen component in the N 1*s* state has been observed after bombardment of InN and GaN surfaces with N_2^+ and Ar^+ ions [173, 174]. However, the corresponding component lies at 7.6 eV (6 eV) higher binding energy compared to the bulk component for InN (GaN) layer. As shown in Fig. 6.14 for the N 1*s* core-level, no evidence of the reported component was observed on the investigated InN layer. However, another nitrogen species could be produced by N-plasma source and incorporated into the crystal structure, which can be assigned to N_y. Since the same N_z component is observed in MOVPE grown InN layer, where the N-plasma source was not applied, the chemical binding configuration of N_z may be attributed to another kind of crystal defects in the near-surface region formed during the growth.

In order to determine the changes in the band bending upon surface decontamination, the VB spectra of all investigated clean N-polar InN layers were analyzed. The

positions of the VBM for the annealed InN layers shifted towards lower binding energies compared to the oxidized layers, as shown in Fig. 6.15: the VBM position decreases by 0.17 eV $\pm$ 0.10 eV for the MOVPE grown InN layer and by 0.57 $\pm$ 0.10 eV and 0.26 $\pm$ 0.10 eV for the smooth and rough MEAglow grown InN layers, respectively. The determined values of the VBM for the clean N-polar InN layers are still much larger than the band gap of InN indicating the downward band bending on InN surface even after surface decontamination.

At the same time, upon surface annealing the bulk components in the In $3d_{5/2}$ and N $1s$ core-levels shifted by 0.04 eV towards lower binding energies for the MOVPE grown InN layer and by 0.06 eV for the MEAglow grown InN layer with the rough surface (by 0.2 eV for the smooth surface). This observation can be interpreted as follows: the surface band bending results in the same energy shift of the VBM and all bulk components, however, different values determined between the VBM position shift and shift of the core-levels upon annealing may be explained, for instance, by formation of surface states slightly above the VBM. In this case, the VB states will overlap with the surface states, resulting in an imprecise determination of the VBM position. However, the tendency remains the same: for the N-polar InN layers surface oxidation leads to the stronger surface downward band bending in agreement with observations performed by Eisenhardt et al. in Ref. [130].

The VB spectra in Fig. 6.15 show domination of the peak at higher binding energy. The determined $P_{II} : P_I$ ratios are 1.15$\pm$0.05 for the MOVPE grown InN layer, 1.08$\pm$0.05 and 1.09$\pm$0.05 for the MEAglown InN layers with the smooth and rough topography, respectively. According to the discussions in Chap. 4, these $P_{II} : P_I$ values correspond to the N-polar InN layers. It could be possible that the lower $P_{II} : P_I$ values for the MEAglow InN layers are due to their polycrystalline structure, where some domains with In-polarity may form. This will lower the $P_{II} : P_I$ ratio compared to the MOVPE grown InN layer, whose crystalline structure is better and probably does not have the polar inverted domains. However, if this true, the crystallite domains with N-polarity are significantly dominated in the investigated InN layers, what can be determined from the $P_{II} : P_I$ ratio.

In the represented VB spectra the Fermi level step at 0 eV cannot be distinguished, however a closer look at the spectra allows the identification of the Fermi edge for the MOVPE and rough MEAglow grown InN layers, as shown in Fig. 6.16 (a) and (c), respectively. The Fermi level step cannot be observed only in the spectrum for the smooth MEAglow grown N-polar InN layer in Fig. 6.16 (b) that might be due to a low signal to noise ratio.

6.1.6 The (1$\times$1) N-polar InN Layer Grown by MOVPE

In order to obtain an information about surface reconstruction, e.g. surface behavior, local electron DOS at the nanoscale, the (1$\times$1) N-polar InN layer grown by MOVPE was studied by STM and STS. For a comprehensive overview of the InN surface, here

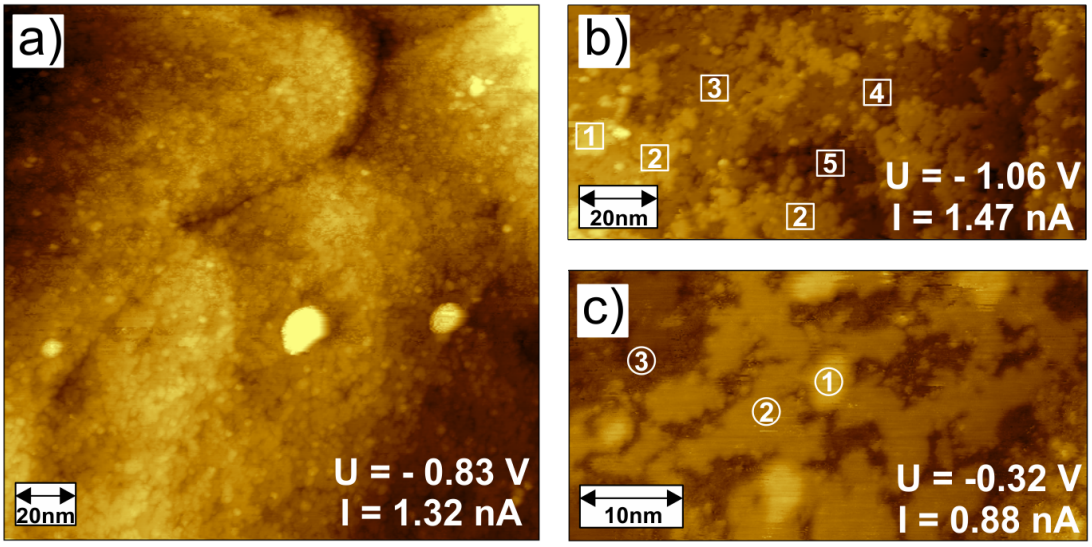

Figure 6.17: STM images of the (1×1) N-polar InN layer taken at the area of a) (180×180)nm^2 b) (130×60)nm^2 and c) (50×25)nm^2. Applied current and sample bias are shown in each image. Numbers on the images correspond to the different terraces.

will be shown a number of STM images of the InN layer corresponding to the different scanning areas.

Fig. 6.17 (a) shows the STM image of the InN layer taken at a large area of (180×180) nm^2 that exhibits a broad overview of the surface topography. A grain boundary and several bright spots can be clearly distinguished in the image. These islands having the form of bright spots were also observed in AFM images shown in Fig. 6.1 and probably correspond to metallic indium. The STM image in Fig. 6.17 (a) does not exhibit a smooth and continuous layer but shows a cloud-like surface structure, where the single terraces can be defined in some regions. Different regions corresponded to five terraces of InN can be distinguished in Fig. 6.17 (b). Each terrace is associated with a monolayer of the crystal lattice and is marked by a number. For instance, the terrace labeled by number 3 does not cover homogenously the layer underneath it (number 4), moreover, in some areas it forms a single small islands on top of it. STM image in Fig. 6.17 (c) shows the same principal for formation of the terraces on the InN layer but under different tunneling condition (lower sample bias and tunneling current compared to the previous images). Three regions can be clearly defined and they correspond to three monolayers of InN.

The STM image in Fig. 6.18 (a) shows another region on the InN surface, where the formed terraces homogeneously cover the surface and exhibit approximately the same length of ∼10 nm by measuring along the sketched arrow. The profile of these terraces is shown in Fig. 6.18 (b), where each terrace is separated from another by the

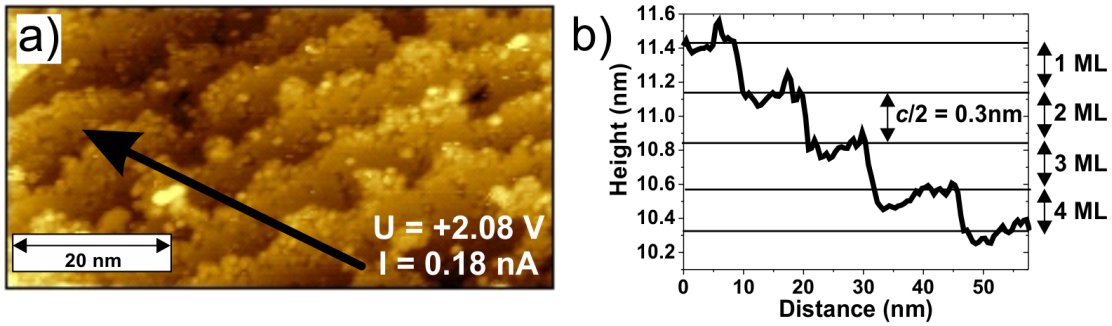

Figure 6.18: a) STM image of the terraces formed on the MOVPE grown InN layer and b) the profile taken along several monolayers (ML) as shown by an arrow in STM image.

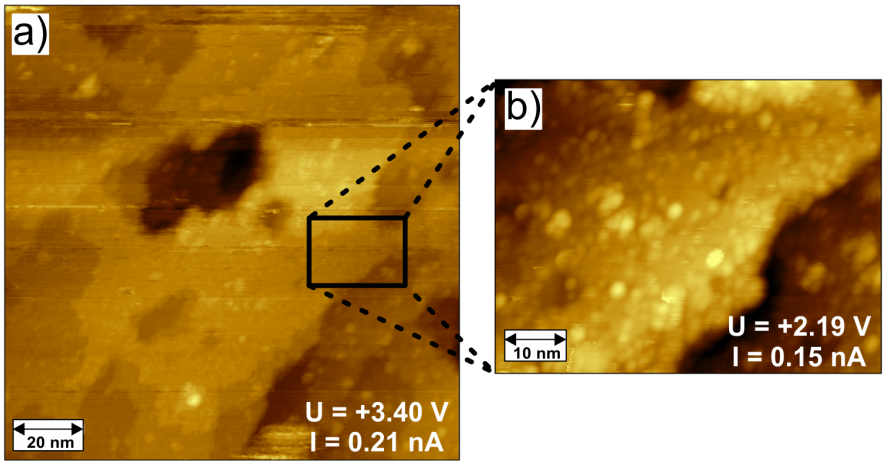

Figure 6.19: a) STM image of the V-defect on the InN layer taken at the area of (130×130) nm^2 and b) the zoomed STM image of the single terrace ((60×50) nm^2).

same distance of $\sim$0.3 nm corresponding to the half of the InN *c*-lattice constant or one monolayer.

As was shown in AFM images (Fig. 6.1), the surface of the studied N-polar InN layer contains pits. An example of this threading dislocation in form of the V-defect is shown in STM image in Fig. 6.19 (a) The V-defect is surrounded by a continuously grown layer. The edges of several monolayers can be distinguished in the inner walls of the pit. From previously shown STM images as well as from Fig. 6.19 (a), one can conclude that the surface is quite smooth within one terrace. However, a closer look at the terrace by zooming into it shows that the terrace consist of a cloudy- or grain-like structure, as shown in Fig. 6.19 (b). This grainy structure was always observed on the InN layer for these scanning areas.

An even closer view of the structure is shown in Fig. 6.20. Both STM images consist of the randomly distributed grains, which size varying from 3 to 8 nm. Such images with a grain-like structure were observed all over the measured sample, once the scanning

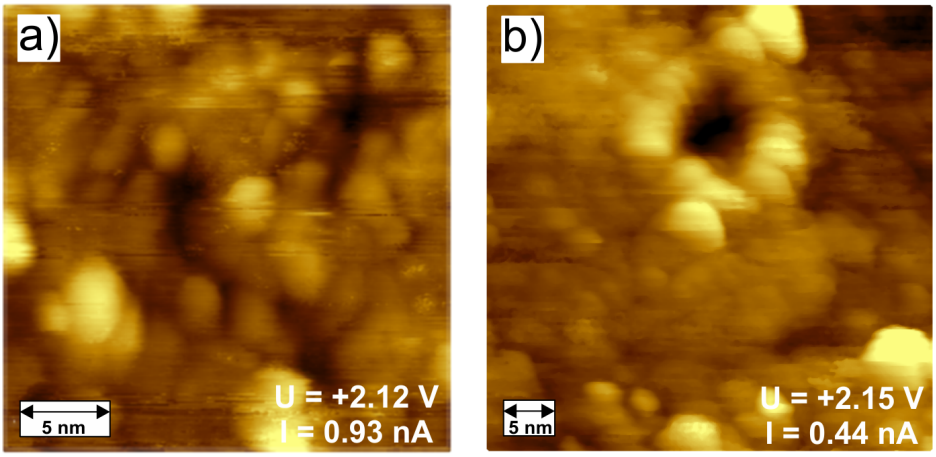

Figure 6.20: STM images showing a) a grain-like structure of the InN layer taken at area of (25×25) nm^2; b) a formed V-defect surrounded by grains ordered in circle (area (45×45) nm^2).

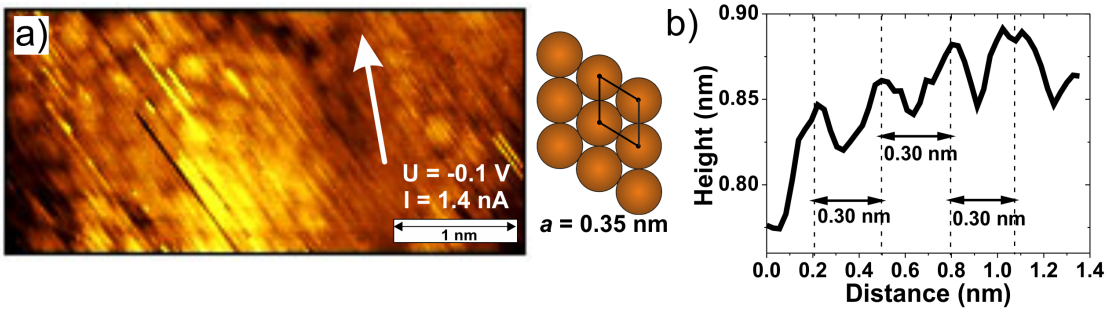

Figure 6.21: a) Atomic-resolved STM image of the N-polar InN layer with a sketched model of the (1×1) reconstruction, b) the profile taken along an arrow shown in the STM image.

area was decreased to 50-30 nm. Moreover, at this scanning area the tunneling condition becomes unstable due to the highly inhomogeneous distribution of the electron DOS that appears in STM image as a grain-like structure. Instability of the scanning tip results in the unintentional horizontal lines, vanished or diffused features in STM images (Fig. 6.20) and should be associated with the scanning artifacts.

Fig. 6.20 (b) shows the V-defect that is smaller than the one shown previously in Fig. 6.19 (a). Interestingly, such kind of the V-defects were always surrounded by grains ordered in a circle (flower-like shape), as shown in Fig. 6.20 (b). However, on the other regions of the layer, the grains do not demonstrate any kind of order. The grains that form the flower-like structure have a higher contrast compared to the other area of the image that is associated with a higher electron DOS around the V-defect. As was shown by Minj et al., indium atoms preferably segregate at the edges of the V-defects [175], therefore, higher DOS observed around the defect may originate from the indium segregation at the edges of the defect.

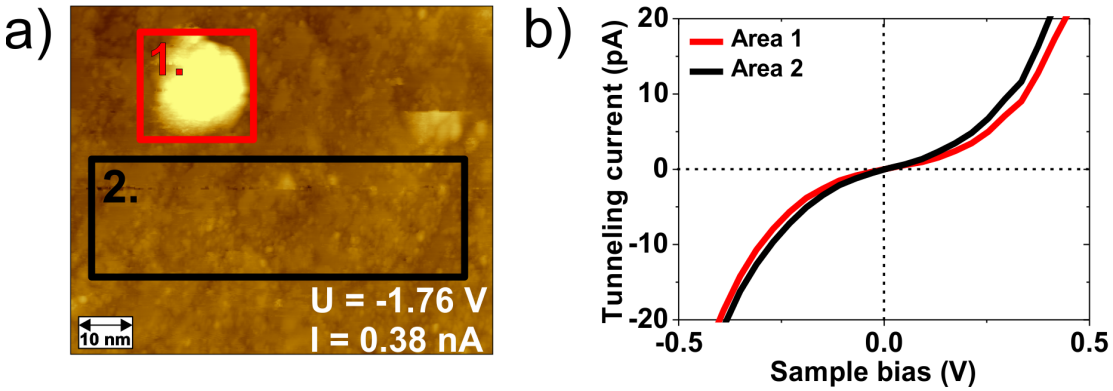

Figure 6.22: a) STM image of the N-polar InN surface with the sketched areas for STS. b) STS I-V curves recorded from the two areas marked in the STM image; each I-V curve is an average of 15-25 single curves.

The nanoscale resolved STM image of the N-polar InN layer was obtained by applying a very low sample bias and high tunneling current (this tunneling condition is often used for investigation of metals by STM). This STM image is shown in Fig. 6.21 (a), where the profile taken along the recorded structure labeled by an arrow in STM image is represented in Fig. 6.21 (b). The distance between the two features is ≈ 0.3 nm that is in good agreement with the *a*-lattice constant of InN. Thus, the observed features correspond to the atoms and the represented STM image shows a well-ordered atomic (1×1) surface reconstruction as sketched in the model. A slight displacement of the atoms from the ideal reconstruction can be explained by a thermal drift and fast changes of the tip position during scanning.

Theoretically it was predicted that N-polar InN layers is terminated by an In-adlayer which cause a metallic behavior of the surface [75]. In order to prove it experimentally, STS was performed on the investigated N-polar InN layer. The I-V curves were recorded from two different areas on the surface: the bright spot (that were also observed in Fig. 6.17 (a)) and the smooth area, as represented in Fig. 6.22. The I-V curve from each area is an average of 15-25 single curves (recorded in the single point spectroscopy mode). No evidence of the band gap is observed from the I-V spectra, where the tunneling current turns to zero only at 0 V, corresponding to the surface metallicity of the layer. Moreover, the I-V curves from the areas 1 and 2 show a very similar behavior. Therefore, it is not possible to distinguish by STS if the spectrum from the area 1 corresponds to the indium terminated surface of the InN island or to the metallic indium droplet. Taking into account the In (101) metallic peak observed by XRD [162], it is very likely that the region 1 refers to the metallic indium droplet, where a higher contrast in STM image indicates a higher DOS compared to the overall area.

Additionally, STS was performed in the form of a grid spectroscopy on the small area of (15×15) nm^2, as shown in Fig. 6.23 (a). For this, the area was automatically divided

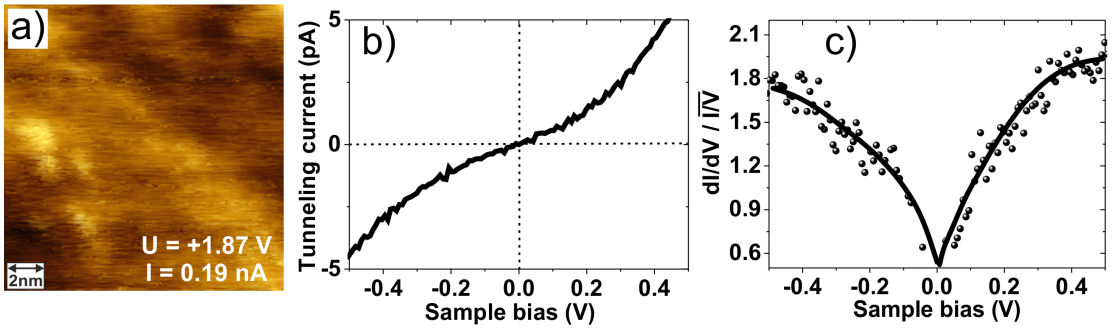

Figure 6.23: a) STM image recorded on the N-polar InN layer at scanning area of (15×15) nm^2; STS was performed on the whole area by using a grid of (30×30) measurement points. The average STS b) I-V curve and c) normalized conductance $(\mathrm{dI/dV})/(\overline{I/V})$ curve from the grid spectroscopy; lines are guide to the eye.

by 30×30 segments and an I-V curve was recorded from the each segment. The small area of measurements gives a more accurate information about the local DOS. As a result of the STS grid measurement, a current image topography for a certain sample bias can be obtained and analyzed for a chosen area. The current imaging can give a detailed information about a current fluctuation on the surface caused, for instance, by defects, different types of atoms or surface states, etc. For the area represented in Fig. 6.23 (a), no significant difference in the current images could be detected that corresponds to the homogeneous charge distribution on the InN layer within a chosen area. Fig. 6.23 (b) shows an average I-V curve based on the grid spectroscopy and a corresponding normalized conductance $(\mathrm{dI/dV})/(\overline{I/V})$ curve (Fig. 6.23 (c)). Similar to the previous STS measurements, the I-V spectrum shows a linear slope at 0 V corresponding to a metallic behavior of the N-polar InN surface.

Ideally, the normalized differential conductance can be interpreted as a local DOS with a Fermi level located around 0 V; it can give an additional information about the surface states and their positions with respect to the Fermi level. However, interpretation of the normalized conductance curve should be performed very carefully and confirmed by different tips, in order to exclude an effect of extrinsic particles adsorbed on the tip, and theoretical calculations. Moreover, the tip induced band bending effect should be also taken into account. The InN layer studied in this work possesses an electron accumulation layer at the surface, which is rough on the nm scale – all of this add even more complicity to the interpretation of the normalized conductance curve. Therefore, in order to avoid incorrect interpretation of the results, the $(\mathrm{dI/dV})/(\overline{I/V})$ curve was used only to determine the surface behavior, i.e. metallicity or conductivity.

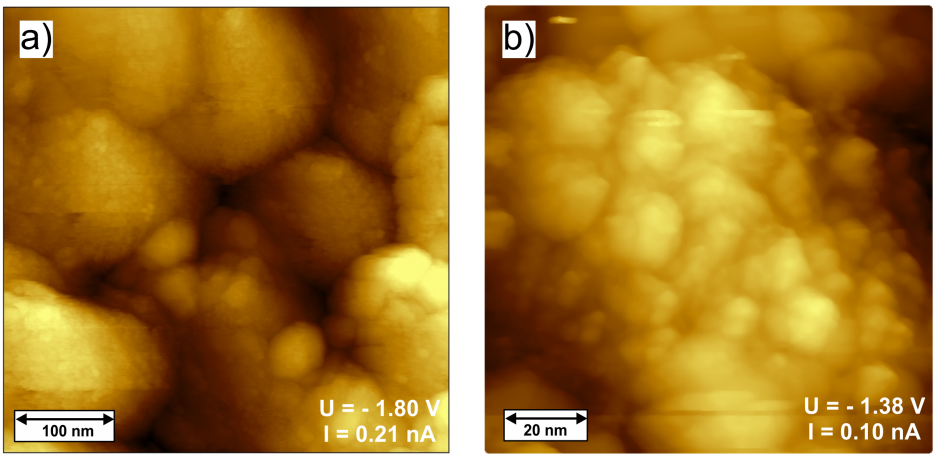

Figure 6.24: Wide-scale STM images of the rough N-polar InN layer grown by MEAglow recorded at the area of a) $(450\times450)\,\mathrm{nm}^2$ and b) $(100\times100)\,\mathrm{nm}^2$.

6.1.7 The $(\sqrt{3}\times\sqrt{3})$R$\pm$30° N-polar InN Layer Grown by MEAglow

As shown by LEED in Fig. 6.12 (c) and (d), both the rough and smooth N-polar InN layers grown by MEAglow have the $(\sqrt{3}\times\sqrt{3})$R$\pm$30° surface reconstructions. In order to confirm this reconstruction by STM, it was sufficient to investigate only one sample. The InN layer with the rough surface (Fig. 6.2 (b)) was chosen for the STM and STS measurements due to the large crystal islands formed on the surface. The size of the bigger crystallites ($\sim$ 100-200 nm) was assumed to be large enough to perform STM imaging within one crystallite under the stable tunneling condition, while for the smooth InN layer grown by MEAglow (Fig. 6.2 (a)) the tunneling conditions were expected to vary much within the chosen scanning area.

The STM image recorded on a large scanning area of $(450\times450)\,\mathrm{nm}^2$ shown in Fig. 6.24 (a), gives an overview of the N-polar $(\sqrt{3}\times\sqrt{3})$R$\pm$30° reconstructed InN surface. The STM image is in good correlation with the topographic AFM image of the surface: small and big islands (crystallites) and their boundaries can be clearly distinguished; crystallites are separated from each other by different distances, some of them are coalesced together. Although the single large crystallite looks flat on a large scale, while decreasing the scanning area to $(100\times100)\,\mathrm{nm}^2$ shows that each crystallite consists of the cloudy-like structure, as represented in Fig. 6.24 (b). No terraces could be observed on the surface, as in the case of the (1×1) InN layer grown by MOVPE.

A closer look into the crystalline structure by imaging the surface area of $(60\times60)\,\mathrm{nm}^2$ represented in Fig. 6.25 (a), shows the smaller prolonged grains with size of 20-30 nm in diameter. Each of the grain consist of nanoscale structures which can be distinguished in Fig. 6.25 (b) and may be assigned to atoms However, due to the unstable tunneling condition on the rough N-polar InN surface and thermal drift, the presumed atoms can

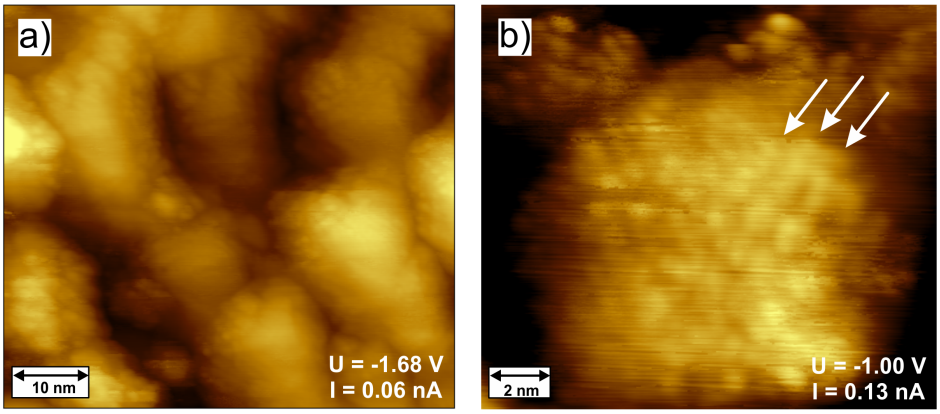

Figure 6.25: STM images of the rough N-polar InN layer grown by MEAglow at the scales of a) $(60\times60)\,\mathrm{nm}^2$ and b) $(15\times13)\,\mathrm{nm}^2$.

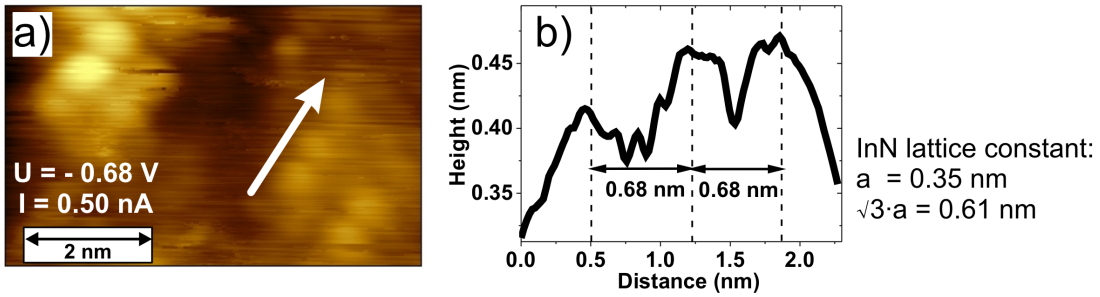

Figure 6.26: a) STM atomically resolved image of the $(\sqrt{3}\times\sqrt{3})\mathrm{R}\pm30^\circ$ reconstructed N-polar InN layer, b) the profile taken along the atoms (sketched with arrow).

not be well-resolved and their ordered structure can be observed only on some of the areas (labeled in STM image with arrows).

A better resolved nanoscale STM image is shown in Fig. 6.26 (a). The profile (Fig. 6.26 (b)) taken along the recorded structures (sketched by an arrow), shows the distance between the nanoscale features to be ~ 0.68 nm that is significantly larger compared to the a-lattice constant of InN. However, in the case of the $(\sqrt{3}\times\sqrt{3})\mathrm{R}\pm30^\circ$ surface reconstruction, the atoms should be separated from each other by a distance of $\sqrt{3}\cdot a$ that is equal 0.61 nm. This correlates good with the distances determined from the profile. A slight difference of 10% between the observed and calculated value can be explained by an error due to the thermal drift and unstable tunneling conditions during the scan. Therefore, the observed nanoscale structures correspond to the atoms and the STM measurements confirm the $(\sqrt{3}\times\sqrt{3})\mathrm{R}\pm30^\circ$ reconstruction previously observed by LEED.

The grid STS was performed on the $(2\times2)\,\mathrm{nm}^2$ of the N-polar InN layer, as marked in square in the STM image in Fig. 6.27 (a). The STS spectrum shows a metallic behavior of the $(\sqrt{3}\times\sqrt{3})\mathrm{R}\pm30^\circ$ InN surface (Fig. 6.27 (b)). Similar to the (1×1) reconstructed

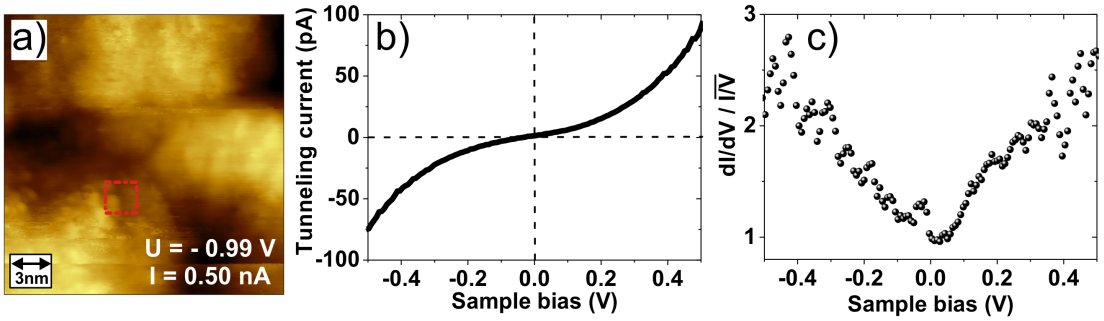

Figure 6.27: a) STM image of the rough N-polar InN layer grown by MEAglow at the scale of $(20\times20)\,\mathrm{nm}^2$, the sketched square refers to the area where grid spectroscopy was performed. b) I-V curve is an average of the grid (15×15 points) spectroscopy, c) normalized conductance $(\mathrm{dI/dV})\,/\,(\overline{I/V})$ of the I-V spectrum.

InN layer, surface metallicity is probably caused by a high indium amount on the surface. The normalized conductance from the I-V curve shown in Fig. 6.27 (c) exhibits pronounced shoulders at $\sim$+0.18 V and $\sim$-0.04 V, which may originate from the surface or from the tip. As was mentioned previously, the interpretation of the normalized conductance curve is a complicated issue, and in this work it is used only for a clear definition of the band gap or surface metallicity of the studied layer.

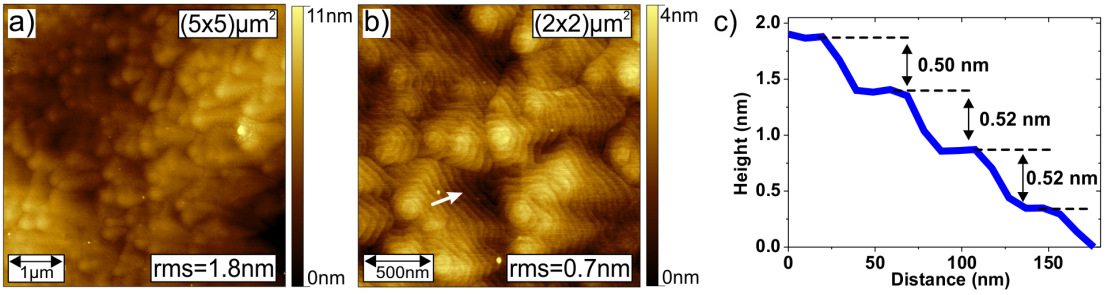

Figure 6.28: AFM topographic images of the In-polar InN layer grown by MBE on the scale of a) $(5\times5)\,\mu m^2$ and b) $(2\times2)\,\mu m^2$; c) profile along the terraces as labeled by an arrow in image (b).

6.2 In-polar InN surfaces

6.2.1 Oxidized In-polar InN Layer

Prior to characterization under UHV conditions, topography of the MBE grown In-polar InN layer was studied by AFM. The In-polar InN layer exhibits a very smooth surface with the rms roughness of 1.8 nm for $(5\times5)\,\mu m^2$ (Fig. 6.28 (a)) that is much smoother compared to the MOVPE grown InN layers. The surface contains screw dislocations with single atomic steps, as shown in Fig. 6.28 (b). The profile along the terraces, marked with an arrow in AFM image, is shown in Fig. 6.28 (c). The terraces are separated by ≈ 0.5 nm with respect to each other. This separation is attributed to 2 ML of InN, although the determined value of 0.5 nm is smaller compared to the InN *c*-lattice constant of 0.567 nm [22]. The difference in values may be explained by the uncertainties during the background subtraction of AFM images. Moreover, the determined value for terrace separation is much higher to be assigned to one monolayer steps, hence, it is correct to attribute it to the 2 ML steps on the InN layer. Metallic indium droplets were not observed on the AFM images as expected after etching the surface by HCl.

The chemical analysis of the oxidized In-polar InN layer was performed by XPS by studying the electron photoemission from the In $3d_{5/2}$, N $1s$ and O $1s$ core-levels as shown in Fig. 6.29. The core-level peaks were recorded at the normal emission and emission at 70° with respect to the surface normal. Relative amounts of the oxygen and carbon determined from the normal emission measurements are 15.6% and 21.0%, respectively, while for the measurements at 70°, relative amounts of oxygen and carbon equal 18.9% and 64.1%. This shows that the oxidized InN surface is highly predominated by carbon species compared to previously studied N-polar InN layers.

The numerically fitted components of the In $3d_{5/2}$, N $1s$ and O $1s$ peaks in Fig. 6.29 are very similar to the one observed for the oxidized N-polar InN layers grown by MOVPE and MEAglow (see Fig. 6.5 and Fig. 6.6). As will be shown later, the studied

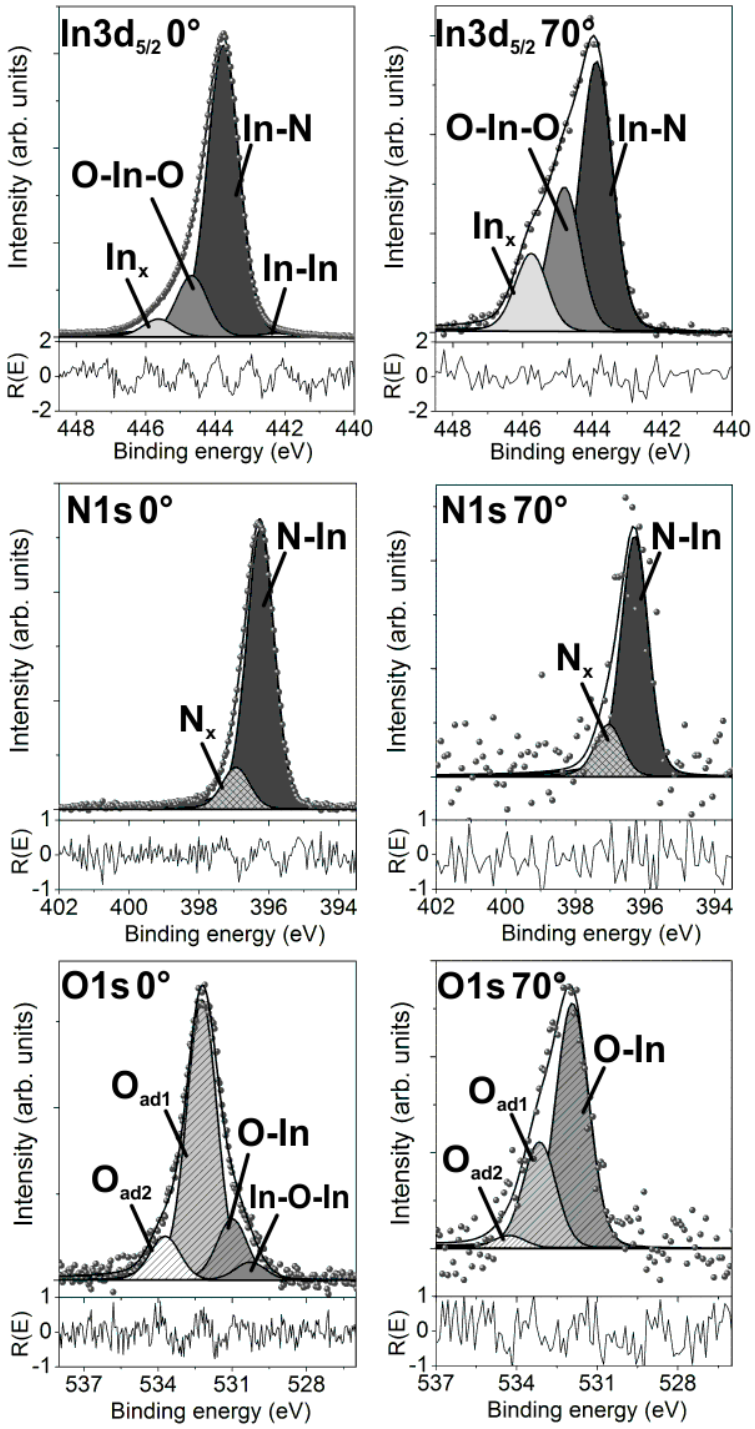

Figure 6.29: The In 3*d*, N 1*s* and O 1*s* core-levels of the oxidized In-polar InN layer grown by MBE for the normal emission and emission at 70° with respect to surface normal.

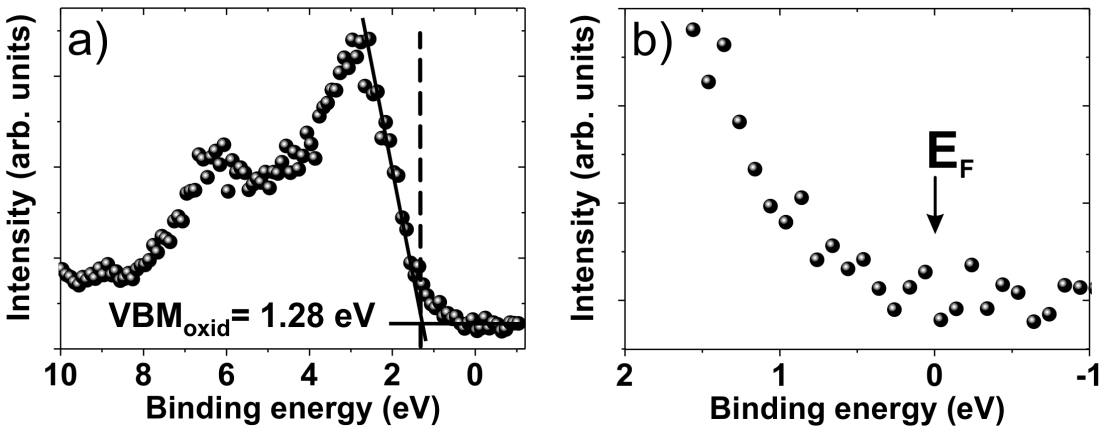

Figure 6.30: a) VB spectrum of the oxidized In-polar InN layer and b) XPS emission near the Fermi edge.

In-polar InN layer possesses a metallic surface behavior, hence an asymmetric parameter was used for the numerical fit of every component in the recorded core-levels for oxidized and clean layers. All fit parameters can be found in Appendix B.

The In $3d_{5/2}$ core-level consists of 4 components: In-In, In-N, O-In-O and In_x. The same components were observed in the case of the MOVPE grown N-polar InN layer (Fig. 6.5) and assumed to have the similar origin. The In-N component at 443.8 eV corresponds to the bulk indium to nitrogen bond. The component at lower binding energy corresponds to the metallic In-In bond. Probably, due to the low signal to noise ratio, the In-In component is not observed for the emission at 70°. The O-In-O and In_x components in the In $3d_{5/2}$ state for emission at 70° show much higher intensity compared to the one shown for the oxidized MEAglow grown InN for emission at 80°. The In_x was assigned to the indium dangling bonds or defects, where an indium atom is bound to a contamination atom (not oxygen) or a complex structure. Since the amount of carbon and oxygen on the MBE grown InN layer is high, this can explain the high intensity of the O-In-O and In_x component in Fig. 6.29.

The N 1*s* core-level recorded from the oxidized In-polar InN shows only two chemical states: the bulk N-In and the N_x component assigned to absorption of contaminations on defects (see discussion for N-polar InN layer in Sec. 6.1.5). A line shape of the O 1*s* core-level recorded at normal emission shown in Fig. 6.29 is very similar to the one observed for the oxidized N-polar InN layers (Fig. 6.5 and Fig. 6.6): two components correspond to the different physisorbed adsorbates (O_{ad1} and O_{ad2}), and two components at the lowest binding energy are assigned to the O-In and In-O-In bonds. The In-O-In component is not observed for the emission at 70° probably due to its low intensity and low signal to noise ratio.

Besides the core-level analysis, the XPS VB was also recorded from the oxidized InN layer as represented in Fig. 6.30. Position of the VBM was estimated to be 1.28 ± 0.10 eV above the Fermi level, indicating a downward band bending on the ox-

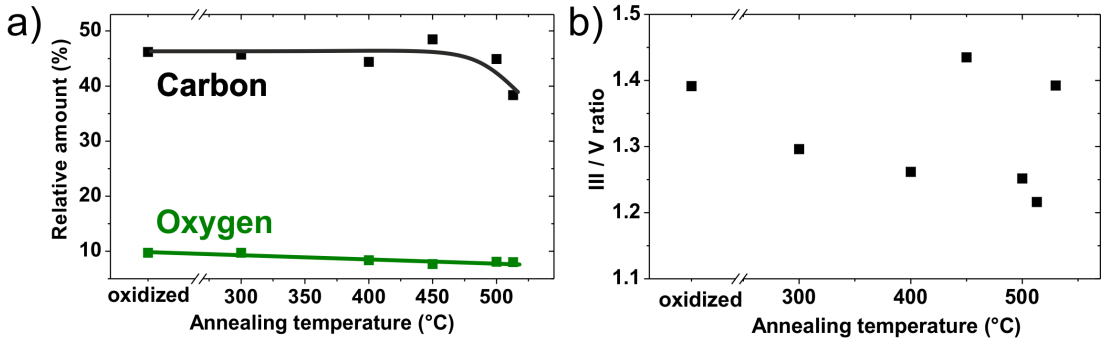

Figure 6.31: a) Relative amount of carbon and oxygen and b) the III/V ratio of the In-polar InN layer after annealing for 10 min at different temperatures. Calculations are based on AES measurements; lines are guide to the eye.

idized In-polar InN layer. Photoemission spectrum near 0 eV in Fig. 6.30 (b) does not show a pronounced Fermi edge at 0 eV, which is in good agreement with absence of metallic indium droplets on the surface.

The VB peak at lower binding energy (peak P_I) significantly dominates the VB spectra. The $P_{II} : P_I$ ratio equals 0.66 ± 0.05 that corresponds to the In-polarity of the layer, based on the discussions in Chap. 4.

6.2.2 Surface Decontamination: Annealing in UHV and Nitrogen Plasma

In the previous chapter an appropriate preparation conditions for the surface decontamination of the N-polar InN layers were determined. It is not necessarily true that the preparation parameters used for the N-polar orientated layer would suit the In-polar InN layers, since for different crystal orientations the binding configurations of the topmost layer with adsorbates is different. However, the preparation conditions also should not be very different. Therefore, investigation of the surface treatment for the oxidized In-polar InN layer will be partially based on the results for the N-polar InN layers.

The surface decontamination of the In-polar InN layer was performed by thermal annealing of the layer for 10 min under UHV conditions and annealing in nitrogen plasma (N*) by using N-plasma source. In order to find an appropriate preparation condition, different annealing temperatures were used and their effect on the surface and crystal structure of the layers were analyzed in details.

Relative amount of surface contaminations, i.e. carbon and oxygen, were determined from AES after annealing the InN layer at 300°C-530°C. As shown in Fig. 6.31 (a), annealing at the temperature of 530°C leads to the decrease of oxygen and carbon only by 17% that is much lower compared to the decontamination observed for the N-polar InN layers (see Fig. 6.8). The III/V ratio values determined from AES after each annealing step are represented in Fig. 6.31 (b). The III/V ratio varies in the range of 1.32 ± 0.10

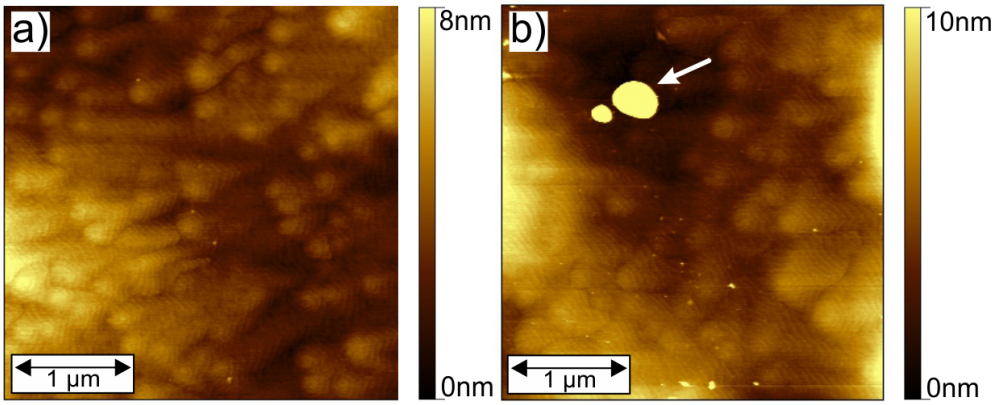

Figure 6.32: AFM image of In-polar InN layer after annealing at a) 500°C and b) 530°C for 10 min. Arrow in image (b) indicates formed indium droplets on the surface.

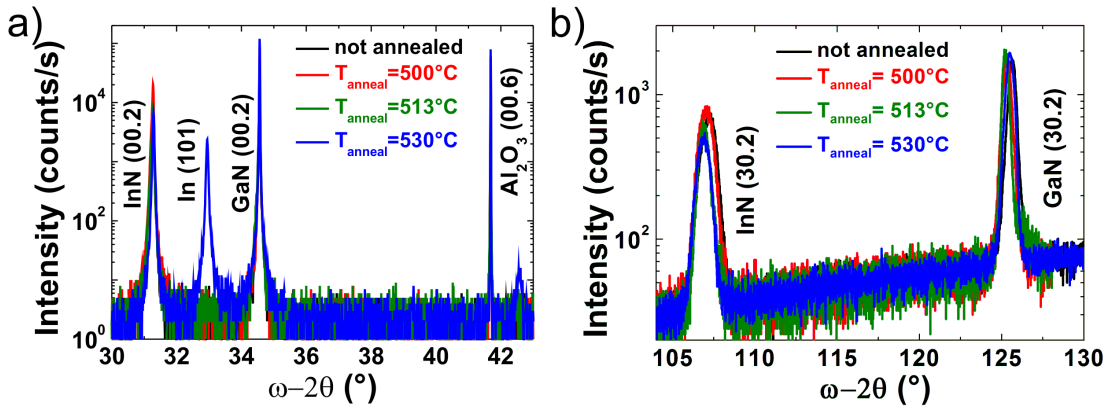

Figure 6.33: XRD ω-2θ scan for the oxidized and annealed at 500°C, 513°C and 530°C In-polar InN layer. Measurements were performed by F. Mehnke, TU Berlin.

along the whole scale and does not show any obvious tendency with increase of annealing temperature. This might be explained by the fact that AES is a very surface sensitive technique and a large amount of residual contaminations makes determination of the In/N ratio inaccurate.

AFM performed on the InN layers annealed at 500°C (Fig. 6.32 (a)) showed no changes in the InN surface topography, while formation of indium droplets was observed after annealing at 530°C, as indicated by arrow in Fig. 6.32 (b) Size of the indium droplets varies from 0.1 μm up to 1 μm with height of 0.2-0.5 μm. The surface between the indium droplets remained unchanged and exhibits screw dislocations and step-like structure. Therefore, annealing temperature of 530°C is too high for the surface decontamination and leads to modification of the surface structure.

In order to determine the effect of annealing temperature on the crystal properties of the In-polar InN layers, XRD measurements were performed on the layers annealed

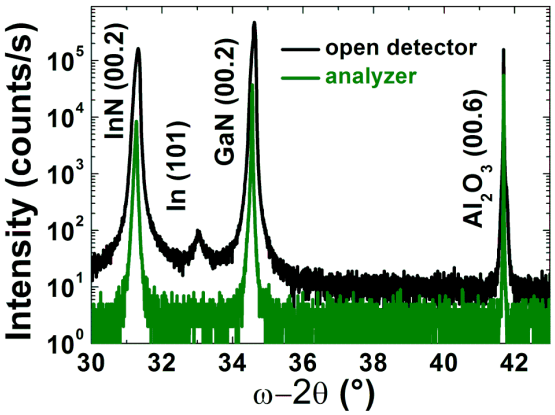

Figure 6.34: XRD ω-2θ scan for the In-polar InN layer annealed for 10 min at 513 °C recorded with open detector and analyzer. Measurements were performed by F. Mehnke, TU Berlin.

Table 6.3: The *c*-lattice constants determined for the In-polar InN layer grown by MBE before and after surface treatment. Calculations are based on the ω-2θ scan from XRD measurements. Annealing was performed for 10 min.

Treatment	h	k	l	2θ	*c*-lattice constant
No	0	0	2	31.271 °	0.571(6) nm
Annealing at 500°C	0	0	2	31.271 °	0.571(6) nm
Annealing at 513°C	0	0	2	31.269 °	0.571(6) nm
Annealing at 530°C	0	0	2	31.287 °	0.571(3) nm

at temperatures above 500°C. The XRD measurement and related calculations were carried out by F. Mehnke at TU Berlin.

Fig. 6.33 shows the XRD ω-2θ scans of the InN layers grown on GaN/Al_2O_3 template before and after annealing at 500°C, 513°C and 530°C. The GaN (00.2) and (30.2) reflections as well as Al_2O_3 (00.6) reflection were not analyzed in details. The metallic In (101) reflection is absent for the as grown layer (not annealed) and the layers annealed up to 513°C, while the intensity of the In (101) reflection increases drastically after increasing the temperature up to 530°C. Although metallic indium is not detected in Fig. 6.33 (a) for the layer annealed at 513°C, a low intensity of the In (101) reflection can be distinguished in the ω-2θ scan performed with an open detector as shown in Fig. 6.34. This indicates formation of indium droplets on the In-polar InN surface even after annealing at 513°C, although in a smaller amount.

Note that in the case of the N-polar InN layers grown by MEAglow, formation of indium droplets was not observed even after annealing at 540°C (Fig. 6.11), while for the In-polar InN layers grown by MBE formation of metallic indium starts already at $\approx$ 513°C and increases significantly with increasing temperature.

Based on the ω-2θ scans the *c*-lattice constant of the In-polar InN layer was determined prior and after annealing at high temperatures. The equations used for calcula-

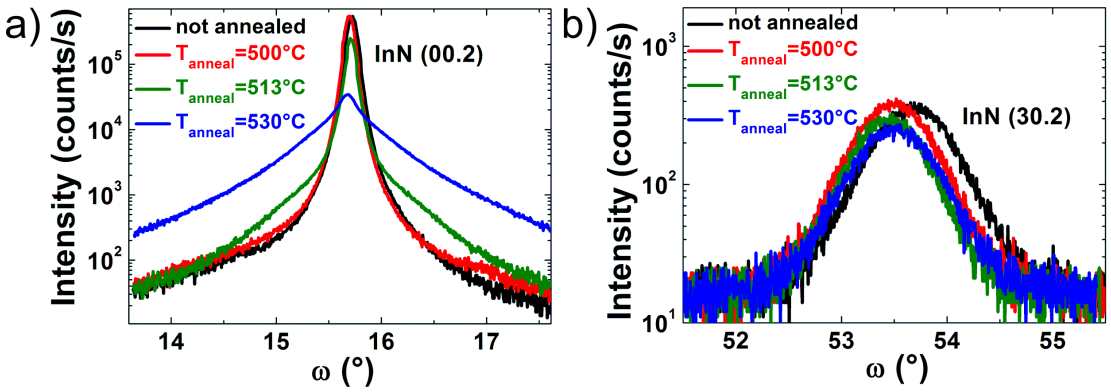

Figure 6.35: ω scan of the symmetric a) InN (00.2) and b) InN (30.2) reflections of the In-polar InN layer prior and after annealing at different temperatures. Measurements were performed by F. Mehnke, TU Berlin.

tion can be found in Appendix C. The results are summarized in Tab.6.3. The determined c-lattice constant remained unchanged after annealing even at 530°C if considering an error bar of the measurements (resolution of the XRD ω-2θ scan is 0.005 °, error bar for the calculated lattice constant is 0.0004 nm). Thus, the crystal lattice did not undergo any lateral suppression or relaxation upon annealing.

Additionally, the ω scan of the InN (00.2) and InN (30.2) reflections were recorded for the InN layers prior and after annealing, as represented in Fig. 6.35. The FWHM of the InN (00.2) reflection is about 0.1° for the untreated layer and starts to increase with increasing of annealing temperature until it reaches the value of 0.29° for the annealing at 530°C. Broadening of the peak is accompanied by a decrease of the peak intensity that is associated with the formation of defects and degradation of InN crystal quality. At the same time, the InN (30.2) reflection does not show such a dramatic changes of the FWHM with increase of annealing temperature.

The density of screw and edge dislocations in the InN layer was estimated from the ω scan of InN (00.2) and InN (30.2) reflections, respectively. The equations for calculation of the dislocation density (DD) are described in Appendix C. Tab.6.4 represents the screw and edge DD, as well as total threading dislocation density (TDD) for the InN prior and after surface annealing at different temperatures. Upon annealing at 530°C, the screw DD increases by one order of magnitude from 2.10×10^8 cm^{-2} for the untreated layer up to 1.79×10^9 cm^{-2} after annealing at highest temperature. The density of the edge dislocations is one order higher than the screw dislocations, and does not change significantly with increasing annealing temperature. As a result, the edge type of dislocations predominates overall TDD which is determined to be 3.46×10^{10} cm^{-2} for the InN layer prior to annealing and 3.67×10^{10} cm^{-2} after annealing at 530°C. It is important to mention that the screw DD for the In-polar InN layer is significantly lower compared to the N-polar InN layer grown by MEAglow, for which the screw DD was

Table 6.4: Screw and edge dislocation density (DD) determined for the In-polar InN layer grown by MBE before and after annealing for 10 min at indicated temperatures. Calculations are based on the ω scan measured by XRD.

Treatment	FWHM InN (00.2) (°)	Screw DD (cm^{-2})	FWHM InN (30.2) (°)	Edge DD (cm^{-2})	Threading DD (cm^{-2})
No	0.101	2.21×10^8	0.784	3.44×10^{10}	3.46×10^{10}
Annealing at 500°C	0.098	2.10×10^8	0.762	3.25×10^{10}	3.27×10^{10}
Annealing at 513°C	0.086	1.63×10^8	0.681	2.60×10^{10}	2.62×10^{10}
Annealing at 530°C	0.287	1.79×10^9	0.792	3.52×10^{10}	3.67×10^{10}

determined to be about $3.5 \times 10^{11}\,cm^{-2}$. Therefore, the overall crystalline quality of the studied In-polar InN layer is much better compared to other InN layers.

Based on the shown results one can conclude that annealing of the MBE grown In-polar InN in UHV does not remove surface contamination significantly even by applying annealing temperature close to InN decomposition temperature. Moreover, annealing temperatures above 500°C results in increase of the screw DD in the InN crystal structure and formation of indium droplets on the surface. This is in agreement with the appropriate annealing temperature of 450-480°C found for the N-polar InN layer grown by MOVPE.

As an alternative preparation method, the In-polar InN layer was annealed for 10 min in nitrogen plasma by applying the N-plasma source at the pressure of $\approx 1 \times 10^{-4}$ mbar. In order to avoid formation of indium droplets and destruction of the lattice crystal, the InN layer was annealed at the temperature of 450°C, which was used for surface decontamination of the MOVPE grown N-polar InN layers under UHV conditions. In this case, a quantitative analysis was performed by XPS. The carbon and oxygen were decreased by 92% and 33%, respectively, which is much higher compared to annealing in UHV.

For comparison, Fig. 6.36 (a) and (b) shows the LEED diffraction pattern obtained from the InN layer after annealing in UHV and nitrogen plasma, respectively. In the case of annealing in UHV, the LEED pattern could be obtained only at high electron energy (> 120 eV) and shows a high background intensity corresponding to the large amount of residual contaminations on the surface. For the InN layer annealed in nitrogen plasma, the LEED diffraction pattern shows small, sharp spots with a low background, indicating a clean well-ordered surface structure of InN layer. In the later case, the LEED patterns could be observed already at $\sim$ 35 eV, however, Fig. 6.36 (b)

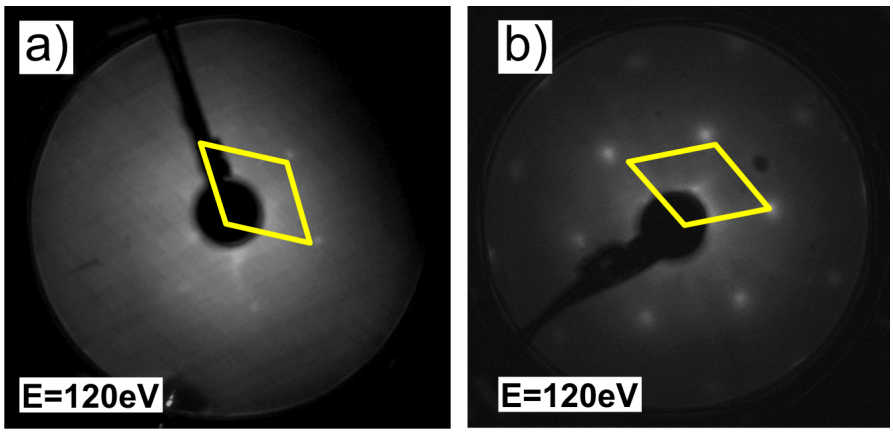

Figure 6.36: LEED diffraction patterns recorded at 120 eV for the In-polar InN layer after a) annealing in UHV at 500°C and b) annealing in N* plasma at 450°C for 10 min.

shows the diffraction pattern recorded at 120 eV, in order to compare it with the one in Fig. 6.36 (a).

Thus, surface treatment of the In-polar InN layer in nitrogen plasma is more effective and required lower annealing temperature compared to annealing in UHV. Higher efficiency of the surface decontamination by using a N-plasma source was also observed by Friedrich et al. [66]. In his work it was shown that an almost complete desorption of carbon from the polar InGaN surfaces can be achieved at 800°C for annealing in UHV or at 600°C for annealing in N-plasma. Similar to the above shown results, much lower annealing temperature is required for the surface deoxidation if annealing is performed in nitrogen plasma.

6.2.3 Surface Properties of the Clean In-polar InN Layer

As was mentioned previously, upon annealing in nitrogen plasma, the In-polar InN layer exhibits the LEED pattern with small and sharp reflexes indicating a clean and well-ordered surface. The LEED pattern recorded at lower electron energy (55.8 eV) compared to Fig. 6.36 (b) corresponds to a signal from a region very near the surface. The small reflexes with high intensity can be well observed on the fluorescent screen. The diffraction pattern corresponds to the (1×1) surface reconstruction of the clean In-polar InN layer. A hexagonal unit cell is sketched in the image, similar to the MOVPE grown N-polar InN layer (Fig. 6.12 (a)).

Analysis of the chemical bonds on the In-polar InN surface was performed by recording the core-level spectra at normal emission and emission of 80° with respect to surface normal. The result are summarized in Fig. 6.38.

Intensity of the In_x component in the In $3d_{5/2}$ core-level peak for both normal emission and emission at 80°, significantly decreased after annealing. As mentioned in Sec. 6.1.5 for the N-polar InN layer grown by MEAglow, the In_x component is at-

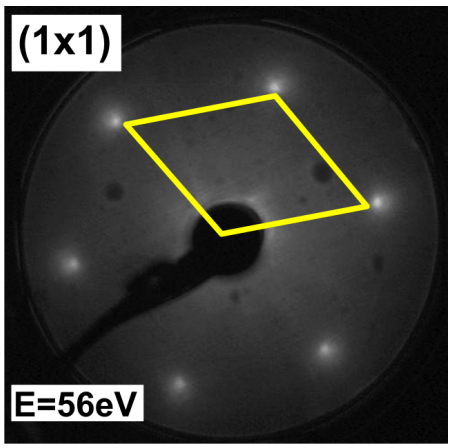

Figure 6.37: LEED diffraction pattern with a sketched hexagonal unit cell recorded from the clean In-polar InN layer at 55.8 eV after annealing in N* plasma at 450°C for 10 min.

tributed to the dangling bonds, surface defects or chemical bonds with complex contamination species. Indeed, behavior of this component is in good agreement with its proposed origin: intensity of the component decreases after the surface decontamination, especially, it is good observed in the case of emission at 80°. Intensity of the In-In component remains unchanged upon the treatment by using N-plasma source, indicating that the chemical bonds associated with the component do not refer to the surface contamination.

The O-In-O component in the In $3d_{5/2}$ state recorded at normal emission shows only small intensity reduction after annealing with respect to the bulk In-N component. The quantitative analysis shows that the oxygen amount is reduced by 33% upon annealing, but since the O-In-O bond remained nearly unchanged, the oxygen desorption is probably occurring from the binding configurations between another atoms, e.g. carbon, hydrogen, or another oxygen species. The O-In-O component in the In $3d_{5/2}$ core-level for emission at 80° (Fig. 6.38) is higher compared to the oxidized sample only because of the higher emission angle used for the clean layer (80°) compared to the oxidized surface (70°).

The N $1s$ core-level recorded at normal emission is dominated mainly by the N-In bulk component, while intensity of the N_x component significantly decreased upon annealing. The surface sensitive XPS measurements for emission at 80° shows appearance of the N_y and N_z components, which were not observed for the oxidized In-polar InN layer. The chemical shifts of the N_y and N_z components are 1.9 eV and 3.0 eV with respect to the bulk N-In component, which is different than previously observed shifts of the N_y and N_z components for the MEAglow grown N-polar InN layer (Fig. 6.14). Hence, the N_y and N_z components for the In-polar InN layer should originate from another chemical compounds than in the case of the N-polar InN. Indeed, the surface treatment of the In-polar InN layers was different compared to the N-polar InN layers. The In-polar InN surface was exposed to the nitrogen plasma produced by N-plasma source, hence, some nitrogen species (e.g. nitrogen ions, molecular nitrogen) may incorporate into the near-surface region of the InN crystal lattice. Moreover, the surface

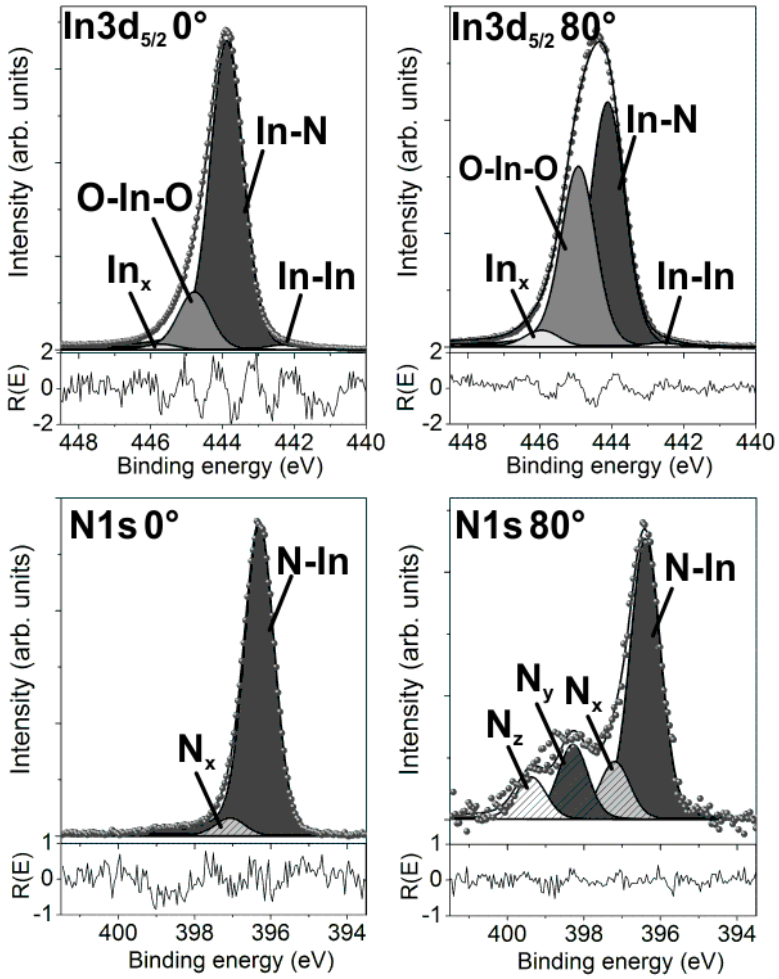

Figure 6.38: The In $3d_{5/2}$ and N $1s$ core-levels of the clean In-polar InN layers for normal emission and emission at 80° with respect to surface normal. The InN layer was annealed in N-plasma at 450°C for 10 min.

treatment by nitrogen plasma may produce some nitrogen defects or complex binding structures on the surface of InN. It is most likely that the observed N_y and N_z components originate from the surface nitrogen species or defects formed upon the treatment by nitrogen plasma source. No other components that could be assigned to N_y and N_z were observed in the In $3d_{5/2}$ or O $1s$ core-level states, indicating that nitrogen atoms from the N_y and N_z components are not bonded to indium or oxygen atoms.

The VB spectrum of the clean In-polar InN layers is shown in Fig. 6.39 (a). The position of the VBM determined from the spectrum is 1.35 ± 0.10 eV below the Fermi level, which is ~ 0.1 eV lower compared to the oxidized surface. Upon annealing, the In-N components in the N $1s$ and In $3d$ states also shift by approximately 0.1 eV towards higher binding energies compared to the oxidized surface. Hence, the VBM and core-

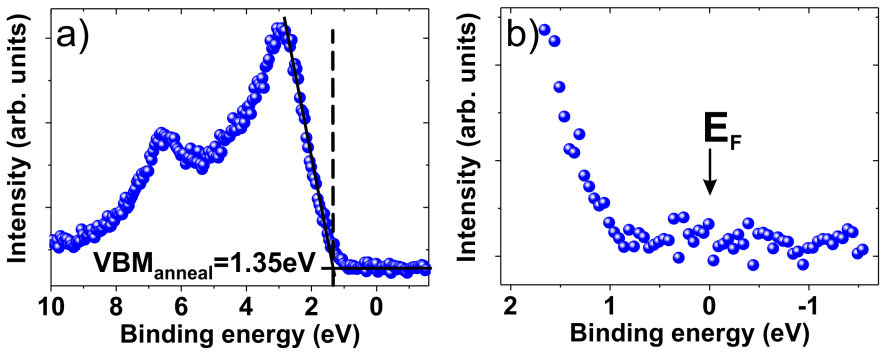

Figure 6.39: a) VB spectrum of the clean (after annealing in N-plasma at 450°C) In-polar InN layer and b) XPS emission near Fermi edge.

level shifts are in good agreement with each other. Therefore, the surface oxidation leads to a decrease of the surface downward band bending for the studied In-polar InN layer, while a stronger downward bending of the conduction and valence bands are observed for the clean In-polar InN layer. This behavior is opposite to the one determined for the N-polar InN layers (see Sec. 6.1.5).

The XPS experiments performed on the MBE grown In-polar InN layer by Eisenhardt et al. showed similar results observed for the studied In-polar InN: upon exposure to oxygen the VBM position is shifted by 0.25 eV towards lower binding energies compared to the as-grown layer, indicating the flattering of the bands on the adsorbate covered In-polar InN layer [129]. Additionally, in this report the shift of 0.1 eV towards lower binding energies compared to the as-grown In-polar InN layer was observed after the InN layer was exposed to water [129]. This shift is in good agreement with the one observed from the studied in this work In-polar InN layer. Thus, the VBM shift may be associated with the formation of water on the surface.

At the same time, surface metallicity cannot be clearly detected by XPS at binding energy near 0 eV. The Fermi edge of the clean In-polar InN layer in Fig. 6.39 is not well-pronounced due to the intensity of the detected electrons. However, it is also an indication that no metallic indium is formed on the layer after the performed thermal treatment of the layer.

Further, the surface characterization was performed by STM and STS. The STM image recorded on the wide scanning area in Fig. 6.40 (a) shows a screw dislocation (marked by black arrow) with corresponding terraces that was previously observed by AFM (Fig. 6.32). The screw dislocation is surrounded by a well-pronounced boundary (marked by white arrow) which may originate for instance, from an uncoalesced growth. Although the topographic AFM images show a smooth structure of the terraces, the STM images show a grain-like structure of each terrace as shown in Fig. 6.40 (b).

A zoom in image of the scanning area shows similar observation as for the N-polar InN layers: the In-polar InN surface on the nanoscale area consists of the clusters (grains), as shown in Fig. 6.41 (a). It seems that for the polar InN layers a surface elec-

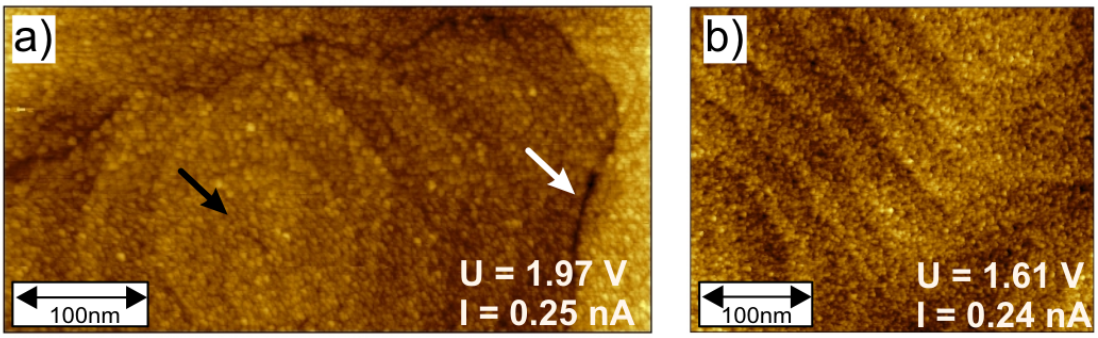

Figure 6.40: a) STM image (480×240) nm^2 of a screw dislocation, b) STM image of a terrace topography. Black and white arrow correspond to screw dislocations and grain boundary, respectively.

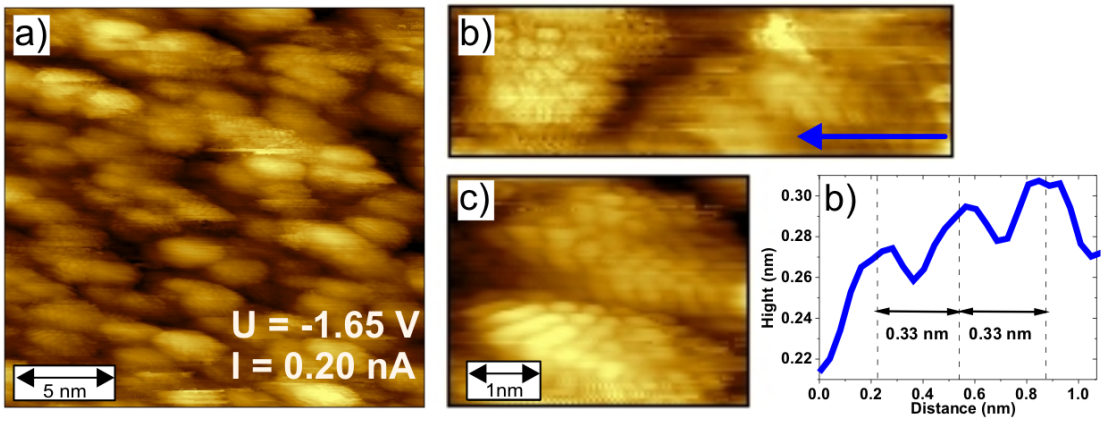

Figure 6.41: a) STM image (20×20) nm^2 of the In-polar InN layers, b) c) atomic-resolved STM images and a profile along the atoms from image (b).

tron distribution is energetically favorable in form of little clusters. This corresponds to the rearrangement of atoms on the surface into nanoscale islands. In terms of surface study by STM, it is always preferable to investigate layers with a flat formed crystal monolayer, as in the case for GaAs, silver or graphene [176]. However, a large area of homogeneously covered single InN monolayer has never been observed on the InN surfaces within this work.

An even closer view of the structure shows that each single cluster consists of the arranged nanoscale structures, Fig. 6.41 (b) and (c). The profile along this structure gives a value for their separation of ~ 0.33 nm that is in good agreement with the a-lattice constant of InN. Hence, the recorded structures correspond to the arranged surface atoms. However, an unstable tunneling conditions caused by grain-like structure result in a non-perfect imaging of the atoms, where some blurred and prolonged features appear in the images.

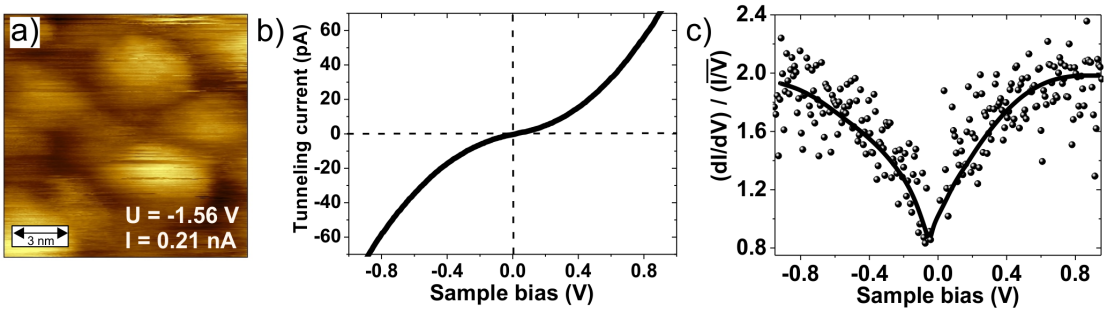

Figure 6.42: a) STM image recorded on the In-polar InN layer at scanning area of (13×13) nm^2; STS was performed on the whole area by using a grid of (15×15) measurement points. b) STS I-V and c) normalized conductance (dI/dV) / $(\overline{I/V})$ curves derived from the average of the scan area; lines are guide to the eye.

In order to determine the behavior of the InN surface, STS has been applied to the In-polar InN layers. STS was performed in the form of grid spectroscopy, already described in Sec. 6.1.4. For this, the STM image was recorded at the small scanning area (Fig. 6.42 (a)) and divided by 15×15 segments. STS I-V curves were recorded in every segment, and showed similar surface behavior for each measurement. An average of these single curves is shown in Fig. 6.42 (b). Tunneling current turns to 0 A only at 0 V, indicating no band gap of the material but a metallic behavior of the surface. This can be even better observed in the normalized conductance (dI/dV) / $(\overline{I/V})$ curve in Fig. 6.42 (c). Similar to the N-polar InN layers, surface metallicity is explained by indium termination [75] that results in the electrons accumulation layer on the In-polar InN surface.

6.3 Discussion

Surface analysis of the N- and In-polar InN layers showed that the applied growth method strongly affects the surface morphology and topography of the InN layers. The In-polar InN layer grown by MBE was found to have the smoothest surface among the studied polar InN layers. This surface consists of pronounced terraces separated from each other by two monolayers, moreover, numerous screw dislocations are present. The surface of the MOVPE grown N-polar InN layer was found to be atomically flat but contains pits and hillocks, as well as small metallic indium droplets. Although no indium droplets have been detected on the investigated MEAglow grown N-polar InN layers, their surfaces exhibit grainy and three dimensional structures, resulting in a very rough surface with increasing the growth temperature.

Based on the performed surface sensitive measurements, i.e. XPS, AES, STM and STS, the models for the (1×1) reconstructed N- and In-polar InN layers and $(\sqrt{3}\times\sqrt{3})$R$\pm30^\circ$ reconstructed N-polar InN surface grown by MEAglow can be pro-

posed. Interpretation of the obtained results based on the several experimental techniques is much more accurate. This is an obvious advantage compared to the previous literature reports, where the atomic models of the InN reconstructions have been derived only from one or two experimental techniques [40, 62, 69]. As was mentioned in Sec. 2.3, nowadays, the known reconstructions on InN surfaces are (1×1), (2×2) and $(\sqrt{3}\times\sqrt{3})$R$\pm30^\circ$ for the In-polar orientation and the (1×1) reconstruction for the N-polar InN layers. However, the atomic arrangements on the surfaces have been determined only by LEED and RHEED techniques so far.

Based on the theoretical calculations, it was predicted that the $[000\bar{1}]$ and [0001] orientated InN layers are always terminated by indium atoms, while a N-terminated structure showed to be unstable on both the N-polar and In-polar InN surfaces [70]. Formation of an In-adlayer on InN results in the presence of metallic indium surface states that lie above the CBM [75]. As a consequence, an electron accumulation layer is formed on the InN surfaces. The VB XPS studies of the In- and N-polar InN layers show presence of the surface electron accumulation on all investigated layers, in good agreement with theoretical prediction, indicating a formation of the metallic surface states of the InN surfaces due to the indium termination.

Theoretically predicted surface termination of the (1×1) N-polar InN layer by a single indium adlayer [75] correlates very well with the In/N ratio value of 1.15 ± 0.10 determined by AES for the MOVPE grown (1×1) N-polar InN layer (Fig. 6.9 (a)). It also explains observed higher amount of indium in the near-surface region of the layer. At the same time, the III/V ratio for the clean (1×1) InN layer calculated by XPS is 1.50 ± 0.05 that is higher compared to the value estimated from AES. This fact might be explained by the different information depths for AES and XPS measurements, different mean free paths of the detected electrons as well as an error of 20% for the quantitative analysis by AES. The surface sensitive XPS measurements (emission at 80° with respect to surface normal), however, are in better agreement with the AES results. Hence, AES and surface sensitive XPS measurements can be considered as more reliable for the determination of material stoichiometry in the near-surface region and show presence of the In-adlayer on the studied (1×1) N-polar InN layer.

The $(\sqrt{3}\times\sqrt{3})$ R$\pm30^\circ$ symmetry has been previously observed only on the group-III-polar InN [62], GaN [63] and InGaN layers [66]. This reconstruction is predicted to consist of indium adatoms located as depicted in Fig. 2.4 (c), resulting in 1/3 times more indium on the surface compared, for instance, to the cleavage surface. Similar arrangement of the atoms in the top-most layer is expected to take place on the studied N-polar $(\sqrt{3}\times\sqrt{3})$ R$\pm30^\circ$ reconstructed InN layer. The In/N value determined by AES and surface sensitive XPS measurements from this layer equals $\approx1.60\pm0.15$ that is 40 ± 10 % larger compared to the (1×1) N-polar InN surface. This observation in a good agreement with the 1/3 times more indium on the $(\sqrt{3}\times\sqrt{3})$ R$\pm30^\circ$ N-polar InN layer compared to the (1×1) N-polar InN surface. Hence, the investigated $(\sqrt{3}\times\sqrt{3})$ R$\pm30^\circ$ N-polar InN layer should consist of the In-adlayer, as in the case for

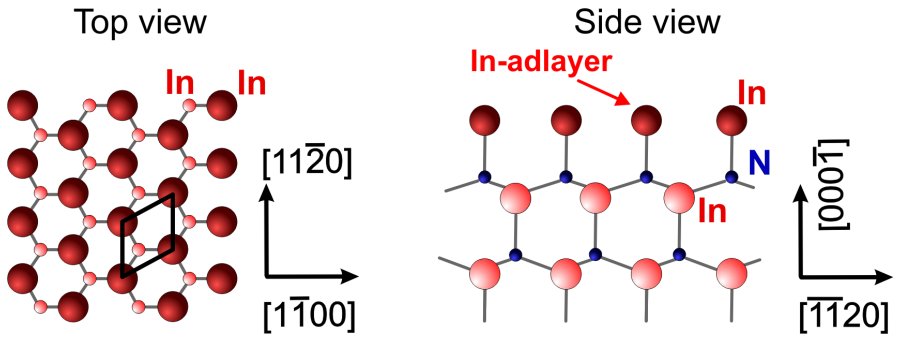

Figure 6.43: Model of the (1×1) N-polar InN layer terminated by indium adlayer (top and side view).

the (1×1) N-polar InN surface, with additional terminated indium adatoms which build the $(\sqrt{3}\times\sqrt{3})$ surface symmetry.

Excess of indium on the studied N-polar InN surfaces is responsible for the observation on the Fermi level edge ($E_F = 0$ eV) on the XPS spectra in Fig. 6.16. The Fermi edge is intrinsic for metals and is not expected to be detected on semiconductors, unless the studied semiconductor possess a metallic behavior. Therefore, presence of the Fermi level in the spectra corresponds to the metallic states on InN layers. Moreover, some surface states can be observed above the VBM for the MOVPE and rough MEAglow N-polar InN layers in form of a residual intensity in the spectra above the background level (Fig. 6.15 and Fig. 6.16). Although the surface states can be analyzed in details by UPS rather than by XPS, one can assume that the observed surface states in XPS spectra correspond to the indium metallic surface states, which lie above the VBM in agreement with the theory [75].

If assume that the $(\sqrt{3}\times\sqrt{3})$ R$\pm30^\circ$ and (1×1) N-polar InN layers are terminated by indium adlayer/adatoms, as was shown from the AES and XPS quantitative analysis, the indium atoms should be observed by STM. It is well-known that STM measurements enable observation of filled or empty electronic states depending on the applied polarity of the voltage. However, in the case of the strong surface downward band bending, when the Fermi level is pinned at the surface above the conduction band minimum, and with an applied negative sample voltage, the electrons from the valence-band and conduction-band states, will tunnel into empty states of a tip (so called accumulation current) [177]. Thus, independent from the applied polarity of the voltage, the STM will always image the conduction-band states. Since the *c*-plane InN layers exhibit a large band bending even for the clean surfaces, the aforementioned accumulation current will contribute during the STM measurements. As a result, it will not be possible to observe filled and empty state separately by switching the sample bias polarity. Indeed, during the STM measurements performed in this work on the N- and In-polar InN layers, a positive and negative applied voltages result in the same imaging of the surface.

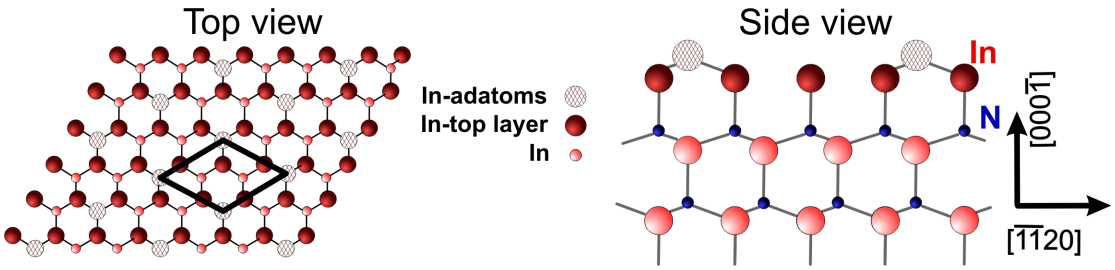

Figure 6.44: The stick-and-ball model of the $(\sqrt{3}\times\sqrt{3})$R$\pm$30° reconstructed N-polar InN layer (top and side views).

Since excess of indium was detected on the surface by XPS and AES, the atoms observed in STM images in Fig. 6.21 (a) must be associated with the indium atoms from the terminated In-adlayer. For the (1×1) N-polar InN layer, the atoms in Fig. 6.21 (a) are arranged in the way that they form a (1×1) reconstructed surface, as depicted in the model on the right-hand side of the STM image, where the distance between the atoms is equivalent to the *a*-lattice constant of InN (≈0.3 nm). Hence, previously determined only by LEED (1×1) InN surface reconstruction (Fig. 6.12 (a) and (b)) is for the first time confirmed by the atomically resolved STM image.

Based on the mentioned experimental techniques and discussions, the atomic model of the (1×1) N-polar InN surface is proposed to consist of the single terminated indium adlayer which covers the top-most nitrogen layer, as shown in Fig. 6.43 for the top and side view. This model and shown results are the first direct confirmation of the theoretically predicted (1×1) reconstructed N-polar InN layer [75]. Similar (1×1) reconstruction has been observed for the (1×1) N-polar GaN, as shown in Fig. 2.4 (a) [61].

Another model for the (1×1) N-polar InN layer was proposed by Veal et al., where they claim that InN surface is covered by ∼2 atomic layers (2 ML) of indium [40]. In their proposed model the top-most N monolayer of the N-polar InN is terminated by an indium adlayer which is covered by ∼2 ML of indium. Hence, in their proposed model the top-most nitrogen layer of N-polar InN layer is actually covered by indium trilayer. In the experiments discussed here such structure was not observed and would be in disagreement with the experimentally determined III/V ratio. The III/V ratios reported in the work of Veal et al. for the normal emission and emission at 60° with respect to surface normal are ∼1.75 and ∼2.6. These values are much higher compared to the one determined in this work for both the (1×1) and $(\sqrt{3}\times\sqrt{3})$R$\pm$30° reconstructed N-polar InN layers. A large III/V ratio observed in Ref. [40] can be explained by the formation of metallic indium clusters (droplets).Although the authors in Ref. [40] claim that they selected only the samples without indium droplets, the strong pronounced Fermi level edge with probably metallic surface states can be observed in the VB spectra (shown in Fig. 2.3 (a)) for all reported samples. Consequently, the model based on the (1×1) N-polar InN layer studied within this work by different experimental methods

provide more reliable results, which contradict with Ref. [40] but agrees with theoretical predictions [70].

Determined excess of indium on the $(\sqrt{3}\times\sqrt{3})$R$\pm$30° reconstructed N-polar InN layer indicates indium termination of the layer. Similar to the (1×1) InN surface, the electron density of states observed in the atomically resolved STM image in Fig. 6.26 (a) must correspond to the top-most indium atoms, which form the $(\sqrt{3}\times\sqrt{3})$ reconstruction rotated by 30°. As discussed previously, the distances between the recorded atoms of ≈0.68 nm are in good agreement with the $\sqrt{3}\cdot a$ that corresponds to the $(\sqrt{3}\times\sqrt{3})$ surface symmetry. Thus, the $(\sqrt{3}\times\sqrt{3})$R$\pm$30° reconstruction of the N-polar InN layer determined by LEED is for the first time confirmed by STM.

Based on the shown experimental results, the model for the $(\sqrt{3}\times\sqrt{3})$R$\pm$30° reconstructed surface for the first time observed on the N-polar InN surface is proposed. The top and side view of this stick-and-ball model is shown in Fig. 6.44. In the model, the top-most nitrogen monolayer is terminated by a single indium adlayer with additional indium adatoms located at T4 or H3 sites. The model is similar to the one for the $(\sqrt{3}\times\sqrt{3})$R$\pm$30° reconstructed In-polar InN layer proposed by Himmerlich et al. [62] (see Fig. 2.4 (c)).

The STS performed on both the (1×1) and the $(\sqrt{3}\times\sqrt{3})$R$\pm$30° reconstructed InN layers show surface metallicity caused by the metallic behavior of the In-terminated layers, in agreement with the aforementioned discussions. This fact also confirms that the structures observed in atomic-resolved STM images correspond to indium atoms.

It is important to emphasize that no N-O bonds were observed in the N 1*s* and O 1*s* core-level spectra for the studied N-polar InN layers. This is in agreement with the model, where the adsorbed oxygen atoms bond to the top-most layer consisted of indium adlayer/adatoms, resulting in the O-In and In-O-In bonds. Moreover, metallic In-In component has been observed in the In $3d_{5/2}$ core-level state only for the MOVPE grown (1×1) N-polar InN layer, where indium droplets were determined on the surface by XRD and AFM. Based on the proposed model for the MEAglow grown $(\sqrt{3}\times\sqrt{3})$R$\pm$30° N-polar InN layer, the metallic In-In bonds must also exist but the corresponding component was not observed by XPS probably due to a small amount of the In-In bonds which originate only from the $(\sqrt{3}\times\sqrt{3})$R$\pm$30° surface reconstruction. However, the In-C and In-In components may also overlap in the In $3d_{5/2}$ state and therefore, not being resolved.

As mentioned above, theoretical studies performed for the In-polar InN layers predicted an indium termination of these layer under all growth conditions [70, 71]. Indeed, this correlates good with the determined by XPS III/V = 2.17 ± 0.05 ratio of the studied (1×1) In-polar InN layer. The III/V ratio is significantly higher compared to the previously described (1×1) and $(\sqrt{3}\times\sqrt{3})$R$\pm$30° reconstructed N-polar InN layers, indicating higher amount of indium on the (1×1) In-polar InN surface.

Similar to the N-polar InN layers, no N-O component was observed in the N 1*s* or O 1*s* core-levels for the In-polar InN layer, while XPS analysis showed presence of the In-O and In-O-In chemical bonds on the surface. Thus, adsorbed oxygen atoms from

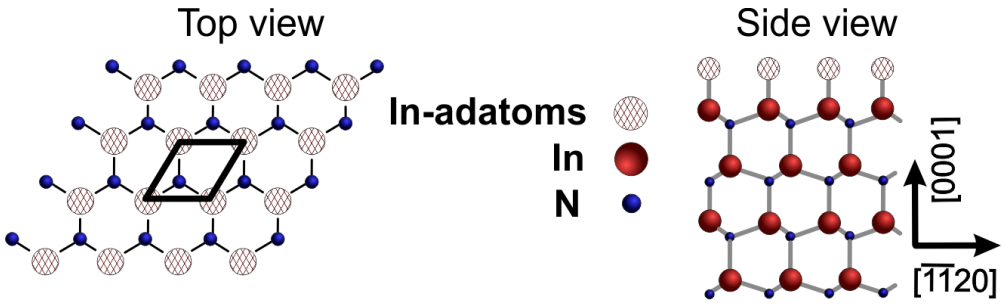

Figure 6.45: The top and side model view of the (1×1) In-polar InN layer.

ambient air bond to indium atoms that must terminate the surface in order to form In-O and In-O-In binding configurations.

The downward band bending of the (1×1) In-polar InN layer was determined from the position of the VBM in the XPS spectrum, while the I-V curve measured by STS showed metallic behavior of the studied InN surface. Hence, like in the case of the above discussed N-polar InN layers, the studied In-polar InN layer possesses surface electron accumulation caused by metallic surface states located above the conduction band, as discussed in Ref. [75] (see Fig. 2.5).

From the aforementioned results for the studied (1×1) In-polar InN layer, the layer is predicted to be indium terminated with a larger amount of indium of the surface compared to the N-polar layers. Thus, the atoms observed on the STM images in Fig. 6.41 (b) and (c) correspond to the top-most indium atoms that build the (1×1) surface symmetry, since the distances between the atoms equal the *a*-lattice constant of InN. These results confirm the (1×1) reconstruction of the In-polar InN layer observed by LEED.

For the In-polar InN layers grown under In-rich conditions, DFT studies showed two possible surface terminations: a contracted In-bilayer [70] or a trimer of In adatoms formed on T4 or H3-sites, corresponding to the 3/4 of indium ML [71]. For the moderate and N-rich conditions, the InN surfaces are predicted to be have the (2×2) T4 structure shown in Fig. 2.4 (b) [70] or a relaxed, unreconstructed In-terminated surface [71]. It is worth mentioning that according to Ref. [71] even at N-rich conditions formation of an In trimer yields the same energy as the (1×1) In-terminated surface, hence, In trimers can form even at N-rich conditions.

Formation of a metallic bilayer has been observed on the (0001) GaN layer, where the contracted Ga bilayer was formed above the Ga top-most layer, hence the first three layers of the surface consist of Ga atoms only. This Ga-bilayer resulted in the surface reconstruction known as pseudo "1×1" (also called 1+1/6) observed by LEED, where the main (1×1) reflexes are accompanied by six surrounded reflexes [61]. The nature of this layer is not fully understood and the structure is proposed to be dynamic, where Ga atoms rapidly move around [61]. The LEED patterns from the In-polar InN layer investigated in this work (Fig. 6.37) did not show any additional reflexes except the

(1×1), therefore, the assumption that the In-polar InN layer has the contracted indium bilayer on top is not appropriate. On the other side, it is also very unlikely that the top-most indium monolayer of the In-polar InN is terminated by In trimers in T4 or H3-sites, since this configuration would correspond to the 6 chemical bonds of a single indium atom, where three bonds are attached to the nitrogen atoms from the bottom layer and other three bonds are attached to the indium adatoms.

A formation of In adatoms on T4-sites has been observed on the (2×2) and ($\sqrt{3}\times\sqrt{3}$) R±30° reconstructed In-polar InN layers [62]. Moreover, Segev et al. predicted a stable (2×2) In_{T4} structure for In-polar InN grown under N-rich and moderate In/N ratio, where In-adatoms are formed at T4 and not at H3-sites. Therefore, similar assumption has been used for the model proposed in this work for the (1×1) In-polar InN layer, where the In adatoms are assumed to be located at T4-sites and terminate the In-polar InN layer by building the In-In bonds, as shown in Fig. 6.45.

The top and side view model of the (1×1) reconstructed In-polar InN layer with a sketched (1×1) hexagonal unit cell is shown in Fig. 6.45. The separation between the indium adatoms in this model corresponds to the *a*-lattice constant of InN and in good agreement with the distances determined from the atomic-resolved STM images (Fig. 6.41 (b) and (c)). In the side view image of the proposed model, the In adatoms are formed above the In top-most layer, resulting in overall 2 ML of indium on the (1×1) reconstructed In-polar InN layer. Indeed, the amount of indium for this layer is much higher compared to the studied N-polar InN layers. The assumed model is approximately in agreement with the III/V = 2.17 ± 0.05 ratio determined by XPS. An additional error bar in III/V values can come from the different mean free paths of the detected electrons and therefore, different escape depth for In and N atoms. The suggested model for the In-polar InN layer with the In-In bonds is in agreement with the In-In component observed in the In $3d_{5/2}$ core-level state. Since no metallic indium droplets were detected on the surface after etching, the metallic bonds can be associated with the bonds from the (1×1) surface reconstruction.

No reports could be found in the literature that experimentally describe in details the atomic arrangement of the (1×1) reconstructed In-polar InN layers. The evidence of the (1×1) In-polar InN surface reconstruction can be found only in the LEED patterns [31, 32, 67, 68]. However, experimental evidence and analysis of the exact bonding configurations of the In-terminated (1×1) In-polar InN layers and the number of indium monolayers on top-most layer have not been reported so far.

In the work of Veal et al., the suggested model for the In-polar InN layer consists of ∼ 3.4 ML of indium coverage, where the top-most layer consists of a laterally contracted and rotated 4/3 ML of indium with the ($\sqrt{3}\times\sqrt{3}$)R±30° periodicity [40, 69]. However, no other experimental groups have confirmed this model. Opposite, a single In adatom layer was suggested to be formed on the (2×2) and ($\sqrt{3}\times\sqrt{3}$)R±30° reconstructed In-polar InN layers [62]. The formation of almost 3.5 ML of indium on the In-polar InN surface is very unlikely. Instead of forming several metallic monolayers,

indium atoms would rather segregate into metallic droplets. Hence, based on the results presented in this work, the model suggested by Veal et al. could not be confirmed.

Moreover, the theoretically predicted unreconstructed In-terminated In-polar InN surface is also in contradiction with the results observed in this work. The LEED patterns of the investigated In-polar InN layer showed the small, pronounced and very sharp (1×1) reflexes (Fig. 6.37), indicating a well-arranged surface reconstruction with the (1×1) symmetry. Thus, in this work, the (1×1) In-polar InN layer is proposed to be terminated by an In adlayer, resulting in two indium layers in the top-most surface region, as sketched in the model in Fig. 6.45. Location of the indium adatoms at T4-site is in good agreement with the predicted stability of the indium adatoms on T4 site for (0001) InN layers [70].

6.4 Summary

In this chapter the surface reconstruction, morphology and electrical properties of the oxidized and clean N-polar and In-polar InN layers were analyzed in details under UHV conditions.

It was shown that two methods can be used for significant surface decontamination of the oxidized on ambient air polar InN layers: annealing at 450°C for 10 min under UHV conditions and annealing in nitrogen plasma by using nitrogen plasma source. Although both treatment are appropriate, annealing in nitrogen plasma lead to the higher reduction of carbon from the InN surface.

Investigations performed on the N- and In-polar InN layers showed that the different growth methods lead to the different surface topography. The smooth surface with pits and hillocks are grown on the N-polar layer by MOVPE, while the smooth and rough surfaces with 3D structures are grown on the N-polar InN layers by MEAglow technique. The In-polar InN layer grown by MBE exhibits the most smoothest surface among all studied layers and consists of the atomically pronounced terraces and screw dislocations on the surface.

The surface reconstructions of the polar InN layers determined by LEED showed formation of the (1×1) reconstructed surfaces on both the MBE grown In-polar and MOVPE grown N-polar InN layers. The $(\sqrt{3}\times\sqrt{3})$R$\pm30^\circ$ surface reconstruction on the MEAglow grown N-polar InN layer has been for the first time observed and analyzed on the $[000\bar{1}]$ InN crystal orientation.

All aforementioned InN surface reconstructions determined by LEED are for the first time confirmed by the atomically resolved STM images. Combination of several experimental techniques and the surface sensitivity of STM, XPS and AES enable to establish the surface atomic models of the studied layers with high accuracy. The (1×1) reconstructed In-polar InN layer is found to be terminated by the single In-adlayer resulting in the two indium atomic layers in the top-most surface region. The (1×1) reconstructed N-polar InN layer is terminated by the single In-adlayer, where the top-

most nitrogen atoms are terminated by indium atoms. The N-polar InN layer with the $(\sqrt{3}\times\sqrt{3})$R$\pm30^\circ$ symmetry consists of the In-adlayer partially terminated by indium adatoms, and has 1/3 times more indium on the surface compared to the (1×1) N-polar InN layer.

All studied oxidized and clean N- and In-polar InN layers posses the downward band bending and therefore, a surface electron accumulation. The clean In-polar InN layer has the strongest downward band bending compared to the studied N-polar InN layers, in good agreement with the previous report [30], where this observation was explained by the different position of the surface states for the In- and N-polar InN layers. The surface downward band bending increases (decreases) upon exposure of the investigated N-polar (In-polar) InN layers to ambient air. The electron accumulation layer is confirmed by STS on the clean polar InN layers, where the studied surfaces show a metallic behavior.

The N-polar InN layer grown by MOVPE showed better crystalline properties, compared to the MEAglow grown layers. However, the MOVPE grown InN layer was about three times thinner than the $\sim$300 nm thick InN layer grown by MEAglow. Despite of the pronounced polycrystalline structure of the MEAglow grown InN, these layers do not posses metallic indium droplets on the surface, unlike after the MOVPE growth. Thus, MEAglow growth technique can be considered as a good alternative method for the growth of InN layers. However, it is desirable to improve the MEAglow growth parameters in order to achieve a single crystalline structure of the N-polar InN layers.

7 Thermal Oxidation of the In-polar InN Layer

The effect of oxidation on the chemical and electrical properties of the In-polar InN layer has been shown in the previous section. The properties of the oxidized in ambient air layer and the subsequently decontaminated (clean) InN layer were analyzed in details and discussed. Water, oxide, carbon and their species will adsorb on the InN surface if the decontaminated under UHV conditions InN layer is again exposed to ambient air, resulting in the same properties as the oxidized layer studied at the beginning.

However, the surface properties of the InN layer might change if the layer is thermally annealed in ambient air. For instance, it has been reported that indium oxide is formed on InN layer upon annealing in ambient air or annealing in nitrogen and oxygen atmosphere [45, 178]. Moreover, it is well-known that crystal properties of InN layers degrade with exposure of the layers on air (oxidation time). Upon a longer exposure to ambient air, incorporation of oxygen and desorption of nitrogen occur on the InN surface resulting in formation of an indium oxide layer [130, 179]. Even during the MOVPE growth of InN layers, impurities, such as oxygen, carbon and hydrogen, may be incorporated into the crystal and result in a poor crystalline quality of the layer. Oxygen incorporation and formation of In_2O_3 crystal grains in InN layers were suggested to be the reasons for overestimation of the InN band gap [1, 45], where in the literature before year 2002 the band gap of InN was assumed to be 1.8-2.2 eV [43, 44]. Hence, surface oxidation plays an important role in the quality of the InN crystals and the oxidation effect and mechanism should be well understood.

In this chapter an effect of oxidation on ambient air and thermal oxidation of the In-polar InN layer will be compared. It will be shown that a thin, well-structures In_2O_3 crystalline layer can be grown on top of the InN layer after the thermal oxidation process. Experimental investigation of the formed In_2O_3 layer is important since this layer may serve, for instance, as a capping layer for InN material system. The properties of the In_2O_3 layer will be analyzed in details by XPS, AES and STM/STS techniques under UHV conditions.

7.1 Thermal Oxidation Process

Initially, an oxidized on ambient air In-polar InN layer was transferred in UHV chamber and annealed at 450°C for 10 minutes in nitrogen plasma, where at the same time the

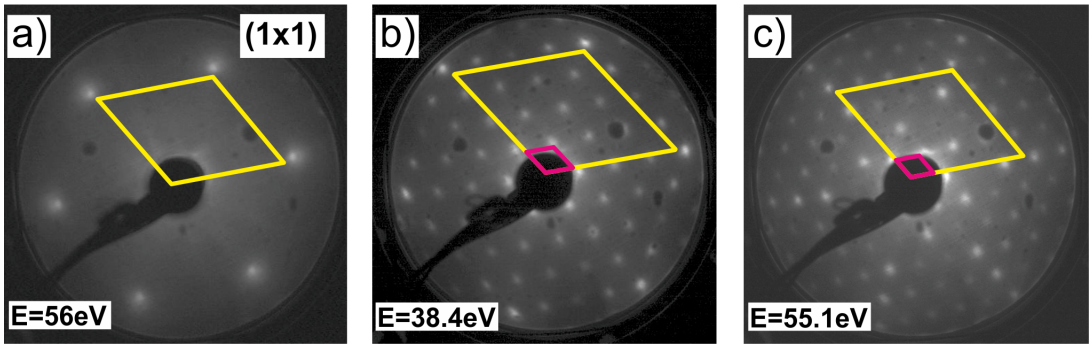

Figure 7.1: LEED diffraction patterns of a) the clean (1×1) reconstructed In-polar InN layer and after thermal oxidation of the In-polar InN layer recorded at b) 38.4 eV and c) 55.1 eV.

ambient air was applied into UHV chamber, so that an overall pressure in the chamber equaled $p \approx 1\cdot10^{-4}$ mbar. This led to the increase of the O-In-O (In-O-In) component in the In $3d_{5/2}$ (O $1s$) core-level state, corresponding to the formation of the indium oxide on the layer, as determined by XPS. In this case, the LEED measurements showed the (1×1) reflexes, similar to the one shown for the clean InN layer in Fig. 6.37. No changes in surface topography and morphology were observed. Hence, one can assume that the surface preparation under aforementioned conditions lead to formation of a thin amorphous indium oxide on the InN surface.

Afterwards, the In-polar InN layer was again annealed under the same conditions (thermal annealing in N* plasma and ambient air in the vacuum chamber), where simultaneously, the layer was exposed to an indium flux, evaporated from an MBE effusion cell. The sample temperature was kept constant at 450°C and overall pressure in the vacuum chamber was $p \approx 1\cdot10^{-4}$ mbar. The whole process was performed for ≈ 11 minutes that would correspond to the deposition of ~ 1 ML of In on the layer if neither InN nor In_2O_3 growth takes place. Further in this chapter, this process will be referred to "thermal oxidation" of InN, while exposure of the InN layer to ambient air at room temperature will be called "oxidation". Note that the term "surface oxidation" in this work implies an absorption of contaminations from ambient air, e.g. carbon, oxygen and hydrogen.

7.2 Surface Properties of the Thermally Oxidized In-polar InN Layer

The LEED measurements performed on the In-polar InN layer straight after the thermal oxidation shows a different diffraction pattern from what is observed on the clean layer. Fig. 6.37 (a) and (c) shows the LEED patterns recorded at near the same energy from the clean and thermally oxidized In-polar InN layer, where the (1×1) hexagonal unit cell is sketched in every image. For a better comparison, Fig. 7.1 (b) shows the LEED

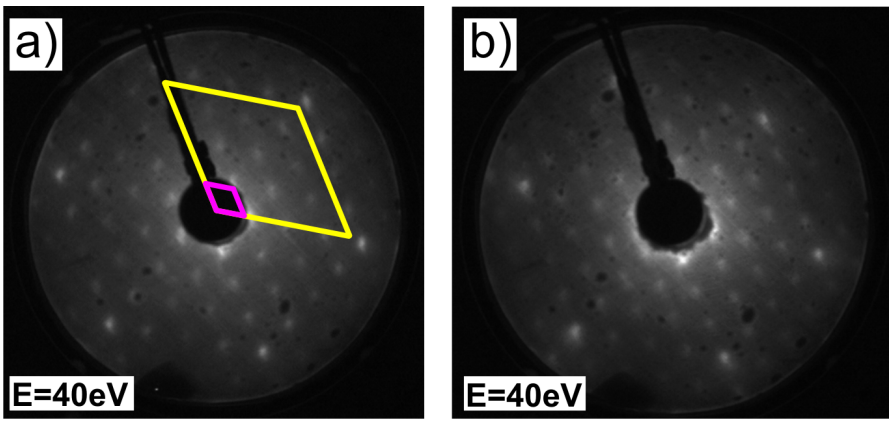

Figure 7.2: LEED diffraction patterns of the thermally oxidized In-polar InN layer after a) exposure to air and transfer in UHV chamber and b) after subsequent annealing of the layer at 450°C under UHV conditions.

pattern recorded from the thermally annealed InN layer at ~ 38 eV, where intensity of the diffraction spots is more intense and the LEED spots can be better distinguished. Besides the main reflexes that represent (1×1) reconstruction (sketched by large unit cell), the LEED patterns from the thermally annealed InN layers show additional reflexes that build similar to a (4×4) surface periodicity (sketched by small unit cell).

After exposure of the thermally oxidized InN layer to ambient air and further transfer it in UHV chamber, the observed surface periodicity remained unchanged as shown in Fig. 7.2 (a): reflexes that build (1×1) and (4×4) symmetry can be clearly observed even for the layer exposed to air without additional treatment. Subsequent annealing of the InN layer at 450°C under UHV conditions also does not affect the surface symmetry (see Fig. 7.2 (b)).

The qualitative analysis based on XPS measurements showed that upon thermal oxidation of the InN layer, the amount of oxygen on the surface increased by 3 times, while the amount of nitrogen decreased by 2 times compared to the clean InN layer. At the same time, the amount of indium on the surface increased by 15%-20%.

According to the shown results, one can assume that the thermal oxidation of the InN layer results either in oxygen induced reconstruction on the In-polar InN layer or in a heterogrowth of a new layer on top of InN, e.g. In_2O_3. If the obtained symmetry corresponds to the new reconstructed InN layer, the chemical bonds associated with the new reconstruction would be immediately affected by extrinsic atoms and molecules upon exposure of the layer to ambient air. As a result, the symmetry would be damaged and only surface preparation under the same conditions could restored the observed reconstruction. However, this is not the case and the observed surface reconstruction remained unaffected by ambient air. Thus, this is a direct indicator that the observed surface reconstruction corresponds to a new formed layer on top of the InN after the thermal oxidation process. According to determined stoichiometry, this layer may be

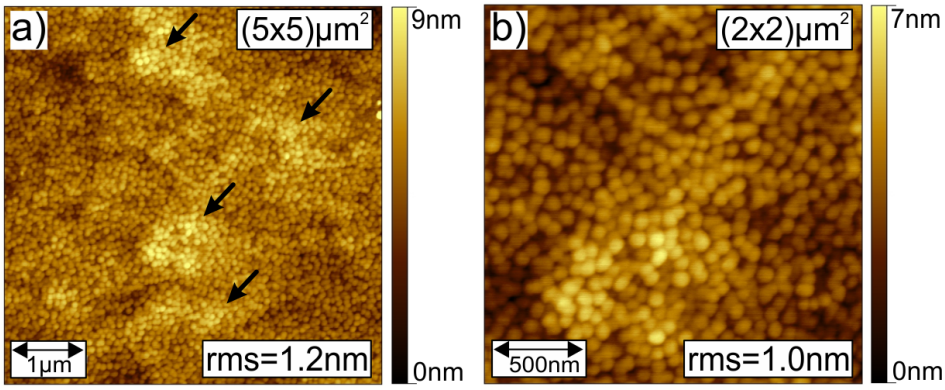

Figure 7.3: AFM topographic images of the In-polar InN layer after thermal oxidation recorded at the scales of a) $(5\times5)\,\mu m^2$ and b) $(2\times2)\,\mu m^2$. Sketched arrows correspond to the presumed positions of screw dislocations observed on the In-polar InN layer before the thermal oxidation.

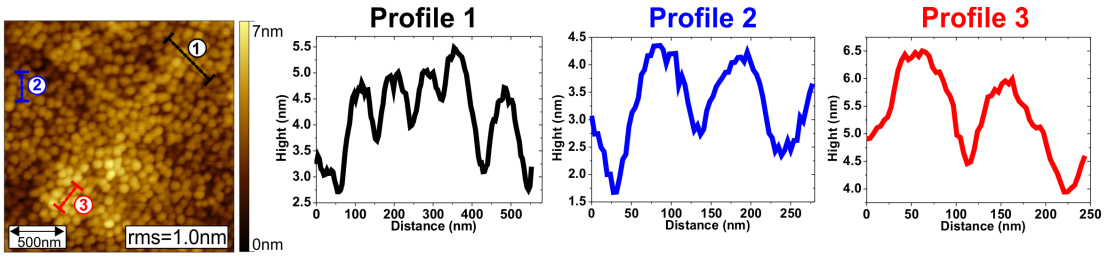

Figure 7.4: AFM topographic images of the thermal oxidized In-polar InN layer and profiles along the formed structures.

indium oxide (In_2O_3). Detailed investigation of this layer is important, since a thin layer on InN surface that is stable at ambient air may serve as a passivation (capping) layer.

The surface topography of the layer grown on top of InN was studied by AFM. As shown in Fig. 7.3, after the thermal oxidation the whole surface is covered by little grains. On the large scan area of $(5\times5)\,\mu m^2$ in Fig. 7.3 (a) it is still possible to distinguish a topography of the underlaying InN surface, e. g. the sketched arrows indicate the estimated top of screw dislocations observed on the InN layer before the thermal annealing (Fig. 6.28). The formed grains homogeneously cover the entire InN surface. Profiles taken along the grains in the AFM image recorded at $(2\times2)\,\mu m^2$ are shown in Fig. 7.4. The size of the grains varies from 70-120 nm, while the height of the grains is 0.6-2.1 nm. Hence, the grown layer is thin enough that the LEED diffraction patterns probably correspond to superposition of both the new layer observed by AFM and the InN surface underneath.

The topography and surface electrical properties of the grown layer on top of InN were studied by STM and STS. Fig. 7.5 (a) and (b) show the STM images of the layer over a large area ($(150\times150)\,nm^2$) recorded at two different spots of the sample. No

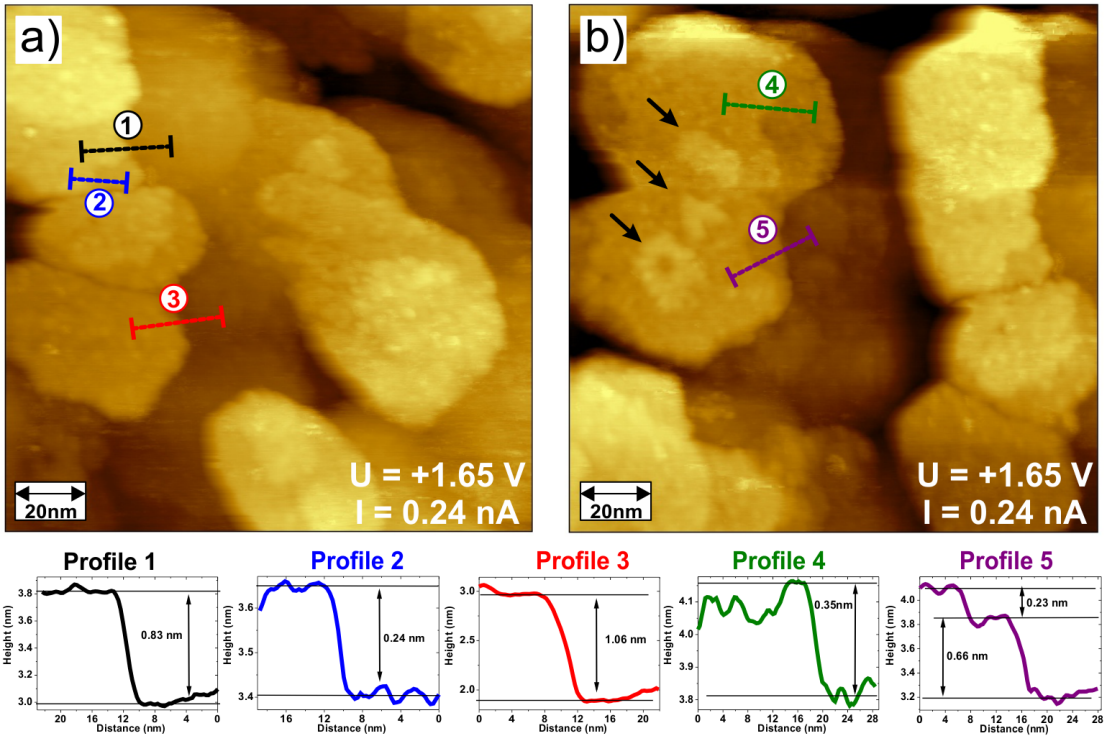

Figure 7.5: STM images taken at the area of (150×150) nm^2. The lines and numbers correspond to the line profiles shown underneath. Sketched arrows indicate the areas formed on the top-most layer.

screw dislocations accompanied by a terrace-like structure are observed on the STM images, as was shown for the clean InN layer prior to the thermal oxidation (Fig. 6.40). The new layer consists of the islands with flat surfaces, which were also observed by AFM. The size of the islands varies between 55 nm and 95 nm, in agreement with AFM. They have a prolonged shape and in some areas smoothly formed terraces of the layers can be clearly distinguished. It seems that layers grow homogeneously on top of each other. Fig. 7.5 (b) exhibits three small islands formed on the top layer of the crystal at left hand side (sketched by arrows). This might represent an initial growth step of the next layer on the surface, where the initially formed small islands coalesce with each other if a further growth is applied.

The line profiles along the edges of the formed terraces or islands (as sketched in STM images) were extracted and shown underneath in Fig. 7.5. The separation between two measured terraces determined from the entire sample shows no obvious arrangement or repeated order: majority of the layers were separated by 0.2-0.3 nm and 0.9-1.1 nm, however, the determined values also varied between 0.2 nm and 1.4 nm. The shown profiles are only several example of the overall extracted and analyzed profiles.

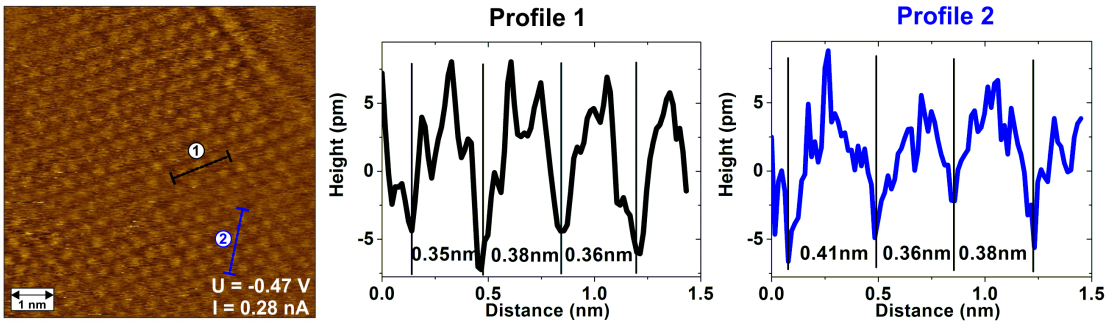

Figure 7.6: Atomically resolved STM image recorded at the area of $(7\times7)\,\mathrm{nm}^2$. The profiles correspond to the lines sketched in STM image.

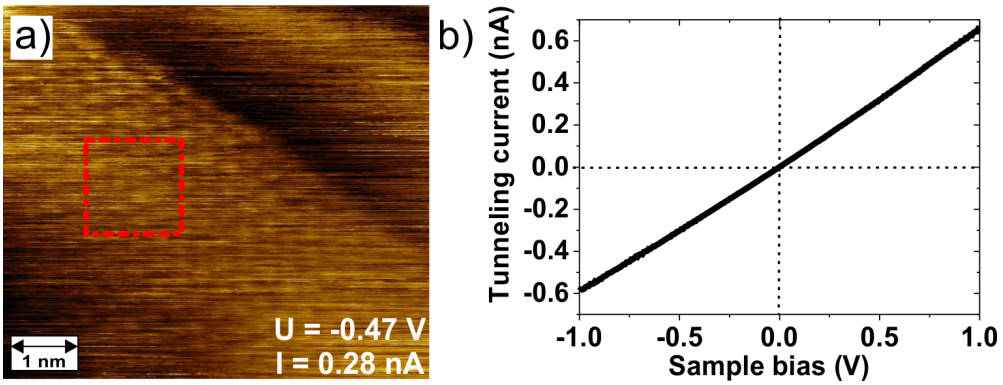

Figure 7.7: a) STM image with a sketched location, where the (15×15) points grid STS was performed, b) I-V curve corresponded to the average of the grid STS.

A closer look at the area of the formed islands revealed an atomically smooth surface as shown in a STM image recorded at $(7\times7)\,\mathrm{nm}^2$, Fig. 7.6. STM shows an atomically resolved image, where a last line at the right top corner of the image corresponds to the edge of the terrace. The profile 1 shows the separation between resolved structures along chosen direction of about 0.36 ± 0.03 nm, that is comparable to the separation along the direction shown for the profile line 2.

A (15×15) points grid spectroscopy was acquired in a $(1.2\times1.2)\,\mathrm{nm}^2$ area, which is sketched in the atomically resolved STM image in Fig. 7.7 (a). As a result, 225 I-V curves were recorded from this area. Fig. 7.7 (b) shows the average over all these curves. The STS measurements exhibit a strong metallic behavior of the surface, where the I-V curve has a linear tendency across the whole applied bias from -1 V to +1 V, different to the behavior observed on the clean InN layer in Fig. 6.42.

X-ray photoelectron analysis was performed on the thermally oxidized InN layer in order to investigate the chemical binding configurations of the grown on top layer. XPS was performed straight after the thermal oxidation of the layer prior to its exposure to ambient air. For comparison, Fig. 7.8 shows an XPS spectra recorded at normal

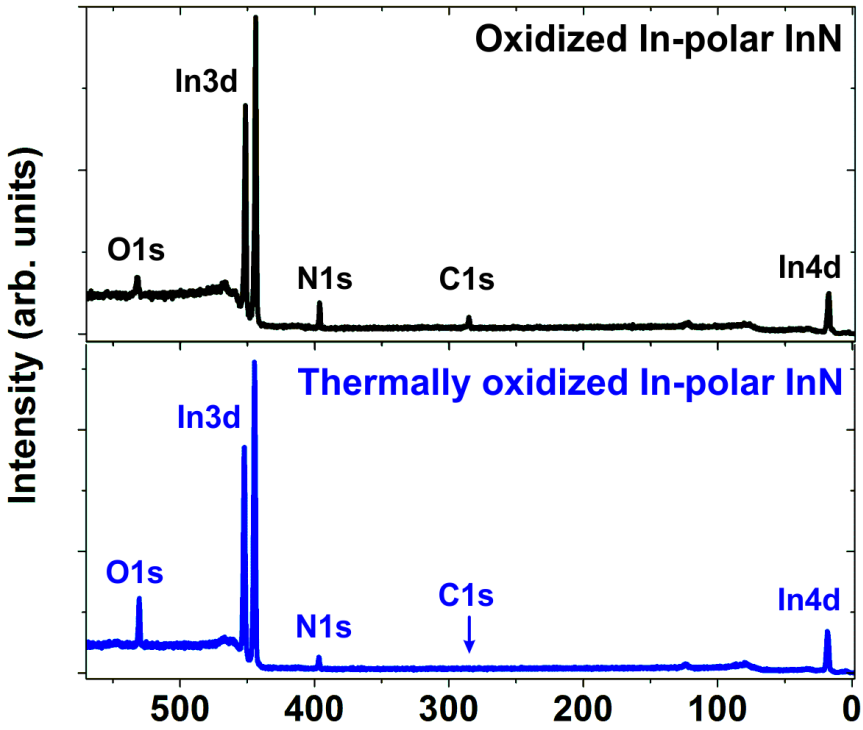

Figure 7.8: The wide range XPS spectra of investigated In-polar InN layer recorded at normal emission from the oxidized layer (i.e. exposure to ambient air) and thermally oxidized layer (i.e. annealing at 450°C for 12 min in N_2 and ambient air with simultaneous deposition of indium). Each emission line corresponds to the core-level electron labeled in the image.

emission from the wide range of binding energies, i.e. 0 eV-600 eV, for the oxidized and thermally oxidized In-polar InN layer. Each emission line (peak) in the spectrum corresponds to the core-level electron state, as labeled in the image.

The XPS spectrum from the thermally oxidized InN layer shows identical core-level emission lines as for the oxidized layer, except the C 1*s* core-level, which was completely desorbed from the surface upon the treatment. No undesirable impurities and elements were detected on the studied surfaces. Upon the thermal oxidation, intensity of the N 1*s* decreases, while intensity of the O 1*s* significantly increases.

The numerically fitted N 1*s*, In $3d_{5/2}$ and O 1*s* core-level emission lines from the thermally oxidized In-polar InN layer are shown in Fig. 7.9 for the measurements recorded at normal emission and emission at 80° with respect to surface normal. The same components observed on the clean and oxidized In-polar InN layer can be found for the thermally oxidized InN layer. As shown by STM, the layer overgrown on InN possesses a strong metallic behavior, therefore, the asymmetric fitting parameters were used for all studied core-levels. All fit parameters can be found in the Appendix B.

The In 3*d* peak is now dominated by the O-In-O component, associated with the formed indium oxide, while intensity of the bulk In-N component significantly de-

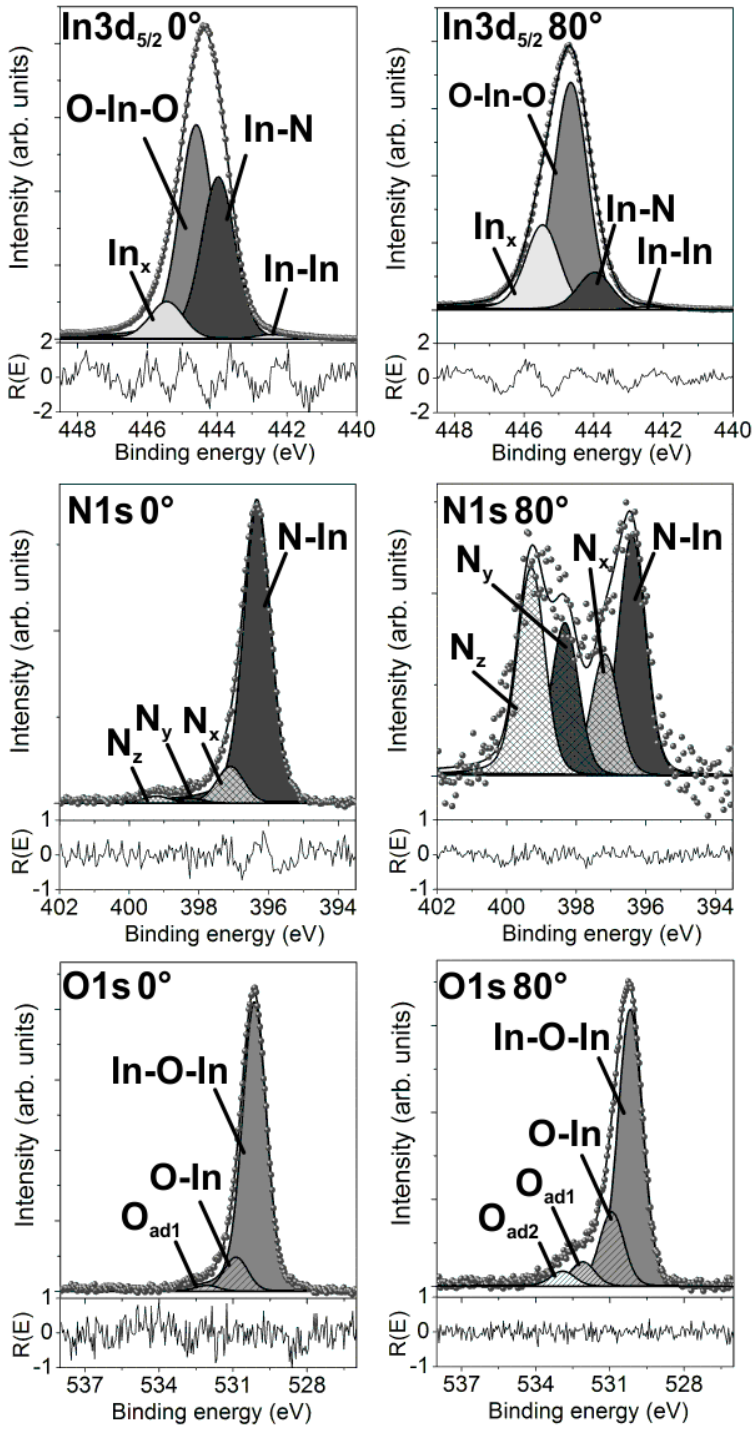

Figure 7.9: The N 1*s*, In 3*d* and O 1*s* core-levels recorded from thermally oxidized In-polar InN layer at normal emission (0°) and emission at 80° with respect to surface normal.

creases, particularly at the very surface region, as shown for the measurement at 80°. The intensity of the In_x component significantly increases after the thermal oxidation compared to the clean layer (see Fig. 6.38), indicating the connection between this component with the surface contaminations which may adsorb on the surface from ambient air. The In-In component is again strongly required in order to achieve a good residual spectrum, corresponding to the presence of the metallic In-In bonds on the surface approximately in the same amount as for the clean InN layer.

The O-In-O component in the In 3*d* peak lies 0.6 eV higher in binding energies than the bulk In-N component. This separation is slightly lower compared to the clean and oxidized In-polar InN surfaces. The In_x component is now shifted by 1.5 eV towards higher binding energies compared to In-N, which is 0.3 eV less than for the oxidized and clean InN layer. The different shifts of the O-In-O and In_x components may be explained by a new binding configurations of the atoms on the surface, i.e. chemical shifts. This is in agreement with the observation, since a crystalline layer is grown on the InN surface upon the thermal oxidation, while formation of the amorphous In_2O_3 layer was assumed in the case of the oxidized InN surface.

The N 1*s* core-level shown in Fig. 7.9 has a significantly lower intensity compared to the clean InN layer but remains still visible for the normal emission measurement, while the peak intensity is very low for the emission at 80°. Thus, nitrogen is almost vanished from the near surface region, where the N-In component at 396.3 eV becomes comparable with the N_x, N_y and N_z components located at higher binding energies. The intensity of the N_x component assigned to the absorption of contaminations on nitrogen defects is comparable to the case of the oxidized InN layer. As was described for the clean InN layer, the components at higher binding energies (N_y and N_z) most likely correspond to the nitrogen species or nitrogen defects produced by N-plasma source on the surface. This can explain the appearance of the N_y and N_z components in the N 1*s* peak compared to the oxidized InN layer (Fig. 6.29), since in this case the N-plasma was applied during the growth of the heterolayer on top of the InN surface. The N-In component of the N 1*s* state at 396.3 eV is in good agreement with the literature, where the same chemical bond was detected at 397 eV [165] or at 396.5 eV [166], measured on an InN layer.

The intensity of the O 1*s* core-level for the thermally oxidized InN surface increases drastically compared to the clean or oxidized InN layer. The O 1*s* core-level mainly consists of the component labeled as In-O-In. Note that such significant domination of only one component was not observed for the oxidized InN layer, as shown in Fig. 6.29. The In-O-In component is attributed to the O-In-O component in the In 3*d* peak and refers to the indium oxide. This indicates that the In_2O_3 layer is formed on the InN surface upon the thermal oxidation. Additionally, the O 1*s* core-level exhibits a shoulder at higher binding energy side that fits well with the O-In component and physisorbed oxygen species, labeled as the O_{ad1} and O_{ad2} components, which predominate in the surface region. The origin of the O-In, O_{ad1} and O_{ad2} components is the same as described for the oxidized In-polar InN layer in Sec. 6.2.1.

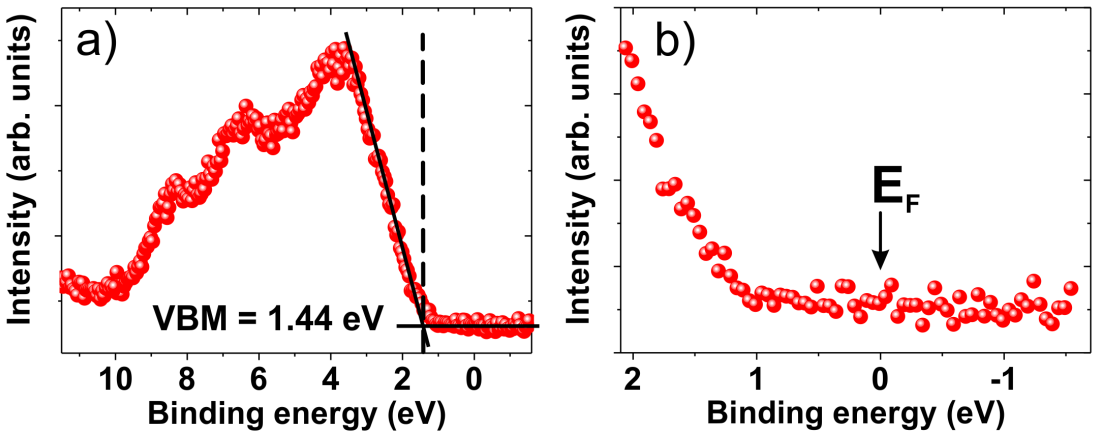

Figure 7.10: a) VB spectrum and b) photoemission near the Fermi level recorded from the thermally oxidized InN layer at normal emission.

Since intensities of the O-In, O_{ad1} and O_{ad2} components of the O 1*s* core-level shown in Fig. 7.9 significantly decrease compared to the oxidized InN layer, neither the In_x nor the N_x component from the In 3*d* and N 1*s* peaks, respectively, can be assigned to the chemical bond with oxygen atoms. Hence, it confirms the previous assumption that the In_x and N_x components are assigned to defects or chemical bonds with complex contamination species.

The VB spectrum recorded from the thermally oxidized InN layer at normal emission is shown in Fig. 7.10 (a) and exhibits three pronounced peaks: at ≈3.7 eV, ≈6.4 eV and ≈8.3 eV. For comparison, the peaks observed in the VB structure for the oxidized and clean InN layer (as shown in Fig. 6.30 (a) and Fig. 6.39 (a), respectively) are located at ≈2.9 eV and ≈6.7 eV. Therefore, the observed VB structure rather corresponds to the new grown layer on top of InN surface (In_2O_3). However, since the bulk In-N components of the InN layer are still observed in the recorded core-level states at normal emission, the VB must also contain a partial contribution of the InN layer.

Thus, the determined position of the VBM = 1.44 ± 0.05 eV corresponds to the In_2O_3/InN heterostructure. The VBM value is 0.09 eV higher compared to the clean In-polar InN layer and 0.16 eV higher compared to the oxidized In-polar InN layer. The photoemission near the Fermi level in Fig. 7.10 (b) shows no pronounced Fermi edge at 0 eV. Although some surface states can be observed below VBM in Fig. 7.10 (a), no highly pronounced metallic surface states can be observed near the Fermi edge in Fig. 7.10 (b), as was the case for the N-polar InN layer (see Fig. 6.16 (a) and (c)). According to this observation, no indium surface segregation (for example in form of indium droplets) took place during the thermal oxidation process of the In-polar InN layer. This is in agreement with AFM, where no indium droplets were detected.

The AES measurements were performed on the thermally oxidized In-polar InN layer. However, since the thermal oxidation was performed in a different vacuum chamber

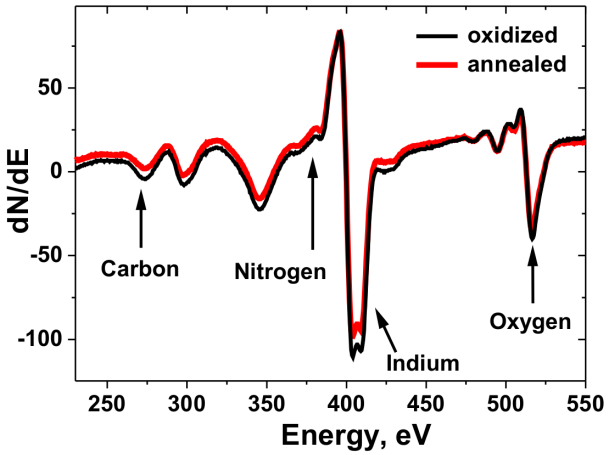

Figure 7.11: AES spectra of the thermally annealed InN layer after its exposure to air (black thin line) and subsequent annealing at 450°C (thick red line).

from the one with the AES equipment, the thermally oxidized InN layer had to be shortly exposed to ambient air and transferred into the UHV chamber equipped by AES. Afterwards, the investigated layer was annealed at 450°C for 10 minutes under UHV conditions in order to desorb surface contaminations adsorbed on the surface from the air. As shown by LEED in Fig. 7.2, the aforementioned procedure did not affect the reconstruction observed in the LEED diffraction patterns.

Fig. 7.11 shows the AES spectra for the thermally oxidized In-polar InN layer after its expose to ambient air and subsequent annealing at 450°C. Compared to the measurements performed by XPS directly after the thermal oxidation, a small amount of carbon contamination was detected on the investigated surface after it was exposed to air. Annealing at 450°C under UHV conditions led to only slight desorption of carbon from the surface. However, despite the residual contamination, the LEED pattern showed the nicely ordered surface, as was shown in Fig. 7.2 (b). Note that AES showed no clear evidence of the nitrogen species on the surface, while indium and oxygen Auger peaks predominate the spectra. Since AES has a higher surface sensitivity than XPS, absence of nitrogen on the surface confirms the assumption that the thermal oxidation of InN layer led to formation of a thin In_2O_3 layer.

7.3 Discussion

The presented results obtained by different characterization techniques show the formation of a heteroepitaxial layer on top of an In-polar InN layer upon its thermal oxidation. The chemical analysis performed by AES and XPS suggest that the formed layer is a crystalline In_2O_3. Indeed, the N species were not detected on the surface by AES, while the In and O were observed in significant amounts. Similar results were obtained by XPS, where the bulk N-In component in the N 1*s* peak was observed only for the normal emission measurements and almost vanished for the measurements at 80°. The O 1*s* and In 3*d* core-levels were dominated by In-O-In (or O-In-O) components that

correspond to the chemical bonds between indium and oxygen atoms in indium oxide crystal structure.

The XPS surface sensitive measurements (emission at 80°) performed on the In_2O_3 showed presence of nitrogen in the near surface region of about 6%, if the sum of oxygen, indium, and nitrogen atoms is considered as 100% of material (Fig. 7.9). An information depth for this measurement is approximately < 1.7 nm, which would mean that the thickness of the deposited layer should be below 1.7 nm. Nitrogen species were not detected by AES, where secondary electron escape depth is 0.5-2 nm. Taking into account the highest height of terraces determined by STM (1.4 nm), one can conclude that the deposited In_2O_3 layer has a thickness of 1.4 ± 0.3 nm. Hence, 10 min of the thermal oxidation of InN layer led to a formation of the thin In_2O_3 layer. In_2O_3 is known to be a direct band gap semiconductor with the band gap of 2.7 - 2.9 eV [180, 181].

A growth of the (111) orientated In_2O_3 layer on polar InN upon thermal oxidation has been also observed previously [45,182,183]. Even an oppositely-grown heterostructure, i.e. InN grown on In_2O_3, has been obtained [184]. Lee et al. have shown that the thermal annealing in air of InN leads to its oxidation into In_2O_3 [178]. They have shown that the oxidation process of InN starts at annealing temperature of 450°C, which is in good agreement with the results shown here. A complete oxidation of an InN layer to In_2O_3 was found to take place at the annealing in air at 850°C for 20 minutes [179].

A supply of indium atoms during thermal oxidation seems to play an important role in the formation of In_2O_3 layer. In the work of Yodo et al. it has been shown that indium droplets formed on the InN layer upon the annealing above 400°C have a higher reactivity with oxygen atoms than the InN layer itself [45]. They showed that metallic indium droplets transform more easily into the (111) oriented In_2O_3 crystal grains by thermal annealing in N_2 mixed with O_2 atmosphere.

The In-polar InN layer in the present work was annealed in N_2 and ambient air that contains oxygen, similar to Ref. [45, 179], however, a supply of metallic indium in the carried out experiments was performed by deposition of indium from the MBE effusion cell and not by formation of indium droplets on the surface. One can assume that upon performed thermal oxidation, the residual amorphous In_2O_3 layer remained after initial cleaning of the In-polar InN by N-plasma serves for the growth of the crystallite In_2O_3 layer, when a metallic indium is supplied.

Most of the papers in the literature report about the properties of 50 nm-1 μm thick In_2O_3 layers grown on top of InN surfaces [182,183,185]. In the work of Lebedev et al., besides a thick MOVPE grown indium oxide layer on InN, also the $\sim$11 Å thick In_2O_3 layer was grown by an oxidation procedure of InN layer in N_2, O_2 and O_3 gases [185]. However, this process required several hours. which is very time consuming compared to the $\sim$10 min thermal oxidation performed in this work. Also, in Ref. [185] not much was shown about the surface morphology, topography and quality of the grown thin In_2O_3 layer. Therefore, results presented here are important in order to understand the

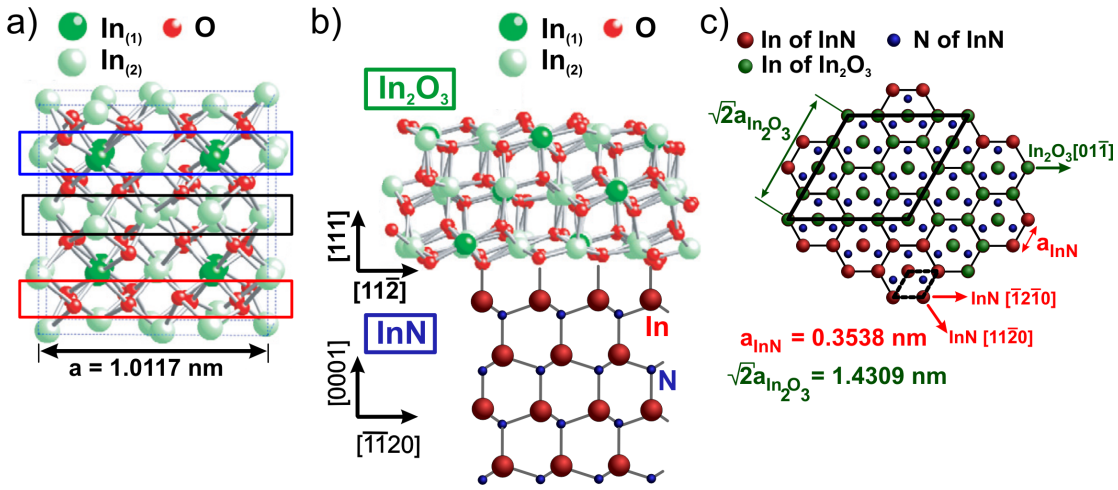

Figure 7.12: a) Unit cell of In_2O_3 bixbyite structure [186]. Sketched rectangles correspond to different type of layers as described in the text. b) Side view of the (111) oriented In_2O_3 grown on In-polar InN (adopted from [186]). c) Atomic arrangement of the (111) In_2O_3/(0001) InN (top view) with sketched unit cells of In_2O_3 (solid line) and InN (dashed line) [183].

properties of the very thin In_2O_3 layers, which may serve as a capping layer for InN surfaces.

The In_2O_3 is known to crystalize into the body-centered cubic (bcc) bixbyite structure with a lattice parameter a of 1.0117 nm [187]. The bixbyite structure can be formed if 12 oxygen atoms are removed from the unit cell. A cubic unit cell of this structure is represented in Fig. 7.12 (a). The unit cell consists of 32 indium atoms and 48 oxygen atoms – 80 atoms in total. Indium atoms in the structure can have two different positions depending on the crystal symmetry: so-called In-b (dark green, labeled as $In_{(1)}$) and In-d atoms (light green, labeled as $In_{(2)}$). There are 24 In-d atoms per unit cell that have higher asymmetry in their coordination, while there are only 8 In-b atoms per unit cell, which are axially symmetrically coordinated. Along the (001) direction, three different layers can be observed in the crystal structure as shown in Fig. 7.12 (a): a layer consisting of In-b and In-d atoms (mixed layer, labeled by blue rectangle in Fig. 7.12 (a)), a layer consisting only of In-d atoms (labeled by black rectangle), and a layer of oxygen atoms (labeled by red rectangle).

Due to the bixbyite structure of In_2O_3, the atomic arrangement on the (111) orientated surface has only a small mismatch with the (0001) InN. The unit cell of the (111) surface is $\sqrt{2}\cdot a_{In_2O_3} = 1.431$ nm correlates well by a factor of 4 with the (0001) InN layer $4\cdot a_{InN} = 4\cdot 0.354$ nm $= 1.416$ nm. The lattice mismatch is only $\approx 1\%$ in the (111) crystallographic plane [183]. Although the crystal lattice of InN matches indium oxide only at higher periodicity (times four), the bixbyite crystal structure reduces this periodicity: three additional atoms are located on the $\sqrt{2}\cdot a_{In_2O_3}$ unit cell side between the main atoms, as marked by blue circles in the top-view image of the

(111)In_2O_3/(0001)InN structure in Fig. 7.12 (c). This matches the crystalline structure of the underneath laying InN layer and allows the growth of the (111) In_2O_3 layer directly on top of the (0001) InN layer.

Such a crystalline structure of the (111)In_2O_3/(0001)InN explains observed by LEED surface reconstruction in Fig. 7.1 that at first glance can be incorrectly interpreted as (4×4) symmetry of InN layer. In fact, the reconstruction shown in LEED originates from the (1×1) termination of the crystalline (111) In_2O_3 layer, in good agreement with Ref. [186, 188]. Moreover, the bixbyite (111)In_2O_3 crystal lattice clarifies the observed structures in the atomically resolved STM images (Fig. 7.6). The determined distances between the observed features in STM images are 0.36 ± 0.03 nm, which correlates well with the fourth of the (111) In_2O_3 unit cell: $1/4 \cdot \sqrt{2} \cdot a_{In_2O_3}$=1/4·1.431nm=0.358nm. Hence, the STM images show the atoms of the (111) In_2O_3 layer, which build a well-ordered $(1\times1)_{In_2O_3}$ surface reconstruction on the atomically flat islands observed by AFM and STM on the large scanning areas.

A side view of the (111)In_2O_3/(0001)InN model is shown in Fig. 7.12 (b), where the top-most terminated indium atoms of the InN layer are bonded to the O-layer of the bixbyite In_2O_3. Due to cation and anion nature of indium and oxygen atoms, respectively, it is unlikely that indium atoms of the InN would bond to the indium atoms of the In_2O_3. The proposed model of the In-polar InN layer in Fig. 6.45 includes 2 ML of indium on top of the layer, however, due to the complex surface chemical reactions and kinetics upon the thermal oxidation procedure and higher reactivity of oxygen with metallic indium [45], the indium adlayer of InN may react with oxygen and be reformed into indium oxide.

The chemical analysis performed by XPS, i.e. line shapes of the recorded core-levels, their numerical fit, is in good agreement with the literature reports for In_2O_3 layers. Based on the literature, the In-O bonds in the In 3*d* state originating from amorphous and crystalline indium oxide layers have very similar binding energies, which fluctuate by 0.5 eV for different publications. The In-N and In-O components in the In 3*d* core-level in Ref. [165, 166] were attributed to InN and amorphous indium oxide In_2O_3 formed upon exposure of InN to air, respectively. In the reported work, the In-O components were shifted by 1.0 eV towards higher binding energies compared to the bulk In-N component and exhibit binding energies of 444.7 eV for Ref. [165] and 445.0 eV for Ref. [166]. In the case of a crystalline In_2O_3 layer, the In-O component in the In 3*d* lays at 443.9 - 444.4 eV ([186, 189]), which is a bit lower compared to the amorphous state. Moreover, it was shown that the peak position strongly depended on the surface stoichiometry, i.e. position of the In 3*d* peak by 0.6 eV lower binding energies for the oxidized surface compared to the reduced surface [189]. In this work, the corresponded component in the In 3*d* peak was labeled as O-In-O, and was shifted by 0.9 eV towards higher binding energies compared to the bulk In-N component for the amorphous In_2O_3 layer which was formed on oxidized InN layer after its exposure to ambient air (O-In-O binding energy equals 443.7 eV). This is in good agreement with the literature reports. The chemical shift by 0.3 eV towards lower binding energies of the In-O-In component

compared to the In-N component has been observed after the formation of the crystallized In_2O_3 layer (O-In-O binding energy equals 444.5 eV), indicating changes in chemical environment between the atoms.

The shoulders at higher binding energies in the In 3*d* and O 1*s* core-level states (see Fig. 7.9) have been also observed by XPS study of Sn-doped In_2O_3 thin films [186,190]. In these studies the shoulders were fitted with one or two components and assigned to the plasmons: interaction between inelastic scattered electrons and electrons in the *s*-like conduction band that leads to creation of plasmons. It was assumed that the plasmon frequency is small (≤ 1 eV), since the electron density in the electron gas is lower than in bulk [190]. In this work, the shoulder at higher binding energies in the In 3*d* core-level was fitted by the component labeled as In_x (Fig. 7.9). The direct correlation between the In_x component and the amount of surface contaminations has been observed and therefore, in this work, the In_x component is not assigned to the plasmon effects.

The plasmon contribution to the XPS spectra was not observed in the O 1*s* core-levels either. The component labeled as O-In in the O 1*s* state (Fig. 7.9) is shifted by 1.9 eV towards higher binding energies compared to the In-O-In component assigned to the In_2O_3 layer. Similar component in the O 1*s* core-level shifted by ca. 2 eV towards higher binding energies was also observed in Ref. [165, 166] and attributed to the physisorbed oxygen on the InN surface, as well as in Ref. [189], where it was attributed to the presence of peroxide species on the surface (a compound with an oxygen-oxygen single bond). Hence, it is in good agreement with the assumption that the O-In component corresponds to the physisorbed oxygen on the surface, e.g. adsorbed oxygen atom on the indium terminated atom of the layer.

The VB features (peaks) observed in the spectrum in Fig. 7.10 (a) correlate well with the shoulders observed in the XPS spectra from a In_2O_3 single crystal and thin layer at about 4 eV, 6.2 eV and 8.5 eV [181, 189, 191]. The VB of In_2O_3 is dominated by O 2*p* states with a small contribution from the In 5*s* [192]. In the study of Hagleitner et al., it was shown that the peak at around 8.5 eV originates from the surface region and according to theoretical calculations was assigned mainly to the In 5*s* states [189]. As mentioned previously, the recorded VB spectrum in Fig. 7.10 (a) is attributed to both the In_2O_3 layer and underneath laying InN layer. Therefore, the VBM position is affected by a In_2O_3/InN heterostructure and determination of the VBM offset at this heterojunction requires reference measurements on the InN and In_2O_3 layers separately [170], which could not be performed in this work due to the low thickness of the In_2O_3 layer. Hence, no prediction concerning the surface band bending can be established in this case.

Depending on the surface termination and crystal orientation of In_2O_3, a downward and upward band bending have been observed on the layers, as reported in the literature. In the work of Hagleitner et al., the downward band bending has been detected on the oxygen reduced (001) In_2O_3 surface of a single crystal, while a slight upward bend banding occurs at the oxidized layer [189]. For the (100) orientated In_2O_3 thin layer,

the position of the VBM was estimated to be 2.90 ± 0.05eV below the Fermi level, indicating a downward band bending on the surface [181]. Moreover, a well-defined peak near the Fermi level can be found in the literature [180, 181, 189, 191]. Some reports associate this peak with the half-filled In 5*s* metallic gap states that should have an acceptor behavior and lead to the upward band bending [189, 192]. Other reports assign this peak to the occupied conduction band states [180, 189, 191], where due to the electron accumulation and a low position of the conduction band minimum at the Γ-point, the Fermi level is pinned at 0.4 eV above the conduction band minimum [193]. However, no peak near the Fermi edge was observed in the measurements shown in Fig. 7.10 (b), which could be due to the very thin In_2O_3 layer. Nevertheless, this is an indicator for the absence of metallic indium states (e.g. droplets) on the surface upon performed thermal oxidation of the InN surface.

Surface structure of In_2O_3, i.e. termination, stoichiometry, thermodynamic stability, has been theoretically studied by Agoston et al. using the density functional theory calculations [192]. In his work it was shown that In_2O_3 surfaces can be oxidized or reduced, due to the formed oxygen vacancies that result in the lack of oxygen on the surface. Based on the theoretical results it was shown that oxygen vacancies are much more easily formed on the In_2O_3 layers with (011) and (111) orientations. As a result, oxygen vacancies accumulate on the (111) In_2O_3 layer, resulting in the reduced surface. This provides an excess of positive surface charge, since oxygen vacancies are known to be donors. At the same time, a higher donor concentration in the surface-like region leads to an electron accumulation layer in the material. In this work, determination of the In_2O_3 surface stoichiometry was performed according to the In/O ratio determined by XPS and AES.

Assuming an ideal crystal structure of In_2O_3, the In/O ratio is expected to be $2/3 \approx 0.67$. However, based on the quantitative AES analysis, the In/O ratio equals 1.45 ± 0.30 for the studied layer. A higher amount of indium on the surface was also observed by XPS, where the In/O ratio was found to be 1.76 ± 0.05 and 1.17 ± 0.05 for the measurements at normal emission and emission of 80°, respectively. However, the signal in XPS measurements refers to both the grown In_2O_3 layer and the InN layer, especially for normal emission measurements. A large error bar for the AES measurements and only small contribution of the InN layer in the XPS signal for the measurements at 80°, results in the assumption that the correct In/O ratio is slightly above one, indicating excess of indium atoms on the surface. One may assume that the In_2O_3 is terminated by indium atoms, similar to the N-polar InN layer, resulting in the surface accumulation layer. However, it is difficult to determine exactly if the In_2O_3 is terminated by one or more indium monolayer. The presence of the electron accumulation layer is in agreement with the work of Agoston et al., where surface accumulation is theoretically predicted on the oxygen reduced surface [192].

The surface electron accumulation on the grown In_2O_3 layer would explain a strong metallic behavior observed by STS (Fig. 7.7). There are not many reports on STS study of In_2O_3 layers, probably due to the presence of the electron accumulation layer.

An STS performed on the (001) In_2O_3 single crystal showed a clear metallic behavior of the surface [189], although not as strong as in the presented work. The significant excess of indium on the investigated In_2O_3 surface that causes surface metallicity, may be explained by the thermal oxidation conditions, where indium was directly supplied from the effusion cell. It seems that the thermal oxidation was performed under In-rich conditions and requires further improvement in order to reduce amount of indium on the formed In_2O_3 surface.

Moreover, behavior of the I-V curves in STS spectra may be affected by a usually observed high conductivity of the undoped In_2O_3 thin films. Recently it was shown that the high conductivity of In_2O_3 layers is caused by surface donors rather than by bulk defects, dopants and incorporated impurities, as it was assumed previously [194]. This theory was based on the theoretical calculations combined with some experimental results. Since the In_2O_3 layer investigated in this work is very thin, one can expect high conductivity of this layer.

Investigations of In_2O_3 layers by STM were intensively performed only within the last 5 years, e.g., on the layers with (100) [195], (001) [189] and (111) [186, 188, 191] crystallographic orientation. For different crystal orientations and surface stoichiometry (i.e.reduced or oxidized layers) detailed STM simulations have been performed [192]. However, none of these publications have reported on the STM performed on the very thin In_2O_3 layers, or have observed a well-ordered (1×1) surface structure similar to that shown in Fig. 7.6. For instance, in the work of Morales et al., the (1×1) reconstructed Sn-doped (111) In_2O_3 layer exhibited a flat surface that consisted of small domains laterally shifted to each other [186]; the neighboring terraces were separated by 0.3 nm, corresponding to mono-atomic steps. The STM images in this work show formed islands with the layer-by-layer grown atomically flat surfaces (Fig. 7.6,7.5). The islands consist of terraces and have a wide range of separation (0.2-1.4 nm). The single In_2O_3 particles with size of 50 - 100 nm have been observed previously only by Segawa et al. [196], where the studied crystallites exhibit a flat surface and a tetragonal bipyramidal shape. Size of the In_2O_3 crystallites was very similar to the one observed in this work by STM and AFM.

It is worth mentioning that indium oxide has found its application in transparent electrodes in optoelectronic devices such as solar cells, displays, etc. [197]. Especially, tin-doped In_2O_3 layers have attracted much attention due to their high optical transparency in the visible range and low resistivity [198, 199]. Oxidation of InN layers are of significant interest for fabrication of metal-oxide-semiconductor field effect transistors (MOSFET) [200], where In_2O_3 layer can be an appropriate gate dialectic material. A strong surface conductivity of the grown in this work In_2O_3 layer might be avoided by changing the preparation conditions of the thermal oxidation process. However, this requires additional investigations and was not studied in this work.

7.4 Summary

Compared to the exposure of InN to ambient air, thermal oxidation of the In-polar InN layer by annealing the layer in nitrogen plasma and ambient air with simultaneous deposition of metallic indium resulted in formation of less than 2 nm thick In_2O_3 layer with a cubic bixbyite lattice structure.

For the first time a comprehensive surface analysis was performed on the very thin In_2O_3 layer grown on InN. The formed In_2O_3 layer has a (111) crystal orientation that was found to be well-matched to the wurtzite (0001) InN. Topography of the indium oxide layer consists of single crystallites with a size of 70-120 nm. Each crystallite has an atomically flat surface with a well-ordered (1×1) arrangement of the atoms as observed by STM. The In/O ratio determined by AES and XPS is above one, indicating excess of indium on the surface. Hence, the In_2O_3 surface is presumed to be terminated by indium atoms resulting in a strong downward band bending. Therefore, an electron accumulation layer is present on the surface of the formed In_2O_3 /InN heterostructure.

The formed thin In_2O_3 layer remains stable on ambient air that is a good indicator for possible application of In_2O_3 as a capping layer. The capping layer will protect InN surface from contaminations and allow to transport as-grown InN layers from one vacuum chamber to another without exposing the InN surface to ambient air. Additionally, oxidation of InN can be used in MOSFET, where In_2O_3 layer is used as a gate dialectic.

8 Surface Characterization of Semipolar In(Ga)N Layers

The polarity of the semipolar InN layers was investigated in Chap. 4, however, not much has been shown about the surface properties of these layers so far. Semipolar group-III nitrides have a big potential to improve efficiency of electronic devices, due to the significant reduction of the quantum confined stark effect along the semipolar crystallographic directions. Therefore, it is important to know and understand properties of these layers. In particular, surface morphology and roughness play an important role in the interfacial properties of optoelectronic devices. Along with the studied InN material, one of the most popular indium nitride alloys is InGaN, in which optoelectronic properties can be tuned depending on the amount of incorporated indium. Until now, not many studies have been performed on the growth and characterization of semipolar InN and InGaN layers, and only few publications report on their surface properties.

The surface studies of the semipolar $(11\bar{2}2)$ InN and $(20\bar{2}1)$ InGaN layers with low amounts of indium will be shown in this chapter. The topography of the layers is characterized by AFM and STM, while electronic and chemical properties is analyzed by XPS and AES. A model of the surface reconstructions on semipolar layers will be proposed and compared with the reported theoretical calculations.

8.1 Semipolar $(11\bar{2}2)$ InN

AFM topographic images show that $(11\bar{2}2)$ InN layers have an undulated surface structure along the $[\bar{1}100]$ direction, Fig. 8.1. An undulated structure is caused by the prolonged stripe-like features on the surface along the $[11\bar{2}\bar{3}]$ direction that is formed during the growth . Depending on the growth temperature, the "stripes" exhibit different forms: a triangle-like shape can be distinguished for the InN layer grown at 530°C (Fig. 8.1 (a)), a slim and long "stripes" are observed for the InN layer grown at 550°C (Fig. 8.1 (b)), while shorter and abrupt features are formed on the layer grown at 560°C (Fig. 8.1 (c)). Note that no indium droplets were observed on the surfaces of studied semipolar InN layers independent from the growth temperature. The rms roughness of the $(11\bar{2}2)$ InN layer measured on (5×5) μm^2 increases from 6.6 nm for the layer grown after 530°C up to 32.7 nm and 20.9 nm for the layers grown at 550°C and 560°C, respectively [162]. It was proposed that an undulation is caused due to a faster lateral growth rate along the $[11\bar{2}\bar{3}]_{InN}$ direction compared to the growth rate along the $[\bar{1}100]_{InN}$ [85].

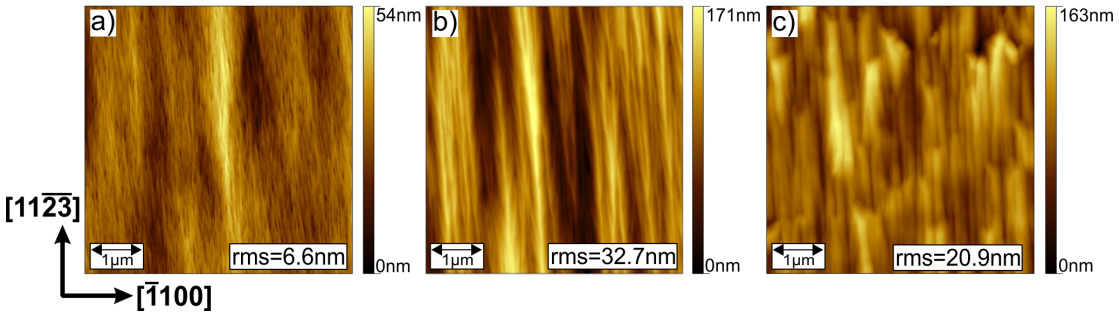

Figure 8.1: AFM images of the (11$\bar{2}$2) InN layers grown on GaN template at temperature of a) 530°C, b) 550°C and c) 560°C. Measured by D. V. Dinh, TU Berlin [162].

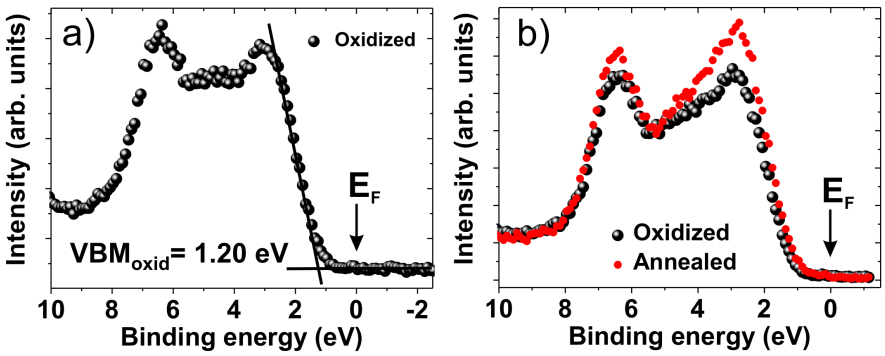

Figure 8.2: VBM of the semipolar InN layers a) grown at 550°C for the oxidized surface and b) grown at 560°C for the surface oxidized and annealed at 450°C. The VB for the annealed layer is normalized on the background of the oxidized layer.

Detailed analysis of the surface structure, amplitude and period of undulations is described in Ref. [162] and will not be discussed here.

A schematic unit cell of the (11$\bar{2}$2) InN layer grown on the epitaxial (11$\bar{2}$2) GaN/ (11$\bar{1}$0) Al_2O_3 structure was shown and discussed previously in Fig. 4.4 (a). Additionally, the polarity of the (11$\bar{2}$2) InN layer along the *c*-direction was determined by XPS to be In-polar, as described in Sec. 4.4. This is true for all the semipolar InN layers represented in Fig. 8.1.

The determined positions of the VBM for the oxidized semipolar InN layers were found to be at 1.30±0.10 eV above the Fermi level for the layer grown at 530°C (see Fig. 4.5 (b)), at 1.20±0.10 eV and 1.15±0.10 eV above the Fermi level for the layers grown at 550°C and 560°C, respectively (Fig. 8.2). Upon the thermal annealing at 450°C for 10 min, which led to the significant reduction of surface contaminations by 82% for oxygen and 80% for carbon, position of the VBM decreased to 1.05±0.10 eV above the Fermi level, as shown in Fig. 8.2 (b) for the InN layer grown at 560°C. Since the band gap of InN is about 0.7 eV, the determined positions of the VBM indicate a surface downward band bending on the oxidized and annealed semipolar InN layers.

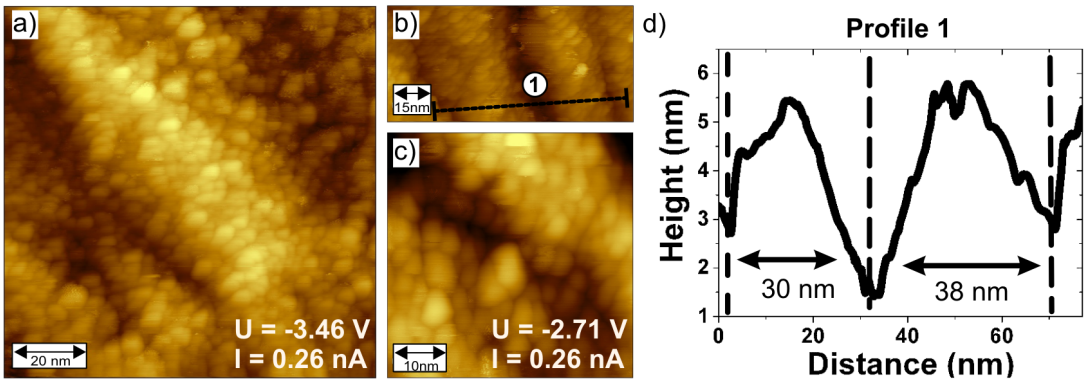

Figure 8.3: STM images of the semipolar $(11\bar{2}2)$ InN layer grown at 530°C recorded at the different places on the sample at the areas of a) $(100\times100)\text{nm}^2$, b) $(100\times50)\text{nm}^2$ and c) $(50\times50)\text{nm}^2$. d) profile along undulation shown in image (b).

The downward band bending on the clean $(11\bar{2}2)$ InN layer is similar to the N-polar InN layers, where the VBM lies at 1.10±0.10 eV above the Fermi level (see Sec. 6.1.5). The In-polar InN layer, however, exhibited the strongest downward band bending (VBM = 1.35±0.10 eV, Fig. 6.39). In the work of Eisenhardt et al. it was shown that N-polar and non-polar (*a*- and *m*-plane) InN layers have the same band alignment – a downward band bending, where the VBM lies at 1.0 eV above the Fermi level, while the In-polar InN has a stronger downward band bending with the VBM at 1.4 eV above the Fermi level [30]. The difference in the band alignments was explained by the different positions of the occupied surface states, which lie close to the VBM for the N- and non-polar InN layers and above the CBM for the In-polar InN layer. Therefore, since the band bending of the semipolar InN layers studied in this work is similar to the N-polar and non-polar layers, one can assume that the occupied surface states for the $(11\bar{2}2)$ InN layer are located near the VBM. However, this assumption requires an experimental confirmation.

Since the semipolar InN layer grown at 530°C possesses the smoothest surface, this layer was chosen for further characterization by STM and STS. Fig. 8.3 shows an overview of the layer topography at large scanning areas. While an undulation period along the $[\bar{1}100]$ direction of this layer can be hardly distinguished by AFM (Fig. 8.1 (a)), the STM images showed an obvious undulation structure with a period of 33±9 nm and a height of 3.7±1.0 nm. An example of the surface profile is shown in Fig. 8.1 (d) measured in the image (b), where the determined width of the structure is about 30 nm and 38 nm. Moreover, all three images in Fig. 8.3 exhibit a grain-like structure of the surface, similar to the In- and N-polar InN layers. It would appear these kinds of features are favorable for InN layers independent from their crystal orientations.

Fig. 8.4 (a) and (b) show atomic-scale STM images of the $(11\bar{2}2)$ InN layer (recorded on two different areas of the sample), where due to the unstable tunneling conditions only particular regions exhibit well-resolved surface structures. The profiles 1 and 2

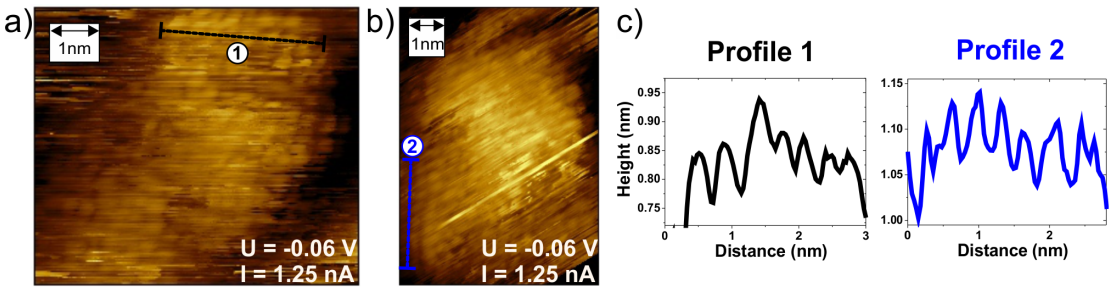

Figure 8.4: a), b) Atomic-resolved STM images of the semipolar InN layer grown at 530°C with c) two profiles corresponded to each image.

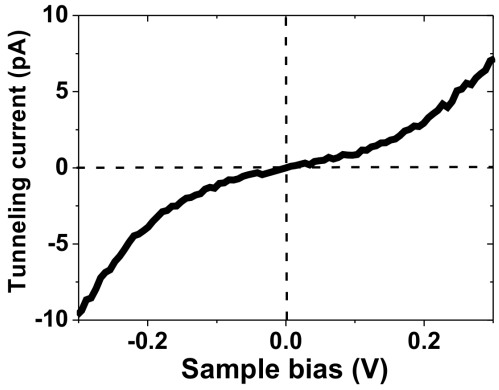

Figure 8.5: STS measured on the semipolar $(11\bar{2}2)$ InN layer – average of the (20×20) points grid spectroscopy.

in Fig. 8.4 (c) correspond to the images (a) and (b), respectively, where the average separation between the measured structures is 0.38 ± 0.07 nm for the first profile and 0.38 ± 0.06 nm for the second profile.

STS performed on the investigated semipolar InN layer shown in Fig. 8.3 (d) is an average of the grid spectroscopy measurements with (20×20) points. The I-V curve shows a clear metallic behavior of the semipolar surface: the tunneling current is observed for the entire region of the applied bias except 0 V This is similar to the I-V curves observed on the N- and In-polar InN layers in previous chapters. Surface metallicity is a consequence of a downward band bending detected on the surface by XPS.

8.1.1 Reconstruction of Semipolar InN Layer

An atomic model (top and side view) of the ideal cleaved unreconstructed semipolar $(11\bar{2}2)$ InN surface is shown in Fig. 8.6. A unit cell is sketched on the top view image (dashed rectangle), where the unit cell length is determined as $a\cdot\sqrt{3}=0.61$ along the $[\bar{1}100]$ direction and $\sqrt{a^2+b^2}=0.67$ nm along the $[11\bar{2}\bar{3}]$ direction (a and b are the lattice parameters of InN). The unit cell of the $(11\bar{2}2)$ InN surface contains more than one indium atom along the $[11\bar{2}\bar{3}]$ direction, and the neighboring indium atoms are slightly shifted to each other.

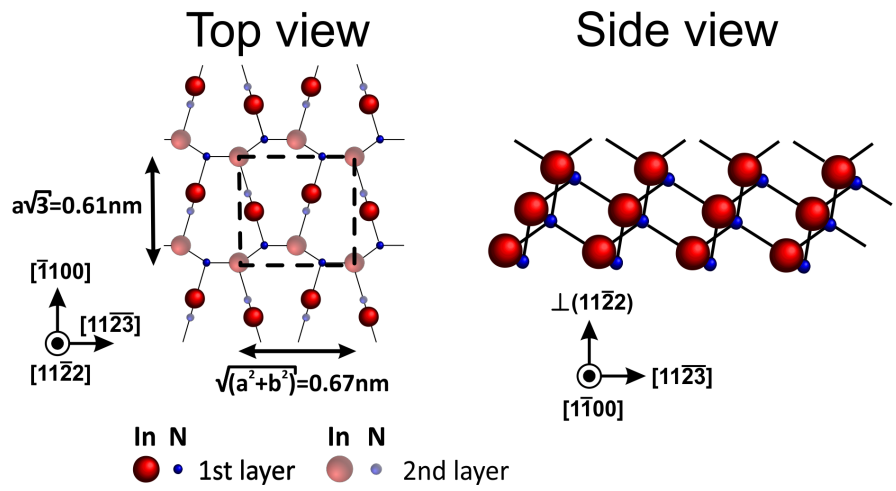

Figure 8.6: Top and side view of the ideal cleaved unreconstructed semipolar (11$\bar{2}$2) InN surface. The *a* and *b* correspond to the lattice parameters of InN. Dashed rectangle shows the unit cell of the (11$\bar{2}$2) plane.

On a real grown semipolar InN layer, the atoms on the surface undergo rearrangement in order to gain the most energetically favorable places. This rearrangement leads to the surface reconstruction that is different compared to the ideal cleaved surface. There are few reports that can be found in the literature concerning surface reconstructions of the (11$\bar{2}$2) nitrides, however, most of them describe theoretically calculated or experimentally determined reconstructions on AlN and GaN layers [201–204]. Only one publication is known to report on the (11$\bar{2}$2) surface reconstruction on InN layers, where theoretically it was predicted that depending on the growth conditions (indium chemical potential) the (11$\bar{2}$2) InN surfaces are stable if terminated by one or two indium atomic layers [205]. The models of these reconstructions for InN layers are shown in Fig. 8.7 (adopted from Ref. [205]). A growth under In-rich conditions results in the formation of two atomic indium layers on the surface, while a N-rich and stoichiometric growth conditions lead to the surface termination by one atomic indium layer (In-adlayer) [205]. Moreover, it was shown that the surface with two terminated indium layers can form at a lower temperature, compared to the surface with In-adlayer, for the fixed indium pressure. It is important to emphasize that unlike for semipolar (11$\bar{2}$2) AlN and GaN layers, the theoretically proposed models for semipolar InN layers have not been proved experimentally so far.

As shown in Fig. 8.7 (a), in the case of (11$\bar{2}$2) InN surface reconstruction with an In-adlayer, the top-most nitrogen atoms from bulk are terminated by In-adatoms (greenish spheres), while for the surface terminated by two In layers, both nitrogen and indium atoms from top-most bulk region are terminated by indium atoms (greenish spheres) (Fig. 8.7 (b)).

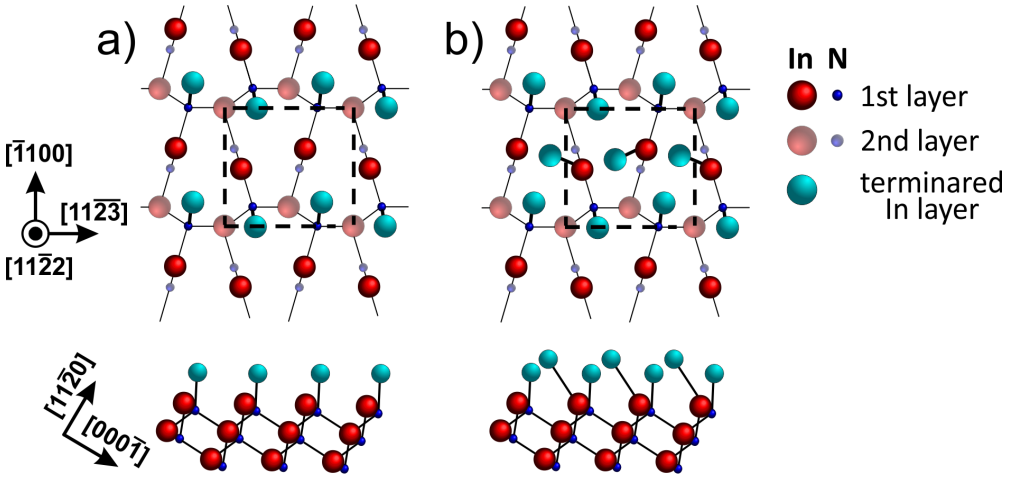

Figure 8.7: Top and side view of the theoretically predicted reconstructed semipolar (11$\bar{2}$2) InN surfaces terminated by a) one atomic layer (In-adlayer) and b) two atomic layers (adopted from [205]). Large and small spheres represent In and N atoms, respectively. Indium atoms associated with terminated layers are shown in greenish color.

One can expect that atomically resolved STM images recorded from the (11$\bar{2}$2) InN surfaces reconstructed as predicted by theory [205], would show the indium atoms from the terminated layers (greenish spheres in Fig. 8.7). According to the top view images in Fig. 8.7, in the case of the formed In-adlayer, the observed by STM In-adatoms should be separated from each other by ∼0.34 nm along the [$\bar{1}$100] directions and by ∼0.61 nm along the [11$\bar{2}\bar{3}$] directions. In the case of termination by two In layers, observed by STM atoms should be separated from each other by approximately 0.31-0.34 nm along the [$\bar{1}$100] and [11$\bar{2}\bar{3}$] directions. Note that although the indium terminated atoms in the shown models are slightly shifted to each other, i.e. located not directly along one row, these dislocations of atoms are below the resolution of STM and probably would not be observed in STM images

The distances between the structures determined in the STM images in Fig. 8.4 (a) and (b) are 0.38±0.07 nm along the both measured directions that is in good correlation with the theoretically predicted (11$\bar{2}$2) InN surface terminated by two indium layers. Hence, the studied semipolar (11$\bar{2}$2) InN layer is most likely possesses the surface atomic arrangement shown in Fig. 8.4 (b) and terminated by two indium layers.

Based on these results, the surface reconstruction of the semipolar (11$\bar{2}$2) InN layer has the highest amount of indium, compared to the studied in this work N- and In-polar InN layers (see Sec. 6.3). Similar to the polar InN layers, the excess of indium on the surface for the semipolar InN layer would explain an electron accumulation layer on the surface, which results in the surface metallic behavior and the downward band bending, observed by STS and XPS, respectively.

Compared to (11$\bar{2}$2) InN layers, semipolar (11$\bar{2}$2) GaN layers were theoretically predicted to have three stable reconstruction upon increasing Ga chemical potential: sur-

face terminated by $c(2\times2)$ Ga-adatoms, which form Ga-dimers on the surface and termination by one and two gallium layers, similar as shown in Fig. 8.7 for the InN layers [203, 205]. These calculations are in good agreement with the experimental studies, where it was shown that the $(11\bar{2}2)$ GaN layers can be covered by less than two gallium atomic layers and by approximately two atomic gallium layers by increasing the Ga-flux [202]. Further increase of the Ga-flux resulted in formation of Ga droplets. In the case of semipolar $(11\bar{2}2)$ AlN layers, surface termination by two aluminum layers and two variations of the (2×2) Al-adatom coverages are predicted to be stable surface reconstructions [201].

It is worth mentioning that in the case of ternary alloy such as InGaN, indium is predominate on the surface: theoretical calculations predicted $(11\bar{2}2)$ InGaN layers to be covered by one or two indium layers [206], similar to the reconstructions for the semipolar InN surfaces in Fig. 8.7. Moreover, depending on the growth conditions, the semipolar InGaN layers can be terminated even by three indium layers, where two layers are located as shown in Fig. 8.7 (b) and the third layer is formed by substituting all gallium atoms from the top-most metallic bulk layer. The coverage of 1 - 2.3 layers of indium on InGaN layers was experimentally confirmed as described in Ref. [204].

8.2 Semipolar $(20\bar{2}1)$ InGaN

After understanding the surface topography and reconstruction of the semipolar InN layers, it is interesting to investigate and compare surface properties of the alloy, such as InGaN. For this, topography, reconstruction and electrical properties of the semipolar $(20\bar{2}1)$ InGaN layers with 6.5% and 10.2% indium composition were analyzed in details.

The $(20\bar{2}1)$ InGaN layers were grown on $(20\bar{2}1)$ GaN substrate at 725°C and 750°C by MOVPE, resulting in the indium compositions of 10.2% and 6.5%, respectively. Estimated thickness of the InGaN layers is about 22 nm. Detailed growth procedure is described in Sec. 2.4.2. The indium content of the InGaN layers were determined by XRD by T. Wernicke at TU Berlin.

AFM images of the studied layers with corresponding profiles are shown in Fig. 8.8. Surface topography exhibits an undulation structure with a period of 135 ± 50 nm and a height of 1.3 ± 0.4 nm for the layer with 6.5% indium, and a period and height of 75 ± 20 nm and 0.70 ± 0.15 nm for the layer with 10.2% indium, respectively. Since the height of the grown structure is small, the overall rms roughness of the layers measured on the $(2\times2)\mu m^2$ does not exceed 1 nm, despite the undulation structure. The undulation structure on the InGaN layers is similar to the one observed on the semipolar $(11\bar{2}2)$ InN layer grown at 550°C shown in Fig. 8.1 (b). However, surface roughness of the $(20\bar{2}1)$ InGaN layers is remarkably better than any of the semipolar InN layers studied in the previous section.

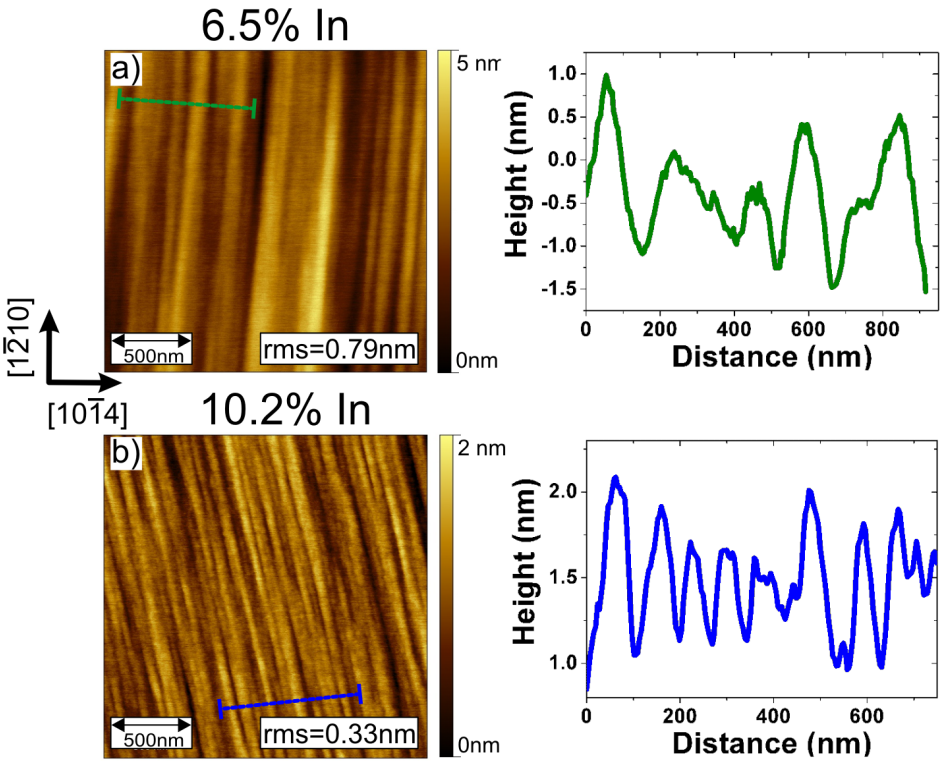

Figure 8.8: AFM images and profiles from the semipolar (20$\bar{2}$1) InGaN surfaces with a) 6.5%, b)10.2% indium.

Similar topography on the semipolar (20$\bar{2}$1) GaN, AlGaN and InGaN layers with indium content below 3% has been observed by Ploch et al. [207]. According to his report, an undulation occurs along the [10$\bar{1}$4] direction and has a period of 20-45 nm for GaN layers and up to 35 nm for InGaN layers which contains 3% indium. Undulation along the [10$\bar{1}$4] direction was proposed to originate from the (10$\bar{1}$0) and (10$\bar{1}$1) microfacets, as shown in Fig. 8.16 (a) [207]. It was assumed that these microfacets are strongly affected by chemical potential.

According to the AFM results from Fig. 8.8, a slight increase of indium amount in ternary alloy (i.e. from ∼3% to ∼6%) leads to a significant increase of the undulation period (i.e. from ∼35 nm up to ∼135 nm). However, the growth conditions and temperature also affect undulation period: it has been shown that for GaN layers, increase of growth temperature and reactor pressure result in higher undulation period [207]. Hence, different growth conditions for the semipolar InGaN layers with 10.2% and 6.5% indium can explain the lower undulation period observed in AFM images for the layer with higher indium amount.

In order to investigate the surface structure and morphology on the atomic scale, the InGaN samples were decontaminated in nitrogen ambient by annealing at 550°C for 15 min at pressure of $\approx 1 \times 10^{-4}$ mbar. The annealing temperature was chosen below

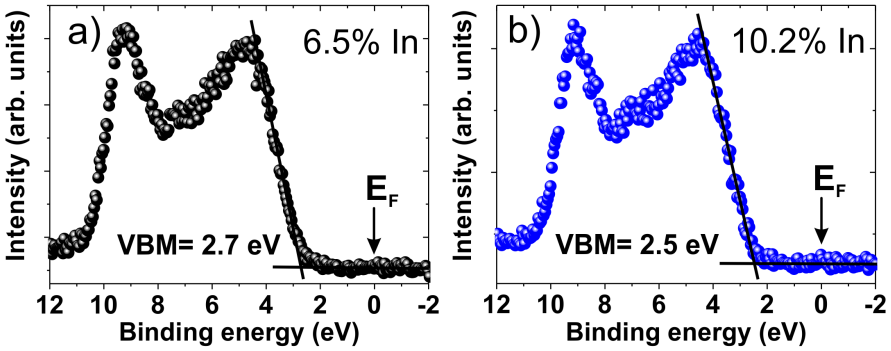

Figure 8.9: VBM of the clean semipolar $(20\bar{2}1)$ InGaN layers with a) 6.5%, b)10.2% of indium

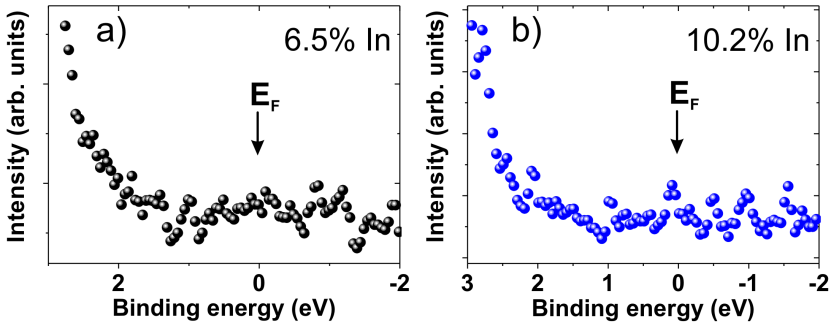

Figure 8.10: XPS emission near the Fermi level recorded from the clean semipolar $(20\bar{2}1)$ InGaN layers with a) 6.5%, b)10.2% of indium

the growth temperature of the layers in order to avoid material decomposition. Moreover, since annealing in N-plasma was shown to be more efficient for surface decontaminations of the In-polar InN (see Sec. 6.2.2) and InGaN layer (Ref. [66]), decontamination in nitrogen ambient was performed for the studied semipolar InGaN layers.

Based on XPS results, surface decontamination led to decrease of oxygen and carbon by approximately 73% and 70%, respectively. The In/Ga ratio determined from the normal emission XRD spectra remained unchanged for oxidized and clean InGaN layers, indicating no indium desorption from the surface at the chosen annealing temperature. The In/Ga ratio was 0.08 and 0.13 for the layers with 6.5% and 10.2% amount of indium. Compared to XRD, where the indium amount is determined as an average for the entire layer, XPS measurements determine the indium content only from the near-surface region. The values of In/Ga ratio and percentage concentration of indium from XRD are in good correlation with each other.

Interestingly, while for the $In_{0.06}Ga_{0.94}N$ layer the In/Ga ratio determined by XPS for the bulk-like (measured at normal emission) and surface-like (emission at 80°) regions are similar, for the $In_{0.10}Ga_{0.90}N$ layer the In/Ga ratio is only 0.03 for the surface-like area compared to the 0.13 for the bulk-like region. It seems that in the latter case, indium is distributed inhomogeneously within the crystal layer and is deficient on the

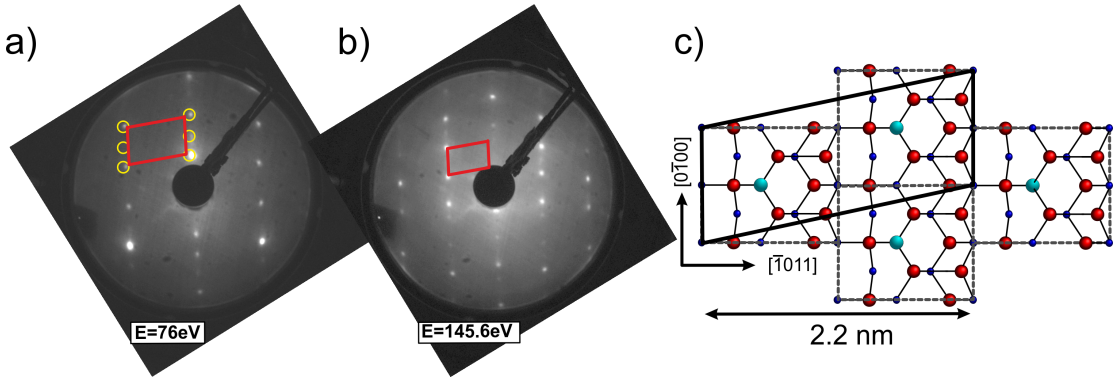

Figure 8.11: LEED of the semipolar (20$\bar{2}$1) $In_{0.06}Ga_{0.94}N$ layer recorded at a) low (76 eV) and b) high (145.6 eV) energies. Some of the diffraction spots in image (a) are marked by circles for a better visualization. The $c(2\times4)$ unit cell corresponded to the represented symmetry is sketched on each image. c) Model of the surface reconstruction that might explain the observed symmetry in LEED patterns; black rectangle corresponds to the $c(2\times4)$ unit cell, red and blue spheres are In(Ga) and N atoms, respectively, the greenish spheres refers to metallic adatoms (adopted from Ref. [208]).

surface. This might be explained by different growth temperature and therefore, growth kinetics between two InGaN layers.

The VB spectra of the semipolar (20$\bar{2}$1) InGaN layers were recorded from the clean surfaces and represented in Fig. 8.9. The VBM positions for the oxidized and annealed $In_{0.06}Ga_{0.94}N$ layer is 2.80±0.05 eV and 2.70±0.05 eV above the Fermi level, respectively. Thus, the VBM is shifted by 0.1 eV towards lower binding energy after surface decontamination. However, the In 3*d* core-level is shifted by 0.3 eV towards lower binding energy upon annealing, indicating that VBM is affected by surface states and has different alignments compared to the shift caused by a band bending.

In the case of the $In_{0.10}Ga_{0.90}N$ layer, the position of the VBM for the oxidized surface is 2.90±0.05 eV above the Fermi level, while for the annealed layer it is 2.50±0.05 eV. The shift of the VBM by 0.4 eV towards lower binding energies is in good correlation with the shift of the In 3*d* core-level. Thus, for this layer, where the surface-like region has a lack of indium atoms, no surface states affect an alignment of the conduction and valence bands. One can assume that presence of the surface states at the $In_{0.06}Ga_{0.94}N$ layer originate from metallic indium and strongly influence position of the VBM on the surface.

Based on the indium composition determined from XRD, the band gap of the studied semipolar InGaN layers was determined to be ∼3.16 eV for the layer with 6.5% In and ∼3.02 eV for 10.2% In. According to the determined positions of the VBM, both InGaN layers exhibit an upward band bending (electron depletion), where the barrier height Φ_B is approximately 0.46 eV and 0.50 eV for the annealed InGaN layers with 6.5% and 10.2% In, respectively. Due to the low difference in indium amount, the

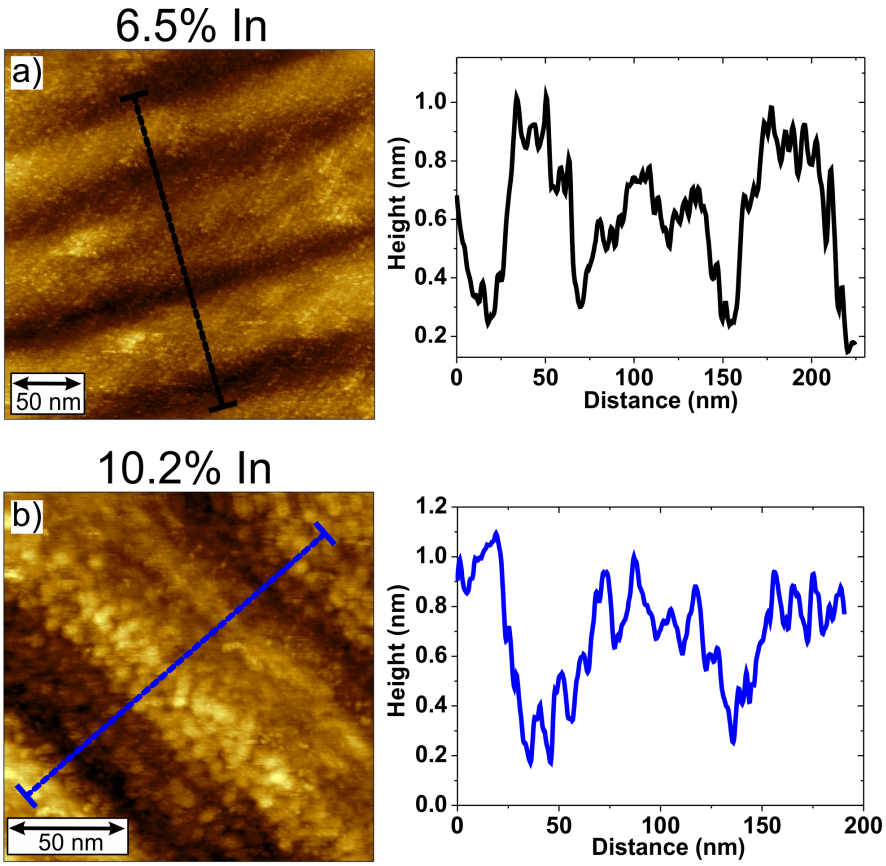

Figure 8.12: STM images of the semipolar $(20\bar{2}1)$ InGaN layers with a) 6.5% and b) 10.2% of indium. Profiles along the images are represented on the right side.

barrier heights are very similar for both clean InGaN layers. The surface oxidation on air, however, differently reduces the barrier heights: Φ_B equals $\sim$0.36 eV for the layer with 6.5% In and $\sim$0.12 eV for the layer with 10.2% In. Therefore, oxidation of the semipolar InGaN layers leads to reduction of the surface upward band bending.

Transition from electron depletion to electron accumulation layer at the $In_xGa_{1-x}N$ surfaces was found to take place for $x \approx 0.3\%$ in the case of polar orientation of the layer: an upward band bending was determined for the layers with indium content below $\approx 30\%$, while a downward band bending occurs for the layers with indium amount above $\approx$30% [161]. Observed upward band bending for the semipolar $(20\bar{2}1)$ InGaN layers is in good agreement with a reported trend for polar InGaN layers, where both InGaN layers with low amount of indium studied in this work exhibit the upward band banding.

Fig. 8.10 represents an XPS emission near the Fermi level for the annealed semipolar InGaN layer. For the layer with 10.2% In the Fermi edge is well-pronounced and can be

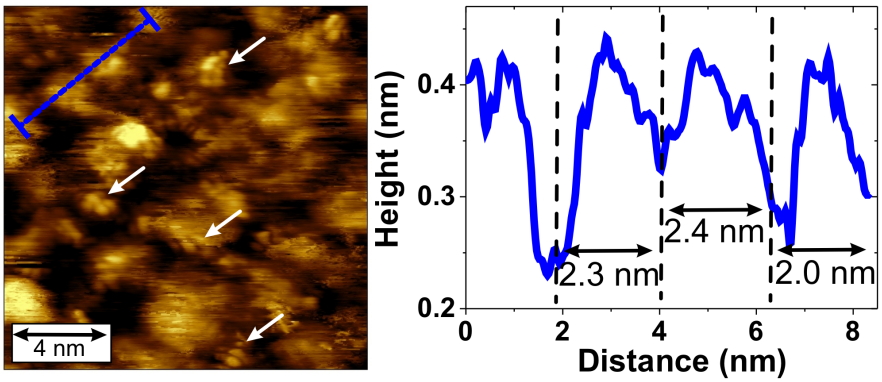

Figure 8.13: STM images of the semipolar $(20\bar{2}1)$ InGaN layers with 10.2% In at nanoscale with the corresponding profile sketched along the image. White arrows correspond to the nano-resolved structures which might be assigned to atoms.

clearly identified, while for the other layer the Fermi edge can not be well-distinguished, probably due to a lower signal to noise ratio.

Study of the $(20\bar{2}1)$ InGaN surface reconstruction was performed by LEED. The LEED patterns recorded from the $In_{0.06}Ga_{0.94}N$ layer with a sketched unit cell are shown in Fig. 8.11 (a) and (b). The LEED diffraction patterns correspond to the centered (2×4) symmetry, i.e $c(2\times4)$, which is different compared to the previously observed (1×1) surface periodicity on the polar InN layers. The LEED pattern could be observed already at $\sim$35 eV, which refers to the clean well-ordered structure at the near-surface region. The identical LEED patterns have been recorded from the InGaN layer with 10% In. Hence, the discussion about surface reconstruction is suitable for both studied InGaN layers.

Further, topography of the semipolar InGaN layers were analyzed by STM. The STM images recorded at a large scanning area (Fig. 8.12) exhibit the undulation surface structures, which were also observed by AFM. Undulation period determined from STM images varied around 70$\pm$20 nm for the layer with 6.5% In and 100$\pm$20 nm for the layer with 10.2% In. The period is in agreement with the AFM images within an error bar. Fig. 8.12 (b) exhibits a well-pronounced slope of the undulation sidewalls.

By decreasing the scanning area to a nanoscale, as in Fig. 8.13, the InGaN surface topography exhibits another kind of undulation with a period of approximately 2 nm, as shown in the profile. Moreover, the STM image in Fig. 8.13 contains areas with resolved nanoscale structures (marked by arrows). However, unstable tunneling conditions, which are a consequence of the undulation topography, make it impossible to obtain atomically resolved STM images.

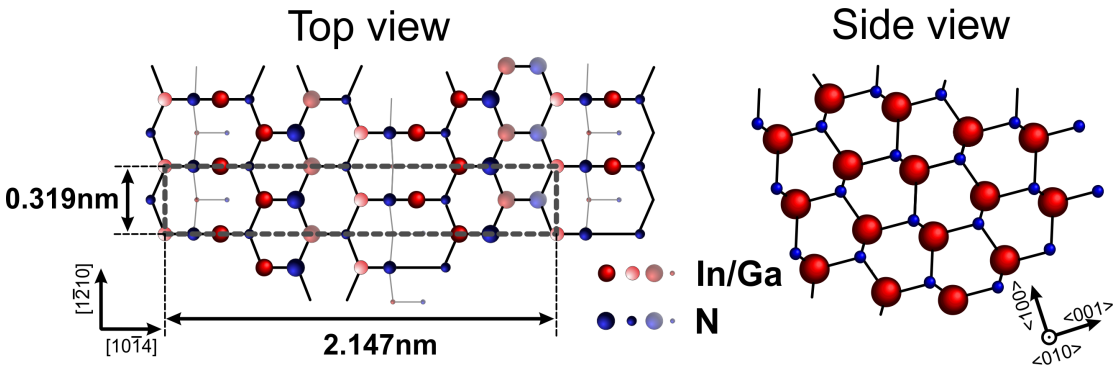

Figure 8.14: Top and side view of the ideal cleaved unreconstructed semipolar (20$\bar{2}$1) InGaN surface. Dashed rectangle shows the unit cell of the (20$\bar{2}$1) plane.

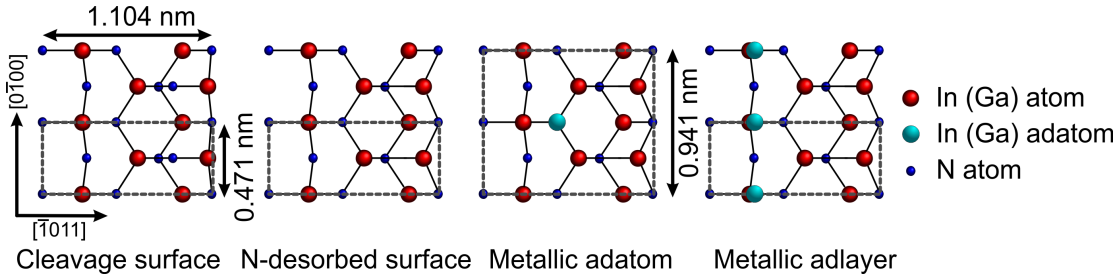

Figure 8.15: An ideal cleavage surface and theoretically predicted surface reconstructions of the semipolar (20$\bar{2}$1) InN (GaN) layers with (1×1) N-desorbed surface, (1×2) N-desorbed surface with a metallic In (Ga) adatom and (1×1) metallic In (Ga) adlayer, as reported in Ref. [208]. Dashed lines in the images correspond to the (1×1) or (1×2) surface unit cells.

8.2.1 Reconstruction of Semipolar InGaN Layers

The model of the ideal cleaved semipolar (20$\bar{2}$1) InN surface is shown in Fig. 8.14 (top and side view). The unit cell of that surface is sketched by a dashed rectangle and contains several In and N atoms, making the unit cell much more complex compared to the previously shown for the semipolar (11$\bar{2}$2) plane. The length of the unit cell is approximately 0.32 nm along the [1$\bar{2}$10] direction and 2.14 nm along the [10$\bar{1}$4] direction.

Compared to the semipolar (11$\bar{2}$2) surfaces of III-nitrides, much less is know about the surface reconstructions of the layers with the (20$\bar{2}$1) orientation. Until now, there is only one publication that can be found in the literature about surface reconstructions on the (20$\bar{2}$1) group-III-nitride layers, i.e. GaN and InN. These theoretical studies were performed by Yamashita et al., where they showed that depending on the growth conditions and therefore, growth kinetics, the semipolar (20$\bar{2}$1) InN (GaN) surfaces can possess one of the following reconstruction: the (1×1) N-desorbed surface, the (1×2) N-desorbed surface with a metallic In(Ga) adatom, and the (1×1) metallic In(Ga) adlayer [208]. A stick-and-ball models of these reconstructions and an ideal cleaved surface are shown in Fig. 8.15. It is important to note that the unit cell of the ideal

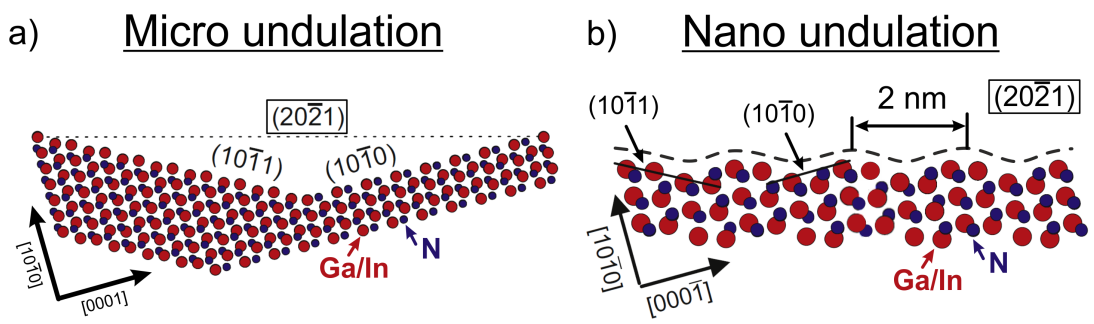

Figure 8.16: Model of a) micro and b) nano undulations on the semipolar (20$\bar{2}$1) InGaN layer taken from Ref. [207].

(20$\bar{2}$1) surface published in Ref. [208] is different compared to the shown in Fig. 8.14. In order to compare the experimental observation from this work with the literature, in the further discussion the unit cell from Ref. [208] and associated with it reconstructions will be assumed as correct ones.

For the ideal (20$\bar{2}$1) surface in Ref. [208], the length of the (1×1) unit cell equals 1.104 nm along the [$\bar{1}$011] direction and 0.471 nm along the [0$\bar{1}$00] direction. The (1×1) surface symmetry is predicted for the (20$\bar{2}$1) layers with N-desorbed reconstruction, where one nitrogen atom is absent in the unit cell compared to the ideal surface and for the layer termination by metallic adlayer. The (1×2) surface symmetry occurs only in the case of surface termination by metallic adatoms, as shown in Fig. 8.15, where the length of the unit cell along the [$\bar{1}$011] direction remains unchanged, while along the [0$\bar{1}$00] direction it equals 0.941 nm.

For the semipolar (20$\bar{2}$1) GaN layers, the N-desorbed surface and Ga-adlayer can be formed under N-rich and Ga-rich growth conditions, respectively, while the Ga-adatom reconstruction can be formed between these two growth regimes [208]. However, for the semipolar (20$\bar{2}$1) InN layers, the In-adlayer is expected to be stable for all growth conditions, while other mentioned reconstruction are predicted to be stable [208]. Since the layers studied in this work are ternary InGaN layers with only low amount of indium, it is not know, which surface reconstructions will be stable on these surfaces.

As shown previously, the LEED diffraction patterns from the (20$\bar{2}$1) InGaN layer exhibit the c(2×4) symmetry, which can be obtained, for instance, from the laterally shifted (1×2) unit cell from Fig. 8.15 for metallic adatom reconstruction. One can assume that if the sketched (1×2) unit cells are located to each other, as shown in Fig. 8.11 (c), the surface symmetry will correspond to the c(2×4) reconstruction (sketched by black rectangle), in good agreement with the observed LEED patterns. All other theoretically predicted surface reconstructions shown in Fig. 8.15 possess the (1×1) unit cell, which are difficult to correlate with the observed c(2×4) symmetry by LEED. Based on this discussion, one can propose that the studied in this work semipolar (20$\bar{2}$1) InGaN layers are terminated by metallic adatoms with the c(2×4) reconstruction

shown schematically in Fig. 8.11 (c). Unfortunately, the proposed surface reconstruction on InGaN layers could not be confirmed by atomically resolved STM images due to the unstable tunneling conditions caused by the undulation structure.

As mentioned previously, the undulation structure observed on the semipolar InGaN layers is formed by the $(10\bar{1}1)$ and $(10\bar{1}0)$ facets, as represented in the model in Fig. 8.16 (a) [207]. The sidewalls of the undulation structure observed on the STM image (Fig. 8.12 (b)) most likely correspond to the mentioned $(10\bar{1}1)$ and $(10\bar{1}0)$ microfacets.

Moreover, the nano undulations with a period of $\sim$2 nm were proposed to exist on the semipolar $(20\bar{2}1)$ surfaces [207]. The schematic model of this structure is shown in Fig. 8.16 (b). Similar nano undulations with a period of $\sim$2 nm were observed in the obtained STM image in Fig. 8.13, confirming the model initially proposed by Ploch et al. [207]. Note that the period of the nano undulation structure shown in STM image is in good correlation with the size of the $c(2\times4)$ unit cell. As shown in the sketched model in Fig. 8.11 (c), the length of the proposed surface reconstruction is 2.2 nm, similar to the nano undulation periods observed in the profile to the STM image (Fig. 8.13). Therefore, one can assume that the origin of the nano undulations can be explained by the $c(2\times4)$ reconstruction formed on the surface.

Note that according to the ideal $(20\bar{2}1)$ InGaN surface in Fig. 8.14, a length of the unit cell along the $[10\bar{1}4]$ direction is $\sim$ 2.1 nm that is also similar to the size of nano undulation. However, for further interpretation of results theoretical calculations concerning surface reconstructions on the surface shown in Fig. 8.14 are highly required.

The structure very similar to the discussed nano undulation can be distinguished in the HRTEM image of the $(20\bar{2}1)$ InGaN-based LED [209]. In this publication, an InGaN/GaN interface in the LED structure shows the pronounced undulation features on the $(20\bar{2}1)$ GaN top-most layer region with a period of $\sim$ 1 nm. This observation is in good agreement with the results shown in this work and provides a good evidence of the nano undulation formation on the semipolar $(20\bar{2}1)$ surfaces of III-nitrides.

8.3 Summary

A detailed surface analysis of the semipolar $(11\bar{2}2)$ InN and $(20\bar{2}1)$ $In_xGa_{1-x}N$ layers with 6.5% and 10.2% indium has been performed.

Both the semipolar InN and InGaN layers have a pronounced undulation surface structure. The undulation period of the $(11\bar{2}2)$ InN layer increases with increasing the growth temperature, corresponding to the higher surface roughness. For the first time the surfaces of the semipolar InN and InGaN layers have been studied by STM. The undulation period of the smoothest $(11\bar{2}2)$ InN layer grown at 530°C determined from the STM images equals approximately 33 nm with a height of around 3.7 nm. Based on the atomically resolved STM images, the studied semipolar $(11\bar{2}2)$ InN layer is proposed to be terminated by two indium layers. Excess of indium on the surface leads

to surface metallicity and downward band bending, as determined by STS and XPS, respectively.

The semipolar $(20\bar{2}1)$ $In_xGa_{1-x}N$ surfaces contain the micro undulations caused by the $(10\bar{1}1)$ and $(10\bar{1}0)$ facets, with a period estimated by AFM of 135 ± 50 nm and 75 ± 20 nm for the layers with 6.5% and 10.2% indium, respectively. Besides micro, the nano undulations were observed for the first time on the $(20\bar{2}1)$ InGaN surfaces. The nano undulations observed by STM have a period of 2 nm in good agreement with the proposed model in Ref. [207]. Moreover, the nano undulations might originate from the atomic arrangement within the $c(2\times4)$ surface unit cell, which was determined from the LEED patterns. The $c(2\times4)$ surface periodicity is caused by the lateral shift of the theoretically proposed (1×2) unit cell for the semipolar InGaN layer. Based on this, the studied semipolar $(20\bar{2}1)$ InGaN layers are assumed to be terminated by metallic adatoms.

The studied semipolar InGaN layers have an upward band bending that is slightly stronger for the layer with higher indium amount. Oxidation of the semipolar InGaN layer on ambient air leads to decrease of the upward band bending, as determined by XPS.

9 Summary and Outlook

This work aims to increase the knowledge about surface properties of InN layers with different crystal orientations in order to improve the quality of InN-based optoelectronic devises and/or understand the challenges that must be overcome to implement InN in the wide range of device application. Following main problems and topics were studied and discussed within this work: polarity determination of InN and GaN layers by XPS, effect of the nitridated sapphire substrates on crystal and surface quality of the subsequently grown InN layers, surface reconstructions of the N- and In- and semipolar InN layers and growth of a thin indium oxide layer on InN surface.

An alternative method for polarity determination of InN and GaN layers was investigated and established for the polar and semipolar orientations of the layers, e.g. (0001), $(000\bar{1})$, $(11\bar{2}2)$ planes. This method implies VB XPS and was shown to be reliable, non-destructive and appropriate for polycrystalline layers with thickness below 100 nm. Polarity of the layers was determined by recording the VB XPS spectra for emission perpendicular to the *c*-plane, i.e., normal emission for the polar layers and emission at 58 ° with respect to the surface normal for the semipolar $(11\bar{2}2)$ orientations, by using a monochromated Al K_α X-ray source ($h\nu \approx 1487$ eV). The group-III and N-polarity correspond to the higher intensity of the VB peak at lower (P_I peak) and higher (P_{II} peak) binding energies, respectively. The ratio between these two VB peaks strongly depends on the crystal orientation and can be calculated from spectra without a background subtraction procedure. Moreover, surface morphology and surface contaminations do not effect the VB peak intensities and thus, the ratio between P_{II} and P_I.

It was shown that the effect of sapphire nitridation plays an important role in the quality improvement of the subsequently grown polar InN layers. In contrast to the previous studies of nitridation mechanism in the literature, the atomic binding configurations of clean sapphire substrates were analyzed in details prior and after nitridation at temperatures between 500°C and 1050°C. The oxygen deficient $(\sqrt{31}\times\sqrt{31})\mathrm{R}\pm 9\,^\circ$ surface reconstruction of the bare sapphire substrate was found to be essential to perform a successful nitridation process. The predominance of the N-Al chemical bonds in the layers nitridated above 800 °C corresponds to the formation of the crystalline AlN layers, while a significant amount of the N-O bonds on the surface for the nitridation temperatures $\leq 800\,^\circ$C refers to the growth of amorphous AlN_xO_y layers. All sapphire nitridation layers possess a defect structure most likely caused by N defects.

The nitridated sapphire layers strongly affect the topography, polarity and crystallinity of the overgrown InN layers. The most appropriate nitridation temperature was found to be 1050°C, leading to the growth of the 1 nm thick AlN layer on sapphire

substrate. Formation of the thin crystalline AlN layer was shown to be enough to drastically improve quality of InN layers. Hence, the formation of the amorphous nitridated layers results in the growth of polycrystalline In-polar InN layers with rough surfaces, while formation of crystalline nitridated layers results in the growth of single crystalline N-polar InN layers with a smooth surface.

Surface characterization of the InN layers required desorption of surface contaminations, since the InN layers were exposed to ambient air after the growth. In order to obtain clean InN surfaces, thermal annealing under UHV conditions and annealing in nitrogen plasma by using a N-plasma source were performed. No destruction or damage of the layers were observed upon annealing below $\sim$500°C, while further increase of the annealing temperature led to degradation of the crystal structure and formation of In-droplets on the surface. Annealing in nitrogen plasma was found to be more efficient than annealing in UHV. An annealing at 450°C for 10-15 min was found to be an optimal preparation condition for the surface decontamination.

The N- and In-polar InN layers were analyzed in details in terms of their chemical binding configurations, atomic periodicity and electronic properties. Moreover, the surface characterizations were performed on the first commercially available MEAglow grown N-polar InN layers and compared to the MOVPE grown N-polar InN layer. The N-polar InN layers have shown to reconstruct into the (1×1) and $(\sqrt{3}\times\sqrt{3})$R$\pm$30° for MOVPE and MEAglow grown layers, respectively. Smooth layers with good crystalline quality are formed upon MOVPE growth, while polycrystalline InN layers with rougher surfaces are grown by MEAglow. The model for each surface reconstruction was proposed based on the several experimental techniques, indicating high reliability of the results. Formation of the In-adlayer was established for the (1×1) reconstructed surface, while additional adatoms on the indium adlayer are formed for the $(\sqrt{3}\times\sqrt{3})$R$\pm$30° N-polar InN layer. Moreover, the surface reconstructions observed by LEED were for the first time confirmed by STM studies.

The studied MBE grown In-polar InN layers have a (1×1) surface periodicity with an atomically smooth surface, whereas MOVPE grown In-polar InN layers have a rough surface and highly pronounced polycrystalline structure. Based on LEED, atomically resolved STM images and quantitative XPS and AES studies, it was shown that the In-polar InN layer is terminated by the single In-adlayer, where In adatoms locate at T4-sites in good agreement with the previously reported theoretical calculations.

This work reports on the first well-resolved STM images of InN layers, including the images recorded on the large scanning areas, which give information about the surface features that cannot be observed by AFM. Moreover, the atomically resolved STM images were obtained and correlate good with the proposed models for the observed surface reconstructions on both In- and N-polar InN layers. XPS and STS measurements reveal that all studied N- and In-polar InN layers exhibit downward band bending and hence, metallic behavior of the surface caused by a surface electron accumulation layer. The Fermi level is pinned at 1.0$\pm$0.1 eV above the VBM for the N-polar layers and at 1.20$\pm$0.15 eV above the VBM for the In-polar InN layers. Adsorption of native oxide

on the polar InN layers leads to increase (decrease) of the downward band bending by several meV for N-polar (In-polar) InN layer.

The In-polar InN layer oxidized in ambient air was compared to subsequently thermally oxidized InN layer. Thermal oxidation of the In-polar InN layer by annealing it in N* plasma and ambient air with simultaneous deposition of metallic indium results in the growth of a thin In_2O_3 layer with a cubic bixbyite lattice structure. For the first time a comprehensive surface analysis was performed on the very thin In_2O_3 layer grown on InN. The In_2O_3 layer has a (111) orientation that is well matched to the wurtzite (0001) InN. Topography of the layer consists of single crystallites, where each crystallite has an atomically flat surface with a well-ordered (1×1) arrangement of the atoms. The surface is terminated by indium atoms and has an electron accumulation layer, similar to InN. Formation of a thin In_2O_3 layer on InN material can be used for capping of InN surface. Moreover, the In_2O_3/InN heterostructures

The last part of this work was dedicated to the surface analysis of the semipolar $(11\bar{2}2)$ InN and $(20\bar{2}1)$ $In_xGa_{1-x}N$ $(6\% < x < 10\%)$ layers. All semipolar layers have a pronounced undulation surface structure along the $[\bar{1}100]$ direction for the $(11\bar{2}2)$ InN and the $[10\bar{1}4]$ direction for the $(20\bar{2}1)$ InGaN layers. This work shows the first studies performed on the semipolar InN and InGaN layers by STM. Based on atomically resolved STM images it was shown that the studied semipolar $(11\bar{2}2)$ InN layer is terminated by two indium layers. Excess of indium on the surface leads to an electron accumulation on the InN surface, which results in the surface metallicity and the downward band bending. For the studied semipolar InGaN layers, besides micro undulations on the surface, nano surface undulations with a period of 2 nm were observed by STM. The nano undulations could be explained by the proposed atomic model with the $c(2\times4)$ surface unit cell, which indicates a termination of the studied semipolar InGaN layers by metallic adatoms. The semipolar $(20\bar{2}1)$ $In_xGa_{1-x}N$ $(6\% < x < 10\%)$ layers have an upward band bending that is slightly stronger for the layer with higher indium amount.

The performed analysis of the atomic, chemical and electronic properties of the (0001), $(000\bar{1})$, $(11\bar{2}2)$ InN layers showed an important effect on polarity, surface and crystal properties of the investigated layers as well as growth of the thin group-III-oxide layers on InN. Based on these results, the knowledge and understanding of fundamental properties of the InN surfaces were significantly improved. Moreover, this work allowed to establishing a new method for polarity determination of group-III-nitrides. Certainly, the obtained results contribute to the improvement and development of the growth parameters, growth regimes, and the associated technological applications of InN layers.

Outlook

Although not all atomically resolved STM images of InN layers were well-resolved and exhibited a well-ordered structure, this work showed for the first time STM results of InN layers with different crystal orientations and thickness above 70 nm, providing an important impact in the understanding of the surface behavior of this material.

According to the STM studies of the InN layers, the inhomogeneous distribution of the DOS on the InN layers in form of grains observed by STM must be taken into account for the application of InN layers in optoelectronic devices, e.g. sensors, solar cells [6, 8, 210]. For instance, an adsorption of organic molecules on the InN surface would lead to a rather complicated interaction process between the surface and the molecules. Thus, the effect of interaction and its interpretation might be misunderstood if one does not take into account the InN surface reconstruction and distribution of DOS on the InN surfaces. Moreover, a large number of grain boundaries that are observed on both reconstructed InN layers, especially on the $(\sqrt{3}\times\sqrt{3})$R$\pm$30°, would affect the efficiency of a solar cell, where any kind of defects increases recombination rate of electrons and holes in the CB leading to a decrease in the photocurrent.

The models proposed for the (1×1) In-polar and the $(\sqrt{3}\times\sqrt{3})$R$\pm$30° N-polar InN layers have not been theoretically analyzed yet. Hence, it is preferable to perform theoretical calculations and test the stability of the proposed InN surface reconstructions.

The thin In_2O_3 film grown on InN might serve as a capping layer. It can protect the InN surface from contaminations upon the layer exposure to ambient air, therefore, resulting in a convenient and easy transfer of the InN layers from the growth chamber into the vacuum chamber for surface analysis. However, additional investigations are required in order to remove the capping In_2O_3 layer from the InN surface, e.g., by using a sputtering process. Moreover, the thermal annealing conditions used for InN layer can be modified in order to avoid termination of the In_2O_3 surface by indium atoms, i.e. avoid surface metallicity. Additional, the growth of a thin indium oxide capping layer performed in this work may be also applied for ternary alloys, e.g. InGaN layers. Particulary, the layers with high amount of indium may be appropriate for this case, since the lattice parameters of the In-rich ternary alloys are close to InN crystal parameters. One can assume that under similar conditions used for the growth of the In_2O_3 layer, the substitution of indium by gallium effusion cell may lead to the growth of thin gallium oxide layers. Especially, it could be used to grow a Ga_2O_3/GaN heterostructure which can be used for application in gas sensors and metal-oxide-semiconductor field-effect transistors [211]. Hence, GaN layers may be used as an alternative substrate for the growth of group-III oxides.

It is worth to analyze the applicability of the XPS VB method for polarity determinations of AlN layers and group-III nitride ternary alloys. The performance of XPS on AlN layers however, remains a challenging issue due to the large energy band gap of AlN ($E_g = 6.2$ eV) that leads to an insulating behavior of these layers. This insulating behavior of the AlN layers can be overcome, for instance, by applying a so-called elec-

tron shower, where the surface is exposed to an electron beam that fills the empty states of atoms and prevent surface charge accumulation. However, this method is suitable only in the case of a constant surface charge. The performed experiments showed that it is not the case for AlN layers: the surface charge can be up to $\sim$160 eV and increase continuously during measurement. Another solution to this problem could be the use of highly n-doped AlN layers. However, nowadays doping of AlN layers remains a challenging issue. Until now the best results for n-doping of AlN (electron concentration of $7.3 \times 10^{14}\,\mathrm{cm}^{-3}$) were achieved by Y. Taniyasu et al. [212].

In the case of ternary group-III nitride alloys, e.g. InGaN layers, XPS experiments should be performed on layers with the same element composition. Otherwise, additional experiments should be done to exclude the fact that different concentration of atoms of one type (e.g., indium in InGaN) affects the $P_{II} : P_I$ ratio. The main difficulty is to obtain the ternary group-III nitride layers with different polarities which can be determined by conventional method. Since no experiments on polarity determination of ternary alloys by wet chemical etching have been reported so far, the CBED technique should be used. This technique requires thick layers with low crystal defect density, which remains a challenge for the growth of some alloys (e.g. InGaN).

Bibliography

[1] V. Davydov, A. Klochikhin, R. Seisyan, V. Emtsev, S. Ivanov, F. Bechstedt, J. Furthmüller, H. Harima, A. Mudryi, J. Aderhold, O. Semchinova, and J. Graul, "Absorption and emission of hexagonal InN. Evidence of narrow fundamental band gap," *Phys. Status Solidi (B)*, vol. 229, pp. R1–R3, 2002.

[2] I. Mahboob, T. D. Veal, L. F. J. Piper, C. F. McConville, H. Lu, W. J. Schaff, J. Furthmüller, and F. Bechstedt, "Origin of electron accumulation at wurtzite InN surfaces," *Phys. Rev. B*, vol. 69, p. 201307, 2004.

[3] H. Lu, W. J. Schaff, L. F. Eastman, and C. E. Stutz, "Surface charge accumulation of InN films grown by molecular-beam epitaxy," *Appl. Phys.Lett.*, vol. 82, p. 1736, 2003.

[4] V. W. L. Chin, T. L. Tansley, and T. Osotchan, "Electron mobilities in gallium, indium, and aluminum nitrides," *J. Appl. Phys.*, vol. 75, pp. 7365–7372, 1994.

[5] G.-G. Wu, W.-C. Li, C.-S. Shen, F.-B. Gao, H.-W. Liang, H. Wang, L.-J. Song, and G.-T. Du, "Near infrared electroluminescence from n-InN/p-GaN light-emitting diodes," *Appl. Phys. Lett.*, vol. 100, no. 10, p. 103504, 2012.

[6] H. Lu, W. J. Schaff, and L. F. Eastman, "Surface chemical modification of InN for sensor applications," *J. Appl. Phys.*, vol. 96, p. 3577, 2004.

[7] R. Ascázubi, I. Wilke, K. Denniston, H. Lu, and W. J. Schaff, "Terahertz emission by InN," *Appl. Phys. Lett.*, vol. 84, p. 4810, 2004.

[8] A. Yamamoto, M. R. Islam, T.-T. Kang, and A. Hashimoto, "Recent advances in InN-based solar cells: status and challenges in InGaN and InAlN solar cells," *Phys. Status Solidi (C)*, vol. 7, pp. 1309–1316, 2010.

[9] N. Marrero, B. González-Díaz, R. Guerrero-Lemus, D. Borchert, and C. Hernández-Rodríguez, "Optimization of sodium carbonate texturization on large-area crystalline silicon solar cells," *Sol. Energy Mater. Sol. Cells*, vol. 91, pp. 1943–1947, 2007.

[10] J. P. Ibbetson, P. T. Fini, K. D. Ness, S. P. DenBaars, J. S. Speck, and U. K. Mishra, "Polarization effects, surface states, and the source of electrons in AlGaN/GaN heterostructure field effect transistors," *Appl. Phys. Lett.*, vol. 77, p. 250, 2000.

[11] P. Waltereit, O. Brandt, A. Trampert, H. H. Grahn, J. Menniger, M. Ramsteiner, M. Reiche, and K. H. Ploog, "Nitride semiconductors free of electrostatic fields for efficient white light-emitting diodes," *Nature*, vol. 406, p. 865, 2000.

[12] X. Wang, S.-B. Che, Y. Ishitani, and A. Yoshikawa, "Step-Flow Growth of In-Polar InN by Molecular Beam Epitaxy," *Jpn. J. Appl. Phys.*, vol. 45, pp. L730–L733, 2006.

[13] Y. Nanishi, Y. Saito, and T. Yamaguchi, "RF-Molecular beam epitaxy growth and properties of InN and related alloys," *Jpn. J. Appl. Phys.*, vol. 42, pp. 2549–2559, 2003.

[14] D. V. Dinh, M. Pristovsek, S. Solopow, D. Skuridina, and M. Kneissl, "Comparison study of N- and In-polar {0001} InN layers grown by MOVPE," *Phys. Status Solidi (C)*, p. 977, 2012.

[15] W. J. Wang, K. Sugita, Y. Nagai, Y. Houchin, A. Hashimoto, and A. Yamamoto, "Polarity control of InN grown by MOVPE on sapphire (0001)," *Phys. Status Solidi (C)*, vol. 4, pp. 2415–2418, 2007.

[16] M. Stutzmann, O. Ambacher, M. Eickhoff, U. Karrer, A. Lima Pimenta, R. Neuberger, J. Schalwig, R. Dimitrov, P. Schuck, and R. Grober, "Playing with polarity," *Phys. Status Solidi (B)*, vol. 228, pp. 505–512, 2001.

[17] Q. Paduano, D. Weyburne, J. Jasinski, and Z. Liliental-Weber, "Effect of initial process conditions on the structural properties of AlN films," *J. Cryst. Growth*, vol. 261, pp. 259–265, 2004.

[18] Y. Zhao, S. Tanaka, Q. Yan, C.-Y. Huang, R. B. Chung, C.-C. Pan, K. Fujito, D. Feezell, C. G. Van de Walle, J. S. Speck, S. P. DenBaars, and S. Nakamura, "High optical polarization ratio from semipolar (2021) blue-green InGaN/GaN light-emitting diodes," *Appl. Phys. Lett.*, vol. 99, p. 051109, 2011.

[19] K. S. A. Butcher, D. Alexandrov, P. Terziyska, V. Georgiev, D. Georgieva, and P. W. Binsted, "InN grown by migration enhanced afterglow (MEAglow)," *Phys. Status Solidi (A)*, vol. 209, pp. 41–44, 2012.

[20] K. S. A. Butcher, D. Alexandrov, P. Terziyska, V. Georgiev, and D. Georgieva, "Initial experiments in the migration enhanced afterglow growth of gallium and indium nitride," *Phys. Status Solidi (C)*, vol. 9, pp. 1070–1073, 2012.

[21] S.-H. Wei, *III-nitride semiconductors for photovoltaic application*. NCPV and Solar Program Review Meeting 2003, 1st. Ed., 2003.

[22] E. Dimakis, E. Iliopoulos, K. Tsagaraki, A. Adikimenakis, and A. Georgakilas, "Biaxial strain and lattice constants of InN (0001) films grown by plasma-assisted molecular beam epitaxy," *Appl. Phys. Lett.*, vol. 88, p. 191918, 2006.

[23] O. Madelung, *Semiconductors: data handbook*. 3rd Ed., Springer, Berlin, Heidelberg, 2004.

[24] L. Pauling, *The Nature of the Chemical Bond*. Cornell Univ. Press, Cornell Univ. Press, Ithaca, Nex York, 3rd edition, 1960.

[25] J. F. Nye, *Physical Properties of Crystals*. Oxford University Press, 1985.

[26] F. Bernardini, V. Fiorentini, and D. Vanderbilt, "Spontaneous polarization and piezoelectric constants of III-V nitrides," *Phys. Rev. B*, vol. 56, pp. R10024–R10027, 1997.

[27] J. Xie, X. Ni, M. Wu, J. H. Leach, U. Özgür, and H. Morkoç, "High electron mobility in nearly lattice-matched AlInN/AlN/GaN heterostructure field effect transistors," *Appl. Phys. Lett.*, vol. 91, p. 132116, 2007.

[28] D. A. B. Miller, D. S. Chemla, T. C. Damen, A. C. Gossard, W. Wiegmann, T. H. Wood, and C. A. Burrus, "Band-Edge Electroabsorption in Quantum Well Structures: The Quantum-Confined Stark Effect," *Phys. Rev. Lett.*, vol. 53, pp. 2173–2176, 1984.

[29] A. E. Romanov, T. J. Baker, S. Nakamura, and J. S. Speck, "Strain-induced polarization in wurtzite III-nitride semipolar layers," *J. Appl. Phys.*, vol. 100, p. 023522, 2006.

[30] A. Eisenhardt, S. Krischok, and M. Himmerlich, "Surface states and electric structure of polar and nonpolar InN - An *in situ* photoelectron spectroscopy study," *Appl. Phys. Lett.*, vol. 102, p. 231602, 2013.

[31] S.-C. Lin, C.-T. Kuo, X. Liu, L.-Y. Liang, C.-H. Cheng, C.-H. Lin, S.-J. Tang, L.-Y. Chang, C.-H. Chen, and S. Gwo, "Experimental determination of electron affinities for InN and GaN polar surfaces," *Appl. Phys. Express*, vol. 5, p. 031003, 2012.

[32] M. Walker, T. D. Veal, H. Lu, W. J. Schaff, and C. F. McConville, "InN{0001} polarity by ion scattering spectroscopy," *Phys. Status Sol. (C)*, vol. 2, pp. 2301–2304, 2005.

[33] M. Sumiya, M. Tanaka, K. Ohtsuka, S. Fuke, T. Ohnishi, I. Ohkubo, M. Yoshimoto, H. Koinuma, and M. Kawasaki, "Analysis of the polar direction of GaN film growth by coaxial impact collision ion scattering spectroscopy," *Appl. Phys. Lett.*, vol. 75, p. 674, 1999.

[34] Y. Hayakawa, D. Muto, H. Naoi, A. Suzuki, T. Araki, and Y. Nanishi, "Polarity determination of InN by atomic hydrogen irradiation," *Jpn. J. Appl. Phys.*, vol. 45, pp. L384–L386, 2006.

[35] T. Mitate, S. Mizuno, H. Takahata, R. Kakegawa, T. Matsuoka, and N. Kuwano, "InN polarity determination by convergent-beam electron diffraction," *Appl. Phys. Lett.*, vol. 86, p. 134103, 2005.

[36] P. Ruterana, A. L. Syrkin, E. Monroy, E. Valcheva, and K. Kirilov, "The microstructure and properties of InN layers," *Phys. Status Solidi (C)*, vol. 7, pp. 1301–1304, 2010.

[37] Q. Zhang, X. Q. Wang, X. W. He, C. M. Yin, F. J. Xu, B. Shen, Y. H. Chen, Z. G. Wang, Y. Ishitani, and A. Yoshikawa, "Lattice polarity detection of InN by circular photogalvanic effect," *Appl. Phys. Lett.*, vol. 95, p. 031902, 2009.

[38] D. Muto, T. Araki, H. Naoi, F. Matsuda, and Y. Nanishi, "Polarity determination of InN by wet etching," *Phys. Status Solidi (A)*, vol. 202, pp. 773–776, 2005.

[39] D. Zhuang and J. H. Edgar, "Wet etching of GaN, AlN, and SiC: a review," *Mat. Sci. Eng. R*, vol. 48, pp. 1–46, 2005.

[40] T. D. Veal, P. D. C. King, P. H. Jefferson, L. F. J. Piper, C. F. McConville, H. Lu, W. J. Schaff, P. A. Anderson, S. M. Durbin, D. Muto, H. Naoi, and Y. Nanishi, "In adlayers on c-plane InN surfaces: a polarity-dependent study by x-ray photoemission spectroscopy," *Phys. Rev. B*, vol. 76, p. 075313, 2007.

[41] S. Ploch, J. Bum Park, J. Stellmach, T. Schwaner, M. Frentrup, T. Niermann, T. Wernicke, M. Pristovsek, M. Lehmann, and M. Kneissl, "Single phase $\{11\bar{2}2\}$GaN on $\{10\bar{1}0\}$ sapphire grown by metal-organic vapor phase epitaxy," *J. Cryst. Growth*, vol. 331, pp. 25–28, 2011.

[42] K. Kusakabe, D. Terui, T. Yamazaki, I. Hashimoto, and K. Ohkawa, "An orthogonal surface phase in semipolar GaN/*r*-plane sapphire," *Appl. Phys. Lett.*, vol. 92, p. 171912, 2008.

[43] T. L. Tansley and C. P. Foley, "Optical band gap of indium nitride," *Appl. Phys. Lett.*, vol. 59, pp. 3241–3244, 1986.

[44] K. Ikuta, Y. Inoue, and O. Takai, "Optical and electrical properties of InN thin films grown on ZnO/α-Al_2O_3 by RF reactive magnetron sputtering," *Thin Solid Films*, vol. 59, pp. 49–53, 1998.

[45] T. Yodo, Y. Kitayama, K. Miyaki, H. Yona, and Y. Harada, "Influences of In_2O_3 Crystal Grains Formed by Annealing on Characteristics of Hexagonal InN

Crystalline Films Grown on Si(111) Substrates," *Jap. J. Appl. Phys.*, vol. 43, pp. L139–L141, 2004.

[46] G. Koblmüller, C. S. Gallinat, S. Bernardis, J. S. Speck, G. D. Chern, E. D. Readinger, H. Shen, and M. Wraback, "Optimization of the surface and structural quality of N-face InN grown by molecular beam epitaxy," *Appl. Phys. Lett.*, vol. 89, p. 071902, 2006.

[47] S. N. Mohammad and H. Morkoç, "Progress and prospects of group-III nitride semiconductors," *Prog. Quantum Electron.*, vol. 20, pp. 361–525, 1996.

[48] B. R. Nag, "Electron mobility in indium nitride," *J. Cryst. Growth*, vol. 269, pp. 35–40, 2004.

[49] P. D. C. King, T. D. Veal, C. F. McConville, F. Fuchs, J. Furthmüller, F. Bechstedt, J. Schörmann, D. J. As, K. Lischka, H. Lu, and W. J. Schaff, "Valence band density of states of zinc-blende and wurtzite InN from x-ray photoemission spectroscopy and first-principles calculations," *Phys. Rev. B*, vol. 77, p. 115213, 2008.

[50] C. Stampfl and C. G. Van de Walle, "Density-functional calculations for III-V nitrides using the local-density approximation and the generalized gradient approximation," *Phys. Rev. B*, vol. 59, pp. 5521–5535, 1999.

[51] J. Furthmüller, P. H. Hahn, F. Fuchs, and F. Bechstedt, "Band structures and optical spectra of InN polymorphs: Influence of quasiparticle and excitonic effects," *Phys. Rev. B*, vol. 72, p. 205106, 2005.

[52] F. Bechstedt, *Nitrides as seen by a theorist: Low-Dimensional Nitride Semiconductors*. edited by B. Gil, p.11, Oxford Univercity Press, Oxford, 2002.

[53] J. Tersoff, "Schottky barriers and semiconductor band structures," *Phys. Rev. B*, vol. 32, pp. 6968–6971, 1985.

[54] F. Bechstedt, F. Fuchs, and J. Furthmüller, "Spectral properties of InN and its native oxide from first principles," *Phys. Status Solidi (A)*, vol. 207, pp. 1041–1053, 2010.

[55] P. D. C. King, T. D. Veal, P. H. Jefferson, S. A. Hatfield, L. F. J. Piper, C. F. McConville, F. Fuchs, J. Furthmüller, F. Bechstedt, H. Lu, and W. J. Schaff, "Determination of the branch-point energy of InN: Chemical trends in common-cation and common-anion semiconductors," *Phys. Rev. B*, vol. 77, p. 045316, 2008.

[56] P. D. C. King, T. D. Veal, C. F. McConville, F. Fuchs, J. Furthmüller, F. Bechstedt, P. Schley, R. Goldhahn, J. Schörmann, D. J. As, K. Lischka, D. Muto, H. Naoi, Y. Nanishi, H. Lu, and W. J. Schaff, "Universality of electron accumulation at wurtzite *c*- and *a*-plane and zinc-blende InN surfaces," *Appl. Phys. Lett.*, vol. 91, p. 092101, 2007.

[57] W. M. Linhart, T. D. Veal, P. D. C. King, G. Koblmüller, C. S. Gallinat, J. S. Speck, and C. F. McConville, "Surface, bulk, and interface electronic properties of nonpolar InN," *Appl. Phys. Lett.*, vol. 97, p. 112103, 2010.

[58] C.-L. Wu, H.-M. Lee, C.-T. Kuo, C.-H. Chen, and S. Gwo, "Absence of Fermi-Level Pinning at Cleaved Nonpolar InN Surfaces," *Phys. Rev. Lett.*, vol. 101, p. 106803, 2008.

[59] P. Ebert, S. Schaafhausen, A. Lenz, A. Sabitova, L. Ivanova, M. Dähne, Y.-L. Hong, S. Gwo, and H. Eisele, "Direct measurement of the band gap and Fermi level position at InN($11\bar{2}0$)," *Appl. Phys. Lett.*, vol. 98, p. 062103, 2011.

[60] L. Ley, R. Pollak, F. R. McFeely, S. P. Kowalczyk, and D. A. Shirley, "Total valence-band densities of states of III-V and II-VI compounds from x-ray photoemission spectroscopy," *Phys. Rev. B*, vol. 9, pp. 600–621, 1974.

[61] A. R. Smith, R. M. Feenstra, D. W. Greve, M. S. Shin, M. Skowronski, J. Neugebauer, and J. E. Northrup, "Reconstructions of GaN(0001) and ($000\bar{1}$) surfaces: Ga-rich metallic structures," *J. Vac. Sci. Technol. B*, vol. 16, pp. 2242–2249, 1998.

[62] M. Himmerlich, A. Eisenhardt, J. A. Schaefer, and S. Krischok, "PAMBE growth and in-situ characterisation of clean (2×2) and $(\sqrt{3}\times\sqrt{3})\,\mathrm{R}30^\circ$ reconstructed InN(0001) thin films," *Phys. Status Solidi (B)*, vol. 246, pp. 1173–1176, 2009.

[63] J. Wang, R. So, Y. Liu, H. Wu, M. Xie, and S. Tong, "Observation of a $(\sqrt{3}\times\sqrt{3})\mathrm{R}\pm30^\circ$ reconstruction on GaN(0001) by RHEED and LEED," *Surface Science*, vol. 600, pp. L169–L174, 2006.

[64] A. Smith, R. Feenstra, D. Greve, M.-S. Shin, M. Skowronski, J. Neugebauer, and J. Northrup, "GaN(0001) surface structures studied using scanning tunneling microscopy and first-principles total energy calculations," *Surface Science*, vol. 423, pp. 70–84, 1999.

[65] A. R. Smith, R. M. Feenstra, D. W. Greve, J. Neugebauer, and J. E. Northrup, "Reconstructions of the GaN ($000\bar{1}$) Surface," *Phys. Rev. Lett.*, vol. 79, p. 3934, 1997.

[66] C. Friedrich, A. Biermann, V. Hoffmann, M. Kneissl, N. Esser, and P. Vogt, "Preparation and atomic structure of reconstructed (0001) InGaN surfaces," *J. Appl. Phys.*, vol. 112, p. 033509, 2012.

[67] R. P. Bhatta, B. D. Thoms, M. Alevli, V. Woods, and N. Dietz, "Surface structure, composition, and polarity of indium nitride grown by high-pressure chemical vapor deposition," *Appl. Phys. Lett.*, vol. 88, p. 122112, 2006.

[68] C.-T. Kuo, S.-C. Lin, K.-K. Chang, H.-W. Shiu, L.-Y. Chang, C.-H. Chen, S.-J. Tang, and S. Gwo, "Is electron accumulation universal at InN polar surfaces?," *Appl. Phys. Lett.*, vol. 98, p. 052101, 2011.

[69] T. D. Veal, P. D. C. King, M. Walker, C. F. McConville, H. Lu, and W. J. Schaff, "In-adlayers on non-polar and polar InN surfaces: Ion scattering and photoemission studies," *Physica B: Condensed Matter*, vol. 401-402, pp. 351–354, 2007.

[70] D. Segev and C. G. Van de Walle, "Surface reconstructions on InN and GaN polar and nonpolar surfaces," *Surf. Sci.*, vol. 601, pp. L15–L18, 2007.

[71] C. K. Gan and D. J. Srolovitz, "First-principles study of wurtzite InN (0001) and $(000\bar{1})$ surfaces," *Phys. Rev. B*, vol. 74, p. 115319, 2006.

[72] C. Nörenberg, M. G. Martin, R. A. Oliver, M. R. Castell, and G. A. D. Briggs, "Heteroepitaxial growth of InN islands studied by STM and AFM," *J. Phys. D: Appl. Phys.*, vol. 35, pp. 615–619, 2002.

[73] H. Zheng, M. Xie, and Q. Xue, "Ordered versus random nucleation of InN islands grown by molecular beam epitaxy," *Surface Science*, vol. 606, pp. 120–123, 2012.

[74] C. D. Lee, Y. Dong, R. M. Feenstra, J. E. Northrup, and J. Neugebauer, "Reconstructions of the AlN(0001) surface," *Phys. Rev. B*, vol. 68, p. 205317, 2003.

[75] C. G. Van de Walle and D. Segev, "Microscopic origins of surface states on nitride surfaces," *J. Appl. Phys.*, vol. 101, p. 081704, 2007.

[76] D. Segev and C. G. Van de Walle, "Electronic structure of nitride surfaces," *J. Cryst. Growth*, vol. 300, pp. 199–203, 2007.

[77] D. Segev and C. G. V. D. Walle, "Origins of Fermi-level pinning on GaN and InN polar and nonpolar surfaces," *Europhys. Lett.*, vol. 76, pp. 305–311, 2006.

[78] E. Sakalauskas, P. Schley, J. Räthel, T. A. Klar, R. Müller, J. Pezoldt, K. Tonisch, J. Grandal, M. A. Sánchez-García, E. Calleja, A. Vilalta-Clemente, P. Ruterana, and R. Goldhahn, "Optical properties of InN grown on Si(111) substrate," *Phys. Status Solidi (A)*, vol. 207, no. 5, pp. 1066–1069, 2010.

[79] A. Yamamoto, M. Tsujino, M. Ohkubo, and A. Hashimoto, "Nitridation effects of substrate surface on the metalorganic chemical vapor deposition growth of InN on Si and alpha-Al_2O_3 substrates," *J. Cryst. Growth*, vol. 137, pp. 415–420, 1994.

[80] B. Maleyre, S. Ruffenach, O. Briot, B. Gil, and A. van der Lee, "Investigation of the influence of buffer and nitrided layers on the initial stages of InN growth on sapphire by MOCVD," *Phys. Status Solidi (C)*, vol. 2, pp. 2309–2315, 2005.

[81] Y.-C. Pan, W.-H. Lee, C.-K. Shu, H.-C. Lin, C.-I. Chiang, H. Chang, D.-S. Lin, M.-C. Lee, and W.-K. Chen, "Influence of Sapphire Nitridation on Properties of Indium Nitride Prepared by Metalorganic Vapor Phase Epitaxy," *Jpn. J. Appl. Phys.*, vol. 38, pp. 645–648, 1999.

[82] M. Drago, C. Werner, M. Pristovsek, U. W. Pohl, and W. Richter, "InN growth on sapphire using different nitridation procedures," *Phys. Status Solidi (A)*, vol. 203, pp. 1622–1625, 2006.

[83] M. Drago, P. Vogt, and W. Richter, "MOVPE growth of InN with ammonia on sapphire," *Phys. Status Solidi (a)*, vol. 203, pp. 116–126, Jan. 2006.

[84] D. V. Dinh, D. Skuridina, S. Solopow, M. Pristovsek, P. Vogt, and M. Kneissl, "Role of nitridation on polarity and growth of InN by metal-organic vapor phase epitaxy," *J. Cryst. Growth*, vol. 376, pp. 17–22, 2013.

[85] D. V. Dinh, D. Skuridina, S. Solopow, M. Frentrup, M. Pristovsek, P. Vogt, M. Kneissl, F. Ivaldi, S. Kret, and A. Szczepańska, "Growth and characterizations of semipolar $(11\bar{2}2)$ InN," *J. Appl. Phys.*, vol. 112, p. 013530, 2012.

[86] S. Ploch, T. Wernicke, D. V. Dinh, M. Pristovsek, and M. Kneissl, "Surface diffusion and layer morphology of $(11\bar{2}2)$ GaN grown by metal-organic vapor phase epitaxy," *J. Appl. Phys.*, vol. 111, p. 033526, 2012.

[87] K. S. A. Butcher, P. P.-T. Chen, and J. E. Downes, "Low activation energy for the removal of excess nitrogen in nitrogen rich indium nitride," *Appl. Phys. Lett.*, vol. 100, p. 011913, 2012.

[88] G. Binnig and H. Rohrer, "Scanning tunneling microscopy," *Helv. Phys. Acta*, vol. 55, pp. 726–735, 1982.

[89] G. Binnig, H. Rohrer, C. Gerber, and E. Weibel, "Tunneling through a controllable vacuum gap," *Appl. Phys. Lett.*, vol. 40, p. 178, 1982.

[90] G. Binnig and H. Rohrer, "Scanning tunneling microscopy," *Surf. Sci.*, vol. 126, pp. 236–244, 1983.

[91] J. Bardeen, "Tunneling from a many-particle point of view," *Phys. Rev. Lett.*, vol. 6, pp. 57–59, 1961.

[92] J. Tersoff and D. R. Hamann, "Theory and application for the scanning tunneling microscope," *Phys. Rev. Lett.*, vol. 50, pp. 1998–2001, 1983.

[93] J. Tersoff and D. R. Hamann, "Theory of the scanning tunneling microscope," *Phys. Rev. B*, vol. 31, p. 805, 1985.

[94] D. Bonnell, *Scanning tunneling microscopy and spectroscopy: theory, techniques, and applications*. John Wiley and Sons Canada, Limited, 1993.

[95] T. Sakurai and Y. Watanabe, *Advances in scanning probe microscopy*. Advances in materials research, Springer, 2000.

[96] H. Güntherodt and R. Wiesendanger, *Scanning tunneling microscopy I: general principles and applications to clean and adsorbate-covered surfaces*. Scanning Tunneling Microscopy, Springer-Verlag, 1994.

[97] H. Güntherodt and R. Wiesendanger, *Scanning tunneling microscopy II: further applications and related scanning techniques*. Scanning Tunneling Microscopy, 2nd Edition Springer-Verlag Berlin Heidelberg New-York, 1995.

[98] H. Güntherodt and R. Wiesendanger, *Scanning tunneling microscopy III: theory of STM and related scanning probe methods*. Scanning Tunneling Microscopy, 2nd Edition Springer-Verlag Berlin Heidelberg New-York, 1996.

[99] R. M. Feenstra, W. A. Thompson, and A. P. Fein, "Real-space obsevation of *pi*-bonded chains and surface disorded on Si(111) 2×1," *Phys. Rev. Lett.*, vol. 56, pp. 608–612, 1986.

[100] J. A. Stroscio, R. M. Feenstra, and A. P. Fein, "Electronic structure of the Si(111) 2×1 surface by scanning-tunneling microscopy," *Phys. Rev. Lett.*, vol. 57, pp. 2579–2583, 1986.

[101] H. R. Hertz, "Über einen Einfluss des ultravioletten Lichtes auf die elektrische Entladung," *Ann. Phys.*, vol. 31, p. 983, 1887.

[102] J. J. Thompson, "Cathode Rays," *Phil. Mag.*, vol. 44, p. 293, 1897.

[103] P. Lenard, "Über die lichtelektrische Wirkung," *Ann. Phys.*, vol. 8, p. 149, 1902.

[104] A. Einstein, "Über einen Erzeugung und Verwandlung des Lichtes betreffenden heuristischen Gesichtspunkt," *Ann. Phys.*, vol. 17, p. 132, 1905.

[105] S. Hüfner, *Photoelectron spectroscopy: principles and applications*. Springer series in solid-state sciences, Springer, 2003.

[106] M. P. Seah and W. A. Dench, "Quantitative electron spectroscopy of surfaces : a standart data base for electron inelastic mean free paths in solids," *Surf. Interf. Anal.*, vol. 1, p. 2, 1979.

[107] K. A. Bertness, J.-J. Yeh, D. J. Friedman, P. H. Mahowald, A. K. Wahi, T. Kendelewicz, I. Lindau, and W. E. Spicer, "Growth structure of chemisorbed oxygen on GaAs(110) and InP(110) surfaces," *Phys. Rev. B*, vol. 38, pp. 5406–5421, 1988.

[108] D. Briggs and P. Seah, *Practical surface analysis: by auger and x-ray photoelectron spectroscopy*. Wiley, 1983.

[109] D. Vij, *Handbook of applied solid state spectroscopy*. Springer, 2010.

[110] J. Watts and J. Wolstenholme, *An introduction to surface analysis by XPS and AES*. Wiley, 2003.

[111] R. Hesse, T. Chassé, and R. Szargan, "Peak shape analysis of core level photoelectron spectra using UNIFIT for WINDOWS," *Fresenius. J. Anal. Chem.*, vol. 365, pp. 48–54, 1999.

[112] S. A. Chambers, T. Droubay, T. C. Kaspar, and M. Gutowski, "Experimental determination of valence band maxima for $SrTiO_3$, TiO_2, and SrO and the associated valence band offsets with Si(001)," *J. Vac. Sci. Technol. B*, vol. 22, p. 2205, 2004.

[113] J. Yeh and I. Lindau, "Atomic subshell photoionization cross sections and asymmetry parameters: $1 \leq Z \leq 103$," *At. Data Nucl. Data Tables*, vol. 32, pp. 1–155, 1985.

[114] J. Yeh, *Atomic calculation of photoionization cross-sections and asymmetry parameters*. Gordon and Breach Science Publishers, Langhorne, PE (USA), 1993.

[115] *CasaXPS Processing Software for XPS Spectra. CasaXPS Manual 2.3.15 Rev 1.0.* Casa Software Ltd., 2009.

[116] M. P. Auger *Compt. Rend.*, vol. 180, p. 65, 1925.

[117] D. Chattarji, *The theory of Auger transitions*. Academic Press, 1976.

[118] T. Carlson, *Photoelectron and Auger spectroscopy*. Modern analytical chemistry, Plenum Press, 1975.

[119] G. McGuire, *Auger electron spectroscopy reference manual: a book of standard spectra for identification and interpretation of Auger electron spectroscopy data*. Plenum Press, 1979.

[120] J. Hudson, *Surface science: an introduction*. Wiley Interscience publication, Wiley, 1998.

[121] G. Ertl and J. Küppers, *Low energy electrons and surface chemistry*. VCH, 1985.

[122] K. A. Rickert, A. B. Ellis, F. J. Himpsel, H. Lu, W. Schaff, J. M. Redwing, F. Dwikusuma, and T. F. Kuech, "X-ray photoemission spectroscopic investigation of surface treatments, metal deposition, and electron accumulation on InN," *Appl. Phys. Lett.*, vol. 82, p. 3254, 2003.

[123] T. Ohashi, Y. Saito, T. Maruyama, and Y. Nanishi, "Effect of atomic hydrogen irradiation on native oxides of InN surface," *J. Cryst. Growth*, vol. 237-239, pp. 1022–1026, 2002.

[124] C. F. Shih, N. C. Chen, and C. Y. Tseng, "Photoelectron spectroscopic investigation of InN and InN/GaN heterostructures," *Thin Solid Films*, vol. 516, pp. 5016–5019, 2008.

[125] C. P. Foley and J. Lyngdal, "Analysis of indim nitride surface oxidation," *J. Vac. Sci. Technol. A*, vol. 5, pp. 1708–1712, 1987.

[126] L. F. J. Piper, T. D. Veal, P. H. Jefferson, C. F. McConville, F. Fuchs, J. Furthmüller, F. Bechstedt, H. Lu, and W. Schaff, "Valence-band structure of InN from x-ray photoemission spectroscopy," *Phys. Rev. B*, vol. 72, p. 245319, 2005.

[127] S. Krischok, V. Yanev, O. Balykov, M. Himmerlich, J. Schaefer, R. Kosiba, G. Ecke, I. Cimalla, V. Cimalla, O. Ambacher, H. Lu, W. J. Schaff, and L. F. Eastman, "Investigations of MBE grown InN and the influence of sputtering on the surface composition," *Surf. Sci.*, vol. 566-568, pp. 849–855, 2004.

[128] F. Litimein, B. Bouhafs, and P. Ruterana, "Full-potential study of d-electrons effects on the electronic structure of wurtzite and zinc-blende InN," *Phys. Status Solidi (A)*, vol. 203, pp. 35–41, 2006.

[129] A. Eisenhardt, S. Reiss, M. Himmerlich, J. A. Schaefer, and S. Krischok, "Changes in the valence band structure of as-grown InN(0001) - 2×2 surfaces upon exposure to oxygen and water," *Phys. Status Solidi (A)*, vol. 207, pp. 1037–1040, 2010.

[130] A. Eisenhardt, M. Himmerlich, and S. Krischok, "Characterization of as-grown and adsorbate-covered N-polar InN surfaces using *in situ* photoelectron spectroscopy," *Phys. Status Solidi (A)*, vol. 209, pp. 45–49, 2012.

[131] H. Naoi, D. Muto, T. Hioka, Y. Hayakawa, A. Suzuki, T. Araki, and Y. Nanishi, "Thermal and chemical stabilities of In- and N-polar InN surfaces," *Phys. Status Solidi (B)*, vol. 244, pp. 1834–1838, 2007.

[132] P. Vermaut, P. Ruterana, and G. Nouet, "Polarity of epitaxial layers and $(\bar{1}2\bar{1}0)$ prismatic defects in GaN and AlN grown on the $(0001)_{Si}$ surface of 6H-SiC," *Philos. Mag. A*, vol. 76, pp. 1215–1234, 1997.

[133] P. A. Stadelmann, "EMS - a software package for electron difitraction analysis and HREM image simulation in materials science," *Ultramicroscopy*, vol. 21, pp. 131–145, 1987.

[134] X. J. Ning, F. R. Chien, P. Pirouz, J. W. Yang, and M. A. Khan, "Growth defects in GaN films on sapphire: The probable origin of threading dislocations," *J. Mater. Res.*, vol. 11, pp. 580–592, 1996.

[135] V. Potin, G. Nouet, and P. Ruterana, "The $\{10\bar{1}0\}$ inversion domains in GaN/sapphire layers: an electron microscopy analysis of the atomic structure of the boundaries," *Philos. Mag. A*, vol. 79, pp. 2899–2919, 1999.

[136] R. Groh, G. Gerey, L. Bartha, and J. I. Pankove, "On the thermal decomposition of GaN in vacuum," *Phys. Status Solidi (A)*, vol. 26, pp. 353–357, 1974.

[137] W. R. L. Lambrecht, B. Segall, S. Strite, G. Martin, A. Agarwal, H. Morkoç, and A. Rockett, "X-ray photoelectron spectroscopy and theory of the valence band and semicore Ga 3d states in GaN," *Phys. Rev. B*, vol. 50, pp. 14155–14160, 1994.

[138] B. Bouhafs, F. Litimein, Z. Dridi, and P. Ruterana, "Theoretical analysis of d electron effects on the electronic properties of wurtzite and zincblende GaN," *Phys. Status Solidi (B)*, vol. 236, pp. 61–81, 2003.

[139] V. M. Bermudez, "Study of oxygen chemisorption on the GaN(0001)(1×1) surface," *J. Appl. Phys.*, vol. 80, p. 1190, 1996.

[140] M. Eickhoff, Neuberger, R. G. Steinhoff, O. Ambacher, G. Müller, and M. Stutzmann, "Wetting behaviour of GaN surfaces with Ga- or N-Face polarity," *Phys. Status Solidi (B)*, vol. 228, pp. 519–522, 2001.

[141] T. K. Zywietz, J. Neugebauer, and M. Scheffler, "The adsorption of oxygen at GaN surfaces," *Appl. Phys. Lett.*, vol. 74, p. 1695, 1999.

[142] M. W. Allen, D. Y. Zemlyanov, G. I. N. Waterhouse, J. B. Metson, T. D. Veal, C. F. McConville, and S. M. Durbin, "Polarity effects in the x-ray photoemission of ZnO and other wurtzite semiconductors," *Appl. Phys. Lett.*, vol. 98, p. 101906, 2011.

[143] T. M. French and G. A. Somorjai, "Composition and Surface structure of the (0001) Face of alpha-Alumina by Low-Energy Electron Diffraction," *J. Phys. Chem.*, vol. 74, p. 2489, 1970.

[144] P. S. P. Wei and A. W. Smith, "Structure of the (0001) surface of alpha-alumina," *J. Vac. Sci. Technol.*, vol. 9, p. 1209, 1972.

[145] E. A. Soares, M. A. Van Hove, C. F. Walters, and K. F. McCarty, "Structure of the α-Al_2O_3 (0001) surface from low-energy electron diffraction: Al termination and evidence for anomalously large thermal vibrations," *Phys. Rev. B*, vol. 65, p. 195405, 2002.

[146] B. Agnarsson, M. Göthelid, S. Olafsson, H. P. Gislason, and U. O. Karlsson, "Influence of initial surface reconstruction on nitridation of Al_2O_3 (0001) using low pressure ammonia," *J. Appl. Phys.*, vol. 101, p. 013519, 2007.

[147] A. Koukitu, N. Takahashi, T. Taki, and H. Seki, "Thermodynamic analysis of $In_xGa_{1-x}N$ alloy composition grown by metalorganic vapor phase epitaxy," *Jpn. J. Appl. Phys.*, vol. 35, pp. L673–L675, 1996.

[148] P. Vennéguès and B. Beaumont, "Transmission electron microscopy study of the nitridation of the (0001) sapphire surface," *Appl. Phys. Lett.*, vol. 75, pp. 4115–4117, 1999.

[149] K. Uchida, A. Watanabe, F. Yano, M. Kouguchi, T. Tanaka, and S. Minagawa, "Nitridation process of sapphire substrate surface and its effect on the growth of GaN," *J. Appl. Phys.*, vol. 79, pp. 3487–3491, 1996.

[150] F. Pesty and P. Garoche, "Low-energy electron beam on an insulator surface: Impact of the charging process on the diffraction by mica muscovite," *Surf. Sci.*, vol. 580, pp. 153–162, 2005.

[151] F. Dwikusuma and T. F. Kuech, "X-ray photoelectron spectroscopic study on sapphire nitridation for GaN growth by hydride vapor phase epitaxy: Nitridation mechanism," *J. Appl. Phys.*, vol. 94, p. 5656, 2003.

[152] C. Heinlein, J. Grepstad, T. Berge, and H. Riechert, "Preconditioning of *c*-plane sapphire for GaN epitaxy by radio frequency plasma nitridation," *Appl. Phys. Lett.*, vol. 71, pp. 341–343, 1997.

[153] L. Rosenberger, R. Baird, E. McCullen, G. Auner, and G. Shreve, "XPS analysis of aluminum nitride films deposited by plasma source molecular beam epitaxy," *Surf. Interface Anal.*, vol. 40, pp. 1254–1261, 2008.

[154] T. Hashimoto, Y. Terakoshi, M. Ishida, M. Yuri, O. Imafuji, T. Sugino, A. Yoshikawa, and K. Itoh, "Structural investigation of sapphire surface after nitridation," *J. Cryst. Growth*, vol. 189-190, pp. 254–258, 1998.

[155] A. Costales, M. A. Blanco, A. M. Pendás, A. K. Kandalam, and R. Pandey, "Chemical bonding in group III nitrides," *J. Am. Chem. Soc.*, vol. 124, pp. 4116–4123, 2002.

[156] N. Laidani, L. Vanzetti, M. Anderle, A. Basillais, C. Boulmer-Leborgne, and J. Perriere, "Chemical structure of films grown by AlN laser ablation: an X-ray photoelectron spectroscopy study," *Surf. Coat. Technol.*, vol. 122, pp. 242–246, 1999.

[157] P. Prieto and R. E. Kirby, "X-ray photoelectron spectroscopy study of the difference between reactively evaporated and direct sputter-deposited TiN films and their oxidation properties," *J. Vac. Sci. Technol. A*, vol. 13, p. 2819, 1995.

[158] M. Losurdo, P. Capezzuto, G. Bruno, G. Namkoong, W. A. Doolittle, and A. S. Brown, "Role of sapphire nitridation temperature on GaN growth by plasma assisted molecular beam epitaxy: Part II. Interplay between chemistry and structure of layers," *J. Appl. Phys.*, vol. 91, p. 2508, 2002.

[159] P. Ruterana, V. Potin, B. Barbaray, and G. Nouet, "Growth defects in GaN layers on top of (0001) sapphire: a geometrical investigation of the misfit effect," *Philos. Mag. A*, vol. 80, p. 937, 2000.

[160] S. X. Li, K. M. Yu, J. Wu, R. E. Jones, W. Walukiewicz, J. W. Ager, W. Shan, E. E. Haller, H. Lu, and W. J. Schaff, "Fermi-level stabilization energy in group III nitrides," *Phys. Rev. B*, vol. 71, p. 161201(R), 2005.

[161] T. D. Veal, P. H. Jefferson, L. F. J. Piper, C. F. McConville, T. B. Joyce, P. R. Chalker, L. Considine, H. Lu, and W. J. Schaff, "Transition from electron accumulation to depletion at InGaN surfaces," *Appl. Phys. Lett.*, vol. 89, no. 20, p. 202110, 2006.

[162] D. V. Dinh, *MOVPE growth of InN and InGaN with different surface orientations*. PhD Thesis, TU Berlin, 2012.

[163] T. Hino, S. Tomiya, T. Miyajima, K. Yanashima, S. Hashimoto, and M. Ikeda, "Characterization of threading dislocations in GaN epitaxial layers," *Appl. Phys. Lett.*, vol. 76, p. 3421, 2000.

[164] V. Darakchieva, K. Lorenz, M.-Y. Xie, E. Alves, L. C. Hsiao, L. C. Chen, L. W. Tu, W. J. Schaff, T. Yamaguchi, and Y. Nanishi, "Unintentional incorporation of hydrogen in wurtzite InN with different surface orientations," *J. Appl. Phys.*, vol. 110, p. 063535, 2011.

[165] L. F. J. Piper, T. D. Veal, M. Walker, I. Mahboob, C. F. McConville, H. Lu, and W. J. Schaff, "Clean wurtzite InN surfaces prepared with atomic hydrogen," *J. Vac. Sci. Technol. A*, vol. 23, p. 617, 2005.

[166] F. Werner, F. Limbach, M. Carsten, C. Denker, J. Malindretos, and A. Rizzi, "Electrical Conductivity of InN Nanowires and the Influence of the Native Indium Oxide Formed at Their Surface," *Nano Lett.*, vol. 9, pp. 1567–1571, 2009.

[167] S. Strite and H. Morkoç, "GaN, AIN, and InN: A review," *J. Vac. Sci. Technol. B*, vol. 10, pp. 1237–1266, 1992.

[168] O. Ambacher, R. Dimitrov, M. Stutzmann, B. Foutz, M. Murphy, J. Smart, J. Shealy, N. Weimann, K. Chu, M. Chumbes, B. Green, A. Sierakowski, W. Schaff, and L. Eastman, "Role of spontaneous and piezoelectric polarization induced effects in group-III nitride based heterostructures and devices," *Phys. Status Solidi (B)*, vol. 216, pp. 381–389, 1999.

[169] T. Böttcher, *Heteroepitaxy of group-III nitrides for the application in laser diodes*. PhD Thesis, University of Bremen, 2002.

[170] A. Eisenhardt, G. Eichapfel, M. Himmerlich, A. Knübel, T. Passow, C. Wang, F. Benkhelifa, R. Aidam, and S. Krischok, "Valence band offsets at oxide/InN interfaces determined by X-ray photoelectron spectroscopy," *Phys. Status Solidi (C)*, vol. 9, pp. 685–688, 2012.

[171] T. Nagata, G. Koblmüller, O. Bierwagen, C. S. Gallinat, and J. S. Speck, "Surface structure and chemical states of a-plane and c-plane InN films," *Appl. Phys. Lett.*, vol. 95, p. 132104, 2009.

[172] I. Bello, W. M. Lau, R. P. W. Lawsom, and K. K. Foo, "Deposition of indium nitride by low energy modulated indium and nitrogen ion beams," *J. Vac. Sci. Technol. A*, vol. 10, p. 1642, 1992.

[173] Z. Majlinger, A. Bozanic, M. Petravic, K.-J. Kim, B. Kim, and Y.-W. Yang, "NEXAFS and XPS study of GaN formation on ion-bombarded GaAs surfaces," *Vacuum*, vol. 84, pp. 41–44, 2009.

[174] A. Bozanic, Z. Majlinger, M. Petravic, Q. Gao, D. Llewellyn, C. Crotti, and Y.-W. Yang, "Characterization of molecular nitrogen in III-V compound semiconductors by near-edge x-ray absorption fine structure and photoemission spectroscopies," *J. Vac. Sci. Technol. A*, vol. 26, p. 592, 2008.

[175] A. Minj, D. Cavalcoli, and A. Cavallini, "Indium segregation in AlInN/AlN/GaN heterostructures," *Appl. Phys. Lett.*, vol. 97, p. 132114, 2010.

[176] R. M. Feenstra, J. A. Stroscio, J. Tersoff, and A. P. Fein, "Atom-selective imaging of the GaAs(110) surface," *Phys. Rev. Lett.*, vol. 58, p. 1192, 1987.

[177] P. Ebert, L. Ivanova, and H. Eisele, "Scanning tunneling microscopy on unpinned GaN($1\bar{1}00$) surfaces: Invisibility of valence-band states," *Phys. Rev. B*, vol. 80, p. 085316, 2009.

[178] I. J. Lee, H. T.-B. Yu, Chung-Jong, K. Hyung-Kook, C.-O. Kim, and J.-Y. Kim, "Observation of Complete Oxidation of InN to In_2O_3 in Air at Elevated Temperatures by Using X-ray Photoemission Spectroscopy," *J. Korean Phys. Soc.*, vol. 49, pp. 2176–2179, 2006.

[179] I. J. Lee, J.-Y. Kim, T.-B. Hur, and H.-K. Kim, "Oxidation study of InN/sapphire (0001) film using in-situ synchrotron X-ray scattering," *Phys. Stat. Sol. (A)*, vol. 201, pp. 2777–2781, 2004.

[180] A. Walsh, J. Da Silva, S.-H. Wei, C. Körber, A. Klein, L. Piper, A. DeMasi, K. Smith, G. Panaccione, P. Torelli, D. Payne, A. Bourlange, and R. Egdell, "Nature of the Band Gap of In_2O_3 Revealed by First-Principles Calculations and X-Ray Spectroscopy," *Phys. Rev. Lett.*, vol. 100, p. 167402, 2008.

[181] A. Bourlange, D. J. Payne, R. G. Egdell, J. S. Foord, P. P. Edwards, M. O. Jones, A. Schertel, P. J. Dobson, and J. L. Hutchison, "Growth of In_2O_3(100) on Y-stabilized ZrO_2(100) by O-plasma assisted molecular beam epitaxy," *Appl. Phys. Lett.*, vol. 92, p. 092117, 2008.

[182] C. Y. Wang, V. Lebedev, V. Cimalla, T. Kups, K. Tonisch, and O. Ambacher, "Structural studies of single crystalline In_2O_3 films epitaxially grown on InN(0001)," *Appl. Phys. Lett.*, vol. 90, p. 221902, 2007.

[183] H. F. Liu, D. Z. Chi, and W. Liu, "Layer-by-layer oxidation of InN(0001) thin films into body-center cubic In_2O_3(111) by cycle rapid thermal annealing," *Cryst. Eng. Comm.*, vol. 14, p. 7140, 2012.

[184] S. Sadofev, Y. Cho, O. Brandt, M. Ramsteiner, R. Calarco, H. Riechert, S. C. Erwin, Z. Galazka, M. Korytov, M. Albrecht, R. Uecker, and R. Fornari, "Growth of wurtzite InN on bulk In_2O_3(111) wafers," *Appl. Phys. Lett.*, vol. 101, p. 172102, 2012.

[185] V. Lebedev, C. Y. Wang, V. Cimalla, S. Hauguth, T. Kups, M. Ali, G. Ecke, M. Himmerlich, S. Krischok, J. a. Schaefer, O. Ambacher, V. M. Polyakov, and F. Schwierz, "Effect of surface oxidation on electron transport in InN thin films," *J. Appl. Phys.*, vol. 101, p. 123705, 2007.

[186] E. H. Morales, Y. He, M. Vinnichenko, B. Delley, and U. Diebold, "Surface structure of Sn-doped In_2O_3 (111) thin films by STM," *New J. Phys.*, vol. 10, p. 125030, 2008.

[187] C. Janowitz, V. Scherer, M. Mohamed, A. Krapf, H. Dwelk, R. Manzke, Z. Galazka, R. Uecker, K. Irmscher, R. Fornari, M. Michling, D. Schmeiß er, J. R. Weber, J. B. Varley, and C. G. V. D. Walle, "Experimental electronic structure of In_2O_3 and Ga_2O_3," *New J. Phys.*, vol. 13, p. 085014, 2011.

[188] K. Pussi, A. Matilainen, V. Dhanak, A. Walsh, R. Egdell, and K. Zhang, "Surface structure of $In_2O_3(111)$ (1×1) determined by density functional theory calculations and low energy electron diffraction," *Surf. Sci.*, vol. 606, pp. 1–6, 2012.

[189] D. R. Hagleitner, M. Menhart, P. Jacobson, S. Blomberg, K. Schulte, E. Lundgren, M. Kubicek, J. Fleig, F. Kubel, C. Puls, A. Limbeck, H. Hutter, L. A. Boatner, M. Schmid, and U. Diebold, "Bulk and surface characterization of $In_2O_3(001)$ single crystals," *Phys. Rev. B*, vol. 85, p. 115441, 2012.

[190] Y. Gassenbauer, R. Schafranek, A. Klein, S. Zafeiratos, M. Hävecker, A. Knop-Gericke, and R. Schlögl, "Surface states, surface potentials, and segregation at surfaces of tin-doped In_2O_3," *Phys. Rev. B*, vol. 73, p. 245312, 2006.

[191] K. H. L. Zhang, D. Payne, R. G. Palgrave, V. K. Lazarov, W. Chen, A. T. S. Wee, C. F. McConville, P. D. C. King, T. D. Veal, G. Panaccione, P. Lacovig, and R. G. Egdell, "Surface Structure and Electronic Properties of In_2O_3 (111) Single-Crystal Thin Films Grown on Y-Stabilized ZrO_2 (111)," *Chem. Mater.*, vol. 21, pp. 4353–4355, 2009.

[192] P. Agoston and K. Albe, "Thermodynamic stability, stoichiometry, and electronic structure of bcc-In_2O_3 surfaces," *Phys. Rev. B*, vol. 84, p. 045311, 2011.

[193] P. King, T. Veal, D. Payne, A. Bourlange, R. Egdell, and C. McConville, "Surface Electron Accumulation and the Charge Neutrality Level in In_2O_3," *Phys. Rev. Lett.*, vol. 101, p. 116808, 2008.

[194] S. Lany, A. Zakutayev, T. O. Mason, J. F. Wager, K. R. Poeppelmeier, J. D. Perkins, J. J. Berry, D. S. Ginley, and A. Zunger, "Surface origin of high conductivities in undoped in_2o_3 thin films," *Phys. Rev. Lett.*, vol. 108, p. 016802, 2012.

[195] E. H. Morales and U. Diebold, "The structure of the polar Sn-doped indium oxide (001) surface," *Appl. Phys. Lett.*, vol. 95, p. 253105, 2009.

[196] M. Segawa, S. Sato, M. Kobune, T. Sodesawa, T. Kojima, S. Nishiyama, and N. Ishizawa, "Vapor-phase catalytic reactions of alcohols over bixbyite indium oxide," *J. Mol. Catal. A: Chem.*, vol. 310, pp. 166–173, 2009.

[197] Z. M. Jarzebski, "Preparation and physical properties of transparent conducting oxide films," *Phys. Status Solidi (A)*, vol. 71, pp. 13–41, 1982.

[198] C. Wang, V. Cimalla, G. Cherkashinin, H. Romanus, M. Ali, and O. Ambacher, "Transparent conducting indium oxide thin films grown by low-temperature metal organic chemical vapor deposition," *Thin Solid Films*, vol. 515, pp. 2921–2925, 2007.

[199] C. Wang, V. Cimalla, H. Romanus, T. Kups, M. Niebelschütz, and O. Ambacher, "Tuning of electrical and structural properties of indium oxide films grown by metal organic chemical vapor deposition," *Thin Solid Films*, vol. 515, pp. 6611–6614, 2007.

[200] A. G. Bhuiyan, A. Hashimoto, and A. Yamamoto, "Indium nitride (InN): A review on growth, characterization, and properties," *J. Appl. Phys.*, vol. 94, pp. 2779–2808, 2003.

[201] E. Kalesaki, L. Lymperakis, J. Kioseoglou, J. Neugebauer, T. Karakostas, and P. Komninou, "Reconstructions and electronic structure of $(11\bar{2}2)$ and $(11\bar{2}\bar{2})$ semipolar AlN surfaces," *J. Appl. Phys.*, vol. 112, p. 033510, 2012.

[202] L. Lahourcade, J. Renard, B. Gayral, E. Monroy, M. P. Chauvat, and P. Ruterana, "Ga kinetics in plasma-assisted molecular-beam epitaxy of GaN$(11\bar{2}2)$: Effect on the structural and optical properties," *J. Appl. Phys.*, vol. 103, p. 093514, 2008.

[203] J. E. Northrup, "GaN and InGaN$(11\bar{2}2)$ surfaces: Group-III adlayers and indium incorporation," *Appl. Phys. Lett.*, vol. 95, p. 133107, 2009.

[204] A. Das, S. Magalhães, Y. Kotsar, P. K. Kandaswamy, B. Gayral, K. Lorenz, E. Alves, P. Ruterana, and E. Monroy, "Indium kinetics during the plasma-assisted molecular beam epitaxy of semipolar (11-22) InGaN layers," *Appl. Phys. Lett.*, vol. 96, p. 181907, 2010.

[205] T. Yamashita, T. Akiyama, K. Nakamura, and T. Ito, "Surface Reconstructions on GaN and InN Semipolar $(11\bar{2}2)$ Surfaces," *Jpn. J. Appl. Phys.*, vol. 48, p. 120201, 2009.

[206] A. Strittmatter, J. E. Northrup, N. M. Johnson, M. V. Kisin, P. Spiberg, H. El-Ghoroury, A. Usikov, and A. Syrkin, "Semi-polar nitride surfaces and heterostructures," *Phys. Status Solidi (B)*, vol. 248, pp. 561–573, 2011.

[207] S. Ploch, T. Wernicke, J. Thalmair, M. Lohr, M. Pristovsek, J. Zweck, M. Weyers, and M. Kneissl, "Topography of $(20\bar{2}1)$ AlGaN, GaN and InGaN layers grown by metal-organic vapor phase epitaxy," *J. Cryst. Growth*, vol. 356, pp. 70–74, 2012.

[208] T. Yamashita, T. Akiyama, K. Nakamura, and T. Ito, "Surface reconstructions on GaN and InN semipolar $(20\bar{2}1)$ surfaces," *Jpn. J. Appl. Phys.*, vol. 49, p. 018001, 2010.

[209] I. L. Koslow, C. Mctaggart, F. Wu, S. Nakamura, J. S. Speck, and S. P. Denbaars, "Improved performance of $(20\bar{2}1)$ long-wavelength light-emitting diodes grown with wide quantum wells on stress-relaxed $In_xGa_{1-x}N$ buffer layers," *Appl. Phys. Express*, vol. 7, p. 031003, 2014.

[210] E. Trybus, G. Namkoong, W. Henderson, S. Burnham, W. Doolittle, M. Cheung, and A. Cartwright, "InN: A material with photovoltaic promise and challenges," *J. Cryst. Growth*, vol. 288, pp. 218–224, 2006.

[211] C.-T. Lee, H.-W. Chen, and H.-Y. Lee, "Metal-oxide-semiconductor devices using Ga_2O_3 dielectrics on n-type GaN," *Appl. Phys. Lett.*, vol. 82, pp. 4304–4306, 2003.

[212] Y. Taniyasu, M. Kasu, and T. Makimoto, "An aluminium nitride light-emitting diode with a wavelength of 210 nanometres.," *Nature*, vol. 441, pp. 325–328, 2006.

Appendix A: Determination of Statistical Significance

Statistical significance is a concept of statistical hypothesis testing. It shows a probability that an observed effect does not occur by chance. The statistical significance is often used to establish the claim that observed experiments happen not by chance alone but caused by some proposed facts. In this work the statistical method was used to determine the statistical significance of the differences between the two polar layers observed by XPS, i.e. between the two $P_{II} : P_I$ mean values for the N-polar and In-polar InN layers.

One of the often used statistical tests is a so-called Student's *t*-test, which is used to determine if two sets of data are significantly enough different from each other. For this work independent two-sample pooled *t*-test with unequal sample size and equal variance was performed. Sample size corresponds to the number of samples in each statistical group. Statistical groups refer to the N-polar and group-III-polar layers. The Student's *t*-test implies a rejection or approval of the null hypothesis which states that any difference between two sets of data is only caused by chance, e.g. due to random error. First, two means ($\bar{X}_1$ and $\bar{X}_2$) and the corresponding standard deviations (S_1 and S_2) are calculated by using the following equations:

$$\bar{X}_1 = \frac{\sum_{i=1}^{n_1} x_i}{n_1}, \bar{X}_2 = \frac{\sum_{i=1}^{n_2} x_i}{n_2} \tag{A1}$$

$$S_1 = \sqrt{\frac{\sum_{i=1}^{n_1} (\bar{x}_1 - x_i)^2}{n_1 - 1}}, S_2 = \sqrt{\frac{\sum_{i=1}^{n_2} (\bar{x}_2 - x_i)^2}{n_2 - 1}}, \tag{A2}$$

where n_1 and n_2 are the number of measurements in the data set 1 and 2. The standard deviation of the two data sets is given by

$$S_{1,2} = \sqrt{\frac{(n_1 - 1)S_1^2 + (n_2 - 1)S_2^2}{n_1 + n_2 - 2}} \tag{A3}$$

The value $N = n_1 + n_2 - 2$ is known in statistics as a degree of freedom and corresponds to the number of ways by which the system can vary. By knowing aforementioned

values it is possible to calculate the statistic t_{exp} value (experimental t value) by the given formula:

$$t_{exp} = \frac{|\bar{X}_1 - \bar{X}_2|}{S_{1,2}\sqrt{\frac{1}{n_1} + \frac{1}{n_2}}} \tag{A4}$$

Now the experimental t_{exp} value can be compared to the theoretical critical t_{theor} value that corresponds to the calculated degree of freedom N and the confidence limit (interval) of interest. The t_{theor} value can be found in books of statistical analysis, the confidence limit shows a reliability of an estimate. Thus, if t_{exp} is bigger than t_{theor} at the chosen confidence limit, the null hypothesis is rejected meaning that the difference between the two experimentally determined mean values is not due to the random results.

The p-value is often used in statistical significance testing in order to reject or approve the null hypothesis. The p-value is calculated by statistical analysis programs based on the calculated N and t_{exp} values and gives the probability of obtaining the results by assuming that the null hypothesis is true. If the p-value is less than a chosen significance level (e.g.0.05), the null hypothesis is rejected and the established claim is statistically significant at the chosen level.

Appendix B: Fitting Parameters of Core-levels

Each table represents the fit parameters for the experimentally obtained core-level spectra which were fitted with theoretical model curves using a commercial UNIFIT software [111]. The table shows the surface core-level shifts with respect to the bulk component ΔE, the Lorenzian broadening γ (lifetime broadening), the Gaussian broadening σ (experimental broadening), branching ratio R, spin orbital splitting SO, Duniach-Sunjic asymmetry α and peak intensity I relative to the bulk component.

B1 Nitridated Sapphire Layers

Clean sapphire layers nitridated at different temperatures recorded at normal emission (0°), Sec. 5.2.

Table B1: Fit parameters of the N 1*s*, O 1*s* and Al 2*p* core-levels recorded at normal emission from the clean sapphire layer nitridated at 700°C.

	ΔE / eV	γ / eV	σ / eV	R	SO / eV	I
$N-Al$	398.50±0.05	0.15±0.01	1.80±0.05	-	-	1.00
$N-O$	+1.65±0,05	0.15±0.01	1.80±0.05	-	-	0.62
N_d	-1.50±0.05	0.15±0.01	1.80±0.05	-	-	1.61
N_x	-3.40±0.05	0.15±0.01	1.80±0.05	-	-	0.09
$O-Al$	532.00±0.05	0.15±0.01	1.50±0.05	-	-	1.00
O_x-Al	-1.25±0.05	0.15±0.01	1.50±0.05	-	-	0.12
O_y	-2.55±0.05	0.15±0.01	1.50±0.05	-	-	0.01
$Al-O$	74.95±0.05	0.15±0.01	1.32±0.05	0.50±0.05	0.40±0.01	1.00
$Al-O_x$	-1.09±0.05	0.15±0.01	1.32±0.05	0.50±0.05	0.40±0.01	0.13

Table B2: Fit parameters of the N 1*s*, O 1*s* and Al 2*p* core-levels recorded at normal emission from the clean sapphire layer nitridated at 800°C.

	ΔE / eV	γ / eV	σ / eV	R	SO / eV	I
$N-Al$	398.50±0.05	0.15±0.01	1.80±0.05	-	-	1.00
$N-O$	+1.65±0,05	0.15±0.01	1.80±0.05	-	-	0.20
N_d	-1.50±0.05	0.15±0.01	1.80±0.05	-	-	0.37
N_x	-3.35±0.05	0.15±0.01	1.80±0.05	-	-	0.06
$O-Al$	531.96±0.05	0.15±0.01	1.50±0.05	-	-	1.00
$O-N$	+1.57±0.05	0.15±0.01	1.50±0.05	-	-	0.02
O_x-Al	-1.25±0.05	0.15±0.01	1.50±0.05	-	-	0.27
O_y	-2.55±0.05	0.15±0.01	1.50±0.05	-	-	0.08
$Al-O$	75.26±0.05	0.16±0.01	1.32±0.05	0.50±0.05	0.40±0.01	1
$Al-O_x$	-1.09±0.05	0.16±0.01	1.32±0.05	0.50±0.05	0.40±0.01	0.32
$Al-N$	-2.21±0.05	0.16±0.01	1.32±0.05	0.50±0.05	0.40±0.01	0.09

Table B3: Fit parameters of the N 1*s*, O 1*s* and Al 2*p* core-levels recorded at normal emission from the clean sapphire layer nitridated at 1050°C.

	ΔE / eV	γ / eV	σ / eV	R	SO / eV	I
$N-Al$	398.50±0.05	0.15±0.01	1.80±0.05	-	-	1.00
N_d	-1.50±0.05	0.15±0.01	1.80±0.05	-	-	0.32
N_x	-3.24±0.05	0.15±0.01	1.80±0.05	-	-	0.04
$O-Al$	533.00±0.05	0.15±0.01	1.50±0.05	-	-	1.00
$O-N$	+1.55±0.05	0.15±0.01	1.50±0.05	-	-	0.05
O_x-Al	-1.25±0.05	0.15±0.01	1.50±0.05	-	-	0.40
O_y	-2.53±0.05	0.15±0.01	1.50±0.05	-	-	0.08
$Al-O$	75.67±0.05	0.16±0.01	1.33±0.05	0.50±0.05	0.40±0.01	1
$Al-O_x$	-1.09±0.05	0.16±0.01	1.33±0.05	0.50±0.05	0.40±0.01	0.56
$Al-N$	-2.21±0.05	0.16±0.01	1.33±0.05	0.50±0.05	0.40±0.01	0.17

Clean sapphire layers nitridated at different temperatures and recorded at emission at 80° with respect to the surface, Sec. 5.2.

Table B4: Fit parameters of the N 1s core-level recorded from the clean sapphire layer nitridated at 700°C and 1050°C at emission of 80° with respect to the surface normal and pass energy of 10 eV.

	ΔE / eV	γ / eV	σ / eV	R	SO / eV	I
$T_{nitr} = 700°C$						
$N-Al$	398.50±0.05	0.15±0.01	1.60±0.05	-	-	1.00
$N-O$	+1.65±0,05	0.15±0.01	1.60±0.05	-	-	0.71
N_d	-1.50±0.05	0.15±0.01	1.60±0.05	-	-	0.94
N_x	-3.40±0.05	0.15±0.01	1.60±0.05	-	-	0.51
$T_{nitr} = 1050°C$						
$N-Al$	398.50±0.05	0.15±0.01	1.65±0.05	-	-	1.00
$N-O_x$	+3.80±0.05	0.15±0.01	1.65±0.05	-	-	0.26
$N-O$	+1.60±0.05	0.15±0.01	1.65±0.05	-	-	0.47
N_d	-1.48±0.05	0.15±0.01	1.65±0.05	-	-	0.17
N_x	-3.45±0.05	0.15±0.01	1.65±0.05	-	-	0.24

B2 Polar InN layers

Table B5: Fit parameters of the In 3*d*5/2, N 1*s* and O 1*s* core-levels recorded at normal emission from the oxidized N-polar InN layer grown by MOVPE (shown in Fig. 6.5). The Duniach-Sunjic asymmetry α equals 0.03 for each component in the shown core-levels.

	ΔE / eV	γ / eV	σ / eV	R	SO / eV	I
$In-N$	443.80±0.05	0.15±0.01	1.14±0.05	0.67±0.05	7.60±0.01	1.00
$O-In-O$	+0.85±0.05	0.15±0.01	1.14±0.05	0.67±0.05	7.60±0.01	0.26
In_x	+1.77±0.05	0.15±0.01	1.14±0.05	0.67±0.05	7.60±0.01	0.66
$In-In$	-1.55±0.05	0.15±0.01	1.14±0.05	0.67±0.05	7.60±0.01	0.01
$N-In$	396.18±0.05	0.15±0.01	0.93±0.05	-	-	1.00
N_x	+0.77±0.05	0.15±0.01	0.93±0.05	-	-	0.29
N_c	+1.63±0.05	0.15±0.01	0.93±0.05	-	-	0.10
$O-In$	531.55±0.05	0.15±0.01	1.30±0.05	-	-	1.00
O_{ad1}	+0.81±0.05	0.15±0.01	1.30±0.05	-	-	0.36
O_{ad2}	+1.91±0.05	0.15±0.01	1.30±0.05	-	-	0.04
$In-O-In$	-1.35±0.05	0.15±0.01	1.30±0.05	-	-	0.12

Table B6: Fit parameters of the In 3*d*5/2, N 1*s* and O 1*s* core-levels recorded at normal emission from the clean N-polar InN layer grown by MOVPE (shown in Fig. 6.13). The Duniach-Sunjic asymmetry α equals 0.03 for each component in the shown core-levels.

	ΔE / eV	γ / eV	σ / eV	R	SO / eV	I
$In-N$	443.71±0.05	0.15±0.01	1.10±0.05	0.67±0.05	7.60±0.01	1.00
$O-In-O$	+0.85±0.05	0.15±0.01	1.10±0.05	0.67±0.05	7.60±0.01	0.19
In_x	+1.74±0.05	0.15±0.01	1.10±0.05	0.67±0.05	7.60±0.01	0.03
$In-In$	-1.41±0.05	0.15±0.01	1.10±0.05	0.67±0.05	7.60±0.01	0.01
$N-In$	396.26±0.05	0.15±0.01	0.92±0.05	-	-	1.00
N_x	+0.71±0.05	0.15±0.01	0.92±0.05	-	-	0.15
N_c	+1.64±0.05	0.15±0.01	0.92±0.05	-	-	0.04
N_z	+2.65±0.05	0.15±0.01	0.92±0.05	-	-	0.01
$O-In$	531.39±0.05	0.15±0.01	1.28±0.05	-	-	1.00
O_{ad1}	+0.81±0.05	0.15±0.01	1.28±0.05	-	-	0.24
$In-O-In$	-1.35±0.05	0.15±0.01	1.28±0.05	-	-	0.25

Table B7: Fit parameters of the In 3*d*5/2, N 1*s* and O 1*s* core-levels recorded at normal emission from the oxidized N-polar InN layer with the rough surface grown by MEAglow (shown in Fig. 6.6). The Duniach-Sunjic asymmetry α equals 0.025 for each component in the shown core-levels.

	ΔE / eV	γ / eV	σ / eV	R	SO / eV	I
$In-N$	443.81±0.05	0.15±0.01	0.92±0.05	0.67±0.05	7.60±0.01	1.00
$O-In-O$	+0.85±0.05	0.15±0.01	0.92±0.05	0.67±0.05	7.60±0.01	0.27
In_x	+1.76±0.05	0.15±0.01	0.92±0.05	0.67±0.05	7.60±0.01	0.03
$In-C$	-1.38±0.05	0.15±0.01	0.92±0.05	0.67±0.05	7.60±0.01	0.01
$N-In$	396.21±0.05	0.15±0.01	0.71±0.05	-	-	1.00
N_x	+0.72±0.05	0.15±0.01	0.71±0.05	-	-	0.22
N_y	+1.61±0.05	0.15±0.01	0.71±0.05	-	-	0.05
N_z	+2.38±0.05	0.15±0.01	0.71±0.05	-	-	0.02
$O-In$	531.27±0.05	0.15±0.01	1.10±0.05	-	-	1.00
O_{ad1}	+0.82±0.05	0.15±0.01	1.10±0.05	-	-	0.92
O_{ad2}	+2.04±0.05	0.15±0.01	1.10±0.05	-	-	0.32
$In-O-In$	-1.35±0.05	0.15±0.01	1.10±0.05	-	-	0.27

Table B8: Fit parameters of the In 3*d*5/2, N 1*s* and O 1*s* core-levels recorded at emission of 80° with respect to the surface normal from the oxidized N-polar InN layer with the rough surface grown by MEAglow (shown in Fig. 6.6). The Duniach-Sunjic asymmetry α equals 0.025 for each component in the shown core-levels.

	ΔE / eV	γ / eV	σ / eV	R	SO / eV	I
$In-N$	443.82±0.05	0.15±0.01	0.93±0.05	0.67±0.05	7.60±0.01	1.00
$O-In-O$	+0.86±0.05	0.15±0.01	0.93±0.05	0.67±0.05	7.60±0.01	0.42
In_x	+1.76±0.05	0.15±0.01	0.93±0.05	0.67±0.05	7.60±0.01	0.11
$In-C$	-1.35±0.05	0.15±0.01	0.93±0.05	0.67±0.05	7.60±0.01	0.02
$N-In$	396.19±0.05	0.15±0.01	0.72±0.05	-	-	1.00
N_x	+0.69±0.05	0.15±0.01	0.72±0.05	-	-	0.33
N_y	+1.64±0.05	0.15±0.01	0.72±0.05	-	-	0.09
N_z	+2.44±0.05	0.15±0.01	0.72±0.05	-	-	0.03
$O-In$	531.36±0.05	0.15±0.01	1.10±0.05	-	-	1.00
O_{ad1}	+0.87±0.05	0.15±0.01	1.10±0.05	-	-	0.88
O_{ad2}	+2.03±0.05	0.15±0.01	1.10±0.05	-	-	0.41
$In-O-In$	-1.35±0.05	0.15±0.01	1.10±0.05	-	-	0.33

Table B9: Fit parameters of the In 3*d*5/2, N 1*s* and O 1*s* core-levels recorded at normal emission from the clean N-polar InN layer with the rough surface grown by MEAglow (shown in Fig. 6.14). The Duniach-Sunjic asymmetry α equals 0.025 for each component in the shown core-levels.

	ΔE / eV	γ / eV	σ / eV	R	SO / eV	I
$In-N$	443.85±0.05	0.15±0.01	0.90±0.05	0.67±0.05	7.60±0.01	1.00
$O-In-O$	+0.81±0.05	0.15±0.01	0.90±0.05	0.67±0.05	7.60±0.01	0.20
In_x	+1.81±0.05	0.15±0.01	0.90±0.05	0.67±0.05	7.60±0.01	0.01
$In-C$	-1.36±0.05	0.15±0.01	0.90±0.05	0.67±0.05	7.60±0.01	0.01
$N-In$	396.27±0.05	0.15±0.01	0.72±0.05	-	-	1.00
N_x	+0.69±0.05	0.15±0.01	0.72±0.05	-	-	0.15
N_y	+1.67±0.05	0.15±0.01	0.72±0.05	-	-	0.06
N_z	+2.46±0.05	0.15±0.01	0.72±0.05	-	-	0.05
$O-In$	530.00±0.05	0.15±0.01	1.10±0.05	-	-	1.00
$In-O-In$	-1.35±0.05	0.15±0.01	1.10±0.05	-	-	0.32

Table B10: Fit parameters of the In 3*d*5/2, N 1*s* and O 1*s* core-levels recorded at emission of 80° with respect to the surface normal from the oxidized N-polar InN layer with the rough surface grown by MEAglow (shown in Fig. 6.14). The Duniach-Sunjic asymmetry α equals 0.025 for each component in the shown core-levels.

	ΔE / eV	γ / eV	σ / eV	R	SO / eV	I
$In-N$	443.80±0.05	0.15±0.01	0.95±0.05	0.67±0.05	7.60±0.01	1.00
$O-In-O$	+0.81±0.05	0.15±0.01	0.95±0.05	0.67±0.05	7.60±0.01	0.26
In_x	+1.80±0.05	0.15±0.01	0.95±0.05	0.67±0.05	7.60±0.01	0.02
$In-C$	-1.35±0.05	0.15±0.01	0.95±0.05	0.67±0.05	7.60±0.01	0.01
$N-In$	396.19±0.05	0.15±0.01	0.72±0.05	-	-	1.00
N_x	+0.69±0.05	0.15±0.01	0.72±0.05	-	-	0.24
N_y	+1.66±0.05	0.15±0.01	0.72±0.05	-	-	0.07
N_z	+2.40±0.05	0.15±0.01	0.72±0.05	-	-	0.07
$O-In$	530.01±0.05	0.15±0.01	1.10±0.05	-	-	1.00
$In-O-In$	-1.35±0.05	0.15±0.01	1.10±0.05	-	-	0.47

Table B11: Fit parameters of the In 3*d*5/2, N 1*s* and O 1*s* core-levels recorded at normal emission from the oxidized In-polar InN layer grown by MBE (shown in Fig. 6.29). The Duniach-Sunjic asymmetry α equals 0.028±0.02 for each component in the shown core-levels.

	ΔE / eV	γ / eV	σ / eV	R	SO / eV	I
$In-N$	443.75±0.05	0.15±0.01	0.98±0.05	0.67±0.05	7.60±0.01	1.00
$O-In-O$	+0.90±0.05	0.15±0.01	0.98±0.05	0.67±0.05	7.60±0.01	0.21
In_x	+1.86±0.05	0.15±0.01	0.98±0.05	0.67±0.05	7.60±0.01	0.06
$In-In$	-1.50±0.05	0.15±0.01	0.98±0.05	0.67±0.05	7.60±0.01	0.01
$N-In$	396.23±0.05	0.15±0.01	0.84±0.05	-	-	1.00
N_x	+0.70±0.05	0.15±0.01	0.84±0.05	-	-	0.15
$O-In$	530.98±0.05	0.15±0.01	1.35±0.05	-	-	1.00
In_{ad1}	+1.23±0.05	0.15±0.01	1.35±0.05	-	-	4.58
In_{ad2}	+2.72±0.05	0.15±0.01	1.35±0.05	-	-	0.72
$In-O-In$	-0.73±0.05	0.15±0.01	1.35±0.05	-	-	0.30

Table B12: Fit parameters of the In 3*d*5/2, N 1*s* and O 1*s* core-levels recorded at emission of 70° with respect to the surface normal from the oxidized In-polar InN layer grown by MBE (shown in Fig. 6.29). The Duniach-Sunjic asymmetry α equals 0.03 for each component in the shown core-levels.

	ΔE / eV	γ / eV	σ / eV	R	SO / eV	I
$In-N$	443.87±0.05	0.15±0.01	0.99±0.05	0.67±0.05	7.60±0.01	1.00
$O-In-O$	+0.92±0.05	0.15±0.01	0.99±0.05	0.67±0.05	7.60±0.01	0.53
In_x	+1.87±0.05	0.15±0.01	0.99±0.05	0.67±0.05	7.60±0.01	0.29
$N-In$	396.29±0.05	0.15±0.01	0.82±0.05	-	-	1.00
N_x	+0.74±0.05	0.15±0.01	0.82±0.05	-	-	0.22
$O-In$	531.91±0.05	0.15±0.01	1.36±0.05	-	-	1.00
In_{ad1}	+1.22±0.05	0.15±0.01	1.36±0.05	-	-	0.43
In_{ad2}	+2.34±0.05	0.15±0.01	1.36±0.05	-	-	0.05

Table B13: Fit parameters of the In 3*d*5/2 and N 1*s* core-levels recorded at normal emission from the clean In-polar InN layer grown by MBE (shown in Fig. 6.38). The Duniach-Sunjic asymmetry α equals 0.03 for each component in the shown core-levels.

	ΔE / eV	γ / eV	σ / eV	R	SO / eV	I
$In-N$	443.86±0.05	0.15±0.01	0.99±0.05	0.67±0.05	7.60±0.01	1.00
$O-In-O$	+0.90±0.05	0.15±0.01	0.99±0.05	0.67±0.05	7.60±0.01	0.19
In_x	+1.83±0.05	0.15±0.01	0.99±0.05	0.67±0.05	7.60±0.01	0.02
$In-In$	-1.52±0.05	0.15±0.01	0.99±0.05	0.67±0.05	7.60±0.01	0.02
$N-In$	396.28±0.05	0.15±0.01	0.83±0.05	-	-	1.00
N_x	+0.77±0.05	0.15±0.01	0.83±0.05	-	-	0.06

Table B14: Fit parameters of the In 3*d*5/2 and N 1*s* core-levels recorded at emission of 80° with respect to the surface normal from the clean In-polar InN layer grown by MBE (shown in Fig. 6.38). The Duniach-Sunjic asymmetry α equals 0.03 for each component in the shown core-levels.

	ΔE / eV	γ / eV	σ / eV	R	SO / eV	I
$In-N$	444.10±0.05	0.15±0.01	1.04±0.05	0.67±0.05	7.60±0.01	1.00
$O-In-O$	+0.82±0.05	0.15±0.01	1.04±0.05	0.67±0.05	7.60±0.01	0.74
In_x	+1.84±0.05	0.15±0.01	1.04±0.05	0.67±0.05	7.60±0.01	0.07
$In-In$	-1.48±0.05	0.15±0.01	1.04±0.05	0.67±0.05	7.60±0.01	0.02
$N-In$	396.38±0.05	0.16±0.01	0.83±0.05	-	-	1.00
N_x	+0.80±0.05	0.16±0.01	0.83±0.05	-	-	0.21
N_y	+1.89±0.05	0.16±0.01	0.83±0.05	-	-	0.27
N_z	+2.98±0.05	0.16±0.01	0.83±0.05	-	-	0.15

B3 Thermally oxidized In-polar InN layer

Table B15: Fit parameters of the In 3*d*5/2, N 1*s* and O 1*s* core-levels recorded at normal emission from the thermally oxidized In-polar InN layer (shown in Fig. 7.9). The Duniach-Sunjic asymmetry α equals 0.03 for each component in the shown core-levels.

	ΔE / eV	γ / eV	σ / eV	R	SO / eV	I
$In-N$	443.95±0.05	0.15±0.01	1.04±0.05	0.67±0.05	7.60±0.01	1.00
$O-In-O$	+0.64±0.05	0.15±0.01	1.04±0.05	0.67±0.05	7.60±0.01	1.32
In_x	+1.48±0.05	0.15±0.01	1.04±0.05	0.67±0.05	7.60±0.01	0.23
$In-In$	-1.54±0.05	0.15±0.01	1.04±0.05	0.67±0.05	7.60±0.01	0.03
$N-In$	396.31±0.05	0.15±0.01	0.82±0.05	-	-	1.00
N_x	+0.77±0.05	0.15±0.01	0.82±0.05	-	-	0.12
N_y	+1.92±0.05	0.15±0.01	0.82±0.05	-	-	0.02
N_z	+2.89±0.05	0.15±0.01	0.82±0.05	-	-	0.02
$O-In$	530.86±0.05	0.15±0.01	1.05±0.05	-	-	1.00
In_{ad1}	+1.17±0.05	0.15±0.01	1.05±0.05	-	-	0.17
$In-O-In$	-0.75±0.05	0.15±0.01	1.05±0.05	-	-	8.48

Table B16: Fit parameters of the In 3*d*5/2, N 1*s* and O 1*s* core-levels recorded at emission of 80° with respect to the surface normal from the thermally oxidized In-polar InN layer (shown in Fig. 7.9). The Duniach-Sunjic asymmetry α equals 0.03 for each component in the shown core-levels.

	ΔE / eV	γ / eV	σ / eV	R	SO / eV	I
$In-N$	443.95±0.05	0.15±0.01	1.05±0.05	0.67±0.05	7.60±0.01	1.00
$O-In-O$	+0.69±0.05	0.15±0.01	1.05±0.05	0.67±0.05	7.60±0.01	6.03
In_x	+1.50±0.05	0.15±0.01	1.05±0.05	0.67±0.05	7.60±0.01	2.26
$In-In$	-1.54±0.05	0.15±0.01	1.05±0.05	0.67±0.05	7.60±0.01	0.08
$N-In$	396.38±0.05	0.15±0.01	0.83±0.05	-	-	1.00
N_x	+0.77±0.05	0.15±0.01	0.83±0.05	-	-	0.51
N_y	+1.93±0.05	0.15±0.01	0.83±0.05	-	-	0.64
N_z	+2.90±0.05	0.15±0.01	0.83±0.05	-	-	0.87
$O-In$	530.91±0.05	0.15±0.01	1.07±0.05	-	-	1.00
In_{ad1}	+1.17±0.05	0.15±0.01	1.07±0.05	-	-	0.33
In_{ad2}	+1.98±0.05	0.15±0.01	1.07±0.05	-	-	0.20
$In-O-In$	-0.75±0.05	0.15±0.01	1.07±0.05	-	-	3.72

Appendix C: Calculations from XRD Measurements

Calculations of crystal lattice constants from 2Θ scan.

In the hexagonal wurtzite structure the distance between the parallel planes of atoms (interplanar spacing) d_{hkl} for a set of parallel planes (*hk.l*) is given by

$$\frac{1}{d_{hkl}^2} = \frac{4 \cdot (h^2 + k^2 + h \cdot k)}{3 \cdot a^2} + \frac{l^2}{c^2}, \tag{C1}$$

where *a* and *c* are the lattice constants; *h*, *k* and *l* are the Miller indexes. By combining Eq.C1 with Bragg´s Law

$$2 \cdot d_{hkl} \cdot \sin\Theta = \lambda_{k_\alpha}, \tag{C2}$$

the lattice constants *a* and *c* can be estimated by measuring two different X-ray reflections, e.g. (30.2) and (00.2). (Θ is an angle measured by XRD).

Calculations of dislocation density from ω scan.

Dislocation density estimation is based on measuring the broadening (ω - FWHM) of the (00.2) and (30.2) reflections. According to Ref. [169], the density of screw type threading dislocations is given by

$$N_s = \frac{\alpha^2}{4.35 \cdot b_s^2}, \tag{C3}$$

where α is the ω - FWHM of the (00.2) reflection and the Burgers vector b_s is given by the *c*-lattice constant of 0.5669 nm for InN from Ref. [22].

$$\alpha = FWHM_{00.2}(rad), \tag{C4}$$

$$b_s = c_0 \tag{C5}$$

Edge type dislocation densities can be calculated by

$$N_e = \frac{\beta^2}{4.35 \cdot b_e^2}, \tag{C6}$$

where β is the ω-FWHM of the (30.2) reflection. The Burgers vector b_e is the a-lattice constant of InN given by $a_0 = 0.3535$ nm [22].

$$\beta = FWHM_{30.2}(rad), \tag{C7}$$

$$b_e = a_0 \tag{C8}$$

All calculations have been performed by F. Mehnke, TU Berlin.

Acknowledgements

This work would not have been possible without the help, cooperation and support of many people. I want to express my heartfelt gratitude to everyone who was directly or indirectly involved in this work and helped me to successfully complete it. In particulary I want to thank the following people:

Prof. Dr. Michael Kneissl for supervising this work and giving me the opportunity to work in his group at TU Berlin.

Dr. Patrick Vogt for his support, supervising and helpful discussions as well as for the nice working atmosphere.

Dr. Duc Van Dinh for providing me with the MOVPE grown InN samples, for the fruitful discussions, new ideas for experiments and collaboration. He was always ready to help me and was looking forward to any scientific discussion.

Prof. Dr. Nobert Esser for his support and useful corrections of this thesis.

Dr. Pierre Ruterana for (HR)TEM measurements, supervision of the Rainbow project, organization of very nice project meetings and his effort during my visit to his group.

Dr. Markus Pristovsek for his interest in InN, sharing of ideas and discussions.

Amelie Biermann, Marcel Ewald and Dr. Thomas Bruhn for teaching me how to work on experimental equipment and UHV chambers, for many hours spent by finding out the cause of problems in the experimental equipment and fixing the UHV-components.

Sabine Alamé and Julian Plaickner for the teamwork and performed measurements during their Diploma (Master) work. I learned with them how to be a good mentor and a good friend at the same time.

Frank Mehnke for the XRD measurements and always a positive atmosphere.

Albert Minj (UNIBO, Italy), Francesco Ivaldi (IFPAN, Poland), Wojtek Linhart (UW, UK), Öcal Tuna (AIXTRON, Germany), Arantxa Vilalta-Clemente (CIMAP, France), Geeta Rani Mutta (CIMAP, France) and all other members of the Rainbow project for all kind of collaborations and the great atmosphere during all training and workshops meetings.

Dr. Marcel Himmerlich for his interest in my research field, discussions and supply of the MBE grown InN samples. Dr. Ingrid Koslow for supplying me with the semipolar InGaN layers and Dr. Marc Hoffmann for the GaN samples.

For proof reading of the manuscript I want to thank Dr. Patrick Vogt, Dr. Duc Van Dinh, Prof. Dr. Nobert Esser and Martin Frentrup as well as Dr. Ingrid Koslow, Dr. Albert Minj and Dr. Andrea Navarro Quezada for performing English corrections.

Claudia Hinrichs for her help with all administrative things and being always ready to help and explain things to me. Engelbert Eder for his help in fixing every possible broken electronic devices starting from a simple torch finishing by complicated power supplies, Matthias Dreier for supplying me with chemical solutions for experiments, and the people of the workshop for their support in all kind of problems.

I want to thank all members of Prof. Dr. Kneissl´s group for the nice and pleasant working atmosphere, traveling after the conferences, as well as video, karaoke and game evenings in the Teelabor. Particulary thanks to Sabine Alamé, Neysha Lobo, Frank Mehnke, Martin Frentrup, Christoph Reich, Dr. Tim Wernicke, Dr. Jens Raß and Dr. Raimund Kremzow.

Outside my colleague-circle, I want to thank all my friends from Moscow, for keeping in touch with me and still remaining friends despite the distance and my long stay abroad, as well as my friends from Germany for making me feel at home in Berlin and for all the great time we have spent together.

Finally I want to express my deepest thank to my brother Stanislav, my parents and grandparent. They have always supported me during the whole time of my work at TU Berlin, they encouraged me and believed in me, I would not be the person I am today without them. Very special thanks to my mother Olga and grandmother Natalia, to whom I dedicate this thesis... .

This work was financially supported by the EU-ITM Rainbow project within the 7th Framework Program (FP7), under grant agreement No. PINT-GA-2008-213238